

RUPRECHT-KARLS-UNIVERSITÄT HEIDELBERG



Klaus Alexander Tadday

---

Scintillation Light Detection and Application of  
Silicon Photomultipliers in Imaging Calorimetry and  
Positron Emission Tomography

Dissertation

HD-KIP-12-22

KIRCHHOFF-INSTITUT FÜR PHYSIK



Dissertation  
submitted to the  
Combined Faculties of the Natural Sciences and Mathematics  
of the Ruperto-Carola-University of Heidelberg, Germany  
for the degree of  
Doctor of Natural Sciences

Put forward by  
Dipl.-Phys. Klaus Alexander Tadday  
born in Ludwigsburg  
Oral examination: 14.12.2011



# Scintillation Light Detection and Application of Silicon Photomultipliers in Imaging Calorimetry and Positron Emission Tomography

Referees: Prof. Dr. Hans-Christian Schultz-Coulon  
Prof. Dr. Norbert Herrmann



## Abstract

This thesis deals with the weak light signals created in organic and inorganic scintillators, and their detection with silicon photomultipliers (SiPM). In this context, two fields of application are studied: hadron calorimetry, and the medical imaging technique of positron emission tomography.

The result of a measurement of Birks' coefficient  $kB$  is presented for the plastic scintillator tiles used in the analogue hadronic calorimeter prototype of the CALICE collaboration. The extracted  $kB$  is significantly larger compared to the default value used in previous Geant4 simulation studies. A new simulation method was developed which enables an improved description of the ionisation quenching effect. The impact on the simulated calorimeter response is demonstrated by means of a particle shower simulation study.

A test environment was developed in order to pursue a complete SiPM characterisation, thus enabling a comparison of different SiPM types. The range of measurements covers the determination of the cross-talk and after-pulse corrected photon detection efficiency, and measurements of the spatial uniformity of single pixels. The characteristics of several different SiPM types and the derived qualification for different fields of application are discussed. In order to investigate the utility of SiPMs for the positron emission tomography application, a small-scale detector prototype was developed. First characterisation studies on the system are presented.

## Zusammenfassung

Diese Arbeit befasst sich mit den schwachen Lichtsignalen von organischen und anorganischen Szintillatoren und deren Nachweis mit Silizium Photomultipliern (SiPM). In diesem Zusammenhang werden zwei Anwendungsgebiete untersucht: Hadronkalorimeter und das bildgebende Verfahren der Positronen-Emissions-Tomographie.

Das Ergebnis einer Messung des Birksschen Koeffizienten  $kB$  wird vorgestellt für die Plastiksintillatorkacheln des analogen hadronischen Kalorimeterprototyps der CALICE Kollaboration. Der ermittelte  $kB$ -Wert ist signifikant größer als der bisher in Geant4-Simulationsstudien benutzte Wert. Eine neue Simulationsmethode wurde entwickelt, mit deren Hilfe eine verbesserte Beschreibung des Ionisations-Quenching-Effekts möglich ist. Der Einfluss auf das simulierte Kalorimetersignal wird anhand einer Teilchenschauer-Simulationsstudie verdeutlicht.

Eine Testumgebung wurde entwickelt um eine vollständige SiPM Charakterisierung zu ermöglichen und verschiedene SiPM Bauarten zu vergleichen. Das Messspektrum umfasst die Bestimmung der Photon-Detektions-Effizienz unter Berücksichtigung der Beiträge des optischen Übersprechens und der auftretenden Nachpulse. Zusätzlich wurde das räumliche Ansprechverhalten einzelner Pixel gemessen. Die gewonnenen Erkenntnisse zu den unterschiedlichen Sensor-typen und die daraus abgeleitete Qualifikation für verschiedene Anwendungsgebiete werden diskutiert. Um die Eignung von SiPMs für die Positronen-Emissions-Tomographie zu untersuchen, wurde ein Detektorprototyp im kleinen Maßstab entwickelt. Erste Charakterisierungsstudien des Systems werden vorgestellt.



# Contents

<b>1</b>	<b>Introduction</b>	<b>1</b>
1.1	Imaging Detectors with Silicon Photomultipliers . . . . .	4
1.1.1	Analogue Hadronic Calorimeter . . . . .	4
1.1.2	Detectors for Positron Emission Tomography . . . . .	6
1.2	Calorimetry . . . . .	8
1.2.1	Interaction of Particles and Radiation with Matter . . . . .	8
1.2.2	Strong Particle Interactions . . . . .	17
1.2.3	Introduction to Scintillators . . . . .	20
1.2.4	Calorimeter Types . . . . .	28
<b>2</b>	<b>Towards Precise Monte Carlo Simulations of the Scintillation Mechanism</b>	<b>33</b>
2.1	Ionisation Quenching in Organic Scintillators . . . . .	34
2.2	Measurement of Birks' Coefficient for the AHCAL Scintillator . . . . .	39
2.3	Simulation of Birks' Law in Geant4 . . . . .	42
2.4	Impact on the Energy Scale of Particle Showers . . . . .	50
<b>3</b>	<b>Photodetection</b>	<b>57</b>
3.1	Photomultiplier Tube . . . . .	57
3.2	Silicon Photodetectors . . . . .	60
3.3	PIN Photodiodes . . . . .	60
3.4	Avalanche Photodiodes . . . . .	62
3.5	Geiger Mode Photodiodes . . . . .	65
3.6	Silicon Photomultiplier . . . . .	67
<b>4</b>	<b>Determination of SiPM Characteristics</b>	<b>75</b>
4.1	Current-Voltage Characteristics . . . . .	75
4.2	Gain . . . . .	78
4.3	Dark-rate . . . . .	82
4.4	Cross-talk Probability . . . . .	85
4.5	After-pulse Probability . . . . .	87
4.6	Photon Detection Efficiency . . . . .	90
4.7	SiPM Uniformity Measurements . . . . .	101
<b>5</b>	<b>Construction and Commissioning of a Small-Scale PET Prototype</b>	<b>111</b>
5.1	Operation Principle of a PET Detector . . . . .	111
5.2	Time-of-Flight Method in PET . . . . .	113
5.3	Background Reduction . . . . .	114
5.4	Classical Detector Module Design . . . . .	116
5.5	Construction of a PET Detector with SiPMs . . . . .	117
5.6	First Results . . . . .	120

<b>6 Conclusion</b>	<b>123</b>
<b>A Supplementary Material</b>	<b>127</b>
A.1 Measurement Setup for Birks' Coefficient . . . . .	127
A.2 Germanium Detector Calibration . . . . .	128
A.3 Light Yield Measurement . . . . .	128
A.4 Simulation of the Test-beam Environment with MOKKA . . . . .	129
A.5 Digitisation . . . . .	130
A.6 GeV to MIP Conversion . . . . .	131
A.7 SiPM Active Area . . . . .	133
A.8 Gain Calibration Factor . . . . .	133
A.9 Pixel Recovery Time . . . . .	134
A.10 PDE Measurement Setup . . . . .	135
A.11 Spectral Response of the PIN Photodiode and LED Emission Spectra . . . . .	136
A.12 Uniformity Scan Setup . . . . .	137
A.13 Determination of the Geometrical Efficiency . . . . .	138
A.14 Effect at Small Sensitivity Thresholds . . . . .	138
A.15 Development of a PET Prototype . . . . .	139
<b>Nomenclature</b>	<b>141</b>
<b>Bibliography</b>	<b>143</b>
<b>Danksagung</b>	<b>149</b>

# Chapter 1

## Introduction

Experimental observations within the last century had a significant impact on our understanding of matter and its constituents. Since most of the fundamental interactions defining the properties of our universe are not instantly visible to the human eye, the relevance of particle detectors, facilitating the measurement and visualisation of particles and radiation, was recognised very soon. An important step towards our subatomic image was made by Rutherford in 1911. His discovery of the atomic nucleus was enabled by a simple type of scintillating detector: a screen coated with a thin layer of zinc sulphide. With this detector, it was possible to measure the deflection angles of alpha particles, scattered off a thin gold foil, counting – by eye – the light flashes produced when the deflected alpha particles hit the scintillating screen.

The invention of the *photomultiplier tube* (PMT) in the 1930s [1, 2], enabled for the first time a quantitative measurement of the weak light flashes produced by particle interactions in a scintillator. This fundamental measurement principle still forms the basis for a large variety of modern particle detectors. Meanwhile new, improved scintillators and photodetectors have been developed to meet the continuously increasing experimental demands in terms of measurement precision and critical operation environments. This thesis is devoted to such a new photodetector development, the *silicon photomultiplier* (SiPM), which has a high potential to replace classical photomultiplier tubes in some of the most recent detector developments in the field of high energy physics calorimetry and medical imaging.

In the years after Rutherford's discovery, it was found that the atomic nucleus is not elementary and consists of protons and neutrons. Advancements in the field of detector instrumentation significantly contributed to the discovery of a multitude of particles: the positron (1932), the muon (1937), the pion (1947), the antiproton (1955) and the neutrino (1956). These discoveries settled the foundation for modern elementary particle physics. A huge development step was initiated with the construction of subatomic particle colliders, providing the unique possibility to investigate the proton structure, and the production and study of short-lived particles under laboratory conditions. The rapidly increasing centre of mass energies initiated a new era of particle physics with the development of the Standard Model – one of the great achievements of science within the last decades. According to the Standard Model, matter consists of two types of fermions (spin 1/2-particles): leptons and quarks. A second component is given by the bosons (spin 1 particles), which mediate the strong, weak and electromagnetic force. A third necessary component of the Standard Model, the Higgs mechanism, could not yet be verified. It is expected to be responsible for the electroweak symmetry breaking, resulting in the separation of the weak and the electromagnetic force and gives the particles their mass. A large variety of alternative and complementary theories exist, such as supersymmetry, models involving extra dimensions, or other extensions of the Standard Model. It is hence one of todays main objectives in the field of particle physics to discover the Standard Model Higgs particle, or particles predicted by alternative theories, if they exist. The chances for such discoveries are good, since

the *Large Hadron Collider* (LHC) at CERN<sup>1</sup>, operating since the end of 2009, is designed to reach an unprecedented centre of mass energy of up to 14 TeV, covering the expected mass of the Standard Model Higgs boson and several supersymmetric particles. However, the measurement precision of a hadron collider is fundamentally limited due to the substructure of the colliding objects, consisting of quarks and gluons. It is experimentally impossible to identify the momentum of the quarks or gluons participating in the interaction, hence it is difficult to precisely determine and control the initial state of the particle collision.

In case of an electron-positron accelerator, the situation is different due to the elementary nature of the colliding objects. One major advantage compared to a hadron collider is the well defined centre of mass energy, easily controlled by the energy of the particle beams. Additionally, precise measurements of the particle spin are possible due to the ability to provide polarised electron and positron beams. The logical successor of the LHC will therefore most probably be an electron-positron collider reaching a higher centre of mass energy compared to previous lepton colliders. Even though the requirements on the detector system are less stringent in terms of radiation hardness or rate capability, with respect to the LHC, the aimed measurement precision requires the development of completely new detector technologies and analysis methods.

In order to achieve the envisaged jet-energy resolution of 3 – 4 %, necessary for the separation of the hadronically decaying W- and Z-bosons, new concepts for the energy measurement have to be found. The particle flow method is a promising approach which attempts to combine the information of the tracking system and the calorimeters to reconstruct the full event topology. To make this method work efficiently, a highly granular calorimetric system is one of the key requirements. It is the aim of the CALICE<sup>2</sup> collaboration to develop calorimeter prototypes that are designed to match the requirements for a future electron-positron collider. Complementary concepts are pursued differing in the used detection mechanism and in the readout technology.

This work is concerned with the development of the *analogue hadronic calorimeter* (AHCAL) prototype [3]. It has a sampling structure made of steel absorber plates, interleaved with plastic scintillator layers, structured into small tiles. A silicon photomultiplier is incorporated into each scintillator tile to measure the light produced. The main advantages of these devices are a high gain  $O(10^6)$ , compactness  $O(1 \text{ mm}^2)$  and the insensitivity to magnetic fields, making them a perfect choice for the AHCAL. In the first prototype version of the AHCAL roughly 8000 SiPMs, produced by MEPhI/Pulsar, are used. They belong to an early generation of these devices, featuring a relatively low *photon detection efficiency* (PDE) in the blue spectral region. For this reason, it was necessary to incorporate a wavelength shifting fibre into each tile which converts the blue light produced in the scintillator tile into green light and guides it to the SiPM where it is measured. New, blue sensitive SiPMs may however facilitate a direct measurement of the scintillation light, thus reducing the complexity and the cost of the detector assembly.

The number of potential SiPM applications has increased during the last years and the multitude of SiPM producing companies and institutes has lead to a steadily growing variety of different detectors. For an objective comparison, the characteristic properties need to be determined. The reference data provided by the manufacturers often don't contain the required information, or the provided characteristics have been determined using different experimental techniques and are therefore not comparable. In order to develop accurate calibration schemes for SiPMs, a comprehensive understanding of their properties is required. However, the complex interplay between the various effects in a SiPM makes the realisation of this goal difficult.

---

<sup>1</sup>European Organisation for Nuclear Research.

<sup>2</sup>Calorimetry for the next linear collider experiment.

---

In order to select the devices best suited for following prototype generations, and in order to disentangle and quantify the individual SiPM effects, it is necessary to establish test environment facilitating a broad range of characterisation measurements. Within the scope of this thesis, such a test environment was developed, comprising a variety of different characterisation measurements and analysis methods. A multitude of different SiPM devices were successfully characterised, providing valuable information about the utility for certain fields of application. Results of this work have been published in a scientific journal [4].

In this work, particular attention is paid to a special application of SiPMs – the *positron emission tomography* (PET). The PET technique has become an inevitable tool in the modern diagnosis of cancer due to its ability of visualising the functional processes in a human body. In a traditional PET detector, classical photomultiplier tubes are coupled to inorganic crystals in order to facilitate a detection of the two back-to-back gamma rays emitted in the annihilation process of a positron. These PMTs may however be replaced in the future by SiPM detectors due to their superior characteristics such as a more compact design, facilitating a higher granularity of the detectors and thus an improved spatial resolution, and their insensitivity to magnetic fields. The latter is a key requirement for a combined application of PET with the method of magnetic resonance imaging. A small-scale prototype of a PET detector was developed and constructed using SiPMs to readout miniaturised arrays of scintillating crystals. The prototype consists of two opposing detector modules which are rotated around the detector field of view in order to mimic a completely equipped detector ring. First results are presented concerning a basic characterisation of the system, including measurements of the energy, time and spatial resolution.

Monte Carlo simulation is an essential tool in the development and operation of particle detectors in high energy physics experiments and imaging detectors in the field of nuclear medicine. For a predictive simulation, the software must correctly implement the relevant physical processes and constants. An aspect of this thesis is therefore dedicated to the ionisation quenching effect in the polystyrene based scintillator tiles of the AHCAL, and its implementation in a calorimeter simulation based on Geant4 [5, 6]. A non-linear dependence between the energy deposition of a particle and the resulting scintillation light is observed for most organic scintillators. A variety of empirical models was developed to describe this effect. A common one is Birks' law [7], in which the effect of ionisation quenching is described by a high density of excited and ionised molecules along the particles track. Birks' formula contains a parameter – Birks' coefficient  $kB$  – which is material specific and has to be determined experimentally. Since no  $kB$ -measurement of the AHCAL scintillator was carried out until this study, the  $kB$  was assumed to be equivalent to the one measured for an other polystyrene based scintillator (SCSN-38, produced by KURARAY), which was used in the hadronic calorimeter of the ZEUS experiment at the formerly HERA<sup>3</sup> accelerator. In the present work,  $kB$  was measured for the AHCAL scintillator using a setup developed at the Max-Planck-Institut für Kernphysik in Heidelberg and a significantly different value was found. Further it was found that the current implementation of Birks' law in the Geant4 simulation package predicts imprecise values for the visible energy deposition of a particle when the specific energy loss,  $dE/dx$ , is changing rapidly during a simulation step, e.g. at low energies. For this reason, an improved simulation method was developed, taking into account the energy dependence of the specific energy loss. This allows to calculate the visible energy with higher precision compared to the standard method. Electromagnetic and hadronic particle showers have been simulated in order to study the impact of the measured  $kB$  and the improved calculation method on the calorimeter response.

---

<sup>3</sup>Hadron-Electron Ring Accelerator.

## 1.1 Imaging Detectors with Silicon Photomultipliers

### 1.1.1 Analogue Hadronic Calorimeter

There is a steady development of particle detection systems ongoing in order to meet the increasing demands of future experiments in high energy physics. The ambitious physics programme of future particle accelerators, such as the proposed *International Linear Collider* (ILC), is challenging since the final states of many interesting physics processes to be studied are characterised by large multiplicities of highly energetic particle jets, or missing transverse energy induced by neutrinos or – if existent – the lightest supersymmetric particles. One of the main considerations for the detector development is the efficient separation of the hadronic decays:  $Z \rightarrow q\bar{q}$  and  $W \rightarrow q\bar{q}$ , via reconstruction of their invariant mass. For a good separation, the di-jet invariant mass resolution should be of the same size as the natural width of the decaying particle which translates into a minimum jet energy resolution of  $\sigma_E/E = 3 - 4\%$ . This corresponds to:  $\sigma_E/E = 30\%/\sqrt{E[\text{GeV}]}$ , for the typical jet energies of  $\sim 100\text{ GeV}$  expected at the ILC. This level of precision cannot be fulfilled with the available detector technology which was developed for accelerators such as the *Large Electron Positron Collider* (LEP), achieving a jet energy resolution inferior by a factor of about two:  $\sigma_E/E \sim 65\%/\sqrt{E[\text{GeV}]}$  [8, 9].

A new approach which has a high potential to meet the requirements of the physics case of the ILC is the *particle flow algorithm* (PFA). The fundamental idea states that the energy of each particle created in the collision should be measured with the detector best suited for it. This approach is motivated by the average energy decomposition of a jet, which is made up primarily of charged particles (62 %), photons (27 %), neutral hadrons (10 %) and a small amount of neutrinos (1 %). The major component of the charged particles in a jet are hadrons. In the traditional approach, hence approximately 72 % of the jet energy is measured with the precision of the combined hadronic and electromagnetic calorimeters, which have an inferior resolution compared to the tracking detector. If on the other hand, the track of each particle in a jet can be identified and separated from other tracks, the energy can be reconstructed with much higher precision since the inferior calorimeter resolution applies only for the relatively small amount of neutral particles in the jet.

The particle flow method has already been successfully used at ALEPH, and other experiments. However, the achievable performance of this concept depends essentially on the particle detector design and has important implications on the calorimetric system. In the traditional approach, calorimeters are devices primarily used to measure the energy of particles or jets, hence the emphasis is mainly put on the energy resolution of the device, whereas only a reduced position resolution is provided. In order to make the particle flow approach most effective, it is necessary to follow the path of each particle through the complete detector, including the calorimeters. In this way, the individual shower fragments can be assigned to the corresponding particles, and thus, a double counting of energy is avoided. To reach this goal, the concept of calorimetry has to be extended by the precise spatial information of each individual energy deposition. These properties are met by a new type of detector, denoted ‘Imaging Calorimeter’, in which the active material is highly segmented in both, lateral and longitudinal direction, providing unprecedented spatial resolution.

The *analogue hadronic calorimeter* (AHCAL) is one of the prototypes built by the CALICE collaboration which develops imaging calorimeters for the next linear collider. It has a sampling structure consisting of alternating layers of absorber material (steel) and active material consisting of plastic scintillator, segmented into small tiles of the size  $3 \times 3 \times 0.5\text{ cm}^3$ . The high channel density of this prototype requires the complete integration of the light sensitive de-

tector and the readout electronics into the calorimeter. In the AHCAL this is achieved by embedding a special photodiode, a so called *silicon photomultiplier* (SiPM), into each scintillator tile. The scintillation light is collected and guided to the SiPM by a wavelength shifting fibre, inserted into a groove on each tile. A picture of a scintillating tile and the SiPM, used in the AHCAL physical prototype is shown in Figure 1.1. This light readout concept is different to the traditional one, where the scintillation light is guided with long fibres to a distant photodetector.

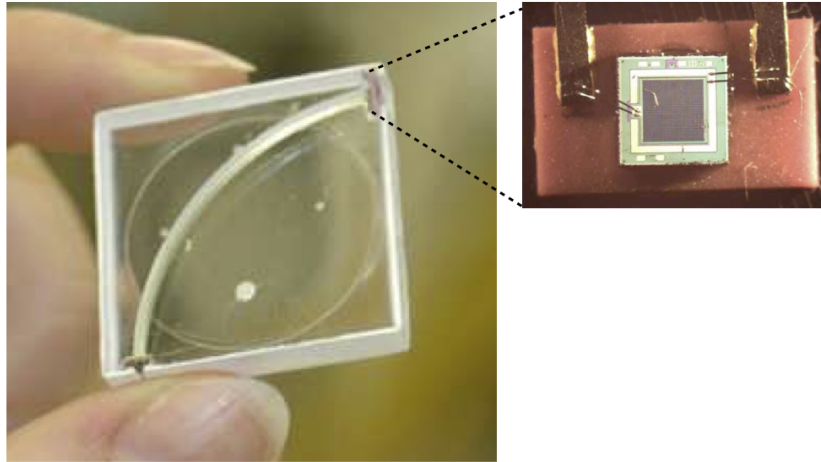


**Figure 1.1** – Scintillating tile ( $3 \times 3 \times 0.5 \text{ cm}^3$ ) of the AHCAL physical prototype. A wavelength shifting fibre is inserted into the tile, shifting the scintillation light from blue to green and guiding it to the  $1 \times 1 \text{ mm}^2$  active area of the SiPM.

In the new concept, the photodetector must have three important characteristics: Firstly, it must be very compact  $O(1 \text{ mm}^2)$  in order to allow embedding it into each scintillator tile without reducing the active detector volume, and secondly, it must be operational in a strong magnetic field since the detector concepts for the next electron-positron colliders foresee the hadronic calorimeter to be placed inside of a magnetic coil. Additionally, the small size and the individual readout of each tile requires the photodetector to feature an internal amplification mechanism in order to generate the needed sensitivity to very small amounts of scintillation light;  $O(15)$  photons per minimum ionising particle. The constraints on the size of the photodetector and the required magnetic field insensitivity ruled out classical photomultiplier tubes as possible candidates. On the other hand, these requirements are met by most of the silicon based photodetectors. However, traditional PIN photodiodes could – despite their reliability – not be used because of the missing photocurrent amplification, and the undesired nuclear counter effect, giving rise to a large signal when the sensor is hit directly by ionising particles. Avalanche photodiodes, as used for example in the CMS electromagnetic calorimeter [10], reveal a much smaller nuclear counter effect, however, the typical amplification of these devices  $O(100)$  is insufficient for the detection of the small light signals produced in the scintillating tiles of the AHCAL. The SiPM is hence one of the ultimate keys for the construction of scintillator based imaging calorimeters.

### 1.1.2 Detectors for Positron Emission Tomography

The capability of radiation and particle detection enables a variety of different applications. Nowadays, particle detectors are not used for scientific purposes only, but they have found a wide application in the medical field. A method which has become a powerful tool in the modern diagnosis of cancer is the *positron emission tomography* (PET), a non-invasive imaging technique, facilitating the visualisation of cancer cells in a living organism.

The basic working principle of the PET method is as follows: a  $\beta^+$  emitter is incorporated into a biologically active molecule – for example glucose – and injected into the blood circulation of the patient, where it is transported mainly to tissues with an increased metabolic activity. The patient is then placed in the centre of the PET detector, consisting of a large number of inorganic scintillator crystals which are coupled to photodetectors, and arranged in a ring like geometry. The annihilation of the emitted positrons produces two back-to-back gamma rays, each with an energy of 511 keV. These photons are detected as coincidence events in the detector and allow to reconstruct a three dimensional image of the metabolic activity. A more detailed description of the PET principle is given in chapter 5.

Most of nowadays PET detectors use classical photomultiplier tubes for the detection of the scintillation light. However, the unique properties of modern SiPM detectors such as compactness, blue light sensitivity, fast timing properties and immunity against magnetic fields make them very promising candidates for this type of imaging detector.

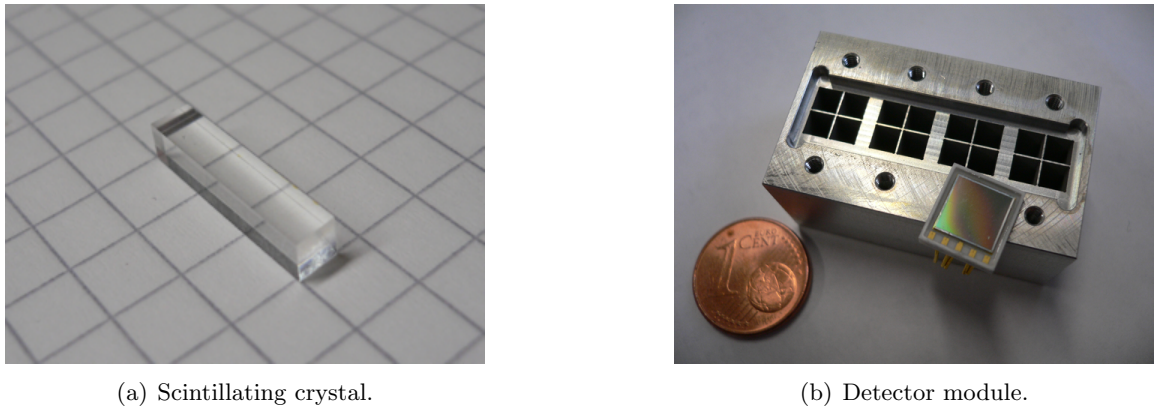
The switch from classical photomultiplier tubes to SiPMs is motivated by the future goals in the PET detector development. The spatial resolution of PET detectors can be improved by increasing the detector granularity and measuring the scintillation light of each crystal separately. For the realisation of this concept, very compact photodetectors are required which can be easily achieved with SiPMs. An other important field of development is the improvement of the detector sensitivity, such that the same image quality can be achieved with a smaller amount of measured data, hence facilitating a reduction of the radiation exposure of the patient. The detector aspects which are important for an improved detector sensitivity are the obtainable energy and timing resolution of the crystal-photodetector system, facilitating an efficient removal of the Compton background and random coincidences. A fast time resolution is also crucial for the *time-of-flight* (TOF) approach, where the reconstruction efficiency is improved by constraining the annihilation point of the positron to a limited region, by measuring the photon arrival times. A coincidence time resolution of around  $\sim 200$  ps – a realistic goal with todays fast scintillation crystals and SiPMs – improves the image signal-to-noise ratio significantly and facilitates a faster image generation such that the required radiation dose is reduced.

An other large field of developments are hybridised applications in which the PET functionality is complemented with other medical imaging techniques. Advantages in the cancer diagnosis are expected from the combination of PET with *magnetic resonance imaging* (MRI). While PET is a useful tool to produce images of functional processes in a living organism, the MRI technique provides precise structural information. In order to facilitate simultaneous PET/MRI scans, it is necessary to implement the PET detector into an MRI detector. This induces major constraints on the compactness of the PET detector and the readout electronics, but even more important is that all detector components must be insensitive to the strong magnetic fields present in an MRI detector. This rules out classical photomultiplier tubes for such an application.

A large european project was initiated with the goal to implement a miniaturised TOF-PET detector into an ultrasound assisted biopsy endoscopic probe [11]. The proximity of the probe

to the affected tissue will increase the probability for detection of smaller functionally marked structures, and hence be helpful in the early diagnosis of pancreatic and prostatic cancers. The small geometrical acceptance of the detector, as well as the requirement of an *in situ* image generation make the TOF principle an essential requirement for this concept.

In summary, the requirements to the photodetectors in future PET devices are: compactness, high efficiency in the blue (400 nm) wavelength region, insensitivity to magnetic fields, and very good timing properties. Therefore, SiPMs are promising candidates for future detectors in nuclear medicine.



(a) Scintillating crystal.

(b) Detector module.

**Figure 1.2** – In figure (a), a small  $3 \times 3 \times 15$  mm $^3$  LFS scintillating crystal is shown, used for the gamma ray detection in the small PET test device described in chapter 5. Figure (b) shows a picture of the empty aluminium matrix, which can be filled with a total of 16 scintillating crystals (shown on the left). The scintillation light is detected by four photosensor arrays (one is shown in the figure), each consisting of  $2 \times 2$  individual SiPMs.

In order to verify the above assumptions and to demonstrate the potential of a highly granular scintillating detector layout with fast and efficient silicon photomultiplier readout, within this thesis a small-scale PET prototype was developed and constructed. Two detector components of this prototype are shown in Figure 1.2, revealing the high degree of miniaturisation achievable with SiPM photodetectors; Figure 1.2(a) shows one of the used scintillator crystals of the dimensions  $3 \times 3 \times 15$  mm, whereas Figure 1.2(b) presents one of the developed detector modules used to precisely couple the scintillating crystals to the active area of the SiPM detector arrays. Two of these detector modules are rotated around the field of view, thus emulating a full detector ring. The flexible design of the prototype facilitates an estimation of the spatial resolution and its dependence on the specific detector configuration; e.g. for different numbers of readout channels or different angles between the detector modules. However, it also provides an environment close to a real PET application, which enables tests of potential readout electronics. The construction and commissioning of the small-scale PET prototype and some first measurement results are presented in chapter 5.

## 1.2 Calorimetry

Traditionally, the science of calorimetry describes the measurement of heat, produced in a chemical or physical reaction [12]. The definition of calorimetry in particle physics is the measurement of the energy of particles. The complete stopping of a particle requires, even with very dense absorbers, large amounts of material. Calorimeters in high energy physics experiments are therefore usually huge devices. The energy carried by the particle is very small in the thermodynamical sense, and heat generated by the absorption is distributed over a large volume, which has the consequence of an immeasurable small temperature increase. Hence an alternative way has to be found for the energy determination. This is usually achieved by measuring only a small fraction of the total energy, converted into another form of energy, such as scintillation light created by excitation of the material, or the electrical charge produced by ionisation of the medium.

Although, the determination of the jet<sup>4</sup> energy remains an important purpose of calorimeters in high energy physics, today's state of the art devices provide more than just a measurement of energy. Imaging calorimeters facilitate, due to the high granularity, a precise spatial information of the individual energy depositions [3]. In contrast, the alternative concept of dual readout calorimeters allows for the separation of electromagnetic and hadronic jet components [13].

According to the diversity of high energy physics experiments, a large variety of calorimeters and measurement technologies exist. Nevertheless, the common feature of all devices is the generation of a signal which is proportional to the energy of the particle. This requires the total energy to be deposited via interactions with the detector material. The following sections provide an overview over the fundamental particle interactions with matter and detection principles which are relevant for high energy physics calorimetry.

### 1.2.1 Interaction of Particles and Radiation with Matter

#### Ionisation and Excitation of heavy particles

A charged particle can ionise or excite the atoms or molecules of the traversed medium by Coulomb interactions or direct collisions with the atomic electrons. For particles which are much heavier than electrons ( $m \gg m_e$ ), the average energy loss due to excitation and ionisation – in the following denoted collisional energy loss – of the medium can be described by the Bethe-Bloch equation [14]:

$$-\frac{1}{\rho} \left\langle \frac{dE}{dx} \right\rangle_{\text{coll}} = 4\pi N_A r_e^2 m_e c^2 z^2 \frac{1}{\beta^2} \frac{Z}{A} \left[ \ln \left( \frac{2 m_e c^2 \gamma^2 \beta^2 T_{\max}}{I^2} - \beta^2 - \delta/2 \right) \right]. \quad (1.1)$$

The following symbols are used:

$z$	— Charge of the incident particle in units of the elementary charge.
$\rho, Z, A$	— Density, atomic number and mass number of the absorbing material.
$N_A$	— Avogadro number.
$r_e, m_e$	— Classical electron radius and electron mass.
$\beta$	— Particle speed in units of the speed of light $c$ .
$\gamma$	— Lorentz factor.
$T_{\max}$	— Maximum energy, transferable to an electron in a single collision.
$I$	— Average excitation energy of the material.

---

<sup>4</sup>A jet is a narrow cone of particles originating from the hadronisation of quarks or gluons.

- $\delta$  — The density effect correction describes the reduction of the  $dE/dx$  which is caused by the polarisation of the traversing medium for high energies.

Figure 1.3 shows the average specific energy loss of muons in copper as a function of the velocity and momentum. Equation 1.1 is valid in the approximate velocity range  $0.1 \lesssim \beta\gamma \lesssim 1000$ , indicated in Figure 1.3. At higher velocities, additional processes such as radiative energy loss become important.

### Ionisation and Excitation of Electrons and Positrons

It should be emphasised that Equation 1.1 is not valid for electrons or positrons, since the identical masses, and the indistinguishability of the colliding objects in case of electrons, requires an individual approach. The collision stopping power of electrons and positrons can be described with the Berger-Seltzer equation [15, 16]:

$$-\frac{1}{\rho} \left\langle \frac{dE}{dx} \right\rangle_{\text{coll}} = 2\pi N_A r_e^2 m_e c^2 \frac{1}{\beta^2} \frac{Z}{A} D(E), \quad (1.2)$$

with

$$D(E) = D_0(E) - 2 \ln(I/mc^2) - \delta$$

and

$$D_0(E) = \begin{cases} \ln[\gamma^2(\gamma+2)/2] + [1 + \gamma^2/8 - (2\gamma+1)\ln 2]/(\gamma+1)^2, & \text{for electrons} \\ \ln[\gamma^2(\gamma+2)/2] + 2\ln 2 - (\beta^2/12)[23 + 14/(\gamma+2) \\ + 10/(\gamma+2)^2 + 4/(\gamma+2)^3], & \text{for positrons.} \end{cases}$$

The same variable symbols as above are used.

### Fluctuations

Equation 1.1 and Equation 1.2 only describe the average energy loss rate due to ionisation and excitation. However, the actual values of the energy loss are subject to large fluctuations giving rise to an asymmetric energy loss spectrum [14]. Depending on the thickness of the absorbing layers, a more or less pronounced asymmetric tail to high energy depositions is observed. This effect is caused by rare collisions with the atomic electrons in which large energies are transferred. In case of very thin layers, e.g. the active layers of a sampling calorimeter, these fluctuations are well described by a Landau distribution, which approaches – but never actually reaches – a Gaussian distribution for thick absorbers.

### Bremsstrahlung

Fast charged particles which traverse a medium, in addition to the ionisation energy loss, lose energy by interactions with the Coulomb field of the nuclei. When the particles are deflected in the field, a fraction of their energy is lost due to the radiation of photons. The following formula can be used to approximately describe the energy loss due to bremsstrahlung – in the

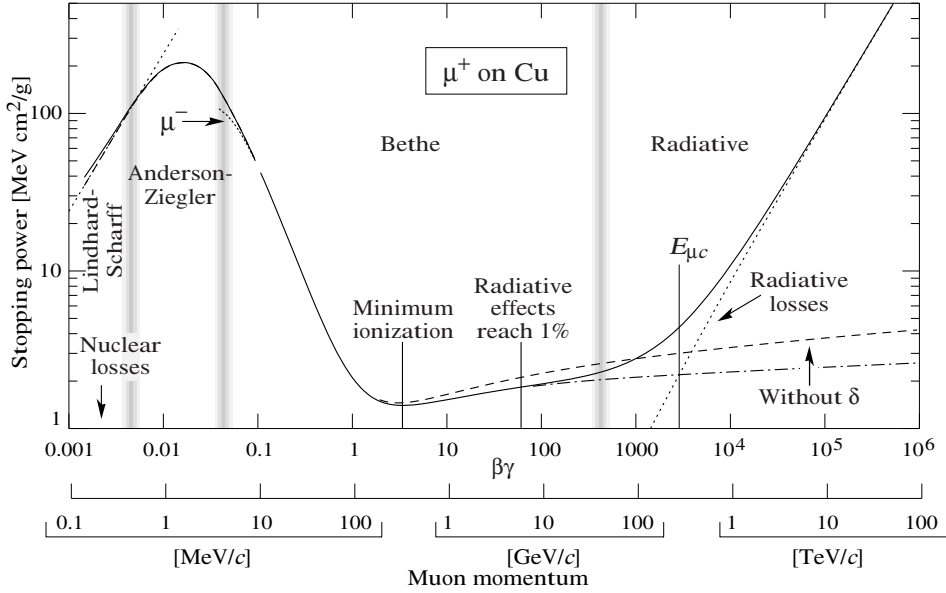


**Figure 1.3** – Average specific energy loss, here denoted ‘stopping power’, of a  $\mu^+$  in copper. The figure has been taken from Ref. [14].

following denoted radiative energy loss – for high energies [17]:

$$-\frac{1}{\rho} \left\langle \frac{dE}{dx} \right\rangle_{\text{rad}} = 4\alpha N_A \frac{Z^2}{A} z^2 \left( \frac{1}{4\pi\epsilon_0} \cdot \frac{e^2}{mc^2} \right) E \cdot \ln \left( \frac{183}{Z^{1/3}} \right), \quad (1.3)$$

where in addition to Equation 1.1, the following symbols are used:

- |                    |  |
|--------------------|--|
| $\alpha$<br>$m, E$ | — Sommerfeld fine-structure constant.<br>Mass and kinetic energy of the incident particle. |
|--------------------|--|

Equation 1.3 reveals two important features of the radiative energy loss which differ strongly from the energy loss due to ionisation and excitation. Firstly, it is proportional to the energy  $E$  of the projectile particle and secondly it scales with the inverse square of the particles mass  $m$ . The radiative stopping power, hence plays an important role for light particles such as electrons or positrons.

A commonly used variable in high energy physics calorimetry is the radiation length  $X_0$  which describes the distance in a given material at which point a highly energetic electron has lost the fraction  $1/e$  of its initial energy due to the emission of Bremsstrahlung. The radiation length is defined by the following equation:

$$-\frac{1}{\rho} \left\langle \frac{dE}{dx} \right\rangle_{\text{rad}} = \frac{E}{X_0}. \quad (1.4)$$

Using Equation 1.3, the following expression for the radiation length can be derived:

$$X_0 = \frac{A}{4\alpha N_A Z^2 r_e^2 \ln(183 Z^{-1/3})} \left[ \frac{\text{g}}{\text{cm}^2} \right]. \quad (1.5)$$

An other often used quantity is the critical energy  $E_c$ . A commonly used definition<sup>5</sup> is the energy, at which the collisional energy loss rate equals the radiative energy loss rate for electrons [14].

$$\left\langle \frac{dE}{dx}(E_c) \right\rangle_{\text{coll}} = \left\langle \frac{dE}{dx}(E_c) \right\rangle_{\text{rad}} \quad (1.6)$$

For the heavy elements used for the absorbing materials in calorimeters, the critical energy can be approximated by the following equation [17]:

$$E_c \sim \frac{550}{Z} \text{ [MeV]} \quad (1.7)$$

Values of the radiation length and the critical energy for a variety of absorber materials used in calorimetry are summarised in Table 1.1.

### Pair Production and Photo-nuclear Interactions

For heavy particles and high energies there are two additional energy loss processes to be considered [17, 19]. Electron-positron pairs can be produced in the Coulomb field of the nucleus, involving a virtual photon. An other process describes the energy loss, caused by the direct interaction of virtual photons with the nucleus. Both processes reveal, in the same way as the radiative stopping power, a proportionality to the kinetic energy. In Figure 1.4, the individual contributions to the energy loss of a muon in iron are shown. It can be seen that the effect of pair production, for high energy muons, has a larger impact compared to the energy loss due to Bremsstrahlung.

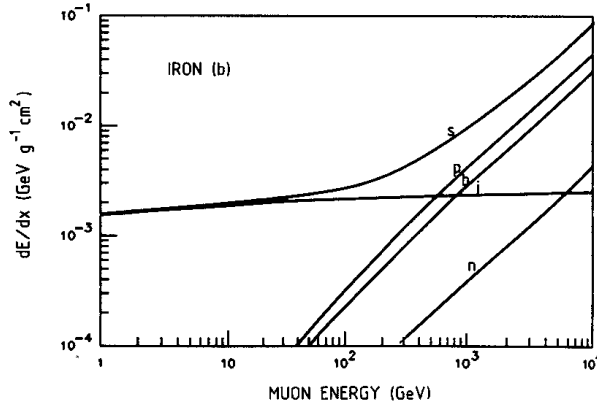


**Figure 1.4** – Contributions to the sum (s) of the individual energy loss processes of muons in iron: ionisation and excitation (i), Bremsstrahlung (b), pair production (p) and photo-nuclear interactions (n). The figure has been reprinted from Ref. [19].

<sup>5</sup>An other definition of  $E_c$ , sometimes referred to is based on the energy loss per radiation length  $X_0$ , instead on the energy loss rate. The differences between both definitions ranges between 15 – 35 % [14, 18].

## Photon Interactions

The detection mechanism of photons differs from other electromagnetic interacting particles. Photons have no electric charge which has the consequence that they do not interact with the Coulomb field of the atomic nucleus or the atomic electrons. For this reason, photons do not directly leave a measurable signal (e.g. ionisation) in a detector. The energy is transferred to charged particles via the Photoelectric effect, Compton Scattering or Pair-production, followed by the energy loss of the charged particles via ionisation and excitation generating a measurable detector signal. The variations in the energy transfer process are large: in case of the photoelectric effect and pair production, the incident photon deposits its total energy whereas only a small fraction of the energy may be deposited by the Compton effect. Therefore it is not useful to describe the energy loss in the same way as it was done for charged particles. Instead, the statistical entity of a beam of photons of a given intensity  $I$  is considered to describe the absorption and scattering of photons in matter (Beer-Lambert law):

$$I = I_0 e^{-\alpha x}, \quad (1.8)$$

where  $I_0$  is the starting intensity and  $x$  is the material thickness. The absorption coefficient  $\alpha$  is a material and photon energy dependent quantity and can be calculated from the cross sections per atom  $\sigma_i$  of the individual photon interaction processes:

$$\alpha = \frac{N_A}{A} \sum_i \sigma_i. \quad (1.9)$$

In the following section, the dominant photon interactions with matter are summarised.

### Photoelectric effect

For the photoelectric effect, the incident photon energy is completely absorbed by an atom, accompanied by the emission of a (photo-)electron. Since energy-momentum conservation has to be fulfilled, the atomic nucleus must be involved in the interaction. For this reason, the photoelectric absorption is most probable for the electrons in the innermost  $K$ -shell of the atom. As a consequence of the excitation from an inner atomic shell, secondary effects take place in combination with the photoelectric absorption. The refill of an empty state in an inner atomic shell with an electron from an upper atomic shell may cause the emission of a gamma ray with a characteristic energy (according to the shell transition). If the transition energy is large enough, it can also be used to free a second electron from the same atom (Auger effect).

The photoelectric cross section is highest for small photon energies and falls rapidly for increasing energies. Further, a strong dependence on the atomic number  $Z$  is observed experimentally:

$$\sigma_{\text{photo}} \propto \frac{Z^n}{E^3}, \quad (1.10)$$

where  $n = 4 - 5$ , depending on the photon energy. This strong  $Z$  dependence indicates, that more than a single atomic electron is involved in the interaction. Figure 1.5 shows the total photon cross section as a function of the energy in lead ( $Z = 82$ ). At distinct positions – close to the absorption edges of the atomic shells – characteristic steps are superimposed to the general  $\sim E^{-3}$  dependence of the photoelectric cross section.

The photoelectric effect forms the basis for almost all photo-detection systems, since the

produced photoelectron carries a large fraction of the initial photon energy. This enables a successful detection and a measurement of the photon energy. For this reason, the photoelectric effect and its implications on the detection mechanism, are discussed in detail in chapter 3.

### Compton scattering

The Compton effect describes the scattering of a photon off a quasi-free atomic electron. A variable fraction of the photon energy and momentum is transferred to the electron in this process. From simple considerations of the process kinematics and energy and momentum conservation, a formula for the energy of the scattered electron (Compton electron), can be derived:

$$E_{e^-} = E_\gamma \frac{\epsilon(1 - \cos \theta)}{1 + \epsilon(1 - \cos \theta)}, \quad (1.11)$$

where  $E_\gamma$  is the incident photon energy,  $\epsilon$  is the photon energy in units of the electron rest energy ( $\epsilon = E_\gamma/m_e c^2$ ), and  $\theta$  is the scattering angle of the photon. The highest Compton electron energy is reached in case of backscattering ( $\theta = \pi$ ) of the incident photon.

For high energies, the Compton effect cross section shows a much less steep energy dependence

$$\sigma_{\text{Compton}} \sim \frac{\ln \epsilon}{\epsilon} \quad (1.12)$$

compared to the photoelectric absorption. It is dominating at intermediate photon energies ranging from several hundreds of keV up to several MeV (lead). However, the cross section decreases with further increasing energies (cf. Figure 1.5) and it starts to be dominated by the pair production process which is dominating at higher energies.

### Pair production

The effect of pair production describes the production of an electron-positron pair in the presence of a Coulomb field, generated by an atomic nucleus or an electron. The incident photon must at least carry an energy which equals the rest mass of the electron-positron pair, plus the energy which is carried away by the recoil nucleus/electron, required for energy momentum conservation. In case of the dominant pair production in a nuclear Coulomb field, the recoil energy of the nucleus can be neglected, giving rise for the effective threshold of  $\sim 2m_e c^2 = 1022$  keV. In the less probable case of an electron recoil particle, twice the energy is required, which explains the higher threshold shown in Figure 1.5.

For high energies ( $E_\gamma \gg m_e c^2$ ), the cross section asymptotically reaches a constant plateau value which is described by the following equation:

$$\sigma_{\text{pair}} = \frac{7}{9} 4\alpha r_e^2 Z^2 \ln \left( \frac{183}{Z^{1/3}} \right) \quad (1.13)$$

$$= \frac{7}{9} \frac{A}{N_a} \frac{1}{X_0} \quad (1.14)$$

The equation in the second row can be derived, using the definition of the radiation length  $X_0$  given in Equation 1.5.

In Figure 1.6, the dominant regions of the individual photon interactions are shown as a function of the atomic number  $Z$  and the photon energy. At low energies and for high  $Z$

materials, the photoelectric absorption is the most probable process to occur. At high energies (several MeV), the pair production becomes the dominant process. At intermediate energies, the Compton process has the highest probability.

### Further Photon Interactions

In addition to the mentioned three processes, which dominate the total cross section, photons interact by a couple of additional processes. In case of photo-nuclear interactions, the photon interacts with the nucleus, creating an excited state, like the giant dipole resonance (cf. Figure 1.5). This process however, only plays a role in a strictly limited energy range and its contribution to the total cross section can in most cases be neglected. An other process, denoted Rayleigh scattering describes the coherent scattering of photons on the atomic electrons. This process has a high cross section at low photon energies. However, since there is no energy exchanged between the photon and the electron, this process does not contribute to the energy loss. It only causes a deflection of the incoming photons.

### Visible Light Absorption

Visible light in the wavelength range from 400 – 700 nm corresponds to photon energies from roughly 1 to 3 eV. Hence the photoelectric effect is by far the most dominant process for visible light, except for very light elements (cf. Figure 1.6). For the development of photodetectors the absorption characteristics of visible light is of great importance, as discussed in chapter 3. In Figure 1.7 the light absorption length in silicon is shown as a function of the photon wavelength. The absorption length differs strongly for different wavelength; red and infrared light may penetrate deeply into the silicon, whereas blue and ultraviolet photons are absorbed with a high probability within a fraction of a  $\mu\text{m}$ . This is one of the challenges in the development of silicon light detectors which are sensitive in blue or ultraviolet light.

### Electromagnetic Particle Showers

If a multi GeV electron, positron, or photon enters a block of absorbing material – for example a calorimeter – it produces a cascade of secondary particles. This process is schematically shown in Figure 1.8. At high energies, i.e. when the particle energy is much larger than the critical energy  $E_c$  of the material, bremsstrahlung is the dominant interaction processes of charged particles. The probability for the emission of a photon after traversing a certain absorber thickness  $x$  can be described by  $P \sim \exp(-x/X_0)$ , where  $X_0$  is the radiation length of the material.

A single high energy electron can radiate a large number of photons before it is slowed down and deposits its remaining energy via ionisation and excitation in the material. Some of the radiated photons are created with a relatively small energy and therefore create low energy electrons via Compton scattering and photoelectric absorption, which in turn loose their energy via ionisation. However, the fraction of photons radiated with high energy will produce additional electrons and positrons in the pair production process which in turn may create additional bremsstrahlung photons so that the multiplication mechanism starts over again. The number of particles in the shower at a given position  $x$  can hence be approximately described by  $N(t) = 2^t$ , where  $t = x/X_0$  corresponds to the number of radiation lengths traversed. If it is assumed that the total energy  $E_0$  is distributed equally among the shower particles, the average particle energy at a certain development stage of the shower is given by:  $E(t) = E_0/2^t$ . The number of particles increases until it reaches its maximum at a given

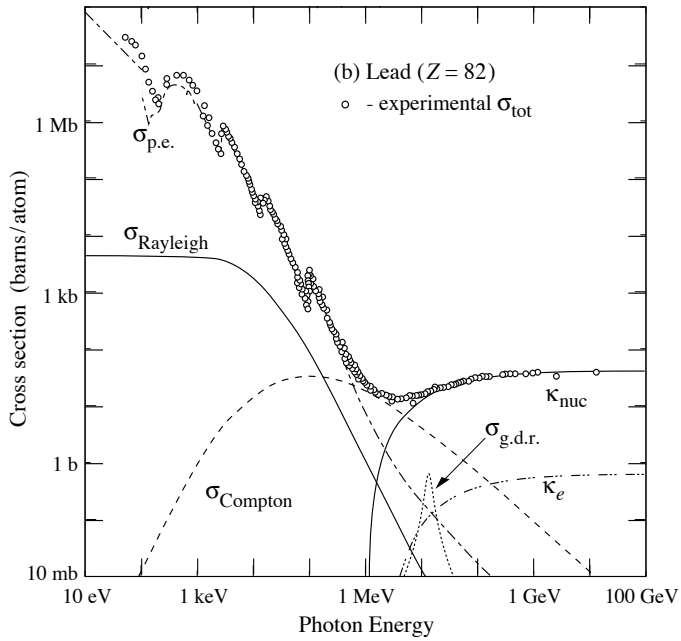


**Figure 1.5** – Photon cross section per atom as a function of the photon energy in lead. At distinct position – close to the absorption edges – characteristic steps are superimposed to the general  $\sim E^{-3}$  dependence of the photoelectric cross section. The following notation is used:  $\sigma_{\text{p.e.}}$  - photoelectric cross section,  $\kappa_{\text{nuc}}$  - pair production in the nuclear Coulomb field,  $\kappa_e$  - pair production in the Coulomb field of the atomic electrons,  $\sigma_{\text{g.d.r.}}$ : photo-nuclear effect (giant dipole resonance). Figure taken from Ref. [14].

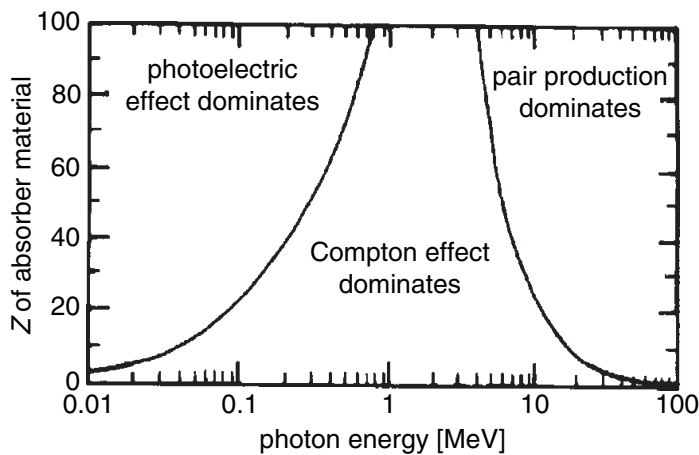


**Figure 1.6** – Dominant regions of the photoelectric effect, the Compton effect and the pair production, as a function of the photon energy and the atomic number  $Z$  of the absorbing material. The drawn lines indicate the gamma energies and  $Z$  values for which the cross sections of the photoelectric effect or pair production equal the cross section of Compton scattering. Reprinted from Ref. [20].

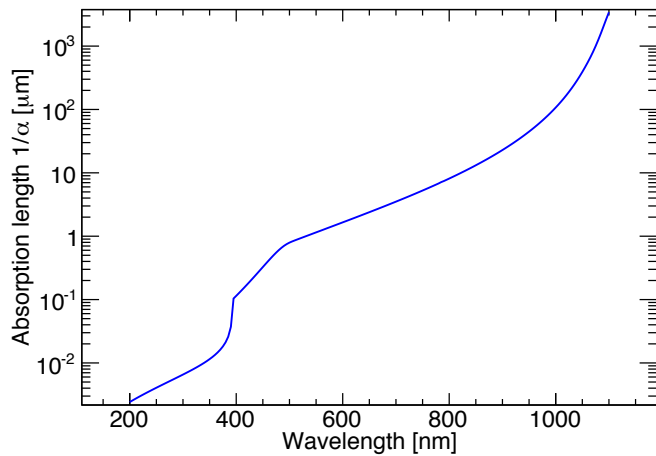


**Figure 1.7** – Photon absorption length  $1/\alpha$  in silicon at room temperature as a function of the wavelength. Red and infrared light can penetrate several tens of microns into the silicon, whereas blue and ultraviolet light is absorbed with a high probability within a fraction of a micrometer. Calculated using the parameterisation given in Ref. [21].

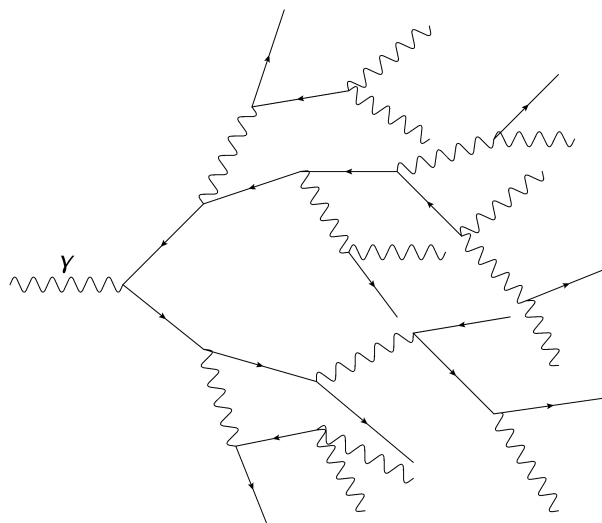


**Figure 1.8** – Schematic view of an electromagnetic cascade. The incoming highly energetic photon creates an electron positron pair, which in turn creates a shower of secondary particles via the processes of bremsstrahlung and pair production. The created charged particles deposit parts of their energy via excitation and ionisation of the absorber material.

thickness  $t_{\max} = \ln(E_0/E_c)/\ln 2$ , where the average particle energy is equal to the critical energy and hence, bremsstrahlung loses its dominant role. This relation shows that calorimeters can cover a very large energy range since the longitudinal extension of the particle shower scales logarithmically with the primary energy. On average 98 % of the the shower energy is contained in a calorimeter of the length  $L = 2.5 \cdot t_{\max} \cdot X_0$ .

The lateral development of electromagnetic particle showers is mainly caused by multiple scattering of the electrons and positrons. Additional lateral spread is caused at low energies by the process of photoelectric absorption and Compton scattering, since the resulting electrons may be created with a large angle to the shower axis. A useful quantity for the description of the lateral shower development is the Molière radius  $\rho_M$ , which denotes the radius around the shower axis in which on average 90 % of the energy is contained. The Molière radius for a certain material can be calculated by the following equation [17]:

$$\rho_M = 21 \frac{X_0}{E_c \text{ [MeV]}}. \quad (1.15)$$

Table 1.1 lists values of the Molière radius for a some materials commonly used in calorimetry.

### 1.2.2 Strong Particle Interactions

Charged hadrons may deposit energy due to the electromagnetic interactions described above, but these particles do also interact via the strong force. A huge diversity of possible interactions exists, such as inelastic collisions with the nuclei of the absorbing material in which the primary particle may disappear and completely different strong interacting particles may be produced. The large variety of possible strong interactions makes the predictions of nuclear interactions complicated. It is hence a common method to describe the probability for strong interactions in a statistical way, using an approach which is similar to the one applied for the description of photon interactions (cf. Equation 1.8 and Equation 1.9). The following formula describes the number of hadrons  $N$  which didn't take part in a nuclear interaction as a function of the traversed material thickness  $x$ :

$$N = N_0 e^{-x/\lambda_{\text{int}}}, \quad (1.16)$$

where  $\lambda_{\text{int}}$  is the nuclear interaction length. It describes the average distance a strongly interacting particle has to travel in a certain material before it will participate in a nuclear interaction. The nuclear interaction length is inversely proportional to the total cross section<sup>6</sup> for nuclear interactions:

$$\lambda_{\text{int}} = \frac{A}{N_A \sigma_{\text{total}}} \propto A^{1/3}. \quad (1.17)$$

The right side of Equation 1.17 is derived, assuming that the total cross section is proportional to  $A^{2/3}$ . The nuclear interaction length depends also on the type of the incoming particle; most of the literature values are based on incident protons. However, as the total cross section for fixed-target pion interactions is considerably smaller at high energies than the one for protons, the resulting nuclear interaction length for pions is longer. This has to be considered in the dimensioning of the absorber thickness in an hadronic calorimeter, other-

<sup>6</sup>The given definition of the nuclear interaction length  $\lambda_{\text{int}}$  is only approximative, since one should in principle differentiate between the elastic and inelastic cross section, whereas the latter one is truly relevant for nuclear interactions as described in Ref. [20].

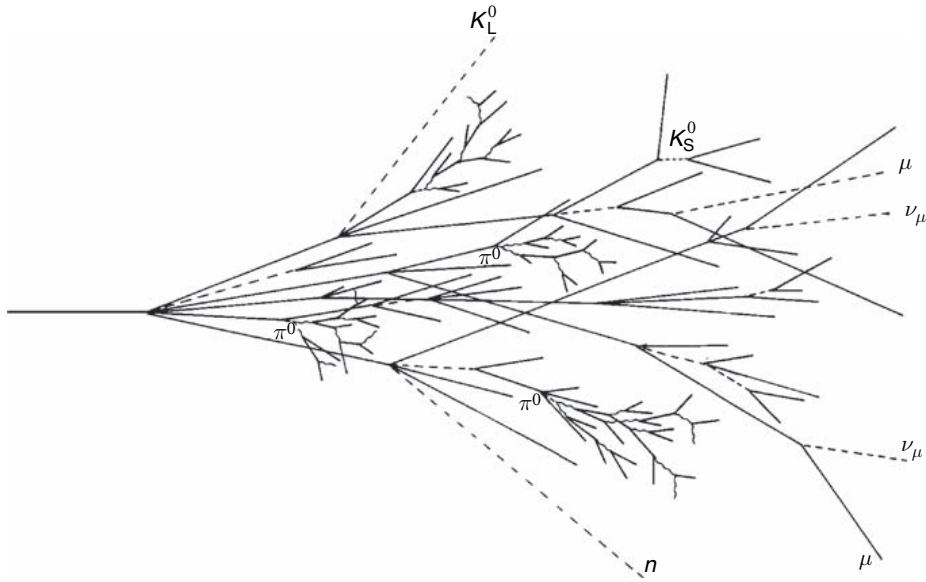


**Figure 1.9** – Schematic view of a hadronic cascade in an absorber material. An important role is played by the  $\pi^0$  particles since they decay dominantly into photons which give rise to the electromagnetic subcomponent of each hadronic shower. Reprinted from Ref. [20].

wise pions will have a high probability of passing through the calorimeter without interacting strongly.

In simple terms, the nuclear interaction length  $\lambda_{\text{int}}$  of hadronic showers, corresponds to the radiation length  $X_0$  for electromagnetic showers.  $\lambda_{\text{int}}$  is useful to characterise the longitudinal and lateral spread of hadronic showers. However, the main difference to the radiation length is given by the size, since  $\lambda_{\text{int}}$  is in general much larger than  $X_0$  as shown in Table 1.1.

### Hadronic Particle Showers

A highly energetic hadron, impinging on a fixed target creates – similar to purely electromagnetic interacting particles – a cascade of secondary particles. However, hadronic showers reveal a much higher complexity than electromagnetic ones since the variety of possible strong interactions is much larger compared to the few well understood processes in an electromagnetic shower. Hence, there are some fundamental differences between these two shower types. In case of an electromagnetic shower, the total energy of the incident particle is finally transferred to the material via ionisation or excitation of the charged particles in the shower. This type of energy can in principle be measured with a suitable detector instrumentation, e.g. by measuring the ionisation charge in a silicon detector, or measuring the produced scintillation light with a photodetector. In case of hadronic showers, a variable fraction of the incident particle energy is not detectable since it ends up causing permanent damage (nuclear breakup) to the absorbing material. In addition, a huge number of neutrons is created in nuclear spallation reactions, which on average leave a much smaller signal in the detector, compared to charged particles.

In Figure 1.9, the schematic development of a hadronic shower is sketched. A large number of secondary particles may be created in the first nuclear interaction. A special role is attributed to the neutral pions produced, since these particles decay almost exclusively into a pair of photons, giving rise to electromagnetic sub-cascades within the hadronic shower (cf. Figure 1.9). An

**Table 1.1** – Properties and shower development parameters of selection of absorber materials, commonly used in calorimetry. The following symbols are used:  $Z$  — atomic number;  $E_c$  — critical energy;  $X_0$  — radiation length;  $\rho_M$  — Molière radius;  $\lambda_{int}$  — nuclear interaction length. To emphasise the difference to an active calorimeter material, the last column lists the properties of a commonly used plastic scintillator base material. The values are taken from Ref. [18].

Material	$Z$	Density [g/cm <sup>3</sup> ]	$E_c$ [MeV]	$X_0$ [mm]	$\rho_M$ [mm]	$\lambda_{int}$ [mm]
Fe	26	7.87	22.0	17.6	16.9	168
Cu	29	8.96	20.0	14.3	15.2	151
W	74	19.3	8.0	3.5	9.3	96
Pb	82	11.3	7.4	5.6	16.0	170
<sup>238</sup> U	92	18.95	6.8	3.2	10.0	105
Polystyrene	-	1.032	94	424	96	795

approximative formula for the electromagnetic fraction  $f_{em}$  can be derived, assuming a simple shower model. In this model, all available shower energy is used to create mesons. Further it is assumed, that only  $\pi^+$ ,  $\pi^-$  and  $\pi^0$  particles are produced, since they are the lightest mesons. From these assumptions it follows, that after the first nuclear interaction  $\sim 1/3$  of the total shower energy is deposited in form of a electromagnetic cascade. In the second nuclear interaction, again, one third of the remaining purely hadronic fraction will be used to create neutral pions, so that the electromagnetic fraction becomes:  $f_{em} \approx 1/3 + (1 - 1/3)1/3 = 1 - (1 - 1/3)^2$ . This process is continued as long as the available energy is higher than the energy required for the production of a meson. Hence, after a finite number of interactions  $n$ , the electromagnetic fraction reaches its maximum which can be calculated with the following equation:

$$f_{em} \approx 1 - \left(1 - \frac{1}{3}\right)^n. \quad (1.18)$$

According to the simple shower model assumed, the electromagnetic fraction increases with the incident particle energy since this also causes an increase of the the number of interactions  $n$ . Even though Equation 1.18 is useful for a qualitative understanding, it does not allow for a precise description of the electromagnetic component, since it is based on many approximative assumptions. An empirical expression, which successfully describes the electromagnetic component is given by the following equation [18, 20, 22]:

$$f_{em} = 1 - \left(\frac{E}{E_0}\right)^{(k-1)}, \quad (1.19)$$

here  $E_0$  denotes the material dependent energy which is required for the production of a meson particle. The numbers which have been found in Ref. [22] vary between  $E_0 = 0.7$  GeV for iron and  $E_0 = 1.3$  GeV for lead. Typical values for the  $k$  parameter are around  $\sim 0.8$ .

The electromagnetic component has several important consequences for the energy measurement with calorimeters which will be discussed in section 1.2.4.

### 1.2.3 Introduction to Scintillators

Scintillators have a long tradition in particle detectors of nuclear and high energy physics experiments such as trigger systems, calorimeters or time of flight detectors, furthermore they are also widely used in nuclear medicine, like Positron Emission Tomography or X-ray computed tomography. Their basic principle of operation is the conversion of the deposited energy of an incoming particle into luminescence light in the visible or ultraviolet wavelength range, which in turn can be detected by a photodetector, generating an electrical signal. A large variety of scintillators exists in the solid, liquid or even gaseous phase. Hence, a suitable scintillator for almost every application exists or can be developed, meeting the necessary requirements. Scintillators are in general categorised into two groups: organic and inorganic scintillators. In the following section, the physical principle of the scintillation mechanism and the typical characteristics of the different scintillator types will be discussed. The outline of this section represents a summary of the detailed descriptions given in Refs. [7, 23].

#### Organic scintillators

The main difference between organic and inorganic scintillators is given by the different measurement tasks they are used for. Particles are usually not stopped in an organic scintillator because of the relatively low density which ranges from  $1.03$  to  $1.20\text{ g cm}^{-3}$  [24]. Hence only a small fraction of the total kinetic energy can be measured in contrast to inorganic scintillators which are usually designed to absorb the incoming particles completely. The processes relevant for the scintillation light production in organic scintillators are typically very fast which results in excellent timing properties. Typical applications of organic scintillators in high energy physics detectors are trigger systems, used to deliver precise timing informations, or sampling calorimeters where only a small fraction of the total shower energy is sampled in the active material. In particular plastic organic scintillators are widely used due to the ability to produce them at a reasonable price in practically any required geometry.

#### The benzene molecule

The light emission (luminescence) of organic scintillators can be understood by means of the benzene molecule  $\text{C}_6\text{H}_6$ , which is shown on the left side of Figure 1.10. In the ground state  $1s^2 2s^2 2p^2$ , the carbon atom has only two valence electrons that could be used for the binding with other atoms. However, it is energetically favoured that one of the electrons in the  $s$ -orbital is excited into a  $p$ -orbital  $1s^2 2s^1 2p^3$ , hence making four bounds possible. In case of the benzene molecule, one  $s$  and two  $p$ -orbitals mix (hybridise) and form three equivalent  $sp^2$ -orbitals which have a planar trigonal structure as shown on the right in Figure 1.10. The electrons in the  $sp^2$ -orbitals form six  $\sigma$  bonds, whereas the remaining six electrons in a  $p$ -orbital form three  $\pi$  bonds which cannot be attributed to a certain position, but are completely shared (delocalised) among the carbon atoms.

The  $\pi$ -electron energy levels, which are schematically indicated in Figure 1.11(a) form the basis for the luminescent properties of organic scintillators. The levels are divided into a series of singlet states  $S_i$ , and a series of triplet states  $T_i$ , where  $i = 1, 2, 3, \dots$  denote the excited singlet and triplet states and  $S_0$  denotes the singlet ground state. In addition there is a series of sub-levels for each state with a much smaller energy spacing, caused by additional vibrational or rotational degrees of freedom present in a condensed material. In the following these states will be denoted as vibrational sub-levels.

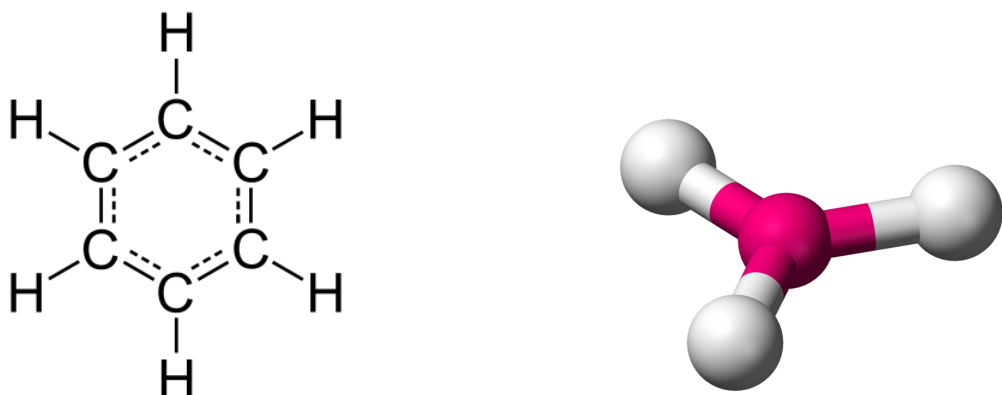


**Figure 1.10** – (left) Schematic description of the benzene molecule. The dashed lines indicate the delocalised  $\pi$ -electrons. (right) Trigonal planar structure. The figures have been taken from Refs. [25, 26].

Three different types of luminescence have been experimentally identified: fluorescence, phosphorescence and delayed fluorescence. The first step of all three processes is the energy deposition in the scintillator by incident ionising radiation, which lifts  $\pi$ -electrons from the singlet ground state up into a vibrational sub-level of an excited singlet state ( $i > 0$ ). Since the time scale of the vibrational interactions is very short  $O(10^{-12} \text{ s})$ , the corresponding vibrational ground state is reached before the excited state decays radiatively. Similarly, it has been observed that radiative transitions from  $S_2$  or  $S_3$  to  $S_0$  – even though having shorter radiative lifetimes than the  $S_1$  state – are suppressed due to a fast and non-radiative internal conversion between the excited singlet states. As a consequence, most electrons end up in the  $S_1$  state from which different processes can follow.

In the case of fluorescence, a radiative transition to the  $S_0$  state occurs which has a fast time scale of typically  $O(10^{-9} \text{ s})$ . For most applications, fluorescence is the desired process as the resulting photons arrive within a short time window after the particle interaction which allows to perform precise timing measurements. Hence, it is one of the major goals in the development of scintillators to reduce the probability of other processes, like phosphorescence where the electrons fulfil a non-radiative inter system crossing between the  $S_1$  and the  $T_1$  state. The following transition between the  $T_1$  and the  $S_0$  state violates the spin conservation rule, consequently its decay time is much larger than that of the fast fluorescence decay  $O(10^{-4} \text{ s})$ . Since the  $T_1$  state is energetically lower than the  $S_1$  state, the photons resulting from the radiative decay have a longer wavelength compared to fluorescence. This is not the case for the so called delayed fluorescence, where the  $\pi$ -electrons acquire enough energy due to vibrational interactions in the  $T_1$  state so that a transition back to the  $S_1$  state becomes possible. This process causes the emission of photons which are delayed with respect to the primary fluorescence emission, which however have the same characteristic wavelength.

A question which arises in the discussion of the scintillation phenomena is, why the emitted fluorescence light isn't reabsorbed immediately after its emission? Such a behaviour would limit the application of scintillators to very thin layers, as only the scintillation photons produced close to the boundary surface could be detected. The answer to this question can be found in the vibrational sub-levels of the  $\pi$ -electron states. Excitation starts from the vibrational ground state of the  $S_0$  level, since it is mostly occupied at thermal equilibrium. According

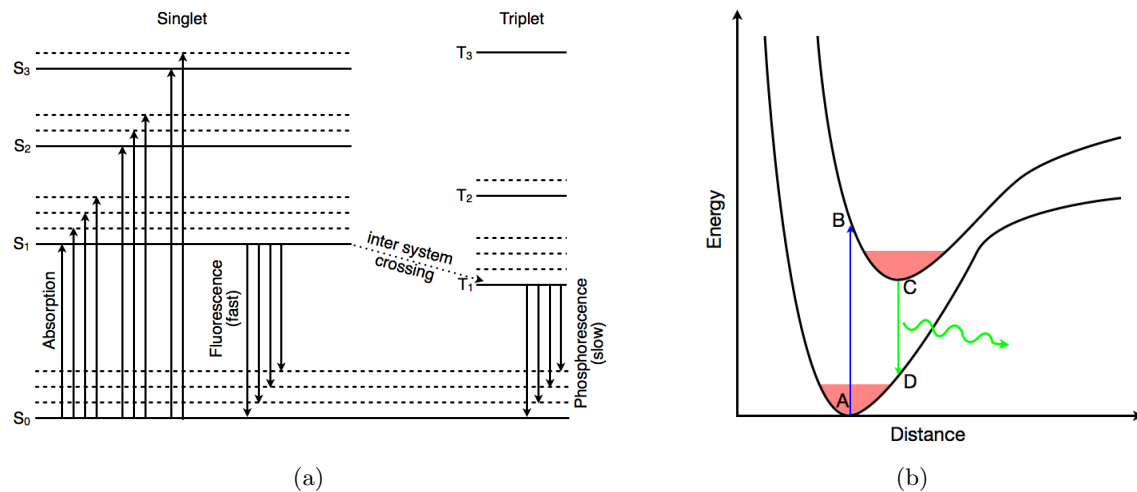


**Figure 1.11** – Figure (a) shows the energy levels of a  $\pi$ -electron system in an organic molecule, redrawn from Ref. [7].  $S_0$  denotes the singlet ground state, where the dashed lines indicate the vibrational sub-levels. The excited singlet states are called  $S_1$ ,  $S_2$  and  $S_3$ . The triplet states  $T_1$ ,  $T_2$  and  $T_3$  can only be populated with a non-radiative inter-system crossing from the excited singlet states. As the de-excitation to the singlet ground state (phosphorescence) violates spin conservation, it has a relatively slow time constant compared to the fast fluorescence process. Figure (b) indicates the physical process which is relevant for the Stokes' shift between the absorption and emission wavelength. Coloured regions indicate the vibrational excitations of the ground state electrons.

to the Franck-Condon principle, the excitation process is represented by a vertical line in Figure 1.11(b) (transition AB). The system hence ends up in a vibrational excited state (point B). However, as the characteristic period of the vibrations is much shorter compared to the time-scale of radiative de-excitation, the vibrational ground state (point C) is reached before a photon is emitted. The wavelength of the emitted light, determined by the transition CD, is hence longer compared to the wavelength required for excitation. This so called Stokes' shift between the absorption and emission spectra is schematically indicated in Figure 1.12 (left). As a result, the scintillator is transparent for parts of the photon emission spectrum, causing that photons can pass through the scintillator without being absorbed immediately.

At room temperature, not all electrons are in a state of minimum energy, but they occupy also states which are slightly higher in energy. Excitation and emission, hence not only occurs from the minimum energy state, which explains the partial overlap between the absorption and emission spectrum.

### Classification of Organic Scintillators

In the previous discussion of the scintillation phenomena it was assumed that the scintillator consists of a single kind of molecules, which means it only has a single  $\pi$ -electron system. However, a drawback of many single molecule organic scintillators is the relatively low fluorescence quantum efficiency, i.e. just a small percentage of the energy carried by the excited molecules ends up as detectable fluorescence. Typical numbers of this fluorescence quantum efficiency

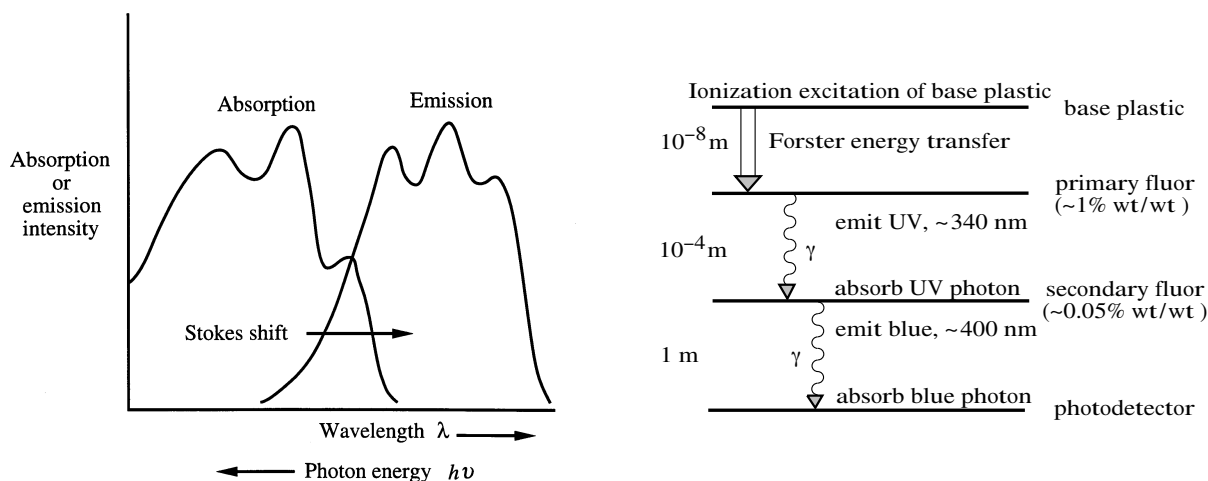


**Figure 1.12** – Typical absorption and emission spectrum of an organic scintillator (left), reprinted from Ref. [27]. The right side shows a typical energy exchange diagram of a ternary scintillator system. The numbers on the left indicate the characteristic ranges of the corresponding transition processes. Figure taken from Ref. [24].

are below  $\sim 20\%$  for most of the plastic base materials [7]. Other difficulties arise due to the characteristic wavelength of the emitted light which is often in the ultraviolet range, making its detection with standard photodetectors inefficient. Further, the overlap between the absorption and emission spectrum may be too large so that only relatively small scintillator volumes can be realised without causing the problem of a non-uniform response where the signal amplitude depends on the position of the impinging ionising radiation. In order to solve these problems, very often several organic scintillators are mixed in order to create the desired properties. Accordingly most organic scintillators are classified into three major groups:

### 1. Unitary systems

Scintillators consisting of a single component. In practical applications, only crystalline unitary systems are used. Examples are: anthracene ( $C_{14}H_{10}$ ), trans-stilbene ( $C_{14}H_{12}$ ) and naphthalene ( $C_{10}H_8$ ).

### 2. Binary systems

Scintillators consisting of two components, a base (solvent) and a primary fluor (solute) which has a high quantum yield close to one. Typical solute concentrations are in the order of  $O(1\%)$ , hence the solvent material determines the interaction with the primary ionising radiation, as the probability for a direct excitation of a solute molecule is very small. To increase the scintillator efficiency, the energy of the excited solvent molecules must be transferred efficiently to the molecules of the primary fluor. To achieve this goal, the solute concentration must be sufficiently large, such that the average distance between an excited base molecule and the next solute molecule is much smaller than the wavelength of light ( $\sim 100 \text{ \AA}$ ). At such distances, the energy transfer between the molecules is dominated by resonant dipole-dipole interactions (Förster energy transfer) which are much faster and more efficient than a radiative transfer. Binary systems hence allow to combine the positive properties of two scintillators, i.e. the chemical stability and the mechanical properties of the solvent with the high quantum yield of the primary fluor.

### 3. Ternary systems

Scintillators consisting of a solvent, primary and secondary fluor. The second fluor is added to the scintillator in order to shift the fluorescence light to longer wavelengths so that it can be detected more efficiently with standard photodetectors. Typical concentrations of the secondary fluor are in the order of  $O(0.01\%)$  causing the dominant energy transfer from the excited primary fluor molecules to be radiative. Hence the second fluor is often referred to as a "wavelength shifter". In Figure 1.12 (right), the typical energy exchange processes of a ternary plastic scintillator is shown. The primary excitation is transferred non-radiatively from the base scintillator to the primary fluor. The resulting ultraviolet fluorescence light is converted by the secondary fluor (wavelength shifter) into blue light which can traverse long distances in the scintillator and be detected by a photodetector, connected to a boundary surface of the scintillator.

Sometimes, scintillator systems are used which make use of a third wavelength shifter to create green scintillation light emission. Often, the third component is not dissolved in the solvent, but it is incorporated locally into the system. One possibility is to insert thin scintillating fibres into a groove machined into the scintillator plate like in case of the scintillating tiles of the AHCAL (cf. Figure 1.1). Such a system facilitates the guidance of the scintillation light over wide distances which is a key requirement if large scintillator structures are used, or if the light has to be guided to a distant photodetector. In Figure 1.13, the typical absorption and emission spectra of such a system are shown. In order to increase the measurable light output, it is necessary that the absorption spectrum of the wavelength-shifter matches the emission spectrum of the primary fluor. The third wavelength-shifter is used to convert the blue light emission from the secondary fluor into green light.

The typical characteristics of some organic scintillators is summarised in Table 1.2. Within the table  $\tau_d$  represents the decay time of the scintillation signal which has an influence on the achievable timing resolution.  $\lambda_{\text{peak}}$  is the wavelength of peak emission which has a large impact on the photodetector choice, and  $n_{\text{peak}}$  is the refractive index at peak emission important for the light coupling between scintillator and photodetector.

The data show that organic scintillators, in particular binary and ternary systems have a fast decay time in the order of several nanoseconds which makes them very useful for fast timing applications, such as trigger systems. An other advantage of plastic scintillators is that they can be produced in practically every desired geometry at a reasonable price. However, the relatively low density and low  $Z$  of the organic materials limits the range of possible applications since huge scintillator structures would be required to completely absorb the electromagnetic and hadronic cascades created by highly energetic particles, in a homogenous system. For such applications, typically inorganic scintillator crystals are used, which are described in following section.

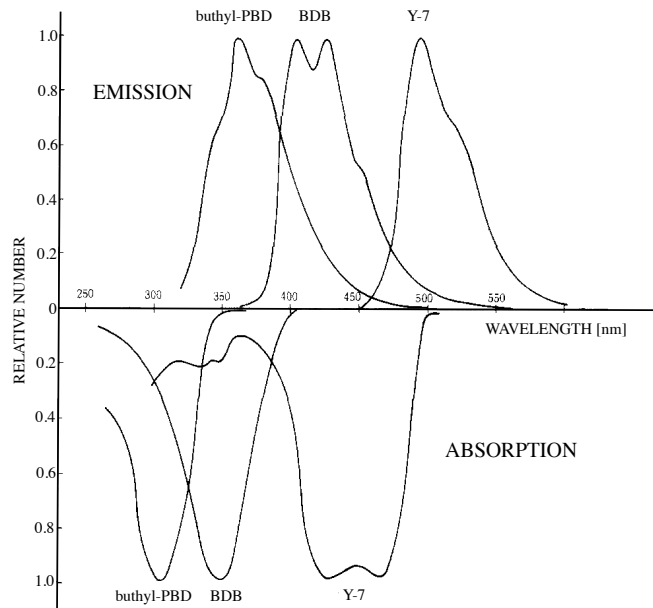


**Figure 1.13** – Absorption and emission spectra of typical fluors used in organic scintillators, taken from Ref. [28]. The absorption spectrum of the secondary fluor (BDB) covers a wide wavelength range of the primary fluor emission (butyl-PBD). The third wavelength shifter shown (Y-7) is used to create green wavelength emission.

**Table 1.2** – Properties of some organic scintillators. The following symbols are used:  $\rho$  — density;  $\tau_d$  — characteristic decay time;  $LY$  — light yield per MeV;  $\lambda_{\text{peak}}$  — peak emission wavelength;  $n(\lambda_{\text{peak}})$  — refractive index at peak emission; PVT — polyvinyltoluene; PS — polystyrene. The values are taken from Ref. [20].

Scintillator	base	$\rho$ [g/cm <sup>3</sup> ]	$\tau_d$ [ns]	$LY$ [Photons/MeV]	$\lambda_{\text{peak}}$ [nm]	$n(\lambda_{\text{peak}})$
Anthracene	-	1.25	30	16000	440	1.62
BC-408 <sup>a</sup>	PVT	1.032	2.1	10000	425	1.58
BC-418 <sup>a</sup>	PVT	1.032	1.5	11000	391	1.58
UPS-89 <sup>b</sup>	PS	1.06	2.4	10000	418	1.60
UPS-91F <sup>b</sup>	PS	1.06	0.6	6500	390	1.60

<sup>a</sup>BICRON company.

<sup>b</sup>AMCRYSH company.

## Inorganic Scintillators

Organic scintillators are due to their relatively low density usually used to measure only a small fraction of the incident particle energy. The task of inorganic scintillators is different, since they are used to measure the total energy of a particle with a high efficiency, i.e. completely absorbing on a short distance. A typical application of inorganic scintillators are electromagnetic calorimeters in high energy physics experiments, where scintillators with a high density and a high radiation tolerance are needed in order to measure the energy of high energy electromagnetic cascades. Another large field of application is the Positron Emission Tomography, where inorganic scintillators are used to determine the energy of 511 keV gamma rays.

The ideal inorganic scintillator would be made of a material with a high density and high atomic number  $Z$  since charged particles and photons deposit their energy mainly in interactions with the atomic electrons. A difficulty is, that most materials which fulfil this requirement are not transparent to visible light, so that even if the particle is stopped efficiently and a high number of scintillation photons is created, these photons cannot be detected.

The luminescent properties of inorganic scintillators are in contrast to organic scintillators not independent on the physical state of the material (solid, liquid gaseous), but they are linked to the crystal lattice and usually do not appear in other phases. Only in the highly ordered crystal state, the large density of atomic electrons can be confined into well separated energy bands making the material transparent for the produced scintillation light.

### Scintillation mechanism

The scintillation mechanism of inorganic crystals is rather different compared to the scintillation mechanism in organic materials. It is based on the energy bands which are created in a crystal material due to interactions of the individual energy levels of the neighbouring atoms. Several different scintillation mechanism in inorganic scintillators exist. In the following we will focus on the most commonly used extrinsically activated inorganic scintillators; i.e. crystals which are doped with so called activator atoms in order to create a better light yield. The basic light production mechanism in such a scintillator is shown in Figure 1.14.

In the first step of the process, electron-hole pairs are created, either due to the energy loss of incident charged particles, by secondary electrons created due to Compton scattering, or by photo-absorption. The electrons/holes which are created at some point of the conduction/valence band move to the bottom of the corresponding energy band by means of elastic scattering. From this point, an exciton state can be formed which is free to move through the scintillator until it is eventually captured by a luminescence centre (activator state), resulting in the emission of scintillation light. Similar to the case of organic scintillators, a wavelength shift (Stokes' shift) appears between the absorption and emission of the luminescence centre, avoiding an instantaneous re-absorption (cf. Figure 1.11(b)). A summary of the properties of some inorganic scintillators, commonly used in high energy physics and positron emission tomography is given in Table 1.3.

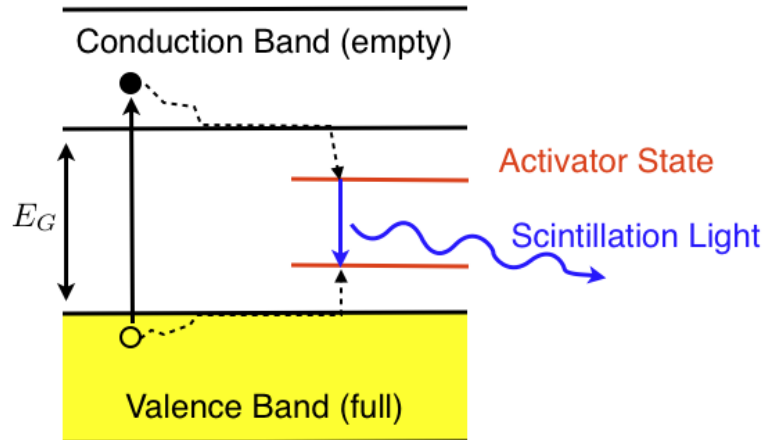


**Figure 1.14** – Energy band structure of an inorganic scintillator. Activator states are created by doping the scintillator crystal with different atoms. If an electron-hole pair is created, for example by photon absorption with  $h\nu > E_G$ , it can travel through the scintillator until it is captured by an activator state causing the emission of scintillation light.

**Table 1.3** – Properties of some commonly used inorganic scintillators in high energy physics and positron emission tomography. The following symbols are used:  $\rho$  — Density;  $X_0$  — radiation length;  $\tau_d$  — characteristic decay time;  $LY$  — light yield per MeV;  $\lambda_{\text{peak}}$  — peak emission wavelength;  $n(\lambda_{\text{peak}})$  — refractive index at peak emission wavelength. The values are taken from Refs. [20, 29, 30].

Scintillator	$\rho$ [g/cm <sup>3</sup> ]	$X_0$ [cm]	$\tau_d$ [ns]	$LY$ [phot./MeV]	$\lambda_{\text{peak}}$ [nm]	$n(\lambda_{\text{peak}})$
NaI:Tl	3.67	2.59	230	38000	415	1.85
CsI	4.51	1.85	30.0	2000	315	1.95
CsI:Tl	4.51	1.85	1000	55000	550	1.79
BGO ( $\text{Bi}_4\text{Ge}_3\text{O}_{12}$ )	7.13	1.12	300	8000	480	2.15
BaF <sub>2</sub> <sup>a</sup>	4.88	2.1	0.7	2500	220	1.54
BaF <sub>2</sub> <sup>b</sup>			630	6500	310	1.5
PWO ( $\text{PbWO}_4$ )	8.28	0.85	10 – 30	70 – 200	430	2.2
LSO ( $\text{Lu}_2\text{SiO}_5:\text{Ce}$ )	7.41	1.2	12 – 40	26000	420	1.82
LaBr <sub>3</sub> :Ce	5.29	-	18	70000	356	1.88
LuAG:Ce	6.73	-	60	> 25000	535	1.84
LFS	7.35	1.15	35	32000	425	1.81

<sup>a</sup>Fast signal component.

<sup>b</sup>Slow signal component.

### 1.2.4 Calorimeter Types

Two main classes of calorimeters are widely used, homogeneous and sampling calorimeters. A homogeneous calorimeter consists of a single kind of material which fulfils two different purposes. Firstly, it should stop the incoming particles with a high efficiency and should therefore have a high density and atomic number  $Z$ . Secondly, it must convert the deposited energy into a measurable signal, e.g. scintillation light, Cherenkov light, or ionisation. Compared to sampling calorimeters described below, the concept of homogeneous calorimeters has the advantage that the full detector volume is used to create the signal as shown in Figure 1.15. The full shower measurement facilitates a better energy resolution of this calorimeter type.

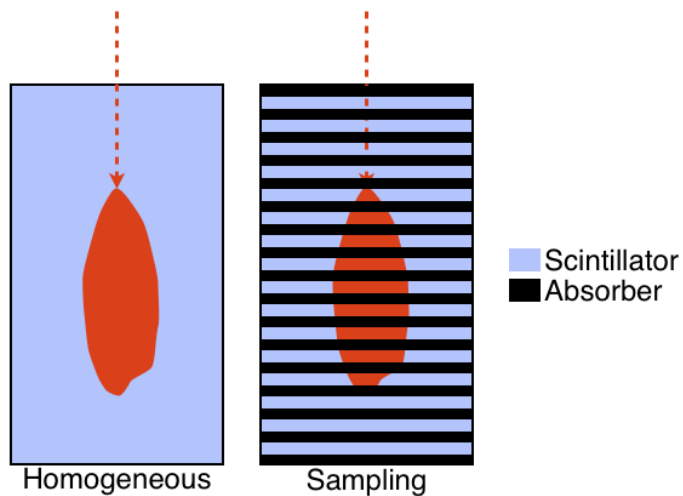


**Figure 1.15** – Schematic view of a homogeneous and a sampling calorimeter with sandwich structure. In case of the homogeneous calorimeter, the full shower is measured as the full detector volume is sensitive. In case of the sampling calorimeter, only the shower fraction sampled with the active scintillator layers is observed.

A sampling calorimeter, on the other hand, consists of two different materials, an absorber and an active material. The task of the absorber material is to efficiently stop the incoming particles by producing a shower of secondary particles, whereas the active material (e.g. an organic scintillator) is used to sample the energy of the shower particles at different positions. Hence, only a fraction of the total shower is observed.

Electromagnetic calorimeters, designed to measure the energy of photons, electrons and positrons, are often realised in the homogeneous concept in order to achieve a high energy resolution. However, the materials used to build homogeneous calorimeters such as scintillating crystals are expensive. Therefore, hadronic calorimeters are – due to their much larger size – often realised in the sampling concept. The possibility of choosing dense absorber materials such as lead or tungstate allows for a compact calorimeter design, and comparably cheap organic scintillators can be used for the active material. In the following, the important effects contributing to the response, and the energy resolution of a sampling calorimeter are discussed.

#### Statistical Shower Fluctuations

In contrast to a homogeneous calorimeter, in a sampling calorimeter only a small fraction of the shower energy – usually a few percent – is observable. The measured signal in such a calorimeter

is indeed approximately proportional to the total shower energy, however, the energy deposited in the active and passive layers is subject to event-to-event fluctuations, so called ‘sampling fluctuations’, which have a significant impact on the energy resolution of the calorimeter.

Additional fluctuations are caused by the angular distribution of the particles in a shower caused by multiple scattering. Particles traversing the calorimeter at an angle  $\theta$  with respect to the calorimeter axis cover a  $1/\cos\theta$  times longer distance in an active layer compared to particles which move along the calorimeter axis. This results in a different energy loss and hence induces additional fluctuations of the calorimeter signal.

It was mentioned in section 1.2.1 that the energy loss of charged particles due to ionisation and excitation is subject to large fluctuations, as there is a finite probability for huge energy transfers in single collisions. These fluctuations become visible in case of thin material layers, such as the active layers of a sampling calorimeter. In Figure A.5 the spectra of visible energy depositions of high energy muons in a sampling calorimeter are shown. The spectra reveal a typical Landau shape which is characterised by a long tail towards large energy depositions. These Landau fluctuations also cause a deterioration of the energy resolution.

### Compensation and Non-Compensation

The strong interaction of hadronic particles has some important consequences on the measurement of the hadronic shower energy. Two different kinds of calorimeters are distinguished: compensating and non-compensating ones. The response of a non-compensating calorimeter to a pion compared to an electron of the same energy is smaller, or differently formulated:  $\pi/e < 1$ . Parts of the energy deposited by the pion is for example used to release nuclear bindings and are therefore fundamentally undetectable. However, each hadronic shower also has a completely detectable electromagnetic subcomponent denoted  $f_{\text{em}}$  which increases with the energy as described by Equation 1.19. Therefore, also the  $\pi/e$  ratio increases with the shower energy, which results, in case of a non-compensating calorimeter, to an intrinsically non-linear response to the hadron energy. In order to quantify the degree of non-compensation in an energy independent way, the  $e/h$  ratio is introduced, where  $h$  describes the response to a hypothetical purely hadronic shower without electromagnetic subcomponent. As there is no such particle shower in reality, the  $e/h$  ratio can only be determined by measurements of the  $\pi/e$  ratio. The pion response can be formulated in the following way:  $\pi = f_{\text{em}} \cdot e + (1 - f_{\text{em}}) \cdot h$ . Division with the electron response  $e$  and inversion leads to the following equation [18]:

$$e/\pi = \frac{e/h}{1 - f_{\text{em}}(1 - e/h)}. \quad (1.20)$$

By fitting the formula to  $e/\pi$  values measured at different energies, the  $e/h$  value can be determined.

As the electromagnetic fraction of a hadronic particle shower is subject to large event-by-event fluctuations, in case of a non-compensating calorimeter, also the measurable energy is strongly fluctuating. Since this results in a degradation of the energy resolution, it is often tried to build compensating calorimeters with an  $e/h$  ratio close to unity. One possible way to achieve this is to decrease the response to the electromagnetic component by using high  $Z$  absorber materials. This enhances the probability for photoelectric absorption in the absorber (cf. Figure 1.6) and since most of the produced photoelectrons cannot escape the absorber due to their limited range, they remain undetected. The other possibility is to increase the response to the hadronic shower component  $h$  which can be achieved by choosing an active material with

a large hydrogen content, e.g. organic scintillators. When neutrons, originating from nuclear interactions with the absorber, collide with the hydrogen nucleus, recoil protons are created which generate a signal in the scintillator. By choosing the sampling fraction appropriately, compensation ( $e/h = 1$ ) can be achieved. When  $^{338}\text{U}$  is used as absorber material, neutrons can induce nuclear fission, thus releasing a huge amount of extra energy which, if necessary, further enhances the response to hadrons.

### Energy Resolution

The energy resolution of a sampling calorimeter is parameterised by the following formula:

$$\frac{\sigma(E)}{E} = \frac{a}{\sqrt{E}} \oplus \frac{b}{E} \oplus c, \quad (1.21)$$

where the first term, denoted ‘stochastic term’, includes the statistical sampling, path length and Landau fluctuations described above. It has the characteristic  $1/\sqrt{E}$  dependence of a Poisson variance. The second term, the so called ‘noise term’ comprises the influence of the detector noise, such as photosensor dark-noise or electronics noise, which for example is caused by signal amplifiers. This type of noise generally has a constant amplitude and therefore becomes negligible at high energies. The last constant term  $c$  accounts for the degradation of the energy resolution due to an imprecise calibration, non-compensation<sup>7</sup>, shower leakage, or other detector specific effects and is the dominant factor for high shower energies.

### The CALICE Analogue Hadronic Calorimeter

The CALICE collaboration [31] is a worldwide community of physicists and engineers which develop highly granular electromagnetic and hadronic calorimeter prototypes for the next generation of electron-positron colliders. A multitude of different calorimeter types and technological approaches are pursued in order to be prepared for the challenging physics case of future particle physics experiments.

This thesis is devoted to the *analogue hadronic calorimeter* (AHCAL) prototype, a sandwich type calorimeter with an unprecedented high segmentation in longitudinal and lateral direction. A photograph of the prototype is displayed in Figure 1.16, showing the AHCAL and two other prototypes during a test-beam measurement at CERN in 2006. The AHCAL has approximate dimensions of  $1 \times 1 \times 1 \text{ m}^3$  and consists of 38 layers of  $\sim 2 \text{ cm}$  thick steel absorber plates, interleaved with highly segmented scintillator layers. The structure of one of the  $0.5 \text{ cm}$  thick scintillator layers is shown in Figure 1.17. It consists of square plastic tiles – such as the one shown in Figure 1.1 – with a side length ranging from  $3 \text{ cm}$  in the centre up to  $12 \text{ cm}$  in the outer region of the layer. The blue scintillation light produced when a particle traverses the scintillation tile is collected by an integrated *wavelength shifting fibre* (WLSF) and guided to a silicon photomultiplier, a pixelated photodiode operated in Geiger mode which is introduced and discussed in detail in chapter 3 and chapter 4. The conversion from blue to green light is necessary since by the time the calorimeter prototype was designed, only SiPMs with a

---

<sup>7</sup>It should be noted that the contribution of non-compensation ( $e/h \neq 1$ ) to the energy resolution for hadronic showers is in principle not expected to be constant. In Ref. [18], therefore an energy dependent factor is proposed which, however, does not yield significantly better fits to available experimental data up to 400 GeV.

sensitivity optimised for green light were available. Further, the WLSF enhances the uniformity in response.

The AHCAL represents the first large scale application of SiPMs with its  $\sim 8000$  channels. Besides the physics performance tests, it was therefore also one of the goals of the project to prove that these novel photodetectors provide the high level of reliability and calibration capability necessary for a large scale experiment. During the test-beam activity from 2006 until 2009 at CERN and Fermilab, the analogue HCAL prototype was exposed to particle beams – mostly pions, muons, electrons and positrons – in the energy range from 1 GeV up to 180 GeV. A detailed description of the test-beam programme, the beam-line and detector setup can be found in Ref. [32].

The data acquired in these test-beam runs is stored in central databases and allows the investigation of hadron shower physics at a level of detail that has never been achieved before. One of the goals in this context is the development and validation of existing particle flow analysis tools [9, 33].

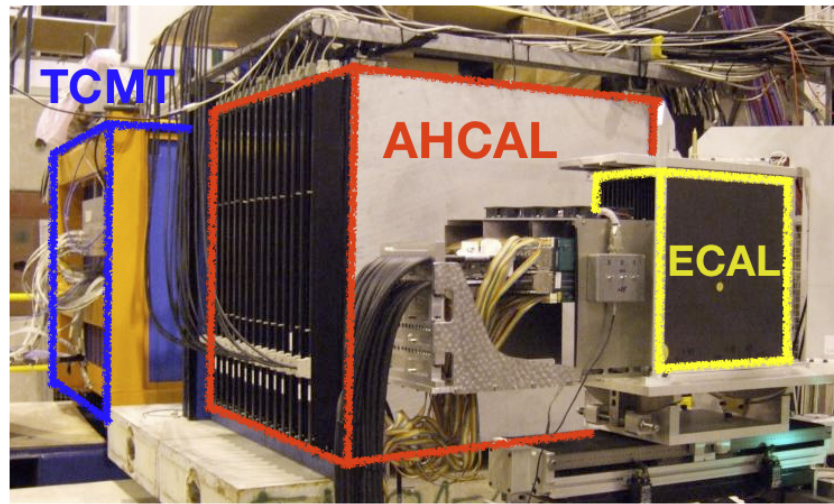


**Figure 1.16** – Photograph of the test-beam setup 2006 at CERN, taken from Ref. [34]. In front of the AHCAL prototype (red) is the ECAL prototype. A *tail catcher and muon tagger* (TCMT) is positioned behind the AHCAL for shower leakage measurements.

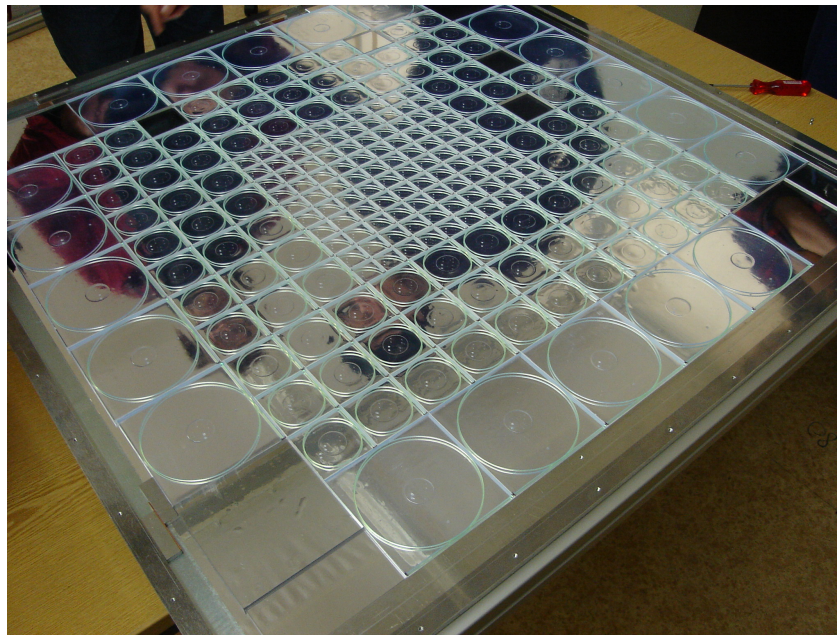


**Figure 1.17** – Photograph of one active layer of the AHCAL physics prototype. The tiles in the centre have a side length of 3 cm, which increases to the outside up to a size of 12 cm.

## Chapter 2

# Towards Precise Monte Carlo Simulations of the Scintillation Mechanism

Monte Carlo techniques have become an inevitable tool in all aspects of physical sciences. Simulation studies provide the unique possibility to conduct virtual experiments, assuming different physical laws, and comparing the results with observations made in real experiments, thus gaining a deeper understanding of the underlying physical processes. In high energy physics, Monte Carlo simulations are present at all stages of an experiment: from the first conceptual idea, the detector development, the data taking, until the final interpretation of results. An important requirement for a predictive Monte Carlo simulation is the precise and detailed implementation of the underlying physical processes, relevant for the particular experiment. This requirement, on the other hand, is contrary to the available computational power, which remains limited. Hence, many physical processes cannot be calculated up to the highest orders of precision and approximations have to be made. It is one of the challenges in the development of Monte Carlo tools, to implement these processes in an approximative way, such that simulation results remain in agreement with the experimental observations.

Parts of this thesis are devoted to the simulation of the scintillation mechanism in organic scintillators, exactly speaking, to the ionisation quenching effect which causes a reduction of the produced scintillation light if the incident charged particle creates a high ionisation and excitation density in the scintillator. A measurement of the light output of the AHCAL organic scintillator tiles created due to the irradiation with low energy electrons was carried out and compared to the results obtained from a Monte Carlo simulation of the corresponding experiment based on the Geant4 [5, 6] software framework. The comparison of the experimental data and the Monte Carlo simulation revealed, that the current implementation of the ionisation quenching effect in combination with the default simulation settings fails to describe the experimental observations precisely; i.e. when the specific energy loss of particles changes significantly in between individual simulation steps. To solve this problem, an improved calculation method of the ionisation quenching effect is proposed, which allows for a precise description. The impact of the improved calculation method is tested by simulating and comparing positron and pion induced particle showers in the AHCAL prototype. The discussion of the results is concluded with studies on the performance of the improved calculation method.

## 2.1 Ionisation Quenching in Organic Scintillators

In the preceding discussion of the fundamental scintillation process (section 1.2.3) it was assumed that a constant fraction of the deposited energy is used to create excited molecular states which upon de-excitation is converted into fluorescent light. This scintillation light can be detected with a suitable photodetector. Following these considerations, a linear relation is expected between the energy deposition of a particle  $E$  and the amount of fluorescent light produced:

$$L = S \cdot E, \quad (2.1)$$

where  $L$  is the scintillation response in a given unit (e.g. number of photons) and  $S$  is the scintillator efficiency (e.g. number of photons per energy deposition). For the following discussion of the ionisation quenching process, it is useful to introduce the differential form of the equation above:

$$\frac{dL}{dx} = S \cdot \frac{dE}{dx}. \quad (2.2)$$

The validity of this equation has been proven for electrons between 125 keV and 3 MeV [35, 36] and muons with energies up to 170 MeV [37]. Within these energy ranges, the mentioned particles have a relatively small specific energy loss in common. In fact it was observed that particles reaching high  $dE/dx$  values such as protons and alpha particles, or electrons at low energies generate a scintillation signal which is not directly proportional to the deposited amount of energy. The origin of this effect is expected to be caused by interactions between the excited and ionised molecules that are generated along the particle track. In case of a low  $dE/dx$ , the distance between the excited and ionised molecules is large, hence no interaction is possible. In contrast, at large  $dE/dx$  values, a high density of excited molecules is generated which enables them to interact, and to de-excite without the emission of photons. This process is referred to as ionisation quenching as it depends mainly on the density of the created ionisation.

### Birks' law

In order to predict values for the specific fluorescence which take into account the ionisation quenching effect, Birks has developed a semi-empirical formula [38] which assigns the reduction of scintillation light to the high density of excited and ionised molecules present around the trajectory of a highly ionising particle. It has become a widely used standard equation as it describes – despite its simple shape compared to other formulas – the non-linear behaviour for a large variety of scintillators and different particle types. In the original derivation it is assumed that two kinds of excited or ionised molecules – denoted ‘damaged’ or ‘undamaged’ molecules – are created around the track of the ionising particle. The quantity of damaged molecules per undamaged molecule is proportional to the specific energy loss,  $B \cdot dE/dx$ , where  $B$  is a constant factor. Further it is assumed that the damaged molecules feature a  $k$ -times higher probability for dissipating the excitation energy non-radiatively compared to the undamaged ones. Taking into account this relation, the formula for the specific fluorescence (Equation 2.2) is reformulated to:

$$\frac{dL}{dx} = \frac{S \cdot \frac{dE}{dx}(E)}{1 + kB \cdot \frac{dE}{dx}(E)}. \quad (2.3)$$

Since there is so far no direct experimental method to determine  $k$  and  $B$  separately, usually the product  $k \cdot B$  is treated as a single parameter which is referred to as Birks' coefficient  $kB$ <sup>1</sup>. For small values of the specific energy loss  $dE/dx$ , Equation 2.3 returns to the simple linear relation described by Equation 2.2. On the other side, for large  $dE/dx$ , the specific fluorescence shows a saturating behaviour, so that the specific energy loss is constant:

$$dL/dx = S/kB = \text{const.} \quad (2.4)$$

The integral of Equation 2.3 over the energy of a particle yields the expected fluorescence light output. Hence, the following light yield is created if a charged particle with energy  $E_0$  completely dissipates its energy in the scintillator:

$$L = \int_0^{E_0} \frac{dL}{dE} dE = S \cdot \int_0^{E_0} \frac{1}{1 + kB \cdot \frac{dE}{dx}(E)} dE. \quad (2.5)$$

If the relation  $kB \cdot dE/dx(E) \ll 1$  is fulfilled for energies within the integration range, Equation 2.5 can be approximated by the simple linear relation  $L = S \cdot E_0$ . However, for most scintillators and particles this condition is not fulfilled which results in a non-linear relation between the particle energy and the light output of the scintillator.

### Other ionisation quenching models

In addition to the model developed by Birks, several other equations have been derived in order to account for the ionisation quenching effect, such as the Wright model [39], the Voltz model [40], or the generalisation of Birks' law introduced by Chou [41]. Here, only the generalised form of Birks' law will be mentioned:

$$\frac{dL}{dx} = \frac{S \cdot dE/dx}{1 + kB \cdot \frac{dE}{dx} + C \cdot \left(\frac{dE}{dx}\right)^2}. \quad (2.6)$$

The formula contains an additional term proportional to the square of the  $dE/dx$ . For experimental data measured with the anthracene scintillator, Equation 2.6 yields the best fit to experimental data if  $C = 0$ , i.e. if the equation is equivalent to Birks' law [7]. However, for several scintillators different to anthracene, a significantly improved description of the data has been reported when Equation 2.6 is applied instead of Equation 2.3 [42]. Anyway, it should be emphasised that the models presented here are of semi-empirical nature and not based on completely established theories as the responsible processes for ionisation quenching are still discussed in the scientific community. Hence, for each scintillator a pragmatic approach of choosing the model which describes the data best should be applied. For this reason, it has been investigated in this work whether the additional parameter of Chou's model enables an improved description of the non-linear response of the AHCAL scintillator tiles, compared to Birks' model.

Figure 2.1 sows a collection of specific fluorescence data for electrons, protons and alpha particles in anthracene crystals as a function of the  $dE/dx$ . The majority of the experimental data can be described well by Birks' law (solid line), in particular the saturating behaviour of the  $dL/dx$  for highly ionising alpha particles is described correctly. The model of Wright

<sup>1</sup>Throughout this thesis, the original notation introduced by Birks' (cf. Refs. [7, 38]) is used. In the literature, however, sometimes a different notation of Birks' coefficient,  $k_B$ , is used (e.g. Refs. [14, 18]), which however does not emphasise the product of parameters and may lead to confusion with the Boltzmann constant.

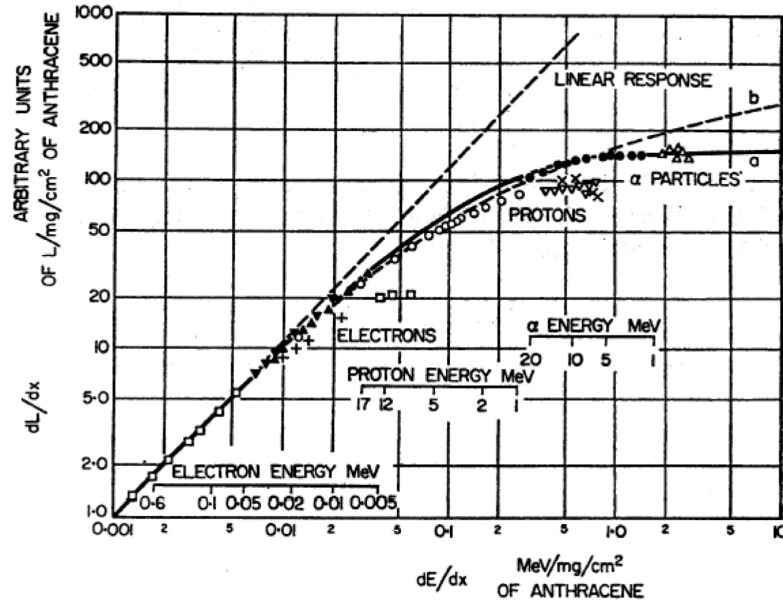


**Figure 2.1** – Specific fluorescence  $dL/dx$  as a function of the specific energy loss  $dE/dx$  for different particles in anthracene. A clear deviation from the linear response curve is observed. Birks law (Equation 2.3) is described by the solid line (a), whereas the dashed line (b) indicates the prediction given by the Wright model. Figure taken from Ref. [7]

(dashed line) shows the same tendency as Birks' model for small  $dE/dx$  values and even gives a slightly better description for a subset of the proton data, however, it significantly overestimates the specific fluorescence for high  $dE/dx$  values.

One important consequence of Birks' law is caused by the fact, that the specific energy loss  $dE/dx$  of different particle types is in general not the same, hence, completely absorbed electrons, protons and alpha particles of the same energy, generate different amounts of fluorescence light. This is shown in on the left of Figure 2.2 where the expected light yield for electrons, protons, alpha-particles and deuterons in anthracene is plotted as a function of the particle energy (cf. Equation 2.5). A large difference between the individual particles is observed, e.g. electrons show a mainly linear energy dependence whereas alpha-particles reveal a strong non-linearity. It is evident that this effect is important for the description of the scintillator light output in Monte Carlo simulation studies. The precise knowledge of  $kB$ , hence is an essential prerequisite for a predictive scintillation detector simulation.

As mentioned above, the scintillator response to electrons is linear for energies higher than  $\sim 125$  keV. Nevertheless, for energies below this threshold, also electrons reveal a non-linear dependence as indicated on the right of Figure 2.2. This behaviour is caused by the specific energy loss which gets very high shortly before the particle is stopped (Figure 2.3). This effect gives rise to a high ionisation density at the end of the particle track, resulting in a reduced amount of detectable fluorescence light due to ionisation quenching. Hence, measuring the light output created by low energy electrons in a scintillator and comparing the results to the prediction by Birks' law, allows for the determination of Birks' coefficient. This instance is used in section 2.2 to determine  $kB$  for the scintillator used in AHCAL prototype.

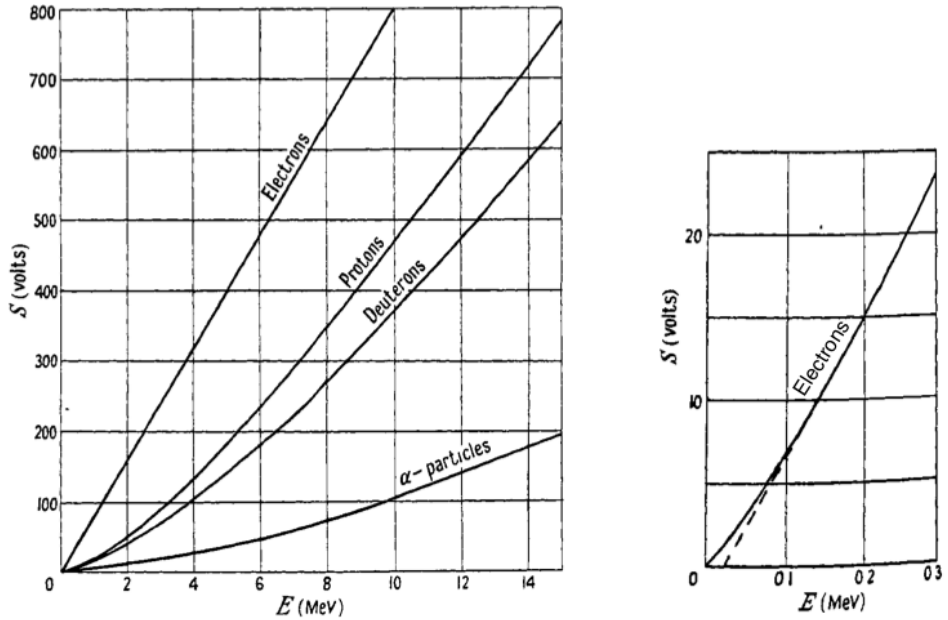


**Figure 2.2** – Scintillator light output as a function of the particle energy. The light output at equivalent energies differs strongly between the individual particle types. The right side shows the electron light output on a magnified scale, revealing the non-linear dependence below  $\sim 125$  keV. Figure taken from Ref. [38].

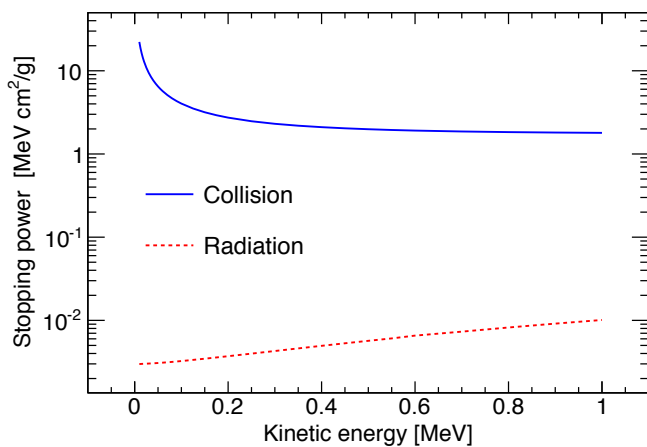


**Figure 2.3** – Collisional and radiative stopping power of an electron in polystyrene as a function of the kinetic energy. The collisional  $dE/dx$  increases strongly for energies smaller than  $\sim 125$  keV. The radiative part of the  $dE/dx$  can be neglected for energies up to 1 MeV. The data for the figure is taken from Ref. [43].

## Quenching factors

The term quenching factor is also widely used to describe the effect of ionisation quenching for heavy particles. It is mentioned here in order to facilitate a comparison of the results presented in this work with common literature. A quenching factor in general defines a ratio between scintillation signals observed for different particle types. Usually the signals are normalised to the electron response due to its almost linear energy dependence (cf. Figure 2.2). A widely used definition of the quenching factor  $Q$  is:

$$Q = \frac{E_{e^-}}{E_{\text{true}}}, \quad (2.7)$$

where  $E_{e^-}$  is the measured particle energy (e.g. proton or alpha-particle) which is calibrated with the electron scale; i.e. the measured signal is treated as if it was generated by an incident electron.  $E_{\text{true}}$  denotes on the other hand the ‘true’ energy of the particle.

The main difference between the concept of quenching factors and Birks’ coefficient  $kB$  is that quenching factors depend per definition on the particle type, whereas  $kB$  can be applied – according to the very concept of Birks’ law – to all particle types. In order to demonstrate the relation between quenching factors and Birks’ coefficient, in Figure 2.4 the quenching factors of electrons (= 1 by definition), protons and alpha-particles in polystyrene are shown. Validity of Birks’ law is assumed with a  $kB$  of  $1.51 \cdot 10^{-2} \text{ cm/MeV}$  – the value measured for polystyrene in section 2.2. The calculated data show that a single Birks’ coefficient is equivalent to particle specific and energy dependent quenching factors. The quenching factor of alpha particles shows only a weak energy dependence which is caused by the saturating behaviour of the  $dL/dx$  for high  $dE/dx$  values, displayed in Figure 2.1. Since the electron response is not anymore linear for low energies (cf. Figure 2.2 (right)), the calculated quenching factors of protons and alpha-particles increase in this energy regime.

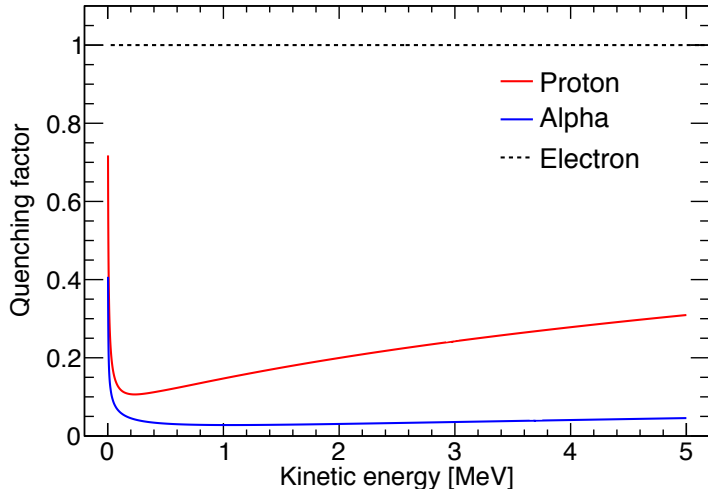


**Figure 2.4** – Quenching factors  $Q$  for electrons, protons and alpha-particles in polystyrene. The  $Q$ -values are calculated using the  $dE/dx$  tables of the corresponding particles, provided by the Geant4 simulation toolkit. It is assumed that the particle deposits its energy following the  $dE/dx$ ; i.e. no secondary particle production is considered. A Birks’ coefficient of  $1.51 \cdot 10^{-2} \text{ cm/MeV}$  is assumed.

## 2.2 Measurement of Birks' Coefficient for the AHCAL Scintillator

### The AHCAL scintillator tiles

The scintillating tiles of the AHCAL physics prototype are made of polystyrene base material, doped with a high concentration of a primary fluor 1.75% PTP and a small concentration of a secondary fluor (wavelength shifter) 0.01% POPOP. The tiles were produced in a casting process in Vladimir (Russia) by the UNIPLAST company. Three different tiles with 3, 6 and 12 cm side length, each 0.5 cm thick were produced as indicated in Figure 2.5, which shows pictures of all three tile sizes. Wavelength shifting fibres of 3 mm thickness (Y11) from the KURARAY company (Japan) are inserted into a small circular shaped groove machined into each tile. The fibre fulfils two important tasks: it helps to increase the response uniformity, as the detectable scintillation signal, created by charged particles of identical energy, depends only weakly on the traversing position. The second important task of the wavelength shifting fibre is the conversion of the blue fluorescence light from the POPOP dopant into green light, as the photon detection efficiency of the used MEPHHI/PULSAR SiPMs – belonging to one of the first generation of SiPMs produced in large quantities – is very small for blue light as will be shown in section 4.6 (cf. Figure 4.29).

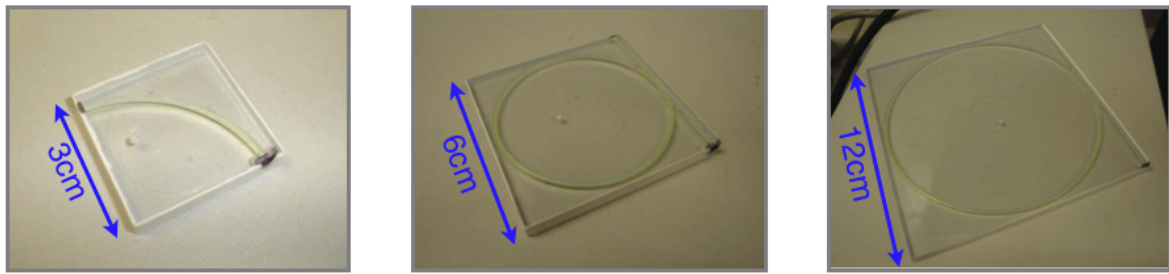


**Figure 2.5** – Scintillator tiles used in the AHCAL (cf. Figure 1.17).

### Experimental setup

The experimental setup used for the measurements was developed at the Max-Planck-Institut für Kernphysik (MPIK) in Heidelberg [44, 45]. It was originally developed to characterise the liquid scintillators of the Double Chooz neutrino reactor experiment, dedicated to the measurement of the non-vanishing neutrino mixing angle  $\theta_{13}$ . Figure 2.6 shows the schematic layout of the setup. The central part is a  $^{137}\text{Cs}$  radioactive source which emits gamma rays with a fixed energy of 662 keV. If such a gamma ray interacts with the scintillator material, it may free an electron via Compton scattering, which in turn will dissipate its energy in the scintillator, hence producing scintillation light. The amount of scintillation light is detected by a photomultiplier tube connected at one side of the scintillator. It should be noted, that only a part of the total scintillation light produced is detected by the photomultiplier tube, as the fraction of photons which is absorbed in the scintillator or the reflector material surrounding the scintillator is unknown. The scattered gamma ray continues its path until it eventually reaches the germanium detector, which is capable to determine the photon energy with high precision. The germanium detector is calibrated by irradiation of mono-energetic photons from various radioactive sources before and after each measurement run as indicated in Figure A.2. If both

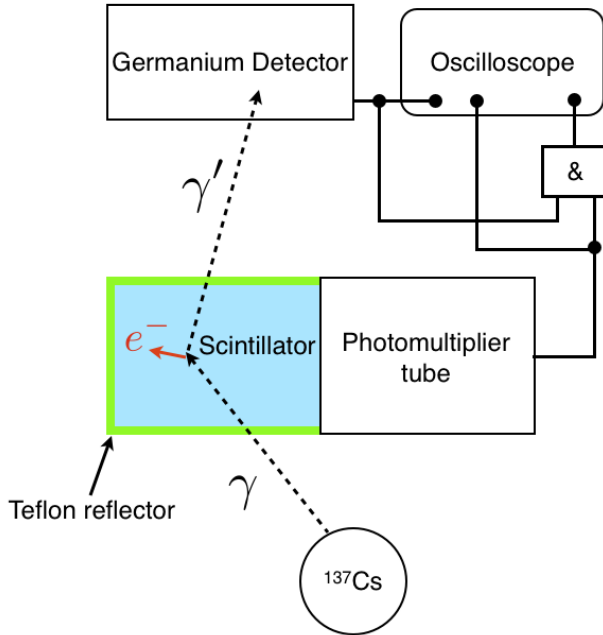


**Figure 2.6** – Experimental setup for the measurement of Birks’ coefficient. A  $^{137}\text{Cs}$  source generates 662 keV gammas (dashed line) which may undergo Compton scattering in the scintillator under study, thus generating a free electron. A photomultiplier tube detects the scintillation light produced and a germanium detector measures the energy of the scattered gamma. A photograph of the setup is shown in Figure A.1.

detectors – photomultiplier and germanium – measure a signal within a short time interval, a coincidence trigger is generated and the corresponding signal waveforms are digitised with an oscilloscope and stored to hard disk.

The setup was operated for roughly one week in order to accumulate enough statistics for the subsequent offline analysis of the raw data. In the following, the individual steps of this analysis are summarised. For each measured event, the energy of the Compton electron is determined by subtracting the energy of the scattered photon  $E_{\gamma'}$ , measured with the germanium detector, from the initial photon energy:  $E_{e^-} = 662 \text{ keV} - E_{\gamma'}$ . The theoretical limit on the electron energy is given by the initial photon energy, however, taking into account the geometrical acceptance, only a reduced energy range of the electrons is covered. In the presented measurement, a sufficient number of coincidence events was accumulated for  $E_{e^-} = 30 - 140 \text{ keV}$ .

The resulting data-set available for analysis contains pairs of values of the electron energy and the relative light output measured by the photomultiplier as shown in Figure A.3(a). For the following step, the data is divided into  $\sim 2 \text{ keV}$  wide energy bins and the most probable value of light yield is determined for each bin by fitting the sum of a Gaussian and an exponential function to the corresponding distribution as indicated in Figure A.3(b). This procedure facilitates a sufficient suppression of background events; e.g. Multiple Compton events, where the gamma deposits only a fraction of its energy via Compton scattering in the germanium detector. As an intermediate result, the light-yield in arbitrary units as a function of the kinetic energy of the electron is obtained.

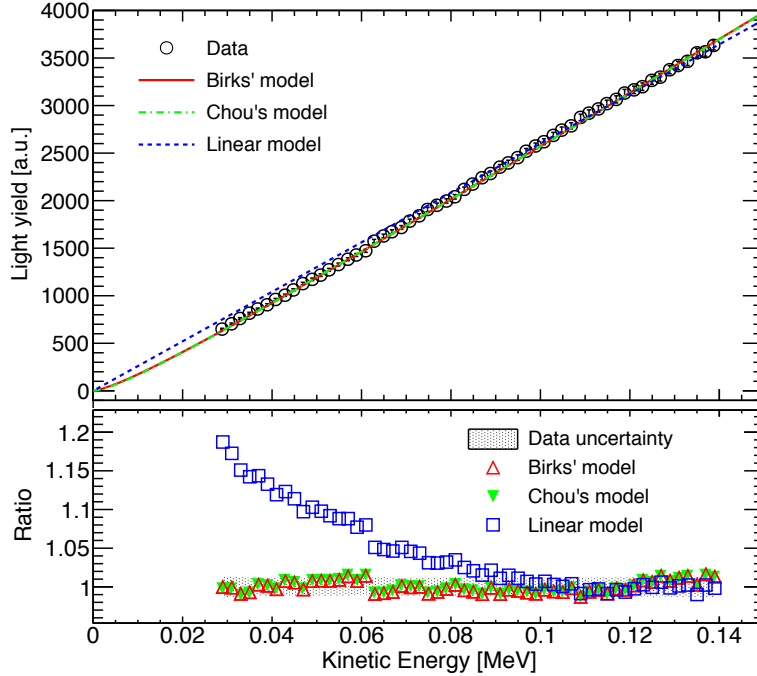


**Figure 2.7** – Light yield (LY) as a function of the electron kinetic energy. The data (circles) is fitted by Birks' law (solid line) and a simple linear model (dashed line). Only energies larger than 120 keV were considered for the linear fit. The lower plot shows the ratio between the calculated and measured light yield as a function of kinetic energy. Birks' law (triangles) describes the data well within the measurement uncertainty (shaded area). The linear model shows large deviations from the data for small energies.

### Measurement Results and $kB$ Determination

The result of the measurement is displayed in Figure 2.7. The measured light yield is plotted as a function of the electron kinetic energy. Statistical and systematic errors are considered, the latter one is estimated to be 1.1 % over the full energy range [44].

In a first step, the data is fitted with a simple linear model with only one free parameter  $S$  (Equation 2.1). The fit is only applied for energy values above  $\sim 120$  keV as in this energy range a linear dependence of the light yield on the electron energy is expected [35]. For smaller energies, a large discrepancy between the linear model is observed, as the  $dE/dx$  of an electron increases rapidly before the particle is absorbed which results in a reduction of the light yield due to ionisation quenching.

In a second step the measured data points are fitted with Birks' model, thus taking into account the effect of ionisation quenching. For this purpose, a program was written using the ROOT software framework [46], which calculates the light yield for certain values of  $S$  and  $kB$  by evaluating the following integral:

$$L = S \cdot \int_0^{E_{e^-}} \frac{1}{1 + kB \cdot \frac{dE}{dx}(E)} dE. \quad (2.8)$$

Here  $L$  is the scintillator light yield and  $E_{e^-}$  denotes the kinetic energy of the electron. The

**Table 2.1** – Summary of the fit results for the different models. The  $\chi^2$  of the linear model is relating to the fit of the limited energy range  $E > 120$  keV, whereas in case of Birks' and Chou's model, the whole data set was considered. The reduced  $\chi^2$  of all presented fits is smaller than unity which indicates a slight overestimation of the systematic errors.

Fit model	$S$ [a.u./MeV]	$kB$ [cm/MeV · $10^{-2}$ ]	$C$ [(cm/MeV) $^2$ · $10^{-5}$ ]	$\chi^2/\text{ndf}$
Linear	$26026 \pm 105$	–	–	0.11
Birks	$29832 \pm 204$	$1.51 \pm 0.07$	–	0.41
Chou	$29480 \pm 878$	$1.25 \pm 0.65$	$6.4 \pm 16.7$	0.42

$kB$  and  $S$  values are varied such that the  $\chi^2$  reaches a minimum which indicates the best fit. For the evaluation of Equation 2.8, the energy dependent values of the specific energy loss  $dE/dx$  are required. These values are calculated using the equation developed by Berger and Seltzer [15, 16] which was introduced on page 9. Since the measured electron energies are well below  $E < 1$  MeV, the radiative part of the stopping power is negligible small (cf. Figure 2.3), hence only the part of the formula describing the collisional stopping power for electrons was used (Equation 1.2). The density effect correction  $\delta$  which yields a reduction of the  $dE/dx$  due to the polarisation of the traversed media can also be neglected because of the low energy. Properties<sup>2</sup> of the polystyrene material required for the calculation are taken from Ref. [43].

Thirdly, the data were fitted with Chou's model (cf. Equation 2.6), considering the third fit parameter  $C$ . Figure 2.7 shows that both models – Birks and Chou – describe the data equally well; the ratio of the calculated over the measured light yield lies within the uncertainty of the measured values.

The fit results are summarised in Table 2.1. As mentioned above, the setup only facilitates measurements of the relative light yield. Hence, the scintillator efficiency  $S$  obtained from the fit has no physical relevance and will not be discussed in the following. It is clear from the presented data that Chou's model – despite the fact of an additional parameter – doesn't describe the data better than Birks' model; the reduced  $\chi^2$  of both fits are almost identical. In order not to complicate calculations unnecessarily, hence only Birks' model is considered in the following.

The best fit of Birks' model to the data is achieved for  $kB = (1.51 \pm 0.07) \cdot 10^{-2}$  cm/MeV. This value is considerably larger than the value for polystyrene based scintillators applied in Geant4 by default  $kB = (0.7943 \pm 0.0142) \cdot 10^{-2}$  cm/MeV [47], which points back to a measurement with the polystyrene based scintillator of the ZEUS hadronic calorimeter SCSN-38, doped with 1.0% b-PBD and 0.02% BDB [28]. The type and concentration of primary and secondary fluors in an organic scintillator has a significant impact on the efficiency of the radiative transition from an excited singlet or triplet state to the ground state (cf. Figure 1.11). A highly efficient radiative energy transfer may reduce the probability for ionisation quenching considerably. Hence, a difference in the  $kB$ -values is expected.

## 2.3 Simulation of Birks' Law in Geant4

A simplified version of the experimental setup was simulated in Geant4 [5, 6] in order to crosscheck the current implementation of Birks' law. In Monte Carlo simulations, the energy

<sup>2</sup>Density:  $\rho = 1.06$  g/cm $^3$ , Average excitation potential:  $I = 67.8$  eV and  $Z/A = 0.5377$ .

loss process and hence also the scintillation light production is handled only in an approximate way compared to the calculation of Equation 2.5. The step size is not infinitesimally small like in the integral calculation, but it has a finite size. The light yield is hence determined by a sum of individual contributions, rather than an integral. Further, secondary particles ( $\delta$  electrons and photons) may be produced depending on the setting of the simulation parameters. These secondary particles yield a different amount of scintillation light because of the non-linear nature of Equation 2.5; i.e. the light yield  $L(E)$ , produced by a single particle with energy  $E$  is in general different to the light yield produced by two particles:  $L(E) \neq L(E_1) + L(E_2)$ , with  $E = E_1 + E_2$ . These differences may be interpreted as if a modified, effective version of Birks' law is applied in the simulation which has the consequence that a different  $kB$ -value is required to describe the experimental data.

In the following section, the differences between the light yield calculation with Equation 2.5, and the calculation implemented in Geant4 is analysed by studying the dependence on the simulation parameters which control the step-size and the production of secondary particles. Further, an enhanced simulation implementation of Birks' law is proposed which predicts values for the light yield which are identical to the values calculated with Equation 2.5.

### Step-size limitation in Geant4

In Geant4 simulations, particles loose their energy in a series of discrete steps. In general it is assumed that the cross sections of the activated physics processes are constant during the individual simulation steps [48]. In order to avoid very large simulation steps which would invalidate the above assumption, the step-size has to be limited. Two different types of energy loss processes have to be considered: discrete processes which are accompanied by the production of secondary particles, and the continuous energy loss.

In case of discrete processes such as  $\delta$ -, or  $\gamma$ -ray emission, each active process proposes an upper limit for the step length, which takes into account the particle history; i.e. how many mean free paths have already been traversed since the last invocation of the corresponding process, or since the particle production. For each simulation step, the proposed step lengths are compared and the process with the lowest proposed step length is invoked. Therefore, the step length is mainly limited by the process with the highest cross-section.

In addition to the discrete processes, particles may continuously dissipate their energy due to ionisation and excitation of the medium. This type of energy loss is described by the collision stopping power formula (Equation 1.2). To avoid large changes of the particles  $dE/dx$ , the maximum energy which may be deposited in a step must be limited. This is achieved by limiting the reduction of the stopping range,  $R$ , of a particle in a step; the stopping range denotes the distance the particle can travel in the current medium until it is stopped. By demanding the particle stopping range not to decrease by a given percentage  $\alpha_R$  in each simulation step –  $\alpha_R = 20\%$  in the default setting – a large change of the specific energy loss  $dE/dx$  is effectively avoided. However, continuation of this procedure down to very small particle energies would cause extremely small simulation steps, slowing down the simulation process without gaining precision. Hence an additional parameter, the final range  $\rho_R$  is introduced, which relaxes the previous constrain for low energies – i.e. if the stopping range of the particle is smaller than  $\rho_R$  – so that the total remaining energy can be deposited in a single step. The default value of  $\rho_R$  applied in the simulation is 1 mm. Taking into account these considerations, the maximum step length proposed by the continuous energy loss  $S_{max}$  can be formulated by the following equation:

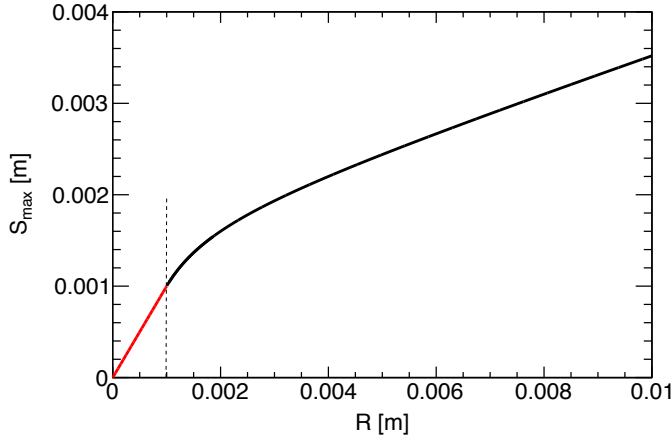


**Figure 2.8** – Maximum step size  $S_{\max}$  as a function of the particle stopping range  $R$ . The red curve indicates the condition when the stopping range is smaller than the final range parameter (here:  $\rho_R = 10^{-3}$  m). In this case no step limit exists such that  $S_{\max} = R$ .

$$S_{\max} = \begin{cases} \alpha_R R + \rho_R(1 - \alpha_R)(2 - \rho_R/R), & \text{if } R > \rho_R \\ R, & \text{if } R \leq \rho_R. \end{cases} \quad (2.9)$$

The second term in the upper equation is only responsible for a smooth transition between the two cases described above. In Figure 2.8, the value of  $S_{\max}$  is presented as a function of the stopping range for the default values of  $\alpha_R$  and  $\rho_R$ . For large values of  $R$ ,  $S_{\max}$  is represented by a linear function with slope  $\alpha_R$ . Hence, a particle may decrease its stopping range by 20% at maximum in a single simulation step. Following the curve to smaller values of  $R$ , the slope increases until it reaches unity when  $R \leq \rho_R$ . Hence, the remaining energy can be deposited in a single step (if no active discrete process proposes a smaller step length).

## Secondary Particle Production Cut

In order to keep the number of particles trajectories in a detector simulation within a reasonable range, secondary particles are only explicitly created when their energy – more precisely the stopping range – is higher than a certain threshold. For this purpose, the secondary particle production cut,  $T_{\text{cut}}$ , is introduced. Each time a process, generating secondary particles is invoked, the stopping range of the potentially created secondary particles is compared to the value of  $T_{\text{cut}}$ . Only if the stopping range is larger than  $T_{\text{cut}}$ , the secondary particle is explicitly generated, creating an additional trajectory. If on the other hand, the stopping range is smaller than  $T_{\text{cut}}$ , the secondary particle is not explicitly generated. In this case, its energy is added to the continuous energy loss of the primary particle described above. For the majority of the following simulation studies presented, a cut value of  $T_{\text{cut}} = 5 \cdot 10^{-5}$  m was applied, as this is the default within the CALICE simulation framework MOKKA [49], used for the simulation of particle showers in the AHCAL prototype. Usage of other values of  $T_{\text{cut}}$  values will be specified explicitly.

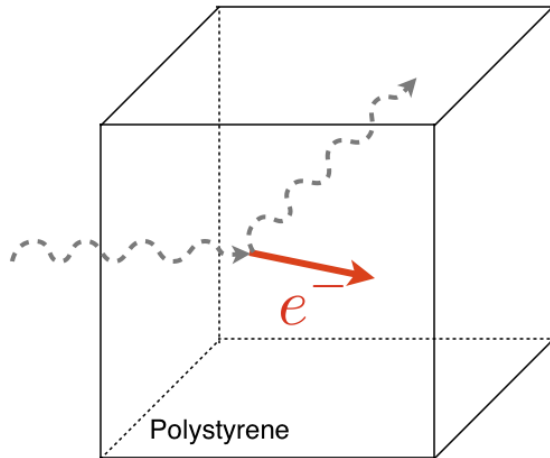


**Figure 2.9** – Simplified experimental setup as simulated with Geant4. It consists of a scintillator block made of polystyrene and a particle gun, which simulates the Compton effect by injecting electrons of a well defined energy into the scintilllator.

### Simulation setup

A simplified version of the experimental setup, described in section 2.2, is simulated using the Geant4 toolkit (cf. Figure 2.9). It consists of a polystyrene scintillator cube, made of polystyrene (*G4\_POLYSTYRENE*), predefined within the NIST database manager of Geant4. The same material definition is used for the scintillating tiles in the official MOKKA simulation framework for the AHCAL. In order not to complicate the simulation unnecessarily, the photons coming from the  $^{137}\text{Cs}$  source, giving rise to the production of Compton electrons within the scintilllator are not simulated. Instead, a particle gun simulates the Compton effect by injecting electrons of a well defined energy into the scintilllator block. For a comparison with the measured data it is only necessary to determine the light yield on a relative scale, hence no simulation of optical processes like propagation and reflection of scintillation photons within the scintilllator is required for the simulation. Instead, the part of the dissipated energy which is not subject to quenching – denoted visible energy  $E_{\text{vis}}$  – and which in a ‘real’ scintilllator gives rise to fluorescence light ( $L = E_{\text{vis}} \cdot S$ ), is taken as a measure for the total light output.

### Default implementation of Birks' law

In the official Geant4<sup>3</sup> release, Birks' law is activated by invoking the *G4EmSaturation* class [50]. The class provides a method for the calculation of the visible energy deposit  $E_{\text{vis}}$  for each simulation step. In the original implementation of this class, a constant specific energy loss per step  $\Delta E/\Delta x$  is assumed where  $\Delta E$  denotes the continuous energy loss and  $\Delta x$ , the length of the step. Accordingly, the visible energy per step  $\Delta E_{\text{vis}}$  is calculated by the following equation (cf. Equation 2.3):

$$\Delta E_{\text{vis}} = \frac{\Delta L}{S} = \frac{\Delta E}{1 + k_B \cdot \frac{\Delta E}{\Delta x}}, \quad (2.10)$$

where  $\Delta L$  denotes the light yield produced in the simulation step. Equation 2.10 represents a valid approximation of Equation 2.3, as along as the step size  $\Delta x$  is small enough, ensuring

<sup>3</sup>Version 9.3

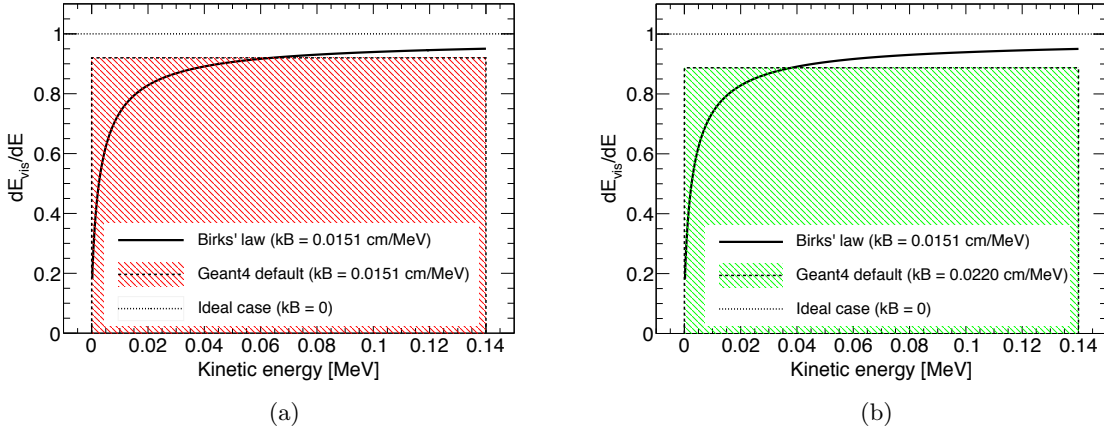


**Figure 2.10** – Figure (a) shows the differential visible energy  $dE_{\text{vis}}/dE$  of an electron as predicted by Birks' law with  $kB = 1.51 \cdot 10^{-2} \text{ cm/MeV}$  (solid line) versus the kinetic energy. The area under the line corresponds to the visible energy. The shaded area represents visible energy simulated with Geant4. The dotted line corresponds to the ideal case of a linear response ( $kB = 0$ ). On the right side, the effective Birks' coefficient  $kB_{\text{eff}} = 0.0220 \text{ cm/MeV}$  is applied in the simulation, in order to force the correct value of the total visible energy.

that the  $dE/dx$  is approximately constant during the simulation step. However, this is not the case if the  $dE/dx$  is changing rapidly in between two consecutive simulation steps which is for example the case for low energy electrons as described below. Hence, Equation 2.10 predicts in such a case imprecise values for the visible energy.

## Simulation Results

A case where the Geant4 approach of a constant  $dE/dx$  is not valid is shown in Figure 2.10(a). Three different calculations of the differential visible energy

$$\frac{dE_{\text{vis}}}{dE} = \frac{1}{1 + kB \cdot \frac{dE}{dx}} \quad (2.11)$$

are indicated for a 140 keV electron, dissipating its total energy in a polystyrene block. This specific energy value is chosen, as it represents the maximum energy of the scattered Compton electrons detected with the experimental setup described above.

In the first calculation, indicated by the dotted line, an ideal linear response is assumed ( $kB = 0$ ); dissipated energy and visible energy are identical ( $dE_{\text{vis}}/dE = 1$ ).

The second calculation, indicated by the solid line, shows the case when the energy dependence of the specific energy loss  $dE/dx$  is correctly taken into account. The  $kB$  value measured in this work has been applied ( $kB = 1.51 \cdot 10^{-2} \text{ cm/MeV}$ ). The value of the differential visible energy  $dE_{\text{vis}}/dE$  is reduced for small energies as the  $dE/dx$  of an electron increases strongly before it is stopped; i.e. large fractions of the deposited energy are lost for detection due to ionisation quenching.

The third calculation, indicated by the dashed line, shows the Geant4 prediction of the differential visible energy when the default simulation parameters are applied. Even for the highest

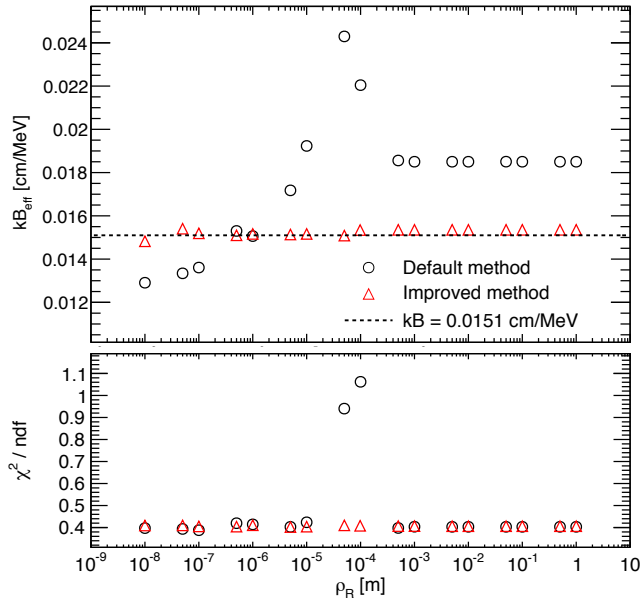


**Figure 2.11** – The upper part shows the Effective Birks' coefficient  $kB_{\text{eff}}$ , determined from the Geant4 based Monte Carlo fit to the measured light output, as a function of the final range parameter  $\rho_R$ . The circles indicate the result when the default calculation method of visible energy is invoked, whereas the triangles show the result when the improved calculation is used. The dashed line indicates the value of  $kB$  determined from the standalone fit described in section 2.2. The lower part of the figure shows the reduced  $\chi^2$  of the corresponding fits.

electron energy measured with the experimental setup, indicated in the figure ( $E = 140$  keV), the corresponding stopping range of the electron in polystyrene –  $R \approx 2.4 \cdot 10^{-4}$  m [43] – is much smaller than the default final range parameter used in the simulation:  $\rho_R = 10^{-3}$  m. Hence, the simulated electron deposits its total kinetic energy in a single simulation step. In the default Geant4 simulation procedure described above, the  $dE/dx$  is assumed to be constant during the simulation step. Hence, the same is true for the differential visible energy  $dE_{\text{vis}}/dE$  as indicated in the figure.

The total visible energy  $E_{\text{vis}}$  is for each of the three different calculations represented by the area under the corresponding line in Figure 2.10; i.e. the integral of Equation 2.11. It is clearly indicated, that the shaded red area – denoting the Geant4 prediction of the visible energy – is much larger than the area under the solid line. Hence, the current default implementation of Birks' law in Geant4 significantly overestimates the visible energy predicted by Birks' law when the energy dependence of the  $dE/dx$  is correctly taken into account. Such a behaviour is expected as the electron  $dE/dx$  (cf. Figure 2.3) is becoming very large at small energies and hence changes rapidly during the simulation step. For small electron energies, the assumption of a constant  $dE/dx$  could only be sustained if smaller values of  $\alpha_R$  and  $\rho_R$  would be applied. This, would however increase the necessary computation time significantly so that an other solution has to be found.

In order to ‘force’ the correct result for the visible energy, even though the default implementation of Birks' law is used, an effective Birks' coefficient  $kB_{\text{eff}}$  must be applied. This approach is demonstrated in Figure 2.10(b), where a larger  $kB_{\text{eff}} = 0.022$  cm/MeV has been assumed which causes the Monte Carlo prediction of the light yield (shaded green area) to

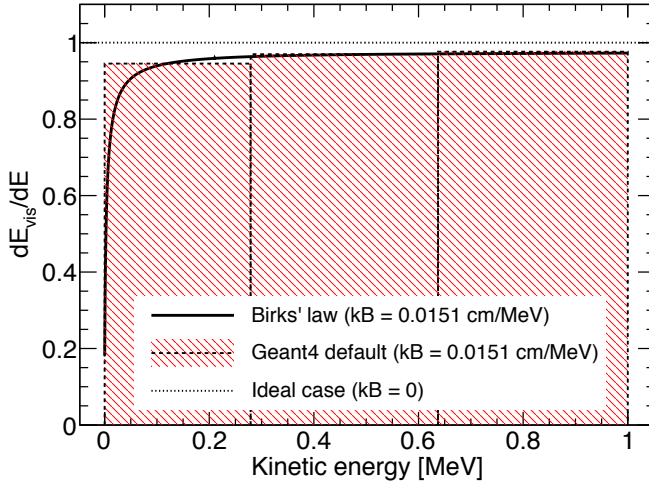


**Figure 2.12** – Differential visible energy  $dE_{\text{vis}}/dE$  of a 1 MeV electron in polystyrene. The default values of  $\rho_R$ ,  $\alpha_R$  and a secondary production cut of  $T_{\text{cut}} = 10^{-3}$  m are used for the Geant4 simulation. The relative error introduced due to the visible energy approximation with rectangles is smaller compared to electrons at lower energies (Figure 2.10).

match the area under the solid line. It should be emphasised, that the determined value of  $kB_{\text{eff}}$  can strictly speaking only be applied to the specific energy it was determined for; in this case:  $E = 140$  keV. Therefore, in order to determine a value of  $kB_{\text{eff}}$  which effectively describes the measured data in the energy range 30 – 140 keV best, the result of the simulation was fitted to the full energy range of the measured data. For this purpose, a computer program was written which simulates 200 electrons for each energy point in Figure 2.7 assuming a certain  $S$  and  $kB$ . The average value<sup>4</sup> of the simulated light yield is determined and compared to the corresponding measured value. The simulation program is executed many times using different values of  $kB$  and  $S$  until the sum of the quadratic difference between the measured and simulated light-yield ( $\chi^2$ ) is minimal. The impact on the simulation step-length on the fit result is determined by applying the fitting procedure for different values of the final range parameter in Geant4, whereas  $\alpha_R$  was fixed to the default value of 20 %.

The fit results, namely  $kB_{\text{eff}}$  and the corresponding reduced  $\chi^2$ , are displayed in Figure 2.11 as a function of the final range parameter. For values of  $\rho_R$  smaller than  $\sim 5 \cdot 10^{-7}$  m, the default method fit yields values for  $kB_{\text{eff}}$ , smaller than  $kB = 1.51 \cdot 10^{-2}$  cm/MeV. This effect can be attributed to the fluctuations<sup>5</sup> of the energy loss applied by default in Geant4. On the other side, for values of  $\rho_R$  larger than  $\sim 10^{-6}$  m the fit yields significantly larger values for  $kB_{\text{eff}}$ . This has the consequence that the simulation overestimates the light output if the  $kB$  value determined from the standalone fit is used. If the  $\rho_R$  value is larger than the stopping range of a 140 keV electron in polystyrene ( $R \approx 2.4 \cdot 10^{-4}$  m), the energy is deposited in a single simulation step. This explains the constant value of  $kB_{\text{eff}}$  at large  $\rho_R$  values. A further increase

<sup>4</sup>The average value is used in order to account for event to event variations caused by the fluctuation of the specific energy loss, different numbers of simulation steps, or the production of secondary particles.

<sup>5</sup>The disabling of fluctuations in the simulation causes that  $kB_{\text{eff}}$  converges against  $kB = 1.51 \cdot 10^{-2}$  cm/MeV for values of  $\rho_R$ , smaller than  $\sim 10^{-6}$  m. However, fluctuations are required in order to describe for example the Landau variations of the deposited energy within the thin scintillator layers of a sampling calorimeter (cf. page 9 and Figure A.5). For the presented data, hence fluctuations are not disabled.

of  $\rho_R$  has consequently no impact on the simulation process.

Since the electrons deposit their energy in a single step for values of  $\rho_R$ , higher than  $R \approx 2.4 \cdot 10^{-4}$  m. Slightly below this value one fraction of the simulated electrons continues to deposit energy in a single step, whereas the other fraction deposits the energy in multiple simulation steps. This transition causes a kink at a well defined position in the Monte Carlo fit function which is responsible for the significantly higher  $\chi^2$  values in the region between  $\rho_R = 10^{-5} - 5 \cdot 10^{-4}$  m. The remaining  $\chi^2$  values are of the same size as the ones determined for the standalone fit listed in Table 2.1.

The point at  $\rho_R = 10^{-3}$  m in Figure 2.11 corresponds to the default parameter applied in Geant4. In this case, a value of  $kB_{\text{eff}} = 1.84 \cdot 10^{-2}$  cm/MeV<sup>6</sup> must be applied so that the measured data is described correctly. Nevertheless, this result has to be approached with caution, since it cannot be applied to other particles than electrons; i.e. as a consequence of the particle specific  $dE/dx$ , the required  $kB_{\text{eff}}$  will also differ from particle to particle. Furthermore, an application of  $kB_{\text{eff}}$  to the simulation of particles at higher energies, compared to the values present in the fitted data set, is in general not possible; i.e. in case of electrons, ionisation quenching becomes a substantial effect only at energies below  $\sim 60$  keV (cf. Figure 2.10), whereas  $dE_{\text{vis}}/dE$  is close to one for higher energies. Therefore, the amount of energy lost due to quenching, in relation to the total kinetic energy of the particle, is larger for low energy compared to high energy electrons. In order to visualise this effect, Figure 2.12 shows the differential visible energy for a 1 MeV electron in polystyrene. The stopping range of a 1 MeV electron in polystyrene is higher than the default final range parameter ( $\rho_R = 10^{-3}$  m). Therefore, the electron dissipates its energy in more than one step. The comparison with a 140 keV electron (Figure 2.10, left) shows that the relative mismatch between the area under the solid line and the shaded area is much smaller in case of the higher energy. An application of the  $kB_{\text{eff}}$  value derived from Figure 2.10(b) would hence cause a significant underestimation of the visible energy.

### Improved visible energy calculation

An improved calculation method of the visible energy was developed by modifying the existing implementation of Birks' law in Geant4. The improved method does not assume a constant  $dE/dx$  during simulation steps, but takes the energy dependence into account. This is achieved by replacing Equation 2.10 with the following more sophisticated calculation:

$$\Delta E_{\text{vis}}^* = \int_{E_f}^{E_f + \Delta E} \frac{1}{1 + kB \cdot \frac{dE}{dx}} dE. \quad (2.12)$$

Here,  $E_f$  denotes the kinetic particle energy at the end of a simulation step, whereas  $\Delta E$  is the continuous energy loss described above. It should be noted that the simulated fluctuations of the specific energy loss do not affect the result of the improved visible energy calculation, since the average  $dE/dx$  values implemented in Geant4 are used. The numerical calculation of the integral is done applying the method of Monte Carlo integration<sup>7</sup>. The algorithm approximates the integral value by a fixed number of function calls  $n_{\text{call}}$ . The  $dE/dx$  values are not calculated for each function call, but they are read from a table, pre-calculated at the beginning of a simulation run. A large value of  $n_{\text{call}}$  yields a higher precision of the calculation, however,

<sup>6</sup>The value differs from the one used in Figure 2.10(b) since here, electrons with initial energies in the range  $E_{e^-} = 30 - 140$  keV are considered in the fit.

<sup>7</sup>The VEGAS algorithm of the GNU scientific library is applied [51].

it also increases the necessary computation time. A detailed discussion about the selection of the optimal  $n_{\text{call}}$  and the resulting performance in terms of required computation time of the improved method is presented in the following section.

In order to determine the influence of the improved calculation method of visible energy, the simulation results are fitted to the measured data in the same way as in the case of the default Geant4 implementation described above. The fit results are shown in Figure 2.11, indicated by the triangles. The new method leads to a clear improvement, as  $kB_{\text{eff}}$  remains compatible with the result of the standalone method ( $kB = 1.51 \cdot 10^{-2} \text{ cm/MeV}$ ) over the full  $\rho_R$  range simulated. Both methods – evaluation of Equation 2.5, and the improved calculation method (Equation 2.12) – can hence be considered equivalent. As a consequence, the definition of an effective Birks' coefficient is not necessary and the value determined with the standalone method can be used without any modifications within the simulation.

### Performance of the improved calculation method for low energy electrons

It was tested how the improved calculation method influences the computation time required for the simulation of low energy electrons. In a first step, it is necessary to determine how many function calls are necessary at all for a precise simulation of the visible energy deposition. For this purpose,  $kB_{\text{eff}}$  is fitted again to the data as described above. However, this time the fit results is determined as a function of the number of function calls,  $n_{\text{call}}$ , whereas  $\rho_R$  is fixed to the default value of  $1 \cdot 10^{-3} \text{ m}$ . The result is shown on in Figure 2.13(a). The value at  $n_{\text{call}} = 0$  corresponds to the the default implementation of Birks' law. The figure shows, that a minimum number of  $\sim 50 - 60$  function calls are required in order to make  $kB_{\text{eff}}$  compatible with  $kB = 1.51 \cdot 10^{-2} \text{ cm/MeV}$  (dashed line). Figure 2.13(b) shows the computation time<sup>8</sup>, required for the simulation of  $2 \cdot 10^6$  electrons with an initial energy of 140 keV in polystyrene. As expected the new method requires a significantly longer computation time; i.e. a factor of  $\sim 10$  between the default implementation ( $n_{\text{call}} = 0$ ) and the minimum required number of function calls of the improved method ( $n_{\text{call}} = 50 - 60$ ). However, it should be noted at this point that the increase of computation amounts to a much smaller value in case of the simulation of particle showers in a calorimeter, discussed in section 2.4.

## 2.4 Impact on the Energy Scale of Particle Showers

In order to determine, how the measured Birks' coefficient and the improved calculation method affect the energy scale of high energy particle showers in a calorimeter, Geant4 based simulation studies of a hadronic calorimeter, matching the CALICE AHACAL design were performed. A brief description of the MOKKA software [49, 52], which provides the test-beam environment for the simulation as well as the geometrical specifications of the simulated AHACAL prototype, is given in section A.4.

### Monte Carlo Analysis

The impact of the the  $kB$  value and the improved calculation method of visible energy is determined by means of a comparative Geant4 simulation study on the basis of raw Monte Carlo samples, created with the aid of the MOKKA software. In this way it is possible to investigate the impact of Birks' law without a possible bias introduced by the digitisation

---

<sup>8</sup>MacBook Pro, 2.4 GHz Intel Core 2 Duo, 2 GB RAM.

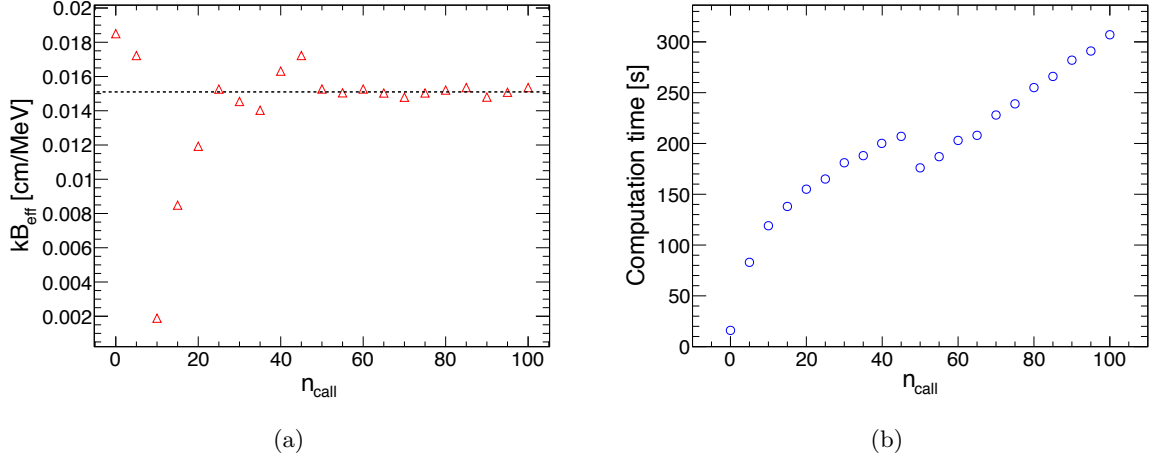


**Figure 2.13** – Figure (a) shows the fitted value of  $kB_{\text{eff}}$  as a function of the number of function calls  $n_{\text{call}}$  used to sample the integral value with the method of Monte Carlo integration. A minimum number of 50–60 function calls are required. Figure (b) shows the required computation time of the improved calculation method for the simulation of  $2 \cdot 10^6$  electrons in polystyrene. The step at  $n_{\text{call}} = 50$  is a feature of the applied integration algorithm and is not investigated further.

procedure (cf. section A.5). In total five different configurations of the simulation program are investigated:

1.  $kB = 1.51 \cdot 10^{-2}$  cm/MeV [improved]
2.  $kB = 1.51 \cdot 10^{-2}$  cm/MeV [default]
3.  $kB = 0.7943 \cdot 10^{-2}$  cm/MeV [default]
4.  $kB = 0.7943 \cdot 10^{-2}$  cm/MeV [improved]
5. Birks' law switched off

The first two configurations make use of the  $kB$  which has been experimentally determined in this work  $kB = 1.51$  cm/MeV, whereas the third and fourth configuration are based on the previously used  $kB = 0.7943$  cm/MeV [47]. For both  $kB$ -values, either the default, or the improved simulation method is applied. In the latter configuration the ionisation quenching effect is not considered at all ( $kB = 0$ ), such that the overall impact of Birks' law can be determined.

The third configuration denotes the default Geant4 setting used for the Monte Carlo production prior to this study. It serves as a reference in the following discussion of the simulation results.

Positrons in the momentum range between 10 up to 50 GeV/c are simulated in the AHCAL prototype, giving rise to purely electromagnetic showers. Similarly, hadronic showers are simulated by using incident pions with a momentum between 5 and 80 GeV/c into the calorimeter. In case of the electromagnetic particle showers, test-beam runs are simulated where the ECAL prototype is removed from the beam-line. For all presented Monte Carlo simulations, the QGSP-BERT physics list is used, which defines the properties of the simulated hadronic showers.

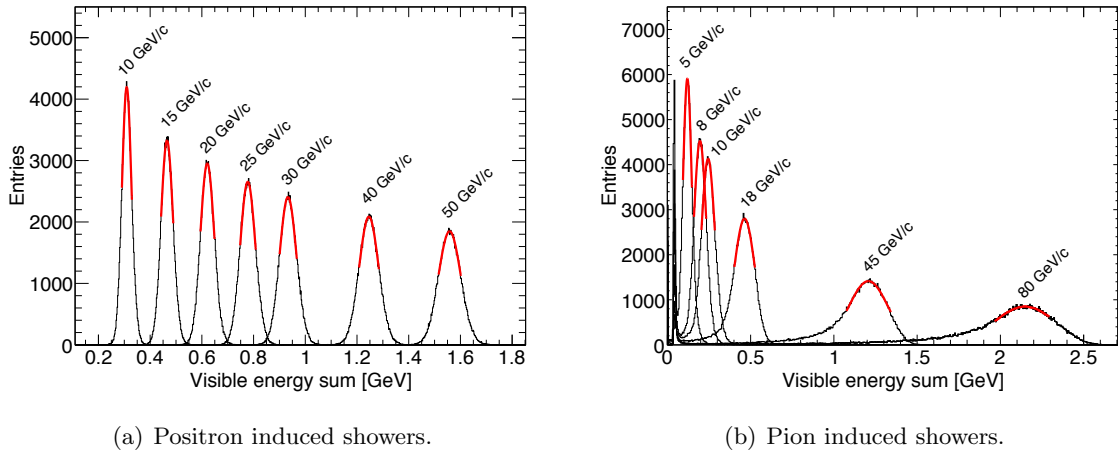


**Figure 2.14** – Sum of visible energy depositions in the active layers of the calorimeter for simulated particle showers. Figure (a) shows simulated positrons, whereas figure (b) shows the simulated positive pions. A Gaussian fit is applied in a  $\pm 1\sigma$  region around each peak value. The simulation was done using the improved visible energy calculation method and the Birks' coefficient  $kB = 1.51 \cdot 10^{-2} \text{ cm/MeV}$ .

Figure 2.14 shows the visible energy sum spectra of the simulated positron and pion induced particle showers. The visible energy sum denotes the sum of all visible energy depositions of an event in the active calorimeter layers (scintillator). For the shown spectra, the measured Birks' coefficient ( $kB = 1.51 \cdot 10^{-2} \text{ cm/MeV}$ ) and the improved calculation method (configuration one) are applied. The most probable energy value of each spectrum is determined by fitting a Gaussian function within a  $\pm 1\sigma$  range around the peak value. In case of the pion induced hadronic particle shower, an asymmetric tail to lower energies is observed. This tail is mainly caused by the length of the simulated AHCAL calorimeter prototype of  $\sim 5\lambda$ , which is too short to fully contain all hadronic showers so that in some events a fraction of the energy is leaking out of the calorimeter<sup>9</sup>. However, the spectra are still well described by the Gaussian function in the specified fit range. Since the particle gun is placed a few meters away from the calorimeter (cf. Figure A.4), to create a realistic test-beam environment, an additional Landau-shaped peak is observed at very small energies in case of the hadronic showers. This peak is generated by highly energetic muons, generated by pions which decay in flight before they hit the first layer of the calorimeter. Since muons have a small specific energy loss  $dE/dx$  over a large energy range, only a small fraction of their energy is deposited in the calorimeter, resulting in a small value of the measured visible energy sum.

In Figure 2.15 the most probable value of the visible energy, determined from the fit in Figure 2.14, is presented as a function of the incident particle momentum. The impact of Birks' law is much larger for hadronic showers, compared to electromagnetic showers. This effect is caused by the different  $dE/dx$  values of the particles which define electromagnetic and hadronic showers. Electromagnetic showers consist mainly of electrons, positrons and photons (cf. page 14ff.). The  $dE/dx$  of electrons or positrons is relatively small over a large energy range and reaches very high values only immediately before the particles are stopped (cf.

<sup>9</sup>The number of nuclear interaction lengths is relatively small, since only the AHCAL is simulated for this study; i.e. no ECAL is placed in front.

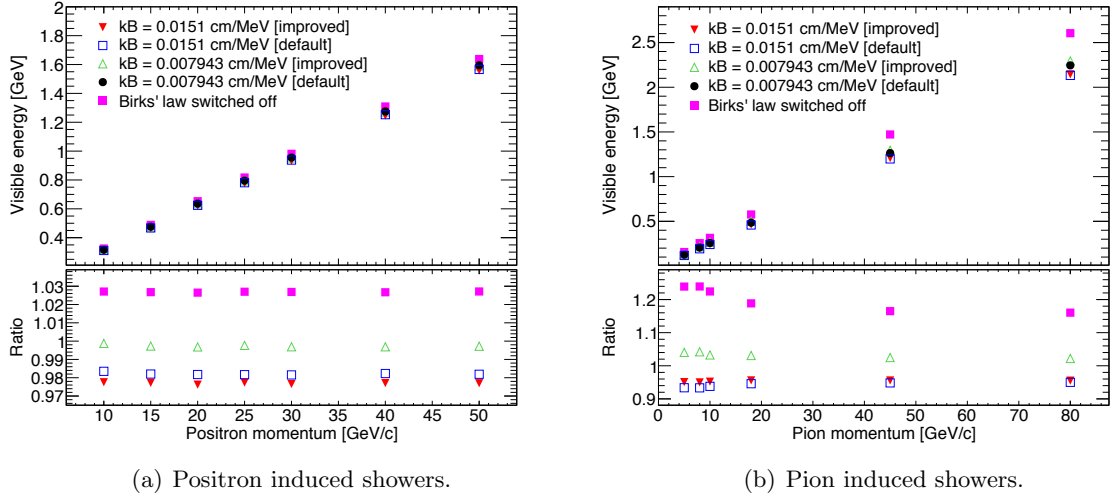


**Figure 2.15** – Most probable value of the visible energy, determined from the energy sum histogram (cf. Figure 2.14), as a function of the particle momentum. The lower plots shows the ratio between the most probable visible energy energy sum for different configurations of the simulation, and the most probable visible energy sum retrieved from the default simulation ( $kB = 0.7943 \cdot 10^{-2} \text{ cm/MeV}$  [default]).

Figure 2.3). As most of the kinetic energy has already been deposited at this point, the fraction of energy which is subject to substantial quenching is relatively small. Therefore, Birks' law has a relatively small impact for electromagnetic showers. In contrast, the baryons and mesons which define the hadronic fraction of a particle shower, typically have a much larger  $dE/dx$  over a wider energy range so that Birks' law has a much larger impact.

In order to study how the different configurations of the simulation relate to the Geant4 setting used prior to this study ( $kB = 0.7943 \cdot 10^{-2} \text{ cm/MeV}$  [default]), the corresponding ratio of the visible energy sum is calculated.

$$\text{Ratio} = \frac{E_{vis}}{E_{vis} (kB = 0.7943 \cdot 10^{-2} \text{ cm/MeV} [\text{default}])} \quad (2.13)$$

The result is shown in the lower part of Figure 2.15.

The visible energy sum of electromagnetic showers is constantly reduced by  $\sim 2.3\%$  over the full energy range simulated, if the measured  $kB = 0.0151 \text{ cm/MeV}$  and the improved calculation method are applied. This may seem as a small correction, however, it should be emphasised that the overall impact of Birks' law ( $\sim 2.7\%$ ) is approximately of the same size. The difference between the default and the improved calculation method is found to be relatively small  $\sim 0.5\%$ , caused by the relatively small overall impact of Birks' law for the particles in an electromagnetic shower which has already been discussed above.

In case of the simulated hadronic showers, the overall impact of Birks' law is much larger and depends on the momentum of the primary pion. The disabling of Birks' law yields an increase of visible energy of up to  $\sim 24\%$ , compared to the reference configuration ( $kB = 0.7943 \cdot 10^{-2} \text{ cm/MeV}$  [default]). The visible energy is reduced by  $\sim 5$  up to  $7\%$  in the simulated energy range, if the measure  $kB$  and the default calculation of visible energy is applied. In contrast to electromagnetic showers, where the improved calculation method yields a reduction

of visible energy, in case of hadronic showers, the improved calculation method yields an increase of the visible energy sum of  $\sim 1\text{--}3\%$  compared to the default method. The combination of both – improved calculation and new  $kB$  – hence yields a reduction of visible energy by  $\sim 4\text{--}5\%$ . The overall impact of Birks' law is larger for low pion energies compared to high pion energies. This effect is caused by the energy dependent electromagnetic fraction within each hadronic shower (cf. page 18ff.). As the energy increases, also the electromagnetic component increases; i.e. in [32] it is shown that the electromagnetic fraction is 32% for 8 GeV and 48% for 80 GeV in case of pion induced hadronic showers, simulated with the AHCAL prototype using the QGSP-BERT physics list. As the electromagnetic component is less affected by quenching effects as described in Equation 1.19, hence a larger amount of visible energy is observed.

Throughout the presented study it is assumed that the value of  $kB$  is independent from the type of particle. This approach is motivated by the original intention of Birks' law of a comprehensive and consistent formulation of the ionisation quenching effect. In order to strengthen this assumption further  $kB$  measurements with different particle types are planned for the future.

## Performance of the Improved Calculation Method for Particle Showers

In high energy physics calorimeter simulations, not only the precision of the simulation process is relevant, but also the performance – i.e. the time required for the simulation – is an important quantity since a large number of particles and a multitude of different physics processes have to be considered.

The factor, by which the computation time is increased due to the improved calculation method presented in this work was determined by simulating electromagnetic particle showers initiated by 15 GeV positrons. For each value of the integral sampling variable,  $n_{\text{call}}$ , 100 simulation jobs have been submitted on the *National Analysis Facility* (NAF) batch system at DESY, each simulating 1000 events. From this, the average run-time of a job is determined as a function of  $n_{\text{call}}$ . The results are presented in Figure 2.16. The average visible energy sum shown in Figure 2.16(a) reaches a stable plateau value at  $n_{\text{call}} \sim 60$ , similar to the simulation of low energy electrons presented in Figure 2.13(a). For much smaller values of  $n_{\text{call}}$ , the integration works improperly which causes a significantly smaller value of the visible energy. In Figure 2.16(b), the ratio between the average simulation time of the improved method, denoted  $\langle T_{n_{\text{call}}} \rangle$ , and the average simulation time of the default method, denoted  $\langle T_{n_0} \rangle$ , is shown. A linear fit is applied, indicating that the simulation time is increased by  $\sim 7.5\%$  for each ten additional function calls. Applying  $n_{\text{call}} \sim 60$ , as proposed by Figure 2.16(a), the simulation time is increased by roughly 40–50% which is much less than the value presented in Figure 2.13(b). This can be attributed to two major differences between the two simulations. Firstly, in case of the calorimeter simulation the visible energy is not calculated for each simulation step, but only for the sensitive detector parts (scintillator), whereas in case of the simulation of low energy electrons the visible energy is calculated for each step. Secondly, the simulation of a realistic detector is much more complex than the simple simulation used to determine  $kB_{\text{eff}}$ . A large variety of additional time consuming calculations have to be done in parallel, so that the calculation of visible energy is not anymore the main factor limiting the performance.

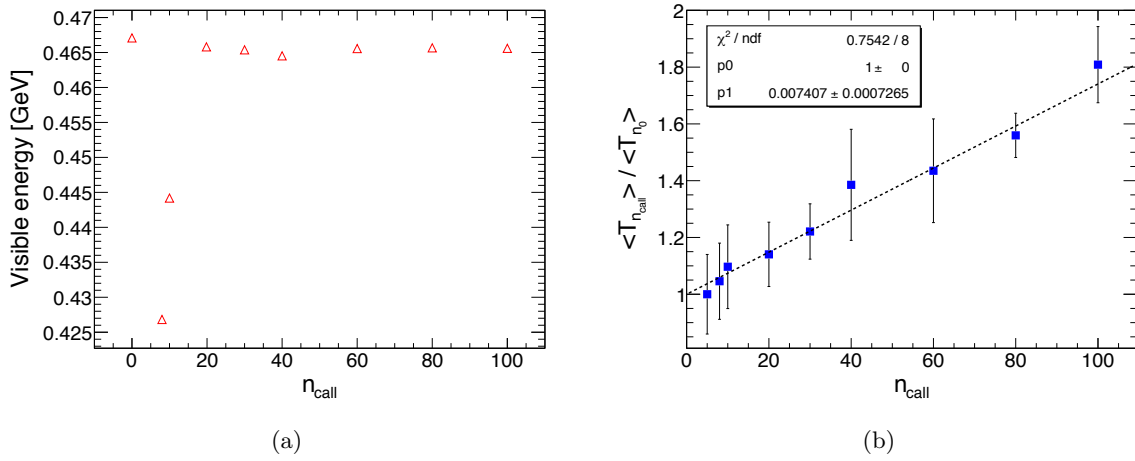


**Figure 2.16** – Figure (a) shows the average visible energy sum of an electromagnetic shower induced by a 15 GeV/c positron as a function of  $n_{\text{call}}$  ( $kB = 1.51 \cdot 10^{-2} \text{ cm/MeV}$ ).  $n_{\text{call}} = 0$  corresponds to the default implementation of Birks' law. Figure (b) shows the ratio between the average computation time of the improved method  $\langle T_{n_{\text{call}}} \rangle$  and the time required by the default calculation of visible energy  $\langle T_{n_0} \rangle$ . The error bars indicate the standard deviation of the simulation run-time.



# Chapter 3

## Photodetection

Within the last seventy years, a large variety of photodetectors has been developed in order to meet the broad spectrum of requirements that arise from different applications. In general, photodetectors can be categorised in two main groups: vacuum devices and solid state detectors. For the sake of completeness it should be mentioned that even a third category of gas based photodetectors exists. However these devices only play a minor role in modern experiments in high energy physics and are therefore not discussed in detail here. The following section provides an overview of some of the most commonly used photodetectors in high energy physics.

### 3.1 Photomultiplier Tube

The first *photomultiplier tubes* (PMT) were developed in the 1930s [1]. This type of detector had an incomparable impact on a large range of experiments as it facilitated for the first time the conversion of weak light flashes into a measurable electrical signal. In Figure 3.1, the basic layout of a typical photomultiplier is shown.

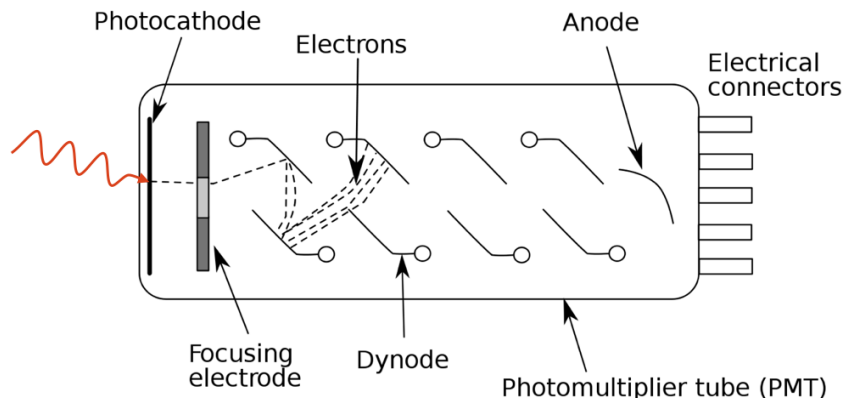


**Figure 3.1** – Schematic view of a linearly focussed photomultiplier tube with a transmission photocathode. Reprinted (modified) from Ref. [53].

Its main component is a vacuum tube containing a specially aligned structure of metal dynodes. The inner walls of the vacuum tube are coated with a thin material layer  $O(\geq 10 \text{ nm})$ . If a photon hits the entrance window of the device, it may release an electron from this material layer if its energy is higher than the work function  $W$ , which equals approximately the sum of the energy gap between valence and conduction band and the electron affinity:  $W \approx E_G + E_A$ . In order to achieve a high detection efficiency, photocathodes are made of materials which are characterised by a small work function such as alkali metals or semiconductors. A resistor array is used to decrease stepwise the negative high voltage applied at the photocathode  $O(\text{kV})$ .

from dynode to dynode down to the anode of the PMT. A photoelectron released from the cathode is therefore subsequently focussed and accelerated towards the first dynode, gaining a typical energy around  $100 - 200$  eV. This energy is sufficient to kick out further electrons from the dynode material via the process of impact ionisation. These secondary electrons are subsequently accelerated towards the next dynode where the process is repeated. Hence, after each dynode stage the total number of electrons is multiplied with the corresponding secondary emission coefficient  $p$ , such that the final number of electrons collected at the anode is given by:

$$G = p^n. \quad (3.1)$$

Here  $G$  denotes the amplification gain of the PMT, and  $n$  corresponds to the total number of dynodes. The high amplification gain from  $10^6$  up to  $10^7$  achieved with PMTs allows for the creation of a measurable electrical signal even for very weak light pulses down to single photons.

## Photon Detection Efficiency

An important characteristic of a photomultiplier tube is the so called *quantum efficiency* (QE) which denotes the probability for electron emission from the photocathode upon absorption of a photon of a certain wavelength. The quantum efficiency mainly depends on the cathode material. Modern photocathodes reach quantum efficiencies higher than 40 % in certain wavelength ranges. However, the quantum efficiency should in general not be confused with the photon detection efficiency, PDE, which denotes the overall probability for photon detection, taking into account the efficiencies of the individual detection stages. In case of a PMT, the photon detection efficiency is determined by three different effects:

$$\text{PDE} = \text{QE} \cdot \text{CE} \cdot P_{\text{mult}}. \quad (3.2)$$

Here CE is the collection efficiency which corresponds to the probability of the released photoelectron to be accelerated towards the first dynode due to the electrical field created by the focussing electrode. Further, it has to be taken into account that an electron reaching the first dynode will not always initiate the multiplication process which is considered in Equation 3.2 by the multiplication probability  $P_{\text{mult}}$  factor. The collection efficiency as well as the multiplication probability strongly depend on the applied high voltage, whereas QE is approximately voltage independent. Typical values of the quantum efficiency are in between 10 – 25 % (cf. Figure 3.2), whereas the product of the collection efficiency and the multiplication probability ranges between 60 – 70 % for most devices.

## Linearity

The photocurrent response of a photodetector should be in a linear relation with the incident photon flux over a wide range since, any deviation from the ideal linear response deteriorates the achievable photon counting resolution. Photomultiplier tubes generally reveal a large dynamical range as the response remains linear for high light intensities, corresponding roughly to  $10^6$  photoelectrons. However, at very high radiation levels, the huge number of electrons causes space charge effects which can reduce the photoelectron collection efficiency, or the multiplication probability. Both effects reduce the signal amplitude.

## Time resolution

One potential advantage of vacuum based photodetectors compared to other detection principles is the good time resolution that can be achieved. This property can be largely attributed to huge cathode-anode distance in these devices, which leads to a small intrinsic detector capacitance. Together with the high voltage applied, this gives rise to extremely short and large amplitude electrical signals. For photomultipliers, the main limiting factor of the time resolution is the transit time spread between photoelectrons released at different positions, or with different velocities from the photocathode. Typical time resolutions of conventional photomultiplier tubes are in the order of several hundred picoseconds [54]. These values can be improved by one order of magnitude with special vacuum based photodetectors such as *micro channel plates* (MCP).

## Noise

The noise of a photodetector is an important characteristic as it determines the achievable photon counting resolution and the smallest signal measurable. Many different sources of noise can be identified and separated from each other. In the following introduction and discussion of the most commonly used photodetectors, the emphasis is placed on two different types of noise: the dark-noise and the multiplication noise of a photodetector. In case of the silicon photomultiplier, introduced in section 3.6, some additional detector specific noise sources will be discussed.

In case of a photomultiplier tube, dark-noise is constantly produced by thermally induced emission of electrons from the photocathode. These electrons are multiplied by the dynode structure in the same way as photoelectrons, hence giving rise to a randomly distributed series of electrical pulses (dark-rate). The dark-rate depends strongly on the photocathode material, its sensitive area and the ambient temperature. Typical values of conventional photomultipliers are in the order of  $O(100 - 1000)$  Hz, however, by cooling the device the thermal noise can be reduced by several orders of magnitude.

Multiplication noise, on the other hand, describes randomly distributed variations in the measured signal, which are caused by statistical fluctuations in the internal multiplication process. A number which is commonly used to characterise these signal fluctuations is the *excess noise factor (ENF)*. It is defined as the ratio between the photodetector signal variation  $\sigma_{\text{out}}$  and the variation<sup>1</sup> of the light signal  $\sigma_{\text{in}}$ :

$$\text{ENF} = \frac{\sigma_{\text{out}}^2}{\sigma_{\text{in}}^2} = 1 + \frac{\sigma_G^2}{G^2}. \quad (3.3)$$

Here  $G$  denotes the gain, and  $\sigma_G^2$  is the gain variation. Typical ENF-values of photomultiplier tubes are between 1.2 and 2 [54]. The gain variation is dominated by statistical fluctuations in the number of secondary electrons emitted from the first dynode. The excess noise factor is of importance for all kinds of experiments, as it reduces the photon counting capabilities for low light measurements, or deteriorates the stochastic term of the energy resolution in a calorimeter (cf. Equation 1.21).

---

<sup>1</sup>Most light sources do not emit a fixed number of photons, but the number is underlying statistical variations described by a Poisson distribution.

Photomultiplier tubes still belong to the most commonly used photodetectors in high energy physics experiments and also in a variety of industry applications. Typical domains of photomultiplier tubes are applications requiring a large internal amplification in order to provide the sensitivity necessary for single photon detection. Further, photomultipliers are unchallenged when large areas have to be instrumented with photosensitive detectors. However, despite the numerous advantages of photomultipliers, semiconductor based photodetectors have become a popular alternative in a variety of applications due to their special properties which are discussed in the following section.

## 3.2 Silicon Photodetectors

Silicon photodetectors provide a couple of advantageous aspects compared to vacuum based detectors such as photomultiplier tubes. As indicated in Figure 3.2, silicon features a higher quantum efficiency over a wide wavelength range, compared to most of the frequently used photocathodes. In a photocathode, the electrons need to acquire enough energy from the incoming photon such that they can be released into the vacuum (external photoeffect). In silicon the electrons only need to be lifted into the conduction band in order to create a measurable electrical signal (internal photoeffect). Further, a PMT photocathode must be extremely thin (tens of nanometers) in order to facilitate an escape of the produced photoelectron. Silicon detectors on the other hand can be produced with larger thickness (hundreds of micrometers) which notably enhances the quantum efficiency for red and infrared light.

In most high energy physics detector systems, strong magnetic fields of several Tesla field strength are used to measure the momenta of charged particles according to the curvature of their tracks. Large fractions of modern particle detectors – including electromagnetic and hadronic calorimeters – are therefore contained in the primary, or at least stray components of this field. The inherent insensitivity to magnetic fields is hence a big advantage of silicon photodetectors compared to conventional photomultiplier tubes which can only cope with moderate magnetic field strengths when provided with a sufficient shielding. The extremely small size of solid state photodetectors is also beneficial for high energy physics detectors as it facilitates high channel densities due to high levels of integration. For these reasons, a large variety of different silicon photodetectors are nowadays used in high energy physics experiments. The following section provides an introduction into the operation principle of the most frequently used devices.

## 3.3 PIN Photodiodes

One of the simplest and commonly used silicon photodetectors is the PIN photodiode. Figure 3.3 shows the schematic layout of such a device. It consists of an intrinsic layer of silicon of typically  $\sim 300 \mu\text{m}$  thickness which is placed in between a heavily doped  $p^+$  and  $n^+$  layer. The additional intrinsic layer, compared to a simple p-n junction, provides several advantages. Due to the low carrier concentration in the intrinsic layer only a small reverse bias voltage is required for a full depletion which results in a large sensitive volume. The photoelectrons created in this volume have a long lifetime since there are no holes left for recombination. The electrical field separates electrons from holes which results in a measurable photocurrent. The thick depletion layer improves the sensitivity for red and infrared photons which can – due to the long absorption length (cf. Figure 1.7) – penetrate deeply into the silicon before they

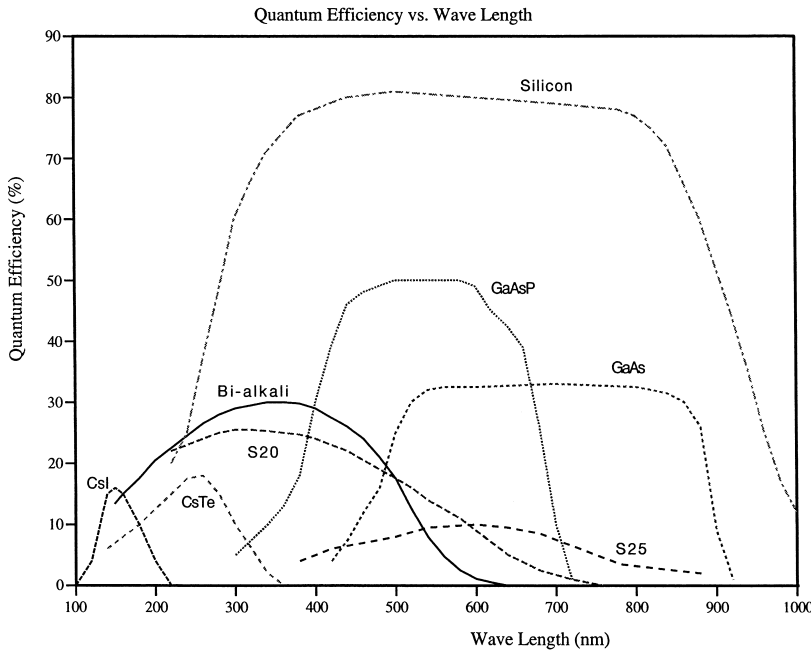


**Figure 3.2** – Quantum efficiency of silicon and some commonly used cathode materials. The figure has been taken from Ref. [54].

get absorbed and create an electron-hole pair. Further, the thick depletion layer reduces the intrinsic device capacitance giving rise to faster signal rise and decay times.

Silicon PIN diodes are popular devices in high energy physics as they are easy to operate due to the low required bias voltage. The missing amplification mechanism has the advantage that once the intrinsic layer is depleted, the device sensitivity and gain – the gain equals unity:  $G = 1$  – are not changed by small variations of the bias voltage or temperature. Further, the PIN photodiode linear response exceeds the linear range of a PMT by several orders of magnitude. These properties make PIN photodiodes suitable for all kinds of light calibration and monitoring purposes. For example in section 4.6, a PIN photodiode is used in the experimental setup to calibrate the incoming photon flux, necessary for a measurement of the photon detection efficiency of silicon photomultipliers. However, the missing internal amplification also has the consequence that small light signals cannot be detected as the resulting electrical signal is too small to be discriminated from the background. A sophisticated low noise charge sensitive signal amplification is required in order to gain sensitivity to several hundreds of photons arriving at the detector at once. Hence, single photon sensitivity as achieved with photomultiplier tubes is not feasible with PIN photodiodes.

An other drawback is the so called nuclear counter effect, observed when PIN diodes are used to read out scintillation crystals in a calorimeter. A minimum ionising particle deposits on average  $\sim 3.8 \text{ MeV}/\text{cm}$  in silicon. Since on average  $3.6 \text{ eV}$  are required to create an electron hole pair, in total  $\sim 30\,000$  electron-hole pairs are created by a MIP in the  $\sim 300 \mu\text{m}$  thick sensitive volume of the PIN diode. This results in a huge fake signal which can easily mimic several MeV of additional energy. This effect is particularly important in case of scintillators with a low light yield. An example for such crystals are the lead tungstate crystals (PWO, cf. Table 1.3) used for example in the CMS electromagnetic calorimeter. The low light yield of these and similar crystals also makes a photodetector with a high sensitivity for weak light

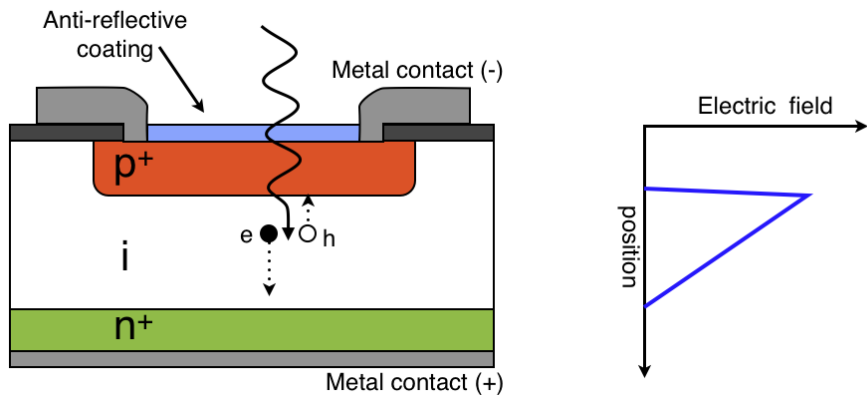


**Figure 3.3** – Doping profile of a PIN photodiode. A high ohmic intrinsic silicon layer (i) is sandwiched between two heavily doped layers ( $p^+$ ,  $n^+$ ). The photosensitive area of the device is covered with a highly transparent protection layer which allows for a simple light coupling with for example a scintillating crystal. Two metal contacts on top and on the bottom provide connection with the voltage supply and signal readout. The right side shows the electric field distribution.

signals necessary. Therefore, so called ‘avalanche photodiodes’ have become popular devices for the construction of electromagnetic calorimeters.

### 3.4 Avalanche Photodiodes

In an *avalanche photodiode* (APD), a modified doping profile and a high reverse bias voltage is applied in order to induce an internal charge amplification mechanism. The primary electron created by the photoelectric absorption can produce an additional electron-hole pair due to the process of impact ionisation. The requirement for this type of interaction is a high electrical field which assures that the energy obtained by the electrons in between two collisions is large enough to lift an additional electron into the conduction band. The secondary charge carriers may subsequently create additional electron-hole pairs such that an avalanche process is initiated. A number commonly used to quantify this process is the ionisation coefficient of the contributing electrons and holes. The coefficient describes the number of secondary electron-hole pairs, created by the process of impact ionisation, per unit length. Its value depends on the electric field and the charge carrier type. In Figure 3.4 the ionisation coefficients of electrons  $\alpha_n$  and holes  $\alpha_p$  are shown for various semiconductor materials as a function of the electric field. At small values of the electric field, the creation of additional electron-hole pairs in the avalanche is only possible for electrons, as  $\alpha_p$  is in silicon much smaller compared to  $\alpha_n$ . This has the important consequence that the avalanche propagates only into the direction of electron acceleration from the n-doped to the p-doped side, and consequently ends when the last electron has left the high field region. Hence, if only electrons can create electron hole pairs (i.e.  $\alpha_p/\alpha_n \ll 1$ ) the total charge generated in the avalanche process is proportional to the number of primary electrons created by the absorption of incoming photons. Conventional avalanche photodiodes are designed to operate in this ‘linear’ mode of amplification; practical amplification factors are in the range from 50 up to 200.

The avalanche process in a conventional APD is schematically indicated in Figure 3.5 which shows the doping profile of the Hamamatsu S8148 APD used in the CMS electromagnetic

calorimeter. The incoming photon lifts an electron into the conduction band which initiates an avalanche of secondary electron-hole pairs. The avalanche only develops into the direction of electron acceleration and is spatially restricted to the high field region at the pn-junction. Below this region, a layer of weakly n<sup>-</sup> doped silicon is inserted which serves as a drift space for the created electrons and reduces the intrinsic detector capacitance for better timing and noise performance. In the shown APD type, the total depletion layer is  $\sim 40 \mu\text{m}$  thick, however, avalanche multiplication happens only in case of the electrons created in the  $\sim 6 \mu\text{m}$  thin layer above the pn-junction. For this reason, the response to ionising particles is reduced by a factor of 50 compared to a conventional PIN diode with a  $300 \mu\text{m}$  thick sensitive layer. The reduced sensitive layer thickness of this APD type, however, also reduces the detection efficiency for red and infrared photons, as these photons are mostly absorbed in the region below the pn-junction; the created electrons drift away from the pn-junction and are consequently not amplified.

The gain of avalanche photodiodes typically reveals a strong dependence on variations of the bias voltage and temperature. For this reason, temperature and voltage should be highly stabilised in particular when operated at high gain values. This property makes the application of APDs rather complicated.

Fluctuations in the avalanche mechanism are responsible for variations of the APD gain,  $G$ . The excess noise factor of an APD can be described by the following equation [56, 57]:

$$ENF = G \cdot k + \left(2 - \frac{1}{G}\right)(1 - k) \quad (3.4)$$

$$\approx G \cdot k + 2(1 - k), \quad (3.5)$$

where the variable  $k$  corresponds to the ratio between ionisation coefficients of electrons and holes  $k = \alpha_p/\alpha_n$ . The second equation is an approximation valid for large values of the gain ( $G > 10$ ). In this case the fluctuations are mainly determined by the finite ionisation coefficient of holes; the additional charge carriers created by holes can – depending on the position – cause a much larger total electrical signal. The equation shows that in order to receive a small excess noise factor, APDs should not be operated at too high gain values; the optimum,  $ENF = 2$ , can only be obtained for small values of the gain. Silicon shows excellent properties for the construction of APDs operated in linear mode as the ratio between electron and hole ionisation coefficients is much larger compared to other semiconductor materials (cf. Figure 3.4).

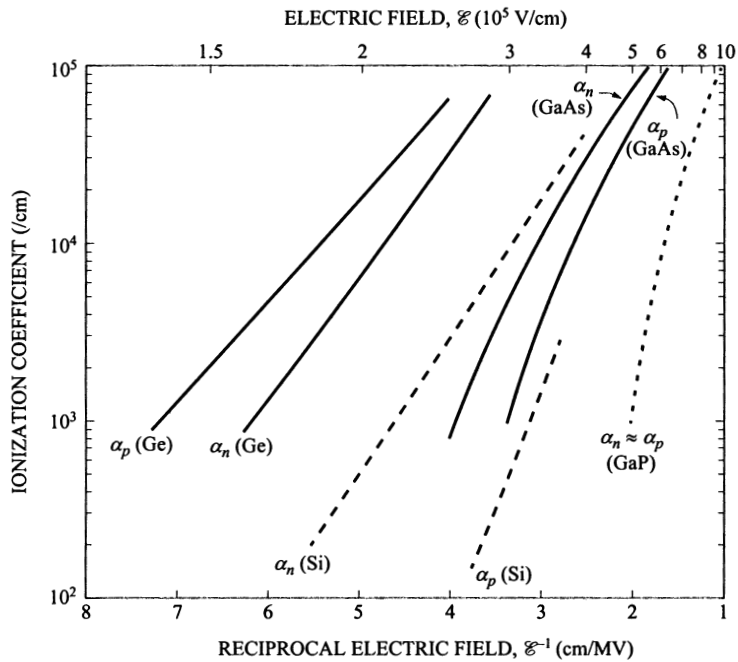


**Figure 3.4** – Impact ionisation coefficients for electrons  $\alpha_n$  and holes  $\alpha_p$  in several semiconductor materials as a function of the electrical field. The figure has been taken from Ref. [55].

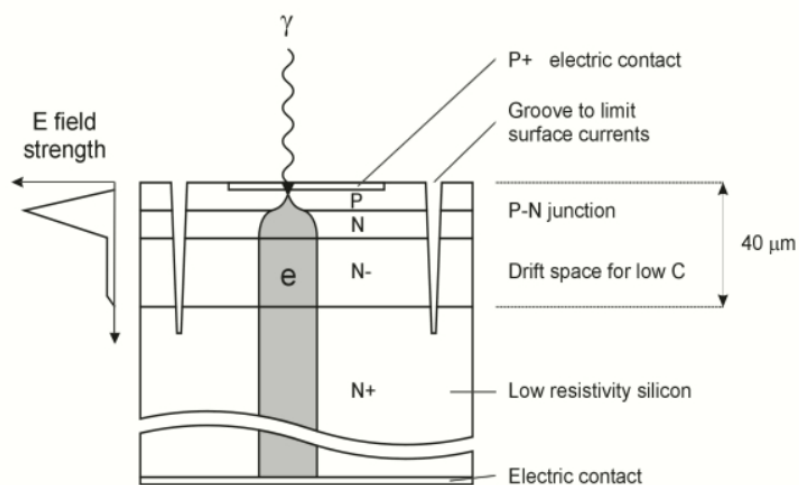


**Figure 3.5** – Schematic view of the Hamamatsu S8148 shallow junction avalanche photodiode. The avalanche multiplication of the created electrons is indicated by the shaded area. The figure has been taken from Ref. [58].

### 3.5 Geiger Mode Photodiodes

In Figure 3.6, the different operation modes<sup>2</sup> of an avalanche photodiode are visualised. At low reverse bias voltages the electric field is not large enough for the impact ionisation process, hence the gain equals unity. The APD behaves therefore like a normal PIN photodiode. Increasing the reverse bias voltage results in the desired APD behaviour; the initial photoelectrons are multiplied in an avalanche process and the resulting electrical signal is proportional to the incoming number of photons. However, single photon sensitivity cannot be obtained as the gain is limited to values

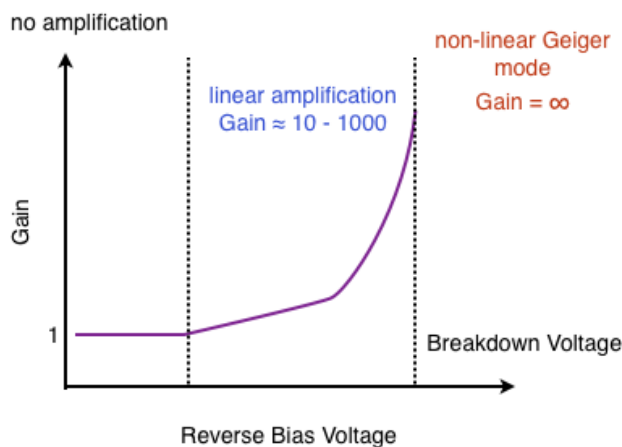


**Figure 3.6** – Schematic gain-voltage dependence of an avalanche photodiode. At low reverse bias voltage, no avalanche multiplication can occur and correspondingly the gain equals one. At higher voltages, avalanche multiplication becomes possible and the gain reaches values between  $\sim 10 - 1000$ . At even higher voltages holes begin to participate in the multiplication and avalanche breakdown occurs – if not quenched – in infinite gain.

below 1000. Higher gain values can be achieved if the bias voltage is further increased until the breakdown voltage is reached. Above this point, also the holes retrieve a significant probability for impact ionisation which results in a so called ‘avalanche breakdown’; as the holes drift into the opposite direction to the electrons, the avalanche propagation is not anymore restricted into a single direction and consequently becomes self-sustaining. The absorption of a photon, or the creation of a thermal electron would result in a high electrical current flowing through the device which continues to flow until it is stopped (quenched) by switching off the bias voltage. In order to achieve a finite gain value and become sensitive for following photons, the avalanche breakdown has to be quenched. This can be achieved in two different ways:

- In the active quenching mode, an external circuit continuously measures the electrical current flowing through the device. If it reaches a certain value, the high voltage is switched off so that the avalanche process ends. After a short time, the voltage is switched on again and the device is – after the a typical recovery time – ready to detect another photon. Active quenching has the advantage that it allows for a fast avalanche stopping and device recovery, so that high photon rates can be measured. It is, however, complex

<sup>2</sup>It should be emphasised that a conventional avalanche photodiode, developed for the operation in the linear amplification region, can in general not be operated in Geiger mode. The high field volume in which avalanche breakdown occurs is so large that thermally induced charge carriers are present practically all the time which results in a continuous breakdown of the device.

to implement this mechanism into every individual pixel. Active quenching is for example applied in case of the recently developed digital SiPMs from Philips [59].

- In the case of passive quenching, a large resistor ( $R_q$ ) is placed in series to the photodiode as shown on the left side of Figure 3.7. On the right side of the figure, a schematic current-voltage diagram of the quenching process is shown. In the first stage, the device is biased a few volts above the breakdown voltage (point A). As long as no charge carrier is present in the high electric field region, no current is flowing through the diode. Hence, the voltage drop at the series resistance,  $U_R$ , equals zero and the diode voltage,  $U_D$ , equals the full reverse bias voltage which is applied. The situation changes when avalanche breakdown is initiated by absorption of a photon, or thermal induced creation of a charge carrier. The internal diode capacitance starts to discharge which causes a rising current flowing through the device (point B). The rising current induces a voltage drop at the quenching resistor  $R_q$ , thus, the voltage across the diode  $U_D$  starts to decrease until it reaches the breakdown voltage  $U_{break}$  where the avalanche process is stopped (point C). Once the avalanche is quenched, the internal device capacitance is recharged and the diode return into the initial state, ready to detect further photons.

The first prototype devices of avalanche photodiodes operated in Geiger mode have already been developed in the 1960's by Hitz and McIntyre [60, 61]. These devices facilitated the detection of single photons due to the high gain values. However, one of the drawbacks was the strong limitation on the photosensitive area, necessary to avoid a continuous breakdown of the device caused by thermally induced charge carriers. Several years later the first devices, denoted *single photon avalanche diode* (SPAD), were commercially available. Passive quenching was used to stop the avalanche breakdown which resulted in relatively small achievable photon count rates below 100 kHz [58]. A general drawback of these devices is the lacking ability to detect more than one photons arriving at the sensor simultaneously; i.e. no information about the light intensity can be retrieved. The signal has always the same amplitude, no matter how many photons have been detected. The logical consequence of the strictly limited dynamical range of SPADs was the development of the silicon photomultiplier.

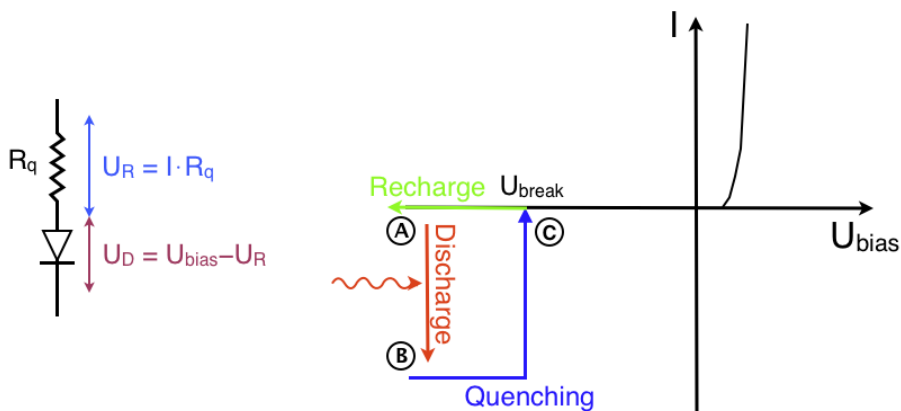


**Figure 3.7** – On the left side, a passive quenching circuit consisting of a photodiode operated in Geiger mode and a large resistor in series. The right side shows a schematic description of the passive quenching mechanism.

### 3.6 Silicon Photomultiplier

A *silicon photomultiplier* (SiPM)<sup>3</sup> consists of a huge number of SPAD cells (pixels) placed on a small area. Typical pixel densities range from one hundred up to several thousand pixels per square millimetre. Figure 3.8 shows a picture of a Hamamatsu SiPM detector with 1600 individual pixels on a  $1 \times 1 \text{ mm}^2$  active area. The right side shows the schematic layout of such a detector. It consists of individual pixels which in turn are made of avalanche photodiodes operated in Geiger mode in series with a high Ohmic quenching resistor ( $R_q = O(100 - 1000) \text{ k}\Omega$ ). Each pixel operates like a binary device; i.e. it creates a standardised signal with a high gain  $O(10^5 - 10^6)$  when hit by a photon. As the pixels are connected in parallel, the signal measured at the device connectors corresponds to the sum of the individual (binary) pixel signals. In this way, a SiPM is capable to detect simultaneously arriving photons and therefore can perform measurements of the light intensity.

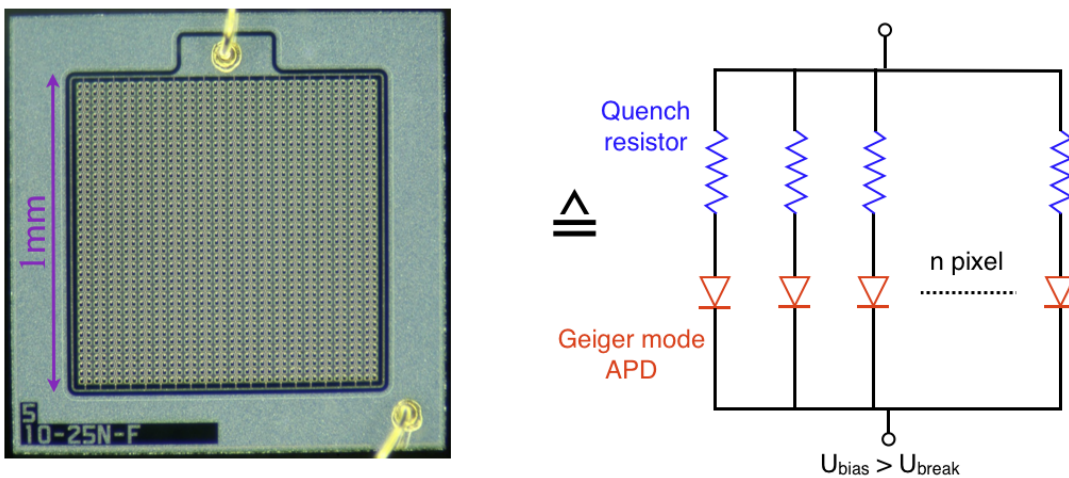


**Figure 3.8** – Layout of a typical Hamamatsu SiPM detector (S10362-025C) with 1600 pixels. Each pixel consists of an avalanche photodiode operated in Geiger mode in series with a quenching resistor. The photosensitive area of the shown device is  $1 \times 1 \text{ mm}^2$

#### SiPM Pixels

Figure 3.9 shows a magnified view of a SiPM surface. The polysilicon quenching resistor of each pixel and the aluminium grid used to connect all pixels in parallel are highlighted by coloured lines (right column). Not the full device surface, but only a certain fraction of it is sensitive to the incoming light. This so called ‘geometrical efficiency’ is one of the main limiting factors of the photon detection efficiency of a SiPM.

A typical SiPM structure is displayed in Figure 3.10, together with the projection of the electric field present at a given distance from the device surface. On top of the device, a silicon dioxide layer serves as a protective coating. The high electric field strength required for the impact ionisation process of electrons and holes is only present in a thin layer in between the strongly doped  $n^+$  and  $p^+$  silicon layers. Below this region, a drift volume is formed by a weakly doped  $p^-$  layer. It enhances the detection probability for red and infrared light which is

<sup>3</sup>There are different names for this type of device in common use such as *multi pixel photon counter* (MPPC), *solid state photomultiplier* (SSPM), *Geiger mode APD* (G-APD), *multi pixel avalanche photodiode* (MAPD), *pixelated photon detector* (PPD), and *metal-resistor-semiconductor APD* (MRS-APD).

able to penetrate several micrometers into the silicon before it is absorbed. Electrons, created in the drift region, move upwards into the high field region where avalanche breakdown occurs. Guard rings are implemented at the pixel boundaries in order to avoid large electric fields at the edges which would result in undesired electrical breakdown.

If a charged particle hits a SiPM detector, it will most probably traverse only the few micron thick depleted region of a single pixel. Even if the primary ionisation process yields a huge number of electron-hole pairs, the resulting signal will be equivalent to the signal of a single photon. For this reason, practically no nuclear counter effect is observed with SiPM detectors. SiPMs are therefore well suited for the application in calorimeters in high energy physics experiments.

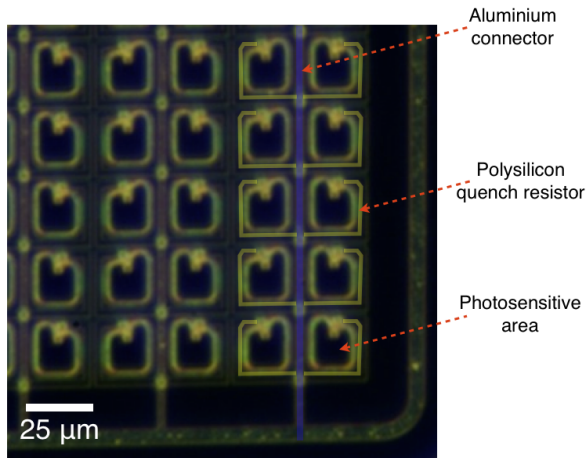


**Figure 3.9** – Magnified view of the individual SiPM pixels (Hamamatsu S10362-025C). For a better visualisation, the aluminium connectors and the quenching resistor made of polysilicon are indicated by coloured lines. Only the specified pixel area is sensitive to incoming light.

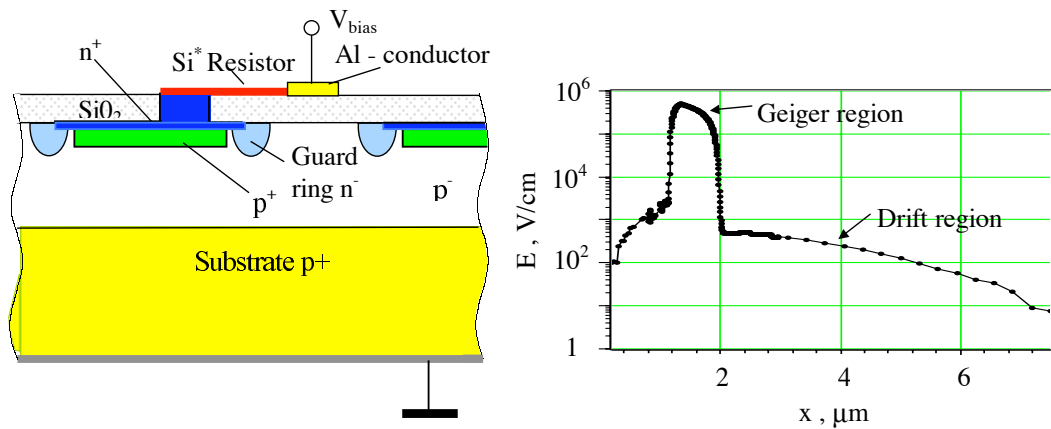


**Figure 3.10** – Typical topology of a SiPM pixel. The strong electric field, necessary for the impact ionisation of electrons and holes is only present in a thin layer at the junction between the n<sup>+</sup> and p<sup>+</sup> doped silicon. At the pixel borders, n<sup>-</sup> doped guard rings are created in order to avoid avalanche breakdown in this region. The p<sup>-</sup> doped silicon forms a drift region which increases the sensitivity for red light and reduces the pixel capacitance. The figure has been taken from Ref. [62].

## SiPM Gain

If a SiPM pixel fires when hit by a photon, or due to thermal excitation, a fixed amount of charge is released which forms the SiPM signal. The simple electrical model underlying this process is shown in Figure 3.11. Two different states of the pixel have to be considered; in the ‘ready mode’, the pixel has been biased up to a few volts over breakdown. As long as no charge carrier is created in the depleted volume, the pixel remains in this state. When a photon is detected, the pixel state changes into the ‘detection mode’. The internal pixel capacitance  $C_{\text{pixel}}$  starts to discharge over the internal pixel resistance  $R_{\text{int}}$  until it reaches the breakdown voltage  $U_{\text{break}}$ . For a successful quenching of the pixel avalanche, the quenching resistor  $R_q$  must be chosen large enough so that the discharge of the pixel determined by the time constant,  $\tau_d = R_{\text{int}}C_{\text{pixel}}$ , is much smaller than the pixel recovery time constant,  $\tau_r = R_q C_{\text{pixel}}$ .

The charge  $Q$  released by the pixel is proportional to the gain  $G$  of the SiPM and can be calculated with the following equation:

$$Q = G \cdot q_e = C_{\text{pixel}} (U_{\text{bias}} - U_{\text{break}}) = C_{\text{pixel}} U_{\text{over}}, \quad (3.6)$$

where  $q_e$  is the electron charge and  $U_{\text{over}}$  denotes the so called ‘over-voltage’.

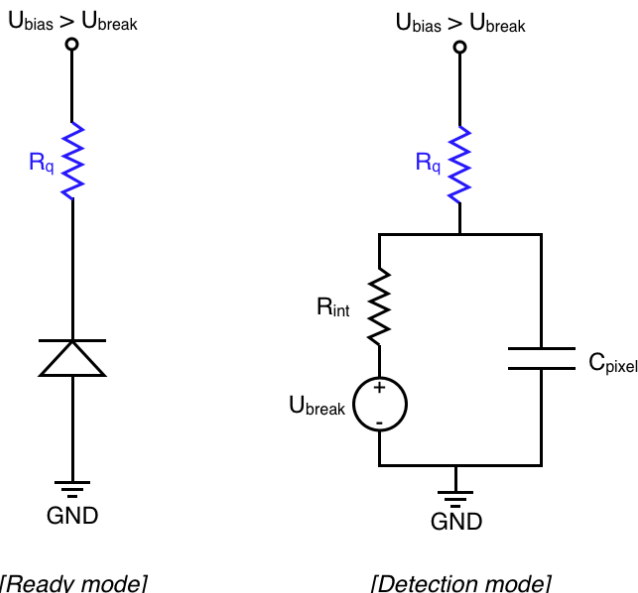


**Figure 3.11** – Simple model of a SiPM pixel. Two different states are considered: a ‘ready mode’, and the ‘detection mode’ which is active when a photon is detected.

## Dynamical Range

SiPMs facilitate, due to the high gain, a measurement of single photons. They are also capable to detect several photons hitting the SiPM simultaneously if they do not hit the same pixel, but are distributed over the active area. However, the maximum number of detectable photons is fundamentally limited by the finite number of pixels. Even with the highest pixel densities, saturation effects appear at high light intensities. This is shown in Figure 3.12, where the response of several different SiPMs, given by the number of fired pixels, is plotted as a function

of the number of created photoelectrons. The following response function is commonly used to describe the SiPM non-linearity:

$$N_{\text{fired}} = N'_{\text{tot}} \cdot \left[ 1 - \exp \left( -\frac{N_\gamma \cdot \text{PDE}'}{N'_{\text{tot}}} \right) \right], \quad (3.7)$$

where  $N_{\text{fired}}$  describes the number of fired pixels and  $N_\gamma$  denotes the number of incident photons. The quantities  $N'_{\text{tot}}$  and PDE' correspond to the effective total number of SiPM pixels, and the effective photon detection efficiency, respectively. These factors are treated as ‘effective’ quantities since they in general depend on the SiPM noise such as the dark-rate and the after-pulse probability described below, as well as on the time and spatial distribution of the incoming light flash. Depending on the operation conditions of the SiPM like the bias voltage or temperature, different values of these effective quantities have to be applied. It is practical impossible to derive an analytical description of the SiPM response function which takes into account all these effects. Such a description may however be achieved with the aid of a Monte Carlo simulation of the SiPM as for example described in [63].

Once, a suitable response function has been determined for the specific operation conditions, it is possible to correct the measured signal values for the saturating behaviour; this is for example done in case of the AHCAL prototype as described in Ref. [32]. However, for high photon quantities the procedure can’t avoid a significant deterioration of the the photon counting resolution as the measurement uncertainty on the number of fired pixels is magnified by the non-linear scale.

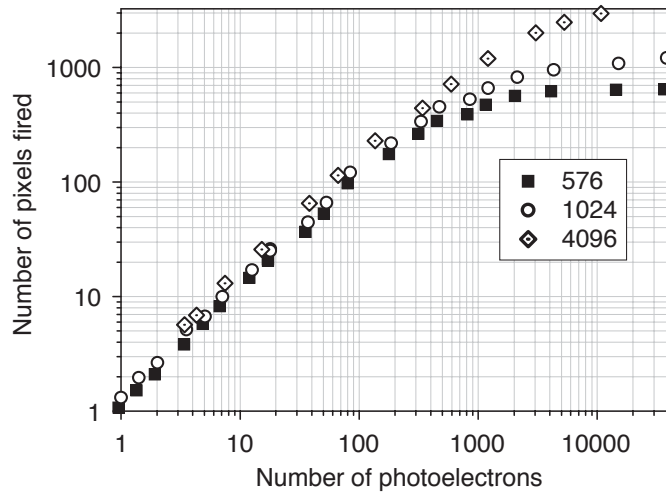


**Figure 3.12** – Dynamical range for several SiPM devices differing in the total number of pixels. The measurement was carried out with short laser pulses of 40 ps duration. In this way it is ensured that each pixels fires only once. The figure has been taken from Ref. [64].

## Photon Detection Efficiency

In case of a silicon photomultiplier, the photon detection efficiency can be written as a product of three individual probabilities:

$$\text{PDE} = P_{\text{geo}} \cdot \text{QE} \cdot P_{\text{trigger}}, \quad (3.8)$$

where  $P_{\text{geo}}$  is the geometrical efficiency, QE denotes the quantum efficiency of silicon and  $P_{\text{trigger}}$  corresponds to the avalanche trigger probability. The geometrical efficiency denotes the ratio between the photosensitive surface and the total active area of the SiPM. Only a fraction of the total active SiPM area is sensitive to light, as a minimum spacing in between the individual pixels is necessary and parts of the surface are covered by the pixel interconnections made of aluminium and the quenching resistors. Only the photons hitting the inner part of the pixel can be detected (cf. Figure 3.9). A general rule of thumb is: the higher the pixel density, the lower the geometrical efficiency since more connectors and quenching resistors are required. This is indicated in Figure A.6, which shows the magnified view of three SiPM detectors with different pixel densities. The geometrical efficiency is one of the main limiting factors for the PDE; typical values of classical SiPM detectors range between  $\sim 20$  and  $70\%$ .

The avalanche trigger probability  $P_{\text{trigger}}$  depends on the depth where the incident photon creates an electron hole pair, and therefore on the wavelength of the photon. The circumstance that electrons in silicon have a much higher ionisation coefficient compared to holes (cf. Figure 3.4), and thus have higher probability for initiating avalanche breakdown, has important consequences on the spectral response of SiPMs. In Figure 3.13, the doping profiles of the uppermost SiPM layers are shown for an ‘n-on-p’ and one ‘p-on-n’ device. At different positions in the depletion layer electron-hole pairs, produced by photon absorption, are indicated. In case of the ‘n-on-p’ device, electrons are accelerated upwards by the electrical field. The electron created in the  $p^+$  layer therefore moves into the direction of the junction, where impact ionisation is possible due to the strong electric field. The corresponding trigger probability  $P_{\text{trigger}}$  is therefore relatively high for such electron-hole pairs. The situation is different in case of the electron-hole pair created in the  $n^+$  layer. Only the hole, which has a much smaller ionisation coefficient, is accelerated towards the  $p^+n^+$ -junction. The corresponding avalanche trigger efficiency is therefore relatively small. The same behaviour applies to the ‘p-on-n’ device; i.e. photons absorbed in the  $p^+$  layer have a higher probability for initiating avalanche breakdown compared to photons absorbed in the  $n^+$  layer. The difference is only the reversed structure, so that the  $p^+$  layer is now on top of the device. The reason for the construction of SiPMs with a ‘p-on-n’ structure is hence the increased detection efficiency in the blue spectral region compared to ‘n-on-p’ devices which are better suited for the detection of red light.

The measurement technique of the photon detection efficiency and the specific response characteristics of several SiPM detectors is discussed in detail in section 4.6.

## Dark-rate

Any electron hole pair created in the depleted volume of a SiPM pixel – independent from its production process – can cause a signal which is completely equivalent to a photon induced discharge. The two main mechanisms responsible for the undesired electron-hole pair creation are sketched in Figure 3.14. In case of the thermally induced creation, an electron from the valence band is lifted into the conduction band due to phonon interaction. The probability of this process is strongly increased if defects or impurities are present in the silicon. Reduction of the process is possible by cooling of the SiPM; typically the thermal generation rate is reduced

by a factor of two for each decrease of the temperature by  $8^{\circ}\text{C}$ , as shown for example in [65].

The field-assisted charge carrier generation (cf. Figure 3.14, right) is only possible in the presence of a strong electric field. In this case, the electrons can tunnel through the band gap. The probability for this process can only be reduced if the electric field, and thus the bias voltage is reduced. This however, also causes a reduction of the gain and the PDE.

Typical values of the dark-rate are in the range of several hundreds of kHz up to several MHz per square millimetre of active SiPM area.

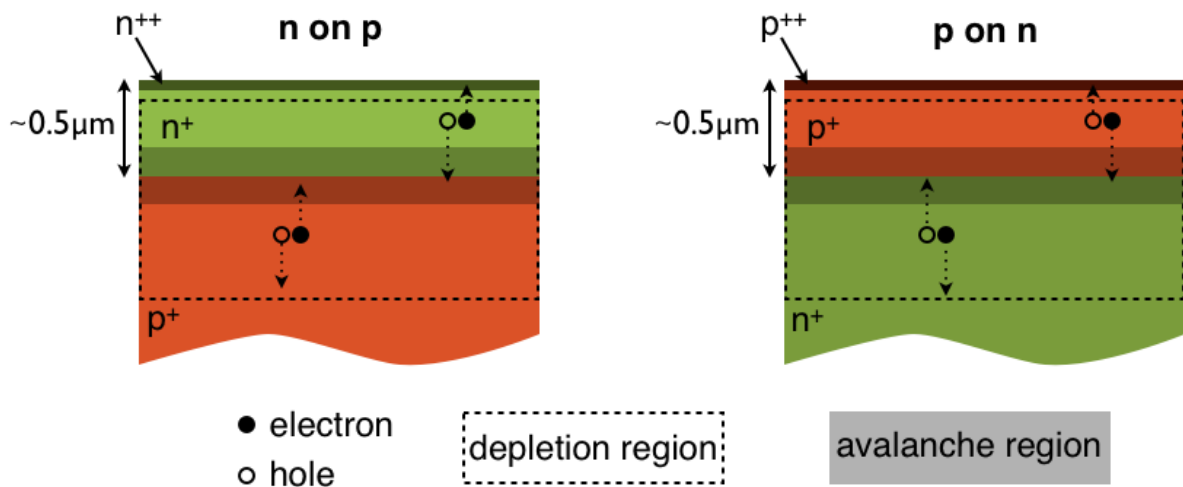


**Figure 3.13** – Doping profiles of the upper SiPM layers of an ‘n-on-p’ and one ‘p-on-n’ device. Electrons created by photon absorption in the p-layer have the highest probability to induce avalanche multiplication.

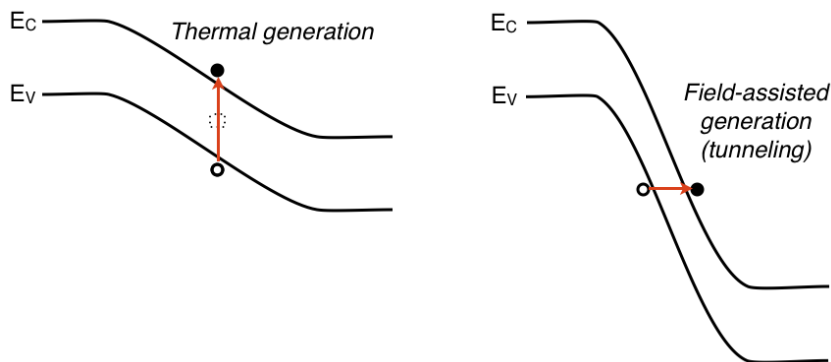


**Figure 3.14** – Visualisation of the two main processes responsible for the creation of electron-hole pairs without photon interaction. On the left, the thermally induced charge carrier generation is shown. The probability for the indicated transition is increased if defects (dotted box) are present. On the right, the field-assisted electron-hole pair creation is sketched. Due to the strong electric field, present at the pn-junction, electrons are able to tunnel through the potential barrier.

## Optical Cross-talk

Already in the 1950s it was observed that a pn-junction in silicon emits light in the visible range when biased above the breakdown voltage [66, 67]. These photons are emitted by ‘hot carriers’ resulting from the avalanche process. The efficiency for the emission of photons with an energy higher than 1.14 eV, thus facilitating the creation of an additional electron-hole pair in silicon, has been measured to be  $2.9 \cdot 10^{-5}$  per charge carrier crossing the junction [68]. For a typical gain value of a SiPM of  $10^6$ , on average 30 photons are created. These photons may either be absorbed in the same pixels, thus contributing to the lateral spread of the primary avalanche, or they may reach a neighbouring pixel where they can initiate a second avalanche. This process is referred to as ‘optical cross-talk’ and is schematically indicated in Figure 3.15.

If the number of additional firing pixels would be constant, optical cross-talk would only cause an effective increase of the gain, and an earlier saturation behaviour. However, the number of additional pixels firing is underlying large fluctuations which deteriorates the achievable photon counting resolution. It is therefore one of the main goals in the development of future SiPM detectors to reduce the cross-talk probability. One possible way to achieve this is to implement so called ‘trenches’, filled with an opaque material, in between the individual pixels as shown in Figure 3.16. In this way, the photons are prevented from entering an adjacent pixel. However, the extra space required for the trenches reduces the geometrical efficiency and thus also the PDE.

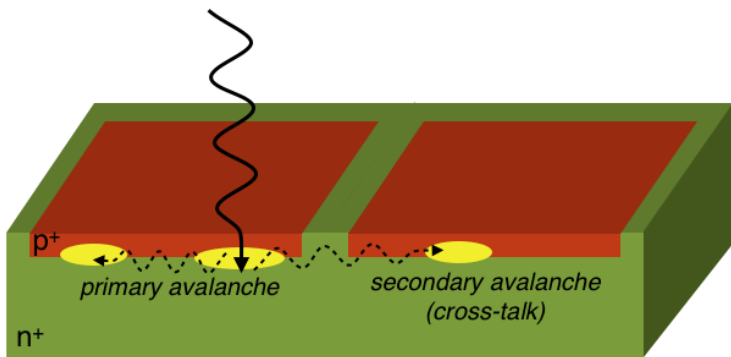


**Figure 3.15** – Schematic description of two neighbouring pixels in a SiPM. The incident photon induces avalanche breakdown in the left pixel. Within this process visible photons are emitted which cause a lateral spread of the avalanche in the pixel. Some of the emitted photons, however, may reach the depleted region of a neighbouring pixel and initiate a second avalanche breakdown (optical cross-talk).

## After-pulses

During avalanche breakdown in a SiPM pixel, charge carriers may become trapped in deep level crystal and impurity defects. If these charge carriers are released when the pixel is already recovered, a second delayed avalanche is triggered. The electrical signal, resulting from the second avalanche cannot be discriminated from a real photon induced signal. As the number of secondary pixels firing due to the after-pulse effect is underlying large fluctuations, the effect significantly deteriorates the achievable photon counting resolution.

However, due to a statistical analysis of the SiPM noise pulses created in the absence of light, it is possible to determine the probability for the occurrence of these after-pulses within

a certain time interval after a primary signal pulse.

### Excess Noise Factor

Due to the operation in Geiger mode with avalanche quenching, statistical variations in the multiplication process – as observed in case of linear APDs – are not present in case of SiPMs. This causes a uniform (binary) pixel response. Naively, one would therefore expect that the excess noise factor is close to unity. However, the effects of after-pulsing and cross-talk introduce a statistical fluctuation of the number of fired pixels which has the consequence of an increased excess noise factor. Typical values for SiPM detectors are around  $\sim 1.5$  [69] which is, however, still less compared to conventional APDs operated in linear mode.

### Time Resolution

SiPM detectors are well suited for fast timing applications due to their quick response and the internal amplification mechanism, causing a large signal even for single photons. The typical depletion layer thickness of a SiPM is only  $\sim 2 - 6 \mu\text{m}$  thin and a large electric field is present (cf. Figure 3.10). Hence the variations of the drift time of the electrons and holes produced at different positions in the depleted layer, are relatively small. Also the vertical avalanche development is a fast process which contributes only little to the time resolution. However, the lateral avalanche built-up is mediated by the slow diffusion process – no horizontal electric field is present – and by the strongly fluctuating emission of photons which are to a large extend reabsorbed in the same pixel (cf. Figure 3.15). These two processes are limiting the time resolution of SiPMs. Nevertheless, the timing properties of SiPM detectors are still very good; typical values are in the order of 100 ps FWHM as presented for example in Ref. [70].

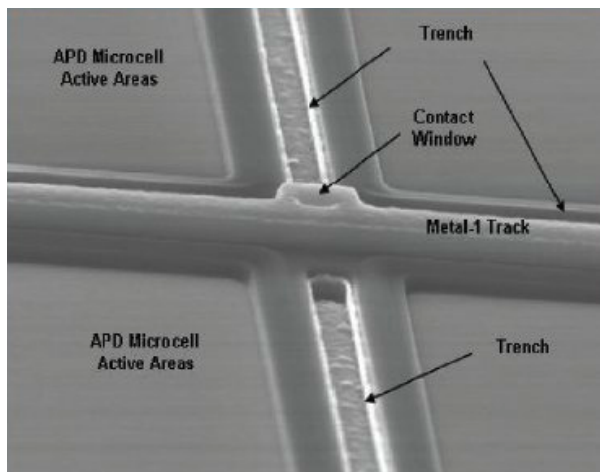


**Figure 3.16** – Microscope picture of trenches in between the individual SiPM pixels. The figure has been taken from Ref. [71].

# Chapter 4

## Determination of SiPM Characteristics

Within the context of this dissertation, a test setup for SiPM measurements was developed and constructed. In order to enable an objective selection of the best suited SiPM detector for a specific application, the developed test stand facilitates independent characterisation measurements using well established standards; i.e. identical measurement techniques are applied for all types of SiPMs. Such measurements are necessary as the available information provided by the SiPM manufacturers is often incomplete, or inconsistent definitions of the applied measurement techniques make an unbiased comparison of the corresponding device characteristics difficult.

The commissioning of the test stand began in the year 2007 within the scope of a diploma thesis [72]. In the following, the range of possible measurements was extended and the measurement techniques were enhanced [65]. Today, the test stand facilitates measurements of the SiPM gain, dark-rate, cross-talk and after-pulse probabilities, photon detection efficiency, and tests on the pixel response uniformity. In addition, measurements of the temperature dependence of the above specified parameters are enabled. Further test setups, e.g. for the measurement of the SiPM dynamical range are currently under development. The diversity of obtainable characterisation data allows for an efficient selection of the SiPMs suitable for the envisaged application in high energy physics calorimetry or positron emission tomography. In addition, a better understanding of the SiPM noise is obtained which allows to specify the optimal operation conditions for a certain application. Results of these characterisation studies have been published in a scientific journal [4].

A variety of different SiPM detectors, from different manufacturing companies have been successfully characterised in the test stand. A list of the tested devices is presented in Table 4.1. In addition, several other SiPM types from the companies SensL, Zecotek and STMicroelectronics have been characterised. The results of these studies are however subject to confidentiality agreements with the manufacturers and are therefore not presented in this work.

The following chapter contains an overview of the most important measurement techniques and a discussion of the obtained results. A deeper insight is provided for the characterisation measurements where the major contributions have been made within the scope of this thesis.

### 4.1 Current-Voltage Characteristics

A basic measurement, enabled by the test stand is the determination of the current-voltage characteristic. The experimental setup for this measurement is shown in Figure 4.1. The central component is a lightproof box which contains the SiPM under study, thus preventing the generation of a photocurrent which would distort the measurement results. The SiPM high voltage ( $U_{bias} < 100$  V) is provided by a power supply which is also serving as an ampere-meter, capable to measure small currents precisely. Despite its simplicity, this type of measurement facilitates the determination of useful information about the specific SiPM and its operation,

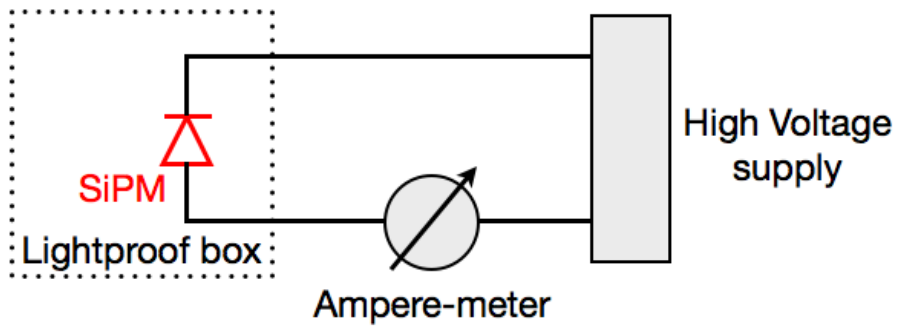


**Figure 4.1** – Schematic view of the setup used to measure the current-voltage characteristics. In the real setup, the voltage source and ampere-meter is combined in a single device (Keithley 6487 Picoammeter/Voltage Source)

e.g. the polarity, the approximate breakdown voltage, and the value of the individual quenching resistors which has a strong influence on the pixel recovery time.

If a forward bias voltage is applied to the SiPM, the current can easily flow through the diodes of the individual pixels (cf. Figure 3.8). Hence, the total SiPM resistance is exclusively determined by the quenching resistors. As the pixels are connected in parallel, the following equation for the value of the quenching resistor can be derived:

$$R_q = R_{\text{total}} \cdot n_{\text{pixel}}. \quad (4.1)$$

Here  $R_{\text{total}}$  corresponds to the SiPM resistance when a forward bias voltage is applied and  $n_{\text{pixel}}$  denotes the total number of pixels.

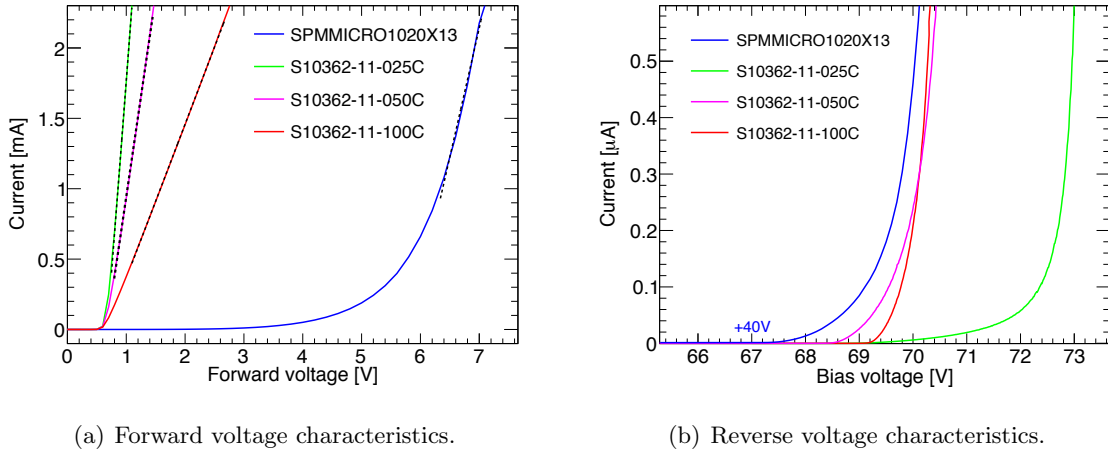
In Figure 4.2(a), the SiPM current of four Hamamatsu MPPCs<sup>1</sup> and one SensL SPM<sup>2</sup> is shown as a function of the applied forward bias voltage. Even if no bias voltage is applied to the SiPMs, a small depletion zone is created in between the p- and n-doped regions due to diffusion of charge carriers. This depletion zone acts as an insulating layer which the charge carriers have to pass. Hence, a minimum forward bias voltage is required to ‘push’ the charge carriers through the depletion layer and to make the SiPM conductive. This voltage value is denoted forward voltage drop and amounts to  $\sim 0.6 - 0.7$  V in most silicon diodes.

In case of the Hamamatsu MPPCs an abrupt current increase is observed when the forward voltage reaches voltages higher than 0.6 V, whereas the current rises only slowly in case of the SensL SPM. The significantly different behaviour points to major differences in the production method of the two SiPM types. However, the effect does not alter or deteriorate the devices response, thus it was not further investigated in this work.

From the slope of the linear current increase which describes the SiPM conductivity, the value of the total device resistance, and thus the quenching resistor can be calculated using Equation 4.1. The result derived from the measurement is displayed in Table 4.2. For a successful passive quenching of the pixel avalanche, the diode bias voltage must fall under the breakdown voltage. The current flowing through a SiPM with small pixel size is smaller compared to a SiPM with larger pixels. Therefore, for smaller pixels a larger quenching resistor is required in order to reduce the voltage drop across the diode sufficiently, thus stopping the avalanche.

<sup>1</sup>Multi Pixel Photon Counter.

<sup>2</sup>Silicon Photomultiplier.



(a) Forward voltage characteristics.

(b) Reverse voltage characteristics.

**Figure 4.2** – Forward and reverse bias voltage characteristics of several Hamamatsu MPPCs and one Sensl SPM (cf. Table 4.1). In case of forward voltage, linear fits (dashed lines) are applied to the curves in order to determine the value of the quenching resistor. In figure (b), an offset of 40 V has been added to the bias voltage of the Sensl device (blue curve) for a better visualisation. The position of an abrupt current increase indicates the approximate breakdown voltage of the corresponding device. Typical operation voltages are a few volts above the breakdown voltage.

**Table 4.1** – Specifications of the tested SiPMs. A complete characterisation has been done in case of the Sensors listed in the upper part of the table. For the remaining devices only a selection of measurements was performed.

SiPM producer and type	Structure	Active area [mm <sup>2</sup> ]	$n_{\text{pixel}}$	Pixel pitch [μm]
Hamamatsu S10362-11-100C	p-on-n	1 × 1	100	100
Hamamatsu S10362-11-050C	p-on-n	1 × 1	400	50
Hamamatsu S10362-11-025C	p-on-n	1 × 1	1600	25
Sensl SPMMICRO1020X13	n-on-p	~ 1 × 1 <sup>a</sup>	1152 <sup>a</sup>	~ 30 <sup>a</sup>
MEPhI/Pulsar (AHCAL)	n-on-p	1 × 1	1156	30
Ketek (prototype device)	p-on-n	3 × 3	576	120

<sup>a</sup>According to manufacturer specification, the device features a circular active area containing 848 microcells of 20 μm size [73]. The numbers quoted here have been experimentally determined in section 4.7 (cf. Figure 4.34 (right)).

If a reverse bias voltage is applied to a SiPM as shown in Figure 4.2(b), the thickness of the depletion zone increases. Charge carriers created in this zone by thermal excitation are separated in the electric field and thus cause a small leakage current  $O(nA)$ . If the voltage is increased, so does the leakage current until eventually full depletion is achieved. If the voltage is further increased, first linear amplification of the thermal generated charge carriers and finally avalanche breakdown occurs which results in an abrupt increase of the current. The point of abrupt current increase allows to determine the approximate value of the breakdown voltage. As indicated in the figure, the tested Hamamatsu MPPCs have a breakdown voltage in between 68 and 69 V; in case of the S10362-11-025C, the actual transition from linear amplification to avalanche breakdown is less pronounced due to its smaller gain (cf. the following section). The SensL SPM has a much smaller breakdown voltage of  $\sim 28$  V.

With the gained knowledge, the bias voltage can be adjusted to an adequate value, a few volts above breakdown. However, the presented method allows only for an approximate estimation of the breakdown voltage, as the precise position of the current increase in Figure 4.2(b) is difficult to determine. A more accurate determination method of the breakdown voltage, based on the measurement of the SiPM gain, is presented in the following section.

## 4.2 Gain

For a correct interpretation of the electronic signals from any kind of detector, a precise knowledge of the photodetector gain is one of the basic requirements. The gain value is not constant over time, but depends significantly on the operation conditions such as the ambient temperature. In order to avoid a deterioration of the energy resolution of a calorimeter by means of an increased constant term in Equation 1.21, it is necessary to measure the gain on a time scale which is short compared to the change of the operation conditions (e.g. temperature day night cycle). Most detector systems in high energy physics therefore comprise a dedicated calibration system which monitors the photodetector gain and reacts with compensating changes of the applied voltage.

The results of the gain measurement have been presented and discussed in Ref. [65, 72]. Nevertheless, the topic is important for the understanding and discussion of the measurements described in the following sections, hence a brief overview over the fundamental measurement technique of the SiPM gain and the obtained results is given in the following.

### Voltage Dependence

When avalanche breakdown is initiated in a SiPM pixel, either by photon absorption or thermal/tunnel excitation, a fixed amount of charge is released which corresponds to the gain of the SiPM (cf. Equation 3.6). If several pixels fire at once, the corresponding charge values are added up. This is indicated in Figure 4.3 where an oscilloscope image of the SiPM thermal noise signals are shown; the amplitudes of the individual electrical pulses are well separated and correspond to a certain number of firing pixels (photoelectrons). In order to determine the gain, the signal has to be integrated over the full duration of the pulse.

The setup for the gain measurement is shown in Figure 4.4. A pulse generator produces short  $O(ns)$  electrical pulses which drive a light emitting diode (LED). The resulting light flashes are guided to the active area of the SiPM with an optical fibre bundle. The SiPM and the LED are contained inside separate lightproof boxes as a common box would result in a significant noise pickup from the large amplitude pulses used to drive the LED. A simple electronics circuit is used to connect the SiPM to the voltage supply and the signal amplifier consisting of a resistor,

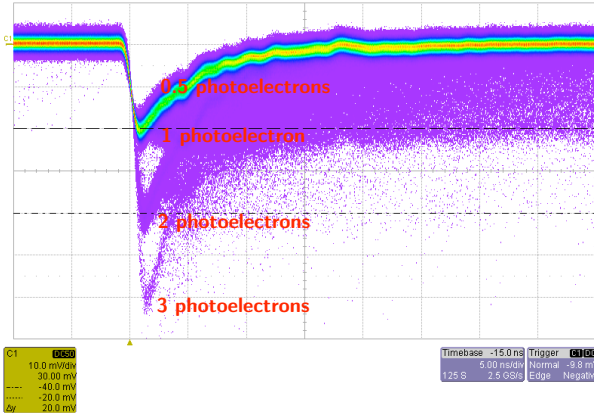


**Figure 4.3** – Oscilloscope image of the SiPM (S10362-11-050C) thermal noise pulses, accumulated during a few seconds time interval. Three different signal amplitudes can be identified, corresponding to one, two, or three firing pixels (photoelectrons). The trigger threshold is set to half a photoelectron. Horizontal scale: 5 ns/div, vertical scale: 10 mV/div.

$R_1 \approx 10 \text{ k}\Omega$ , and a capacitor,  $C_1 \approx 0.1 \mu\text{F}$ . The capacitor  $C_1$  serves as a fast responding current source for the SiPM during breakdown. The large value of  $R_1$  protects the SiPM from a permanent damage due to large currents. The resistor  $R_2$  is required to close the electrical circuit and hence facilitate a stable bias voltage of the SiPM. In the shown configuration of the electronics amplifier, the value of  $R_2$  should be much larger compared to the internal impedance of the voltage amplifier of  $50\Omega$ . Otherwise large fractions of the signal would directly flow into ground and get lost. A typical value used in the described setup is  $R_2 \approx 3 \text{ k}\Omega$ .

The SiPM signals are amplified<sup>3</sup> by a factor of 50 before they are fed into the integration input of the *charge to digital converter*<sup>4</sup> (QDC), based on the CAMAC<sup>5</sup> bus standard. Amplification is necessary in order to transfer the original charge values of the SiPM pulse:  $O(10^6 q_e = 0.16 \text{ pC})$ , to the sensitivity range of the QDC:  $O(10 \text{ pC})$ . The signal is integrated over a fixed time interval between 50 and 200 ns. This interval is defined by the digital gate input which is created when the gate generator module receives the trigger signal from the pulse generator.

The result of a gain measurement is displayed in Figure 4.5 which shows the so called ‘single photoelectron spectrum’ recorded with the QDC. Each of the well separated peaks corresponds to a certain number of fired pixels, also referred to as photoelectrons (pe). The gain of the SiPM corresponds to the distance between the individual peaks. There are several basic methods used to determine the gain values from the spectrum. One possibility is to fit a suitable function to the spectrum; this can either be a simple superposition of individual Gaussians, or a more sophisticated fit function which takes into account Poisson photo-statistics and the cross-talk probability as described for example in Ref. [76]. The method which was used throughout this thesis is the determination of the equivalent power spectral density of a single photoelectron spectrum by calculating the discrete Fourier transformation. The gain value can in this case be determined from a peak in the spectral power spectrum; details on the method can be found in Ref. [72].

The result of the gain measurement at different values of the reverse bias voltage is displayed

<sup>3</sup>Phillips Scientific model 774.

<sup>4</sup>LeCroy model 2249A 12 channel analogue to digital converter, 10 bits resolution (1024 channels), 256 pC full scale range [74].

<sup>5</sup>Computer Automated Measurement and Control [75].

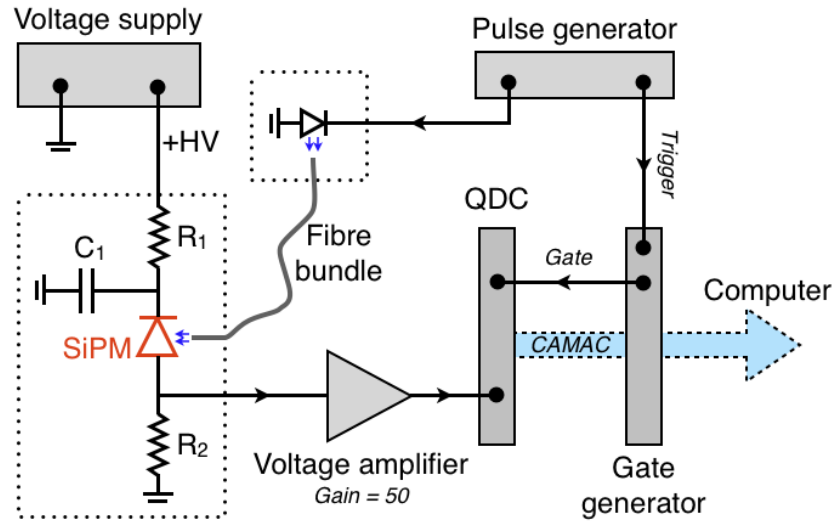


**Figure 4.4** – Experimental setup for the SiPM gain determination. The centrepiece is a charge to digital converter (QDC) which integrates the incoming SiPM pulse over a time interval which is defined by the width of the gate signal.

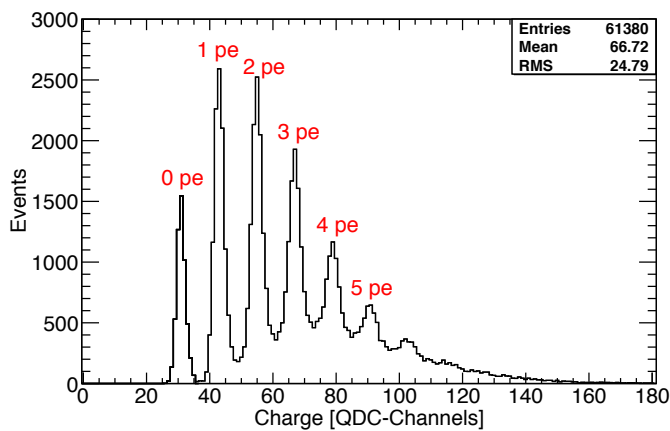


**Figure 4.5** – Typical single photoelectron spectrum recorded with the experimental setup (S10362-11-025C). The first peak (0 pe) corresponds to the integrated charge when no pixel is firing. The second peak corresponds to one firing pixels and so on. The individual peaks are well separated which indicates the good photon counting capabilities of a SiPM.

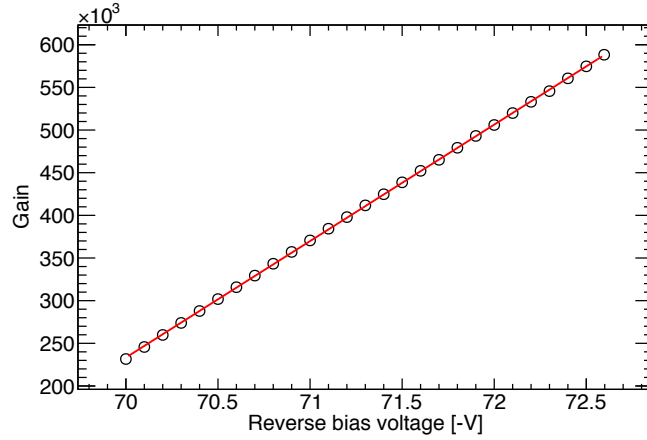


**Figure 4.6** – Typical gain-voltage dependence of a SiPM (S10362-11-025C). The individual data points are well described by a linear function with two parameters (red line).

in Figure 4.6. A conversion factor (cf. section A.8) is used for the calibration from the QDC-channel scale to the gain scale. As expected from the simple pixel model described in section 3.6, a linear dependence between the bias voltage and the SiPM gain is observed. The following function is fitted to the data points in order to determine the breakdown voltage  $U_{\text{break}}$  and the pixel capacitance  $C_{\text{pixel}}$ :

$$G = \frac{C_{\text{pixel}}}{q_e} (U_{\text{bias}} - U_{\text{break}}) \quad (4.2)$$

The characteristic values are listed in Table 4.2. The pixel capacitance is mainly determined by the size of the individual pixels:  $C_{\text{pixel}} \propto A/d$ , where  $A$  denotes the pixel area and  $d$  is the thickness of the insulating depletion layer. In case of the Hamamatsu MPPCs, the pixel capacitance shows the expected proportionality to the pixel area. Hence, the depletion layer thickness is approximately the same for the devices. The capacitance of the SensL SPM indicates a smaller depletion layer thickness, caused by a different doping structure. The highest gain values are achieved for large pixel capacitances; i.e. at a fixed over-voltage the gain increases with the capacitance. Large pixels also yield a high geometrical efficiency which allows for higher PDE values. However, the reduced dynamical range of such devices limits the possible range of applications.

**Table 4.2** – Characteristic values of the pixel capacitance  $C_{\text{pixel}}$ , breakdown voltage  $U_{\text{break}}$ , and quenching resistor  $R_q$  determined with the experimental test stand. The presented values for  $U_{\text{break}}$  and  $C_{\text{pixel}}$  are reprinted from [65, 72].

SiPM	Pixel pitch [ $\mu\text{m}$ ]	$C_{\text{pixel}}$ [fF]	$U_{\text{break}}$ [V]	Gain <sup>a</sup> [ $10^5$ ]	$R_q$ [ $k\Omega$ ]
S10362-11-025C	25	$23.2 \pm 0.1$	$68.4 \pm 0.1$	1.45	$293 \pm 4$
S10362-11-050C	50	$102.0 \pm 0.2$	$68.2 \pm 0.2$	6.37	$140 \pm 1$
S10362-11-100C	100	$423.6 \pm 0.1$	$69.0 \pm 0.1$	26.43	$91.3 \pm 0.2$
SPMMICRO1020X13	$\sim 30$	$58.9 \pm 0.1$	$27.9 \pm 0.1$	3.67	$629 \pm 38$

<sup>a</sup>Value at  $U_{\text{over}} = 1$  V. Uncertainties of the gain measurement are in the order of  $\sim 5\%$ .

## Temperature Dependence

The gain of a SiPM shows a strong dependence on the temperature. This can be mainly attributed to the temperature dependence of the breakdown voltage. At high temperatures, the electron and hole mobility in silicon is reduced due to phonon scattering which has the consequence of a reduced probability for impact ionisation. The breakdown voltage hence increases with the temperature.

By actively controlling the SiPM temperature during the gain measurement in a range from  $-10$  up to  $30^\circ\text{C}$ , the increase of the breakdown voltage was quantified for two different SiPMs (S10362-11-050C/-100C). Independent from the pixel size, a temperature coefficient of  $dU_{\text{break}}/dT \approx 55 \text{ mV/K}$  was measured. In order to realise a constant gain operation of the SiPM, hence temperature variations have to be compensated by adjustments of the bias voltage so that the over-voltage remains constant ( $U_{\text{over}} = U_{\text{bias}} - U_{\text{break}} = \text{const}$ ). If on the other hand no bias voltage corrections are applied ( $U_{\text{bias}} = \text{const}$ ), the gain decreases with increasing temperature according to the following equation:

$$\frac{dG}{dT} = -\frac{C_{\text{pixel}}}{q_e} \cdot \frac{dU_{\text{break}}}{dT}. \quad (4.3)$$

For this reason, a high pixel capacitance causes the negative effect of a strong temperature dependence. Concerning temperature stability, it is therefore beneficial to use SiPMs with a small pixel capacitance and to operate these devices at a higher over-voltage to reach the required gain value.

## 4.3 Dark-rate

There are several possibilities for a reduction of the noise rate. The reverse bias voltage can be lowered, which, however yields a smaller gain value, and even more important, a reduction of the photon detection efficiency. Another very efficient possibility is the cooling of the SiPM which often cannot be realised in high energy physics particle detectors because of the requirements in hermeticity and power consumption. The dark-rate of a SiPM, hence often represents an unavoidable source of noise. As the majority of thermal noise pulses have a small amplitude corresponding to one firing pixel, the dark-rate has the strongest negative effect for small light signals. The thermal noise rate deteriorates the energy resolution of a calorimeter mainly for low particle energies, whereas its influence is getting smaller for higher energies. Within the description of the sampling calorimeter energy resolution given by Equation 1.21, the dark-rate mainly contributes to the noise term which is proportional to the inverse of the energy.

For the calorimeter performance at low particle energies, it is important to precisely measure and understand the dark-rate characteristics of the variety of available SiPM detectors, thus facilitating a selection of the best suited devices and the optimal operating voltage.

## Voltage Dependence

A schematic description of the dark-rate measurement setup is shown in Figure 4.7. The amplified SiPM pulses are fed into a discriminator module<sup>6</sup>. The basic operation principle of the discriminator is schematically indicated in Figure 4.8. When the SiPM signal amplitude exceeds a certain threshold value which can be defined via the CAMAC interface of the discriminator

---

<sup>6</sup>LeCroy model 4416.

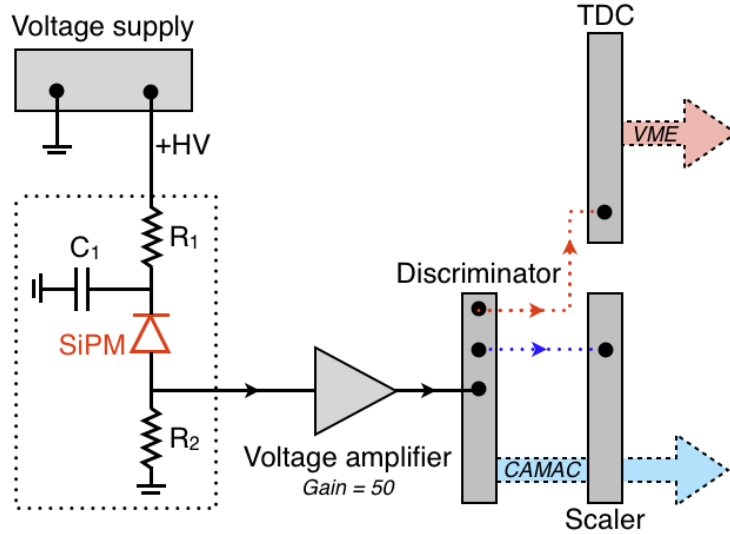


**Figure 4.7** – Experimental setup for the measurement of the dark-rate, cross-talk and after-pulse probability. The amplified SiPM signal is fed into a CAMAC based threshold discriminator module. The logical output signal of the discriminator is during the dark-rate and cross-talk measurement connected to the input of CAMAC based scaler module (blue connector line). In case of the after-pulse measurement, the discriminator signal is analysed with a VME based time to digital converter (TDC).

module, a 3 ns short logical pulse is generated. These pulses are counted by a scaler module<sup>7</sup> during a well defined time interval, so that the SiPM pulse rate can be determined.

The measured dark-rate is shown in Figure 4.9 as a function of the applied over-voltage for a variety of different SiPM types. The threshold of the discriminator is set to the 0.5 photoelectron level for this measurement (cf. Figure 4.3), hence all SiPM pulses – down to the single pixel level – are taken into account. The range of measured dark-rate values ranges from  $\sim 300$  kHz up to several MHz per mm<sup>2</sup> and increases with the applied over-voltage. This has two main reasons: firstly, the overall avalanche trigger probability increases with the applied voltage. Hence, the charge carriers created in the depleted volume of the SiPM cause avalanche breakdown with higher efficiency. Secondly, the number of charge carriers in the depleted volume is higher as the probability for field assisted electron-hole pair creation rises with increasing bias voltage.

The figure also shows that the dark-rate of SiPMs with an n-on-p structure (SensL) is higher compared to the dark-rate of p-on-n devices (Hamamatsu). The reason for this effect is again the much larger ionisation coefficient of electrons compared to holes; electrons created in the p-doped layer drift into the direction of the junction whereas electrons created in the n-doped layer drift away from the high field region. Hence the volume of the depleted p-type silicon generates the major contribution to the dark-rate. As the p-type layer is usually thinner in case of p-on-n type SiPMs (cf. Figure 3.13), the corresponding dark-rate is lower.

SiPMs with a smaller number of larger pixels can achieve a higher geometrical efficiency compared to a huge number of small pixels. Hence the total photosensitive area, and therefore also the total depleted volume is larger which results in a higher dark-rate. This effect can also be observed in Figure 4.9, as the dark-rate of the MPPCs with larger pixels is higher compared to the ones of smaller pixels.

<sup>7</sup>LeCroy model 2550B.

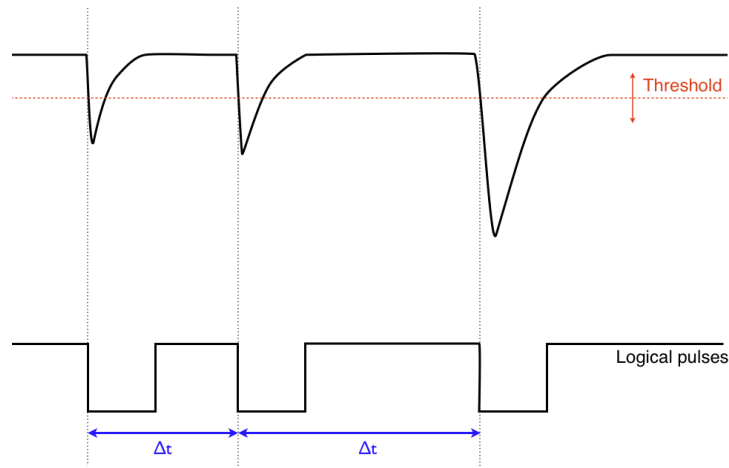


**Figure 4.8** – Schematic description of the discriminator operation principle. If a SiPM signal pulse exceeds the adjustable discriminator threshold, a logical output pulse of  $\sim 3$  ns width is generated. For the dark-rate and cross-talk measurements, these logical pulses are counted with the scaler module. In case of the after-pulse measurement described in section 4.5, the time difference  $\Delta t$  between consecutive pulses is determined with a time to digital converter.

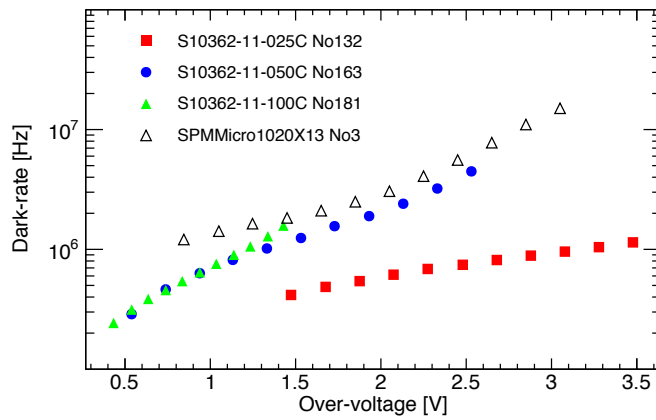


**Figure 4.9** – Dark-rate at the 0.5 photoelectron threshold as a function of the over-voltage for the tested SiPM detectors.

## 4.4 Cross-talk Probability

In Figure 4.3, the overlaid traces of several thousands of thermal noise pulses are shown. Not only single photon equivalent pulses are observed, but also pulses with an amplitude corresponding to two or more firing pixels are observed. These pulses cannot be explained by the dark-rate alone as the probability for two or more pixels to fire within a short time interval is – despite the relatively high characteristic dark-rates – extremely small. For example the measured dark-rate of a S10362-11-050C at  $U_{over} = 1.5$  V is roughly  $\sim 1$  MHz and the signal rise time is  $\sim 1$  ns. The probability for two pixels firing at the same time is hence proportional to  $P_{\text{double}} \propto 1 \text{ ns} \cdot 1 \text{ MHz} = 0.1\%$ ; however, Figure 4.3 reflects a much larger effect. The reason for this discrepancy is the cross-talk probability of SiPMs which was introduced in section 3.6.

For the measurement of the cross-talk probability the same setup is used as for the dark-rate determination. In addition to a variation of the SiPM bias voltage, for this type of measurement also the discriminator threshold is varied over a certain range. An example of such a threshold scan at a fixed over-voltage is shown in Figure 4.10. A characteristic step function is observed. When the threshold reaches integer multiples of the single photoelectron amplitude, the count rate drops as the corresponding pulses do not exceed the threshold anymore.

The rate measured at the 1.5 photoelectron threshold includes all events with one or more additional cross-talk induced pixel avalanche. The ratio:

$$P_c = \frac{\nu_{1.5 \text{ pe}}}{\nu_{0.5 \text{ pe}}} \quad (4.4)$$

hence corresponds to the cross-talk probability; as mentioned above, the probability for two pixels firing at the same time by chance  $P_{\text{double}}$ , can be neglected if the dark-rate is smaller than a few MHz. In order to determine the cross-talk probability as a function of the over-voltage, several threshold scans have been recorded for each SiPM device at different values of the over-voltage. For a determination of the  $\nu_{0.5 \text{ pe}}$  and  $\nu_{1.5 \text{ pe}}$  count rates, the 1.5 pe and the 2.5 pe thresholds have to be estimated. This is achieved by calculating the absolute value of the derivative of the individual threshold scans which is equivalent to the pulse height spectrum. The first two local minima of these pulse height spectra correspond to the 1.5 pe and the 2.5 pe thresholds and can be determined in an automated fitting procedure as described in Ref. [65].

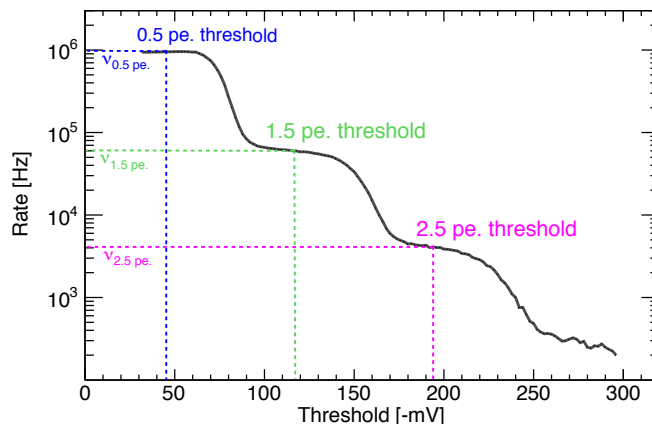
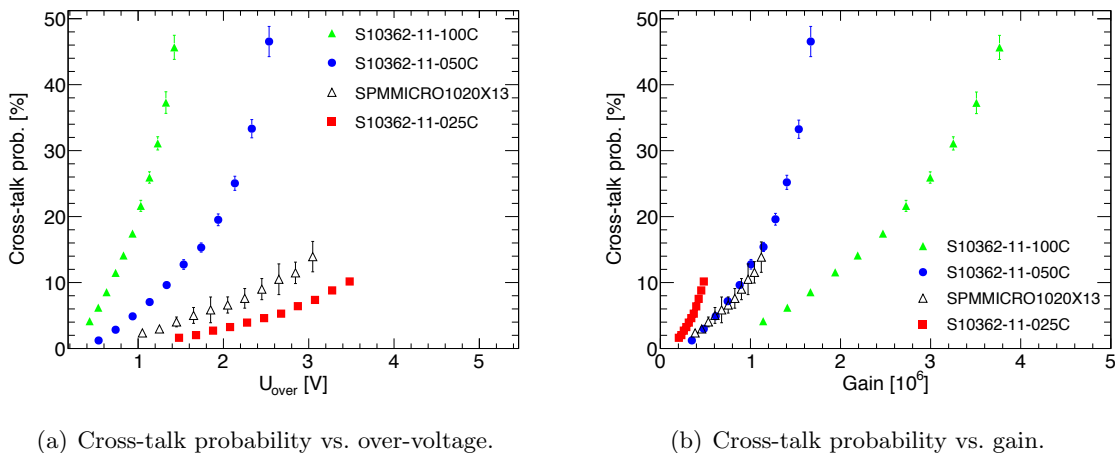


**Figure 4.10** – Dark-rate of a Hamamatsu S10362-11-050C, operated at a constant over-voltage of  $U_{over} = 1.3$  V as a function of the discriminator threshold. The coloured lines indicate the 0.5, 1.5 and 2.5 photoelectron thresholds and the corresponding noise rates  $\nu_{0.5 \text{ pe}}$ ,  $\nu_{1.5 \text{ pe}}$ , and  $\nu_{2.5 \text{ pe}}$ .

The determined cross-talk probabilities for the tested SiPM devices are shown in Figure 4.11. The cross-talk probability increases strongly with the applied over-voltage. This can be attributed to two different effects: the avalanche trigger efficiency is higher at higher voltages. Hence, an electron-hole pair created in the depleted layer of the SiPM due to absorption of a cross-talk photon has a higher probability to trigger avalanche breakdown. The second, more important effect is the increase of gain with the applied over-voltage. If a larger number of charge carriers is crossing the pn-junction of the SiPM, a higher number of photons is radiated which increases the cross-talk probability. This is indicated in Figure 4.11(b) where the cross-talk probability is displayed as a function of the SiPM gain. This representation of the data reveals that the cross-talk probability at a constant gain value is smaller in case of large pixel sizes compared to smaller pixels sizes. The reason for this behaviour is expected to be caused by the different distances a photon has to travel – averaged over the pixel area – until it reaches the depletion layer of a neighbouring pixel.

Even though the SensL SPMMICRO1020X13 has a pixel size of  $\sim 30 \times 30 \mu\text{m}^2$ , which is much smaller compared to the Hamamatsu S10362-11-050C with a  $\sim 50 \times 50 \mu\text{m}^2$  pixel size, the SensL devices features a comparable cross-talk probability at a given gain value. The relatively small cross-talk probability of the SensL SPMs can be mostly attributed to the special trench technology which is applied in these devices (cf. Figure 3.16). However, the optical trenches in between the pixels reduce the total photosensitive area which may be one of the reasons for the smaller photon detection efficiency compared to the Hamamatsu MPPCs as discussed in detail in section 4.6.



(a) Cross-talk probability vs. over-voltage.

(b) Cross-talk probability vs. gain.

**Figure 4.11** – Cross-talk probability for various SiPM detectors as a function of the over-voltage (a) and gain (b); published in [4].

## 4.5 After-pulse Probability

In the oscilloscope picture displayed in Figure 4.3, a large number of secondary pulses is observed which follow the triggered pulse. In contrast to this observation, almost no pulses are present in the time interval before the trigger threshold is exceeded. This asymmetry is partially caused by the trigger condition which only selects pulses exceeding the threshold on the rising edge, however, the prominence of the effect indicates that once a SiPM pulse has been created, either by thermal excitation or photon absorption, the probability for observing further pulses in the subsequent time interval is increased; the reason for this observation is the after-pulse mechanism, described in section 3.6. The amplitude of these after-pulses depends on the time difference to the preceding pulse  $\Delta t$ . As indicated in Figure 3.11, the SiPM pixel recovery can be modelled as a capacitance  $C_{\text{pixel}}$  which is (slowly) recharged via the quench resistor  $R_q$ . The charge fraction carried by the after-pulse, which depends on the recovery state of the pixel, is hence described by

$$\xi(\Delta t) = 1 - \exp(-\Delta t/\tau_r), \quad (4.5)$$

where  $\tau_r = R_q \cdot C_{\text{pixel}}$  is the recovery time of the pixel. If  $\Delta t$  is smaller compared to  $\tau_r$ , only a small signal – much smaller than the 1pe pulse – is created whereas the full amplitude is reached for  $\Delta t \gg \tau_r$ .

It is not possible to separate the after-pulses from photon generated signals on a single event basis. However, it is possible to quantify the after-pulse effect on a statistical basis by measuring the distribution of time difference between subsequent SiPM pulses, as shown below. It is useful to begin the statistical description of the dark-rate with the probability density of the thermal noise rate; i.e. the reduced dark-rate without after-pulses. The probability for observing a certain number  $n$  of thermal noise pulses in a given time interval  $\Delta t$  is described by the Poisson distribution:

$$P_\mu(n) = \frac{\mu^n e^{-\mu}}{n!}, \quad (4.6)$$

where  $\mu$  denotes the mean number of thermal pulses observed in the time interval  $\Delta t$  at a given average thermal noise rate  $\nu_{\text{tp}}$ ;  $\mu = \nu_{\text{tp}} \cdot \Delta t$ . The probability to measure exactly zero pulses in the given time interval is correspondingly described by the following equation:

$$P_\mu(0) = e^{-\mu} = e^{-\nu_{\text{tp}} \cdot \Delta t} = 1 - \int_0^{\Delta t} p_{\text{tp}} d\Delta t'. \quad (4.7)$$

In the last step, the thermal noise probability density  $p_{\text{tp}}$  has been defined. It can be easily proven that the following Ansatz solves the equation:

$$p_{\text{tp}} = \nu_{\text{tp}} e^{-\nu_{\text{tp}} \cdot \Delta t}. \quad (4.8)$$

The probability density for after-pulses can be derived in analogy to the thermal noise rate so that one gets:

$$p_{\text{ap}} = \nu_{\text{ap}} e^{-\nu_{\text{ap}} \cdot \Delta t}, \quad (4.9)$$

where  $\nu_{\text{ap}}$  denotes the after-pulse rate parameter, i.e. the inverse of the after-pulse time constant:  $\nu_{\text{ap}} = 1/\tau_{\text{ap}}$ .

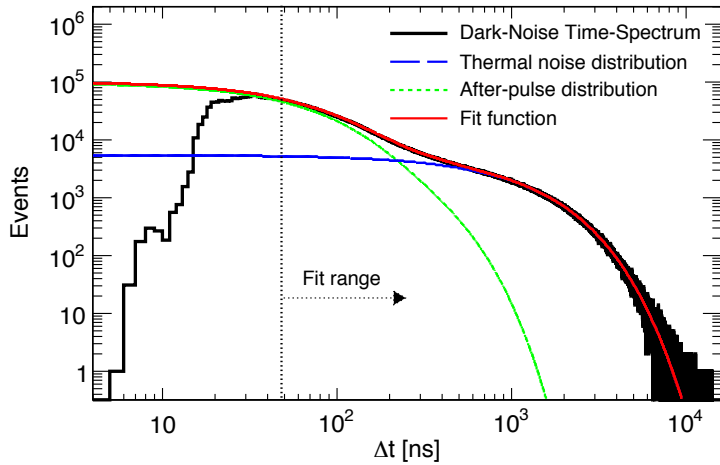


**Figure 4.12** –  $\Delta t$  time distribution measured with a S10362-11-050C MPPC at a reverse bias voltage of  $-70.6\text{ V}$ . A function (red line) is fitted to the distribution which is the sum of the thermal-noise (blue line) and after-pulse (green line) distribution. The fit is only applied in the indicated range as for small time differences, the efficiency of the measurement is reduced due to overlapping logical pulses and the dead time of the TDC.

The after-pulse probability has been determined using a similar setup as used for the measurement of the dark-rate and cross-talk probability (cf. Figure 4.7). The difference is that instead measuring the pulse rate with the scaler module, the time structure of the SiPM pulses is analysed using a *time to digital converter* (TDC). The 3 ns wide logical pulses created by the discriminator contain the precise time information of the rising edge of the original SiPM pulse as indicated in Figure 4.8. The TDC is programmed to measure the time difference,  $\Delta t$ , between subsequent pulses.

A typical result of such a time distribution measurement is presented in Figure 4.12. The spectrum corresponds to the unnormalised probability density to measure a pulse – thermal or after-pulse – at a given time  $\Delta t$  after a preceding pulse. The measured spectrum (black line) is not well represented by a single exponential function describing only the thermal noise distribution (blue line). Instead, two additional exponentials are required to describe the data precisely:

$$n_{\text{dr}} = n_{\text{tp}} + n_{\text{apf}} + n_{\text{aps}} \quad (4.10)$$

$$= N_{\text{tp}}/\tau_{\text{tp}} e^{-\Delta t/\tau_{\text{tp}}} + N_{\text{apf}}/\tau_{\text{apf}} e^{-\Delta t/\tau_{\text{apf}}} + N_{\text{aps}}/\tau_{\text{aps}} e^{-\Delta t/\tau_{\text{aps}}}. \quad (4.11)$$

Here  $n_{\text{dr}}$  corresponds to the unnormalised time distribution of dark-rate events:  $n_{\text{dr}} = p_{\text{dr}} \cdot N_{\text{dr}}$ , where  $N_{\text{dr}}$  is the integrated number of measured dark-rate events.  $n_{\text{apf}}$  and  $n_{\text{aps}}$  describe the distributions of fast and slow after-pulses and are defined analogously.  $\tau_{\text{tp}}$ ,  $\tau_{\text{apf}}$ , and  $\tau_{\text{aps}}$  denote the thermal, fast after-pulse, and slow after-pulse time constants, respectively. In the same way,  $N_{\text{tp}}$ ,  $N_{\text{apf}}$  and  $N_{\text{aps}}$  correspond to the integrated number of thermal, fast after-pulse, and slow after-pulse events. As mentioned above, the after-pulse effect is caused by trapped electrons which are released according to an exponential time distribution with a characteristic time constant. The observation of two time constants thus indicates the presence of two types of trapping centres in the silicon.

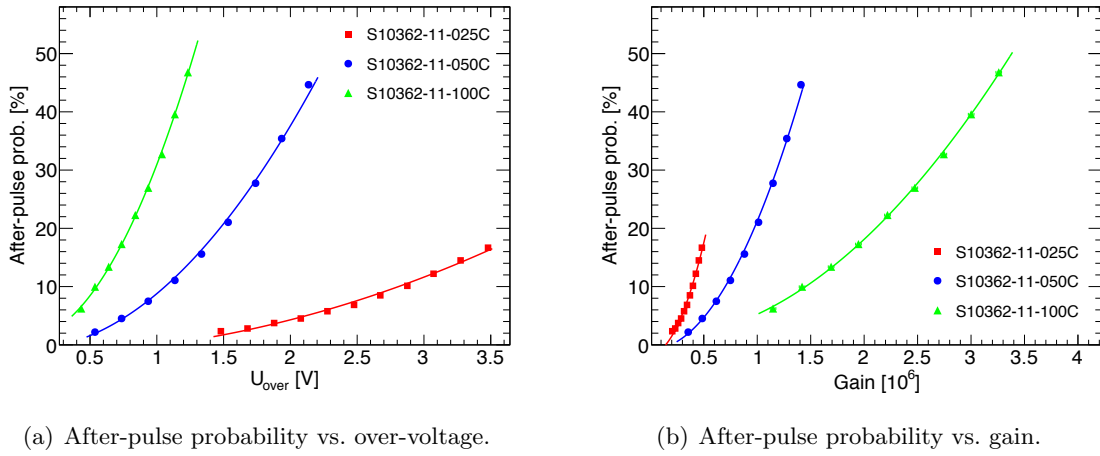


**Figure 4.13** – After-pulse probability of the tested SiPM samples as a function of the over voltage (a) and gain (b). The data points have been fitted with a quadratic function with a constant term ( $y = a + bx^2$ ); published in [4].

The fit with Equation 4.11 is only applied for time differences  $\Delta t$  larger than a certain value between 20 and 100 ns which depends on the SiPM type. For smaller values, the efficiency for pulse detection is reduced due to the recovery time of the SiPM and the dead time of the discriminator and TDC. The probability for the occurrence of an after-pulse is hence given by

$$P_{\text{ap}} = \frac{\int_0^\infty \xi \cdot (n_{\text{apf}} + n_{\text{aps}}) d\Delta t}{\int_0^\infty [n_{\text{tp}} + \xi \cdot (n_{\text{apf}} + n_{\text{aps}})] d\Delta t}. \quad (4.12)$$

The function  $\xi$  takes into account that after-pulses appearing within a short time have a smaller amplitude and therefore have a reduced contribution to the after-pulse probability (cf. Equation 4.5). The values for the pixel recovery time  $\tau_r$ , required for the calculation of  $\xi$  are listed in Table A.2.

The results of the after-pulse measurement are presented in Figure 4.13. The after-pulse probability depends quadratically on the applied over-voltage and hence also on the gain. The more charge carriers are created in the avalanche process, the higher is the probability that one of them gets trapped. Further, the avalanche trigger probability is higher for high voltages which further increases the after-pulse probability. Figure 4.13(b) shows the after-pulse probability as a function of the gain. Similar to the case of the cross-talk probability, the after-pulse probability is higher in case of smaller pixels at constant gain values. The longer recovery times of larger pixels certainly is responsible for a part of this effect. To settle this question completely, however, a deeper investigation of the effect is necessary.

## 4.6 Photon Detection Efficiency

The photon counting resolution achievable with any kind of photodetector is fundamentally limited by statistical fluctuations of the detection process. The relative size of these fluctuations is decreasing with the number of photons contained in the light flash, and with an increasing photon detection efficiency (PDE). SiPMs are, however, mainly used to measure extremely weak light signals consisting of only a few photons, as for example in case of the AHCAL prototype where only  $O(15)$  photons are created if a minimum ionising particle traverses one of the 5 mm thin scintillation tiles. For a precise measurement of these signals, hence, a high PDE is of importance. The setup for the measurement of the PDE represents therefore a central part of the characterisation test stand.

One difficulty in the measurement of the absolute PDE for SiPM detectors is caused by the SiPM noise; i.e. the thermal noise, cross-talk and after-pulse effect. One example of the influence of these effects on the generation of the measurable signal is shown in Figure 4.14. The process starts with the successful detection of a photon which would in an ideal detector cause a signal charge of  $Q = Gq_e$ . However in the real SiPM detector, a thermal noise pulse may appear within the signal integration time and the instant cross-talk effect may cause multiplication of the initial charge ( $Q = 3Gq_e$  in the shown example). In addition, after-pulses may appear which again increase the signal charge so that it is summed up to  $Q = 4Gq_e$ . A naive measurement of the signal charge, ignoring the effect of thermal noise, cross-talk and after-pulses would hence result in a significant overestimation of the photon detection efficiency. For this reason, a PDE measurement setup was developed and constructed within the scope of this thesis which allows for the determination of the absolute PDE of SiPMs by taking into account and correcting for the effects of the SiPM noise described above. The PDE can be determined over a spectral range from 350 up to 1000 nm.

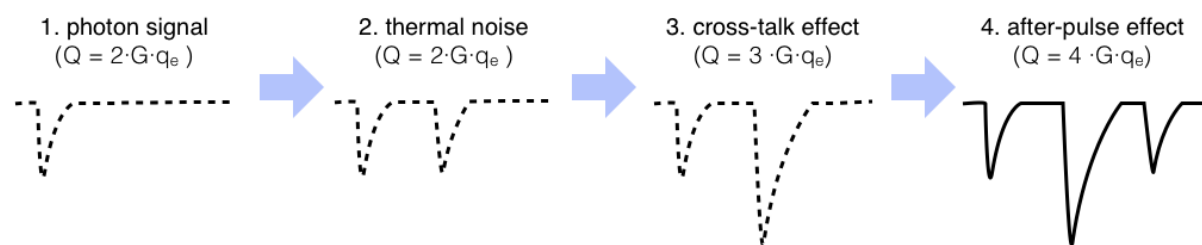


**Figure 4.14** – One example of the impact of thermal noise, cross-talk and after-pulse effect on the SiPM signal resulting from the detection of a single photon (point 1). The thermal noise (point 2) creates an additional single pixel pulse in the signal integration time which results in a doubling of the signal charge  $Q$ . The cross-talk effect (point 3) appears instantly with the photon detection, or thermal noise pulse. Finally, point 4 shows the generation of a single after-pulse so that the total signal charge equals now four times the initial photon signal charge. Only the final signal, taking into account the various effects, is observable whereas the other signal stages are unknown.

## Absolute PDE Measurement

The basic definition of the photon detection efficiency is the ratio of the detected number of photons with respect to the incident number of photons:

$$\text{PDE} = \frac{N_{\text{detected}}}{N_{\text{incident}}}.$$
 (4.13)

The principle of the PDE determination is hence the measurement of the SiPM response to a calibrated source of light; i.e. a light source which emits a well known number of photons directly onto the active area of the SiPM. In the measurement presented here, such a calibrated light source is created with the usage of an integrating sphere<sup>8</sup> which forms the central component of the setup shown in Figure 4.15. The parts of the setup used for the absolute PDE determination (without the disturbance of cross-talk and after-pulses) described in this section are marked with blue and grey colours.

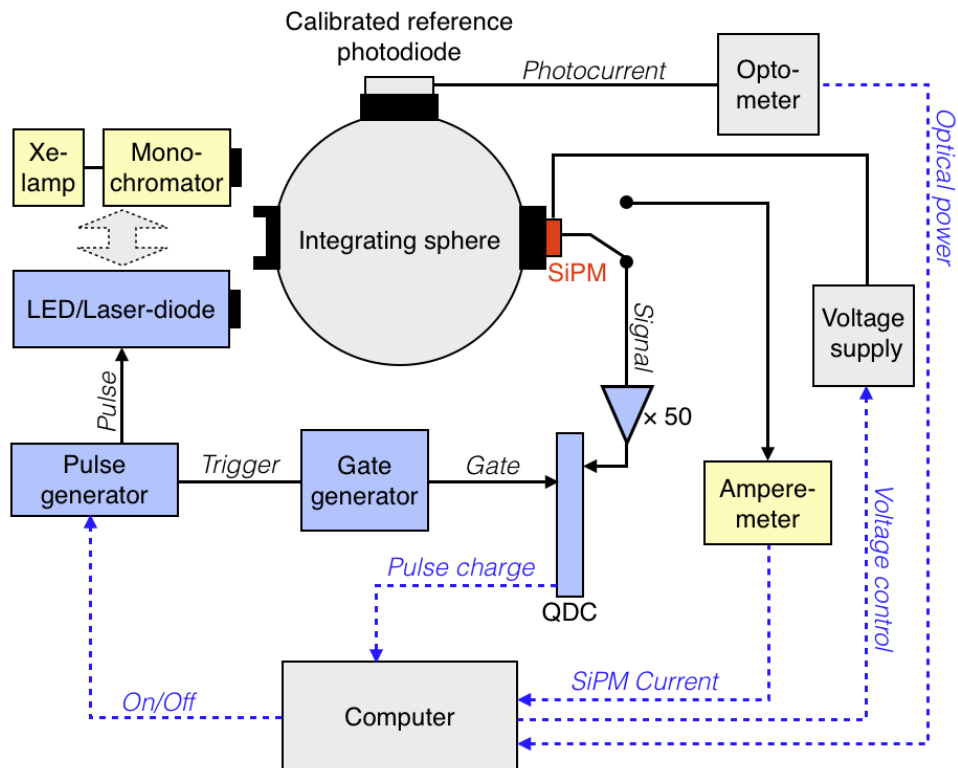


**Figure 4.15** – Schematic description of the PDE measurement setup. The central part is an integrating sphere which distributes the incoming beam of light uniformly between the two connector ports where a calibrated photodiode and a SiPM are positioned. The parts of the setup marked with blue colour are used for the absolute PDE determination, the yellow parts belong to the relative spectral sensitivity measurement, whereas the grey components are required for both measurements. The setup is controlled by a LabVIEW program from a computer in the laboratory. A photograph of the setup is shown in Figure A.7.

<sup>8</sup>Newport Corporation, Model 819D-SL-3.3.

## Experimental Setup

A pulse generator creates short  $O(1\text{ ns})$  voltage pulses which are used to operate one of the LEDs and laser-diodes in the wavelength range from blue to the near infrared. The peak emission wavelength of these light sources is listed in Table 4.3. The light pulses created are injected into the integrating sphere which is schematically indicated on the left side of Figure 4.16. The inner walls of the sphere is coated with Spectralon [77] material which has a high reflectivity in the wavelength range used for this measurement. As the incoming light is diffusely reflected many times at the inner walls, the light observed at one of the exit ports has almost ideal Lambertian characteristics; i.e. the light intensity is approximately proportional to the cosine of the angle to the surface normal vector (a line crossing the sphere centre). The light intensity at one of the ports is almost independent from the angle of light input. Therefore, no time consuming and error-prone alignment of the different light sources (LEDs, laser diodes, xenon lamp) is required which improves the measurement precision and reproducibility of the setup.

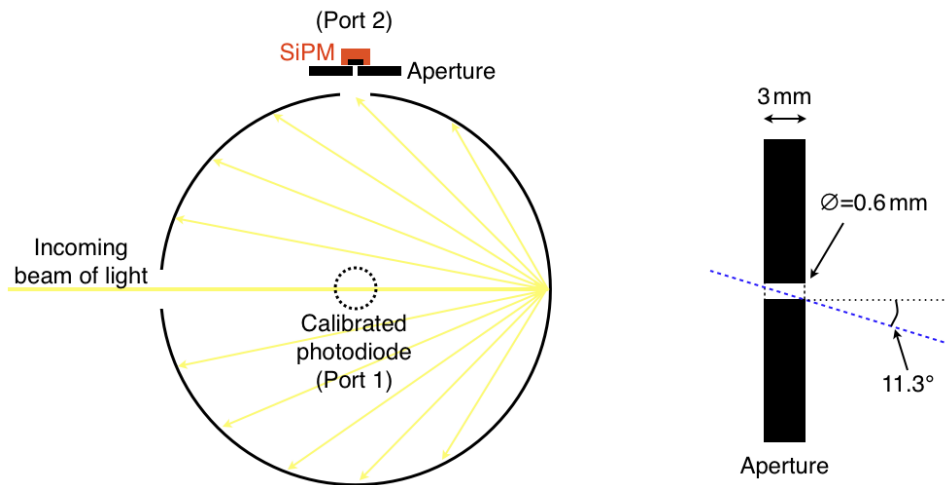


**Figure 4.16** – The left side shows a schematic view of the integrating sphere. The incoming light is reflected many times at the inner walls until it reaches one of the two exit ports. Port 1 of the sphere is equipped with a calibrated photodiode (dashed line). The SiPM is placed behind an aperture at port 2. The angle between each of the ports is 90 degree which avoids a direct illumination. The right side shows a magnified view of the aperture in front of the SiPM. The light acceptance is limited to angles smaller than  $\sim 11.3^\circ$ .

One port of the sphere is equipped with a silicon PIN photodiode<sup>9</sup> which was individually calibrated by the producer over the wavelength range form 200 up to 1100 nm according to NIST standards. The calibration data, shown in Figure A.8, is stored on a optometer device which measures the average current generated by the photodiode and calculates the corresponding optical power for the specified wavelength. Since the PIN photodiode has no internal amplification mechanism, the response and calibration is not influenced by temperature variations as discussed in section 3.3.

The SiPM is placed at port 2 in front of a 3 mm thick aperture made of brass with a hole diameter of 0.6 mm. The aperture has been chemically treated in order to reduce the light reflection probability. The photons reaching the SiPM detector are hence limited to angles smaller than  $\sim 11.3^\circ$  with respect to the surface normal as indicated in Figure 4.16 (right).

<sup>9</sup>Newport Corporation, Model 818-UV/CM.

The measured PDE is therefore almost not affected by the angular dependence of photon absorption. Another reason for using an aperture is the small active area of  $1 \times 1\text{mm}^2$  of most tested SiPMs; for a precise measurement of the PDE it is required that all light passing through the aperture hits the active area of the SiPM. Photons hitting photo-insensitive regions outside of the active area cannot be detected and would therefore cause an underestimation of the PDE.

### Power Ratio

Whereas the calibrated PIN photodiode with a circular active area of  $\sim 1\text{cm}^2$  is directly mounted on port 1, the SiPM is placed behind an aperture with a small hole diameter. The light quantity reaching the SiPM is hence much smaller with respect to the light quantity measured by the PIN photodiode. For a comparison of these photon fluxes, required for the calculation of the PDE according to Equation 4.13, hence a ‘power ratio’,  $R_{0.6}$ , is introduced. It denotes the ratio between the light quantity measured at port 1, and the one measured at port 2 behind the aperture with the 0.6 mm hole diameter. Its value is determined experimentally by changing the positions of the PIN photodiode from port 1 to port 2 while light from the laser diodes and LEDs is injected into the sphere at constant intensity. The measurement is repeated several times in order to get an estimate for the uncertainty. The measured values of the power ratio  $R_{0.6}$  are listed in Table 4.3. A dependence on the photon wavelength is found which is expected to be caused by wavelength dependent reflection properties of the aperture; i.e. in case of higher reflection probabilities, more photons can pass through the aperture whereas less photons arrive in case of a lower reflection probability.

The large values of  $R_{0.6}$ , listed in Table 4.3 cause an improvement of the measurement precision as they increase the light quantity observed by the PIN photodiode with respect to the one observed by the SiPM. This is important as the SiPM has due to its high gain the capability to detect single photons whereas the sensitivity of the PIN photodiode ( $G = 1$ ) is much smaller and allows only for the measurement of several hundreds of photons.

**Table 4.3** – Summary of the characteristics of the laser diodes and LEDs used for the absolute PDE determination. The peak emission is determined from the measured emission spectra shown in Figure A.9.

Light source type	Peak emission wavelength [nm]	Power ratio $R_{0.6}$
LED	465	$4200 \pm 20$
Laser diode	633	$3852 \pm 16$
Laser diode	775	$4328 \pm 7$
LED	870	$4625 \pm 55$

### SiPM Positioning

The light passing the aperture creates a light spot on the SiPM surface. For a precise measurement it must be assured that the total light spot hits the active area of the SiPM. The SiPM is for this purpose placed very close in front of the aperture and moved along the x and y axis by means of a manual positioning stage with a precision of  $\sim 0.1\text{ mm}$ . The signal profile of such an axis scan is shown in Figure 4.17. In the centre region of the profile, a plateau region

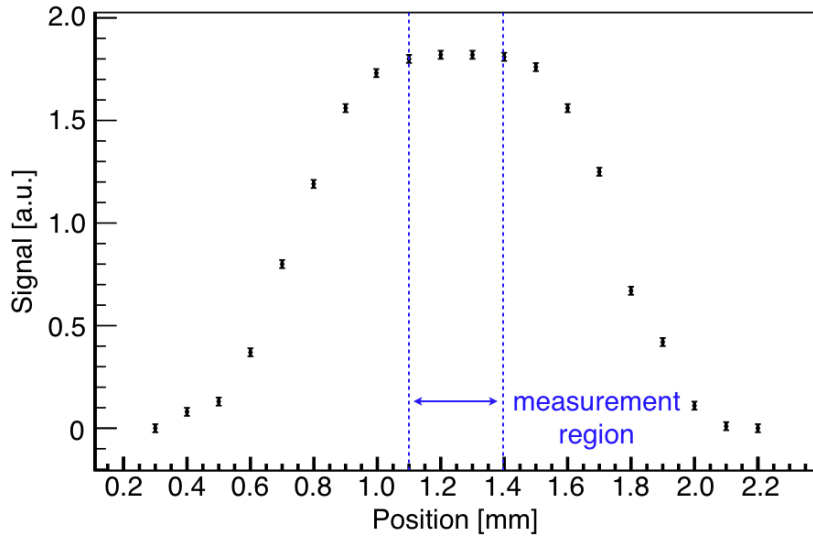


**Figure 4.17** – Typical signal profile of a  $1 \times 1\text{mm}^2$  SiPM scanned along the x-direction in front of the aperture with 0.6 mm hole diameter. A plateau can be identified in which the Signal does not depend on the position as the total light spot hits the active SiPM area. The PDE measurements were performed within the indicated range.

can be identified in which the SiPM signal reaches its maximum value. The appearance of this plateau indicates that the light spot is smaller compared to the active area of the SiPM. The SiPM is placed in the centre of the plateau for the PDE measurement. The circumstance that the SiPM signal is approximately constant in the plateau region allows for a precise and reproducible positioning of the SiPM; i.e. the measurement result remains the same even if a slight dealignment of the SiPM occurs.

## Statistical Analysis

The signal of the SiPM created when photons from the pulsed light source are detected is first amplified by a factor of 50 and integrated by a QDC already used for the gain measurement described in section 4.2. The gate signal is adapted to each individual SiPM type in between 50 and 100 ns in order to guarantee a full integration of the SiPM pulse. A typical charge spectrum recorded with the QDC is shown in Figure 4.18.

The number of photons contained in a pulse from the LED or the laser diode is expected to be Poisson distributed. In case of an ideal SiPM detector without any noise, hence the measured signal spectrum also corresponds to a Poisson distribution:

$$P_\mu(n_{\text{pix}}) = \frac{\mu^{n_{\text{pix}}} e^{-\mu}}{n_{\text{pix}}!}, \quad (4.14)$$

where  $n_{\text{pix}}$  denotes the number of detected photons (firing pixels) per light pulse and  $\mu$  is the corresponding average value. However, the QDC spectrum shown in Figure 4.18 describes a distorted Poisson distribution; i.e. the average is shifted to higher values due to the effects of cross-talk, after-pulses and the thermal noise. Usage of the uncorrected average value of this spectrum would hence yield a significant overestimation of the PDE.

The cross-talk and after-pulse effect can only occur when at least one pixel is already firing, hence the first peak of the spectrum, containing the events where no photon was detected, is

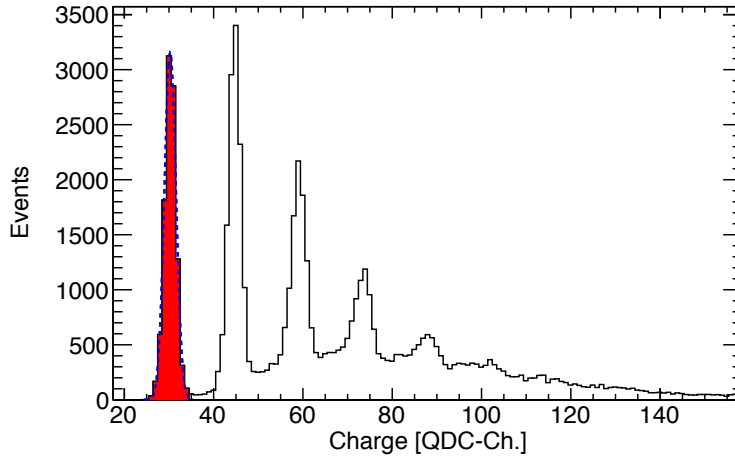


**Figure 4.18** – Typical example of a single photoelectron spectrum recorded during the PDE measurement (SiPM type S10362-11-025C). A Gaussian function (blue dashed line) is fitted to the first peak. The number of events with zero pixels firing is determined by integration of the spectrum from 0 to the mean of the Gaussian plus three sigma (red area).

not influenced by cross-talk and after-pulses. Using Equation 4.14 it is therefore possible to determine the mean value of the spectrum without the effects of cross-talk and after-pulses by measuring the probability to detect zero photons:

$$P_\mu(0) = e^{-\mu} \quad (4.15)$$

$$\Rightarrow \mu = -\ln(P_\mu(0)) = -\ln\left(\frac{\epsilon \cdot N'_{0\text{pe}}}{N_{\text{tot}}}\right). \quad (4.16)$$

Here  $N'_{0\text{pe}}$  denotes the number of events contained in the zero photoelectron peak and  $N_{\text{tot}}$  corresponds to the total number of recorded events determined by the integral over the whole spectrum. The value of  $N'_{0\text{pe}}$  is determined by fitting a Gaussian function to the first peak and integration from zero up to the Gaussian mean plus three times the standard deviation.  $\epsilon$  is a correction factor which accounts for the thermal noise rate as described in the following.

### Thermal Noise Correction

Even though the number of zero photoelectron events,  $N'_{0\text{pe}}$ , is not biased by cross-talk and after-pulses, it is influenced by the thermal dark-rate. This is indicated in Figure 4.19 which shows a QDC spectrum recorded when the pulse generator is switched off and the integration gate is triggered randomly. All histogram entries lying above the zero photoelectron peak are caused by the thermal noise. In order to correct for this effect, a correction factor is defined which transforms the observed number of zero photoelectron events,  $N_{0\text{pe}}^{\text{dark}}$ , back to the total number of events  $N_{\text{tot}}^{\text{dark}}$ :

$$\epsilon \cdot N_{0\text{pe}}^{\text{dark}} \stackrel{!}{=} N_{\text{tot}}^{\text{dark}} \quad (4.17)$$

$$\Rightarrow \epsilon = \frac{N_{\text{tot}}^{\text{dark}}}{N_{0\text{pe}}^{\text{dark}}}. \quad (4.18)$$

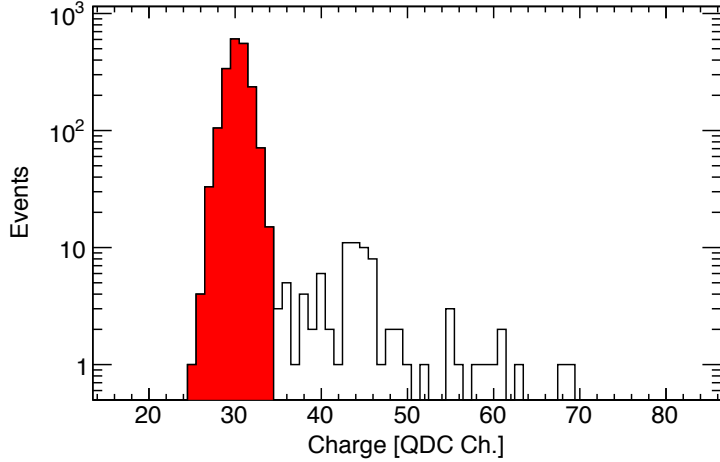


**Figure 4.19** – Typical example of a dark-rate spectrum recorded with the QDC (SiPM type S10362-11-025C). The number of events in the first peak (red area) is determined in the same way as in case of Figure 4.19.

The probability for the observation of a dark-count within the integration gate is given by  $P_{dark} = \epsilon - 1 = \nu_{dark} \cdot T_{gate}$ . Here  $\nu_{dark}$  denotes the SiPM dark-rate and  $T_{gate}$  is the measurement gate. Typical values of  $P_{dark}$  are in the range of a few percent. As the dark-rate depends on the applied over-voltage, the same applies for the correction factor. For each light pulse spectrum recorded, hence also a dark-rate spectrum is recorded at the same voltage in order to determine the correction factor  $\epsilon$ .

### PDE Determination

Charge spectra as the ones shown in Figure 4.18 and Figure 4.19 have been recorded in a range of different over-voltages. From these spectra, the noise corrected value of the average number of detected photons per light pulse,  $\mu$ , is determined and the absolute photon detection efficiency is calculated according to the following formula:

$$PDE = \frac{N_{\text{detected}}}{N_{\text{incident}}} = \frac{\mu}{P_{\text{opt}}[W]/(h \cdot \nu \cdot f \cdot R_{0.6})}. \quad (4.19)$$

The denominator corresponds to the average number of photons per light pulse, incident on the active SiPM area.  $P_{\text{opt}}$  denotes the average optical power (unit Watts) measured with the calibrated PIN photodiode. In order to derive the average number of photons contained in a pulse, the power ratio  $R_{0.6}$ , the pulsing frequency of the light flashes  $f$ , Planck's constant  $h$  and the photon frequency  $\nu$  have to be taken into account.

The results of the voltage dependent absolute PDE measurement are presented in Figures 4.25 – 4.30 (left). As expected, the PDE increases with the applied over-voltage. This can be attributed to the voltage dependence of the avalanche trigger probability  $P_{\text{trigger}}$  (cf. Equation 3.8). For high over-voltages, the avalanche trigger efficiency reaches its maximum value close to unity and correspondingly a saturation behaviour of the PDE is observed.

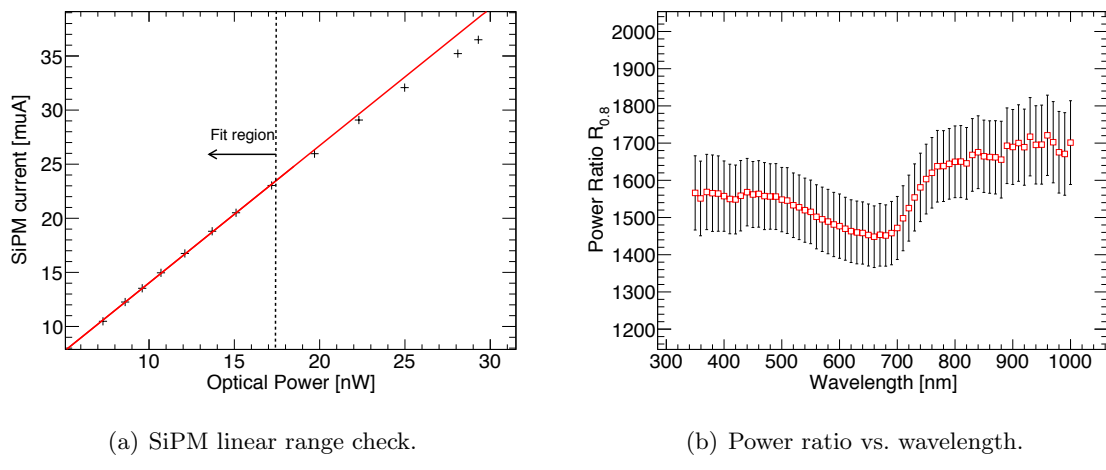
For the application of the described statistical method it is necessary that the zero photo-electron peak is well separated from the one photoelectron peak as shown in Figure 4.18 and

Figure 4.19. This requirement, however, can only be fulfilled in a limited voltage range; i.e. at too low over-voltages, the gain of the SiPM is not large enough for a peak separation, given by the finite QDC resolution. The same is true at too high over-voltages, as the thermal noise rate, and the crosstalk and after-pulse probabilities are increased resulting in an unstable behaviour of the SiPM which reflects in a broadening and shift of the individual peaks. For this reason, the over-voltage range of the PDE measurement differs from SiPM to SiPM.

### Relative Spectral Sensitivity Measurement

The statistical analysis method which forms the basis for the absolute PDE determination without the effects of cross-talk and after-pulses, requires a pulsed light source and could therefore only be performed for the wavelengths listed in Table 4.3. Hence, in order to determine the PDE over a wide spectral range an additional measurement of the relative spectral sensitivity is conducted.

The setup is shown in Figure 4.15; only the yellow and grey components are required for this measurement. A xenon lamp operated in continuous wave mode is used as the light sources. It is suitable for this measurement as it has an emission spectrum which ranges from the ultraviolet up to the infrared region. An other positive feature is the high stability of the light intensity – once it has stabilised after  $\sim 10$  minutes – which makes an adjustment of the driving current during the measurement unnecessary. In order to select a specific wavelength  $\lambda$  for the measurement, a monochromator is used. The light throughput efficiency of the monochromator – more precisely the efficiency of the used grating – is a function of the wavelength. For small wavelengths, the efficiency is reduced which limits the practicable wavelength region to values higher than 350 nm. The sensitivity of most SiPM detectors is very small for wavelength larger than 1000 nm which sets the upper limit for the measurements. As shown in Figure A.7, an optical filter wheel is placed in between the monochromator and the integrating sphere. It is required to filter out the higher order wavelengths  $\lambda_i$  which also fulfil the condition of constructive interference ( $\lambda_i = \lambda/i$ , with  $i = 1, 2, 3\dots$ ).



**Figure 4.20** – Figure (a) shows the photocurrent of the Ketek SiPM as a function of the optical power measured with the PIN photodiode. The bias voltage was set to  $U_{\text{bias}} = 36.6$  V. At high photon fluxes, a non-linear dependence is observed. Measurements of the relative spectral sensitivity are only performed in the region of linear response. Figure (b) shows the Power ratio  $R_{0.8}$  between the photocurrent measured at port1 and the photocurrent measured at port 2.

A pico-ampere meter is used to measure the photocurrent of the SiPM. Hence the measurement includes the effect of optical cross-talk and after-pulses which however, is not a problem as the aim of this measurement is only the measurement of the *relative* spectral sensitivity. The cross-talk and after-pulse probabilities are independent on the wavelength and therefore do not bias the result.

For this type of measurement it is not required that all photons hit the active area of the SiPM. Hence, the SiPM is placed behind a slightly larger aperture with a 0.8 mm hole diameter. In this way, almost the complete  $1 \times 1\text{mm}^2$  active SiPM area is illuminated which exploits a higher dynamical range. The non-linear SiPM response to high photon fluxes could yield a distortion the measured spectral sensitivity. Therefore, the light intensity is adjusted such that each individual SiPM is operated within the linear range as shown in Figure 4.20(a). This procedure is in particular important in case of SiPMs with a relatively low pixel density such as the Ketek or Hamamatsu S10362-11-100C devices.

In a similar way as described above a power ratio  $R_{0.8}$  is introduced to take into account for the different photon quantities reaching the calibrated photodiode and the SiPM. As the power ratio of the absolute PDE measurement described above,  $R_{0.6}$ , is wavelength dependent, also  $R_{0.8}$  has been determined as a function of the wavelength. For the measurement, the calibrated photodiode is placed alternatively at port 1 and at port 2 and the measured photocurrents are determined. The procedure was repeated several times in order to get an estimate for the uncertainty due to measurement fluctuations. As shown in Figure 4.20(b), the power ratio varies by  $\sim 10\%$  which is, as above, expected to be caused by the wavelength dependent reflection properties of the aperture.

Typical examples of the optical power measured with the calibrated photodiode and of the measured SiPM photocurrent are shown in Figure 4.21. The relative spectral sensitivity is then calculated according to:

$$S(\lambda) = \frac{I_{\text{SiPM}}(\lambda)/(G \cdot q_e)}{P_{\text{opt}}(\lambda)/(R_{0.8}(\lambda) \cdot h \cdot \nu)}, \quad (4.20)$$

where  $I_{\text{SiPM}}$  denotes the photocurrent of the SiPM measured with the picoampere-meter,  $G$  is the SiPM gain, and  $q_e$  is the electron charge.

## Discussion of the PDE Results

The results of the PDE measurement are presented on the right side of Figures 4.25 – 4.30. The relative spectral sensitivity  $S(\lambda)$  has been scaled to the maximum PDE measured with the 633 nm laser diode. The laser-diode was chosen for the scaling as the spectral width of the corresponding emission spectrum is much smaller compared to the ones of the LEDs as shown in Figure A.9. The results of the absolute PDE measurement with the other LEDs and laser-diodes is also included into the plot; good agreement with the scaled relative sensitivity curves is observed. For a better overview, a summary of the results is presented in Figure 4.22.

The systematic uncertainty of the presented measurements is dominated by the uncertainty of the power-ratios  $R_{0.6}$  and  $R_{0.8}$  (cf. Table 4.3 and Figure 4.20(b)) the calibration uncertainty of the calibrated photodiode and the precision of the pico-ampere meter. In case of the absolute PDE determination, the statistical uncertainty is estimated by repeating each measurement several times.

A relatively high photon detection efficiency in the blue and ultraviolet spectral range is as expected observed for the SiPM detectors with a p-on-n structure (Hamamatsu and Ketek).

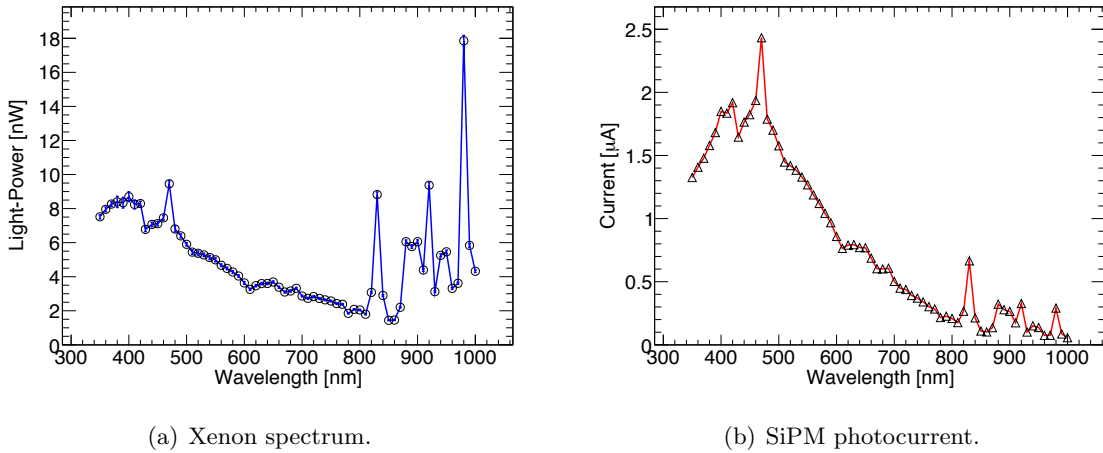


**Figure 4.21** – Figure (a) shows the spectrum of the Xenon-lamp  $P_{\text{opt}}$ , measured with the calibrated photodiode. Figures (b) shows the measured SiPM current  $I_{\text{SiPM}}$  as a function of the wavelength (S10362-11-050C).

Hence, these devices are well suited for the direct detection of the extremely weak blue scintillation light flashes produced in organic scintillators by minimum ionising particles required for example in case of the AHCAL application. The readout without wavelength shifting fibre allows for the reduction of the cost of the scintillating tile system and it improves the timing response as the decay time of the wavelength shifting fibre is skipped. Several different concepts of such direct readout schemes have been investigated in Refs. [78–80] and promising candidates for future calorimeters could be identified.

The devices with a n-on-p structure have a smaller PDE in the blue and ultraviolet spectral region. This is clearly illustrated in Figure 4.29, showing the PDE of the MEPhI/Pulsar SiPM used in the physical AHCAL prototype. The device belongs to one of the first SiPM detectors produced in large quantities. The maximum PDE has been measured for red light ( $\lambda \sim 650 \text{ nm}$ ). However, the value only slowly decreases to shorter wavelength giving the device an acceptable sensitivity in the green wavelength region. The results underline the requirement of the wavelength shifting fibre mediated tile readout, as the value of the PDE in the blue region of direct scintillator emission ( $\sim 400 \text{ nm}$ ) is very low. The PDE of the SensL SPMMICRO1020X13 reaches the maximum value at  $\sim 500 \text{ nm}$ . The value, however, decreases strongly for shorter wavelength giving the device only a relatively small PDE for blue light.

As presented in Table 4.4, the measured peak PDE values at maximum over-voltage are significantly smaller compared to the reference PDE values quoted by the producer Hamamatsu. The difference amounts to 24 % (S10362-025C), 36 % (-050C), and 43 % (-100C). Large fractions of this discrepancy is most probably caused by the measurement method used to derived the producer reference data which includes the effects of optical cross-talk and after-pulses. The cross-talk and after-pulse probabilities are higher for SiPMs with larger pixels (cf. Figs. 4.11 and 4.13) which explains the larger discrepancy for the devices with larger micro-cells. Similar observations have been reported in Refs. [81–83]. The reference PDE value quoted from the producer SensL is compatible with the presented measurement results.

The impact of the geometrical efficiency  $P_{\text{geo}}$  on the PDE can be identified best in case of the Hamamatsu MPPCs. Three different devices have been tested which differ in the pixel density (100, 400 and 1600 pixels per  $\text{mm}^2$ ). The device with the largest pixel size and correspondingly

the highest geometrical efficiency (S10362-11-100C) has as expected the largest PDE. However, a small pixel density also has the consequence of a reduced dynamical range. Application of such ‘PDE-optimised’ devices is hence limited to experimental areas where exclusively weak light signals have to be measured, which is for example the case in some astrophysical experiments. The limited dynamical range makes these devices, however, unsuitable for calorimetric applications where the large scintillator signals present for example in the core of an electromagnetic cascade, as well as the weak signals from single minimum ionising particles have to be measured with high precision. In order to avoid the deterioration of energy resolution which arises due to the non-linear response, hence SiPMs with a high pixel density ( $n_{\text{pixel}} > 1000/\text{mm}^2$ ) are required for calorimetry.

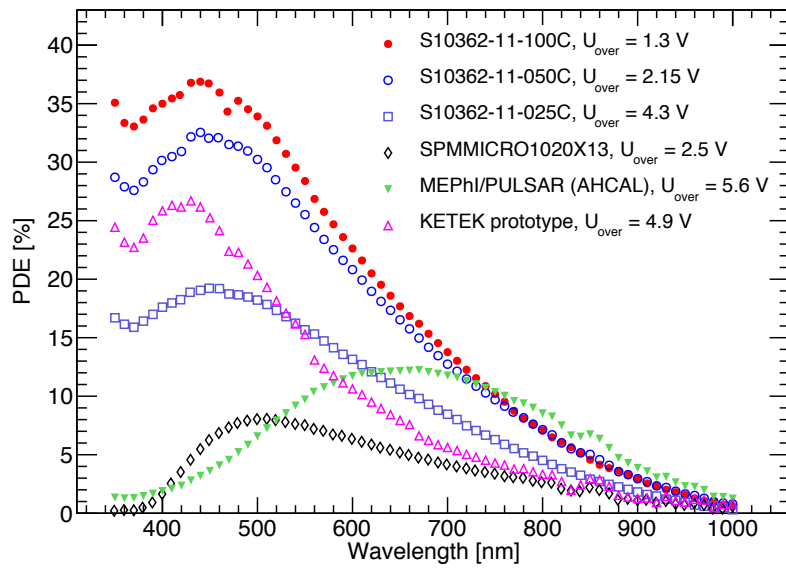


**Figure 4.22** – Photon detection efficiency as a function of the wavelength for a variety of SiPM devices. The SiPMs have been operated at the highest over-voltage where a stable SiPM operation and hence a precise absolute PDE determination with the statistical method is still possible. For a better visualisation, the error bars are not drawn (cf. Figures 4.25 – 4.30).

## 4.7 SiPM Uniformity Measurements

The preceding sections are dedicated to the ‘global’ SiPM characteristics; i.e. those parameters which are averaged over the total number of pixels on the SiPM (total active SiPM area). In contrast, the following section describes measurements of the gain, photosensitivity and cross-talk probability of individual SiPM pixels.

The experimental setup is schematically indicated in Figure 4.23. For this measurement, the SiPM is contained inside of a lightproof box which has only a small opening on the frontside for a controlled illumination. The box is mounted on a positioning stage, capable to move the SiPM within the x-y plane with the precision of one micrometer. A laser-diode creates short light pulses; approximately half of the light is focussed to a photodiode which monitors the light intensity during the measurement. The remaining fraction of light is directed to a spatial filtering system, featuring a pinhole with  $5\text{ }\mu\text{m}$  hole diameter. This system is used to alter the light beam properties; i.e. to create an approximately Gaussian intensity profile. After the spatial filter, the light beam is expanded using a microscope objective. A second objective is used to finally focus the beam on the active area of the SiPM. The current setup only allows for an indirect determination of the light spot diameter, by measuring the signal change during a transition from an insensitive to sensitive area; e.g. between two SiPM pixels. The focussing is adjusted until the abruptness of the signal change is maximal which indicates the optimal position. The diameter of the light spot achieved with this method is  $\sim 5\text{ }\mu\text{m}$ , which is sufficiently small compared to the smallest pixel pitch of  $25\text{ }\mu\text{m}$  of the tested SiPM devices. In the future, the setup will be equipped with a CCD camera, hence facilitating a direct measurement of the light spot properties.

The signal of the SiPM is read out in the same way as described in section 4.2; i.e. charge spectra are recorded using a QDC with a gate provided by the gate generator which in turn is

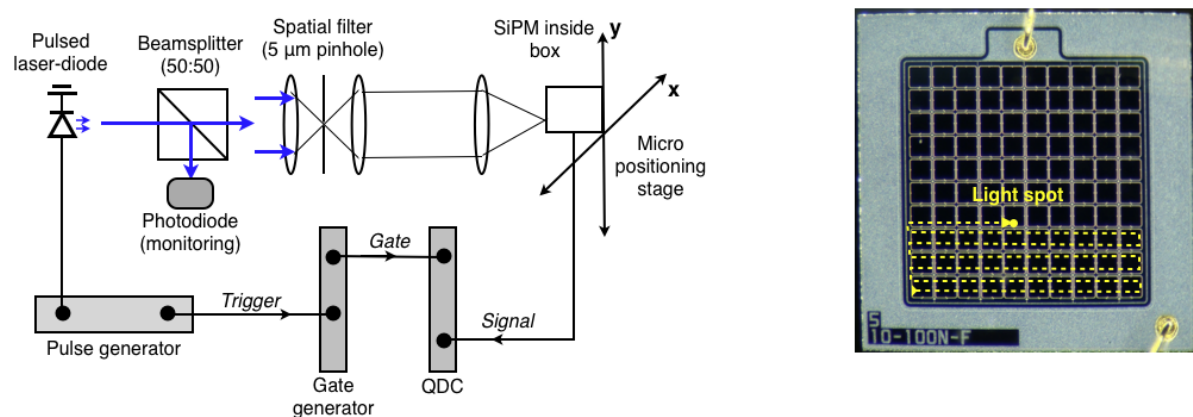


**Figure 4.23** – Schematic description of the Uniformity scan setup. The light of a laser diode operated in a pulsed mode is focussed to a small light spot of  $\sim 5\text{ }\mu\text{m}$  diameter onto the active area of the SiPM by means of a spatial filtering system. The SiPM is contained inside of a aluminium box with only a small opening in order to effectively shield it from the electronics noise created during the operation of the positioning stage. The signal of the SiPM is fed into a QDC and integrated over the duration of the gate signal. A photodiode constantly measures the light intensity and hence allows to correct for variations in the offline analysis of the acquired data. A photograph of the setup is shown in Figure A.10.

triggered by the laser-diode pulse generator. The duration of the QDC integration gate signal is set to the smallest possible value, still containing the full SiPM pulse (30 ns). This facilitates a reduction of the signal contribution coming from after-pulses which would otherwise bias the measurement of the pixel cross-talk probability described below. A difference to the regular gain measurement is that only single pixels are illuminated instead of the total device area. Hence, the setup allows for the characterisation of individual SiPM pixels and the device uniformity.

The active SiPM area is raster scanned with the focussed light spot as indicated on the right of Figure 4.23. The step size chosen for the measurement is  $3\text{ }\mu\text{m}$ , in x and y-direction. For each position, 10 000 light flashes are sent to the SiPM and the charge of the generated signal pulses is measured. In addition, the photocurrent of the monitoring photodiode and the temperature are written to the data file. During the offline analysis of the data, automatic corrections are applied taking into account the variation in the monitoring photocurrent. Two typical charge spectra recorded during a measurement are shown in Figure 4.24. The acquired spectra are analysed in order to determination the following three independent quantities:

- **Surface photosensitivity**

The same statistical method used to determine the absolute PDE (cf. section 4.6) is used to determine the photosensitivity of the SiPM active area without the contributions of optical cross-talk and after-pulses. For this purpose, the number of events in the zero photoelectron peak are integrated and the corresponding number of detected photons is calculated with Equation 4.16. Only the relative PDE can be determined as the actual number of photons contained in the light pulse cannot be determined with this type of experimental setup. Hence, the maximum number of detected photons is scaled to 100 % for a presentation of the results.

- **Single pixel gain**

By measuring the distance between the peaks in the spectrum shown in Figure 4.24(b), the gain of the SiPM can be determined as a function of the position. However, the method of the gain measurement only delivers precise values when at least two peaks can be identified in the charge spectrum. When the light spot is focussed to an insensitive area, the pixel discharge is exclusively caused by the thermal noise. It is hence unknown which one of the pixels is firing. For this reason, a minimum sensitivity is required for the gain determination; in the measurement presented here a minimum of 50 % photosensitivity is required. In the remaining regions the gain is set to zero.

- **Single pixel cross-talk probability**

When the light spot is focussed to a single pixel, only the corresponding pixel is expected to give a signal. However, due the optical cross-talk effect it is possible that two or more pixels give a signal. The probability for this effect can be calculated with the information provided by the spectrum shown in Figure 4.24(b). All events with an integrated charge larger than the single photoelectron peak are expected to be caused by optical cross-talk. Hence, the cross-talk probability can be calculated with the following equation:

$$P_c = \frac{N_c}{N_{1pe} + N_c}. \quad (4.21)$$

Here,  $N_c$  denotes the number of cross-talk induced events; i.e. the events corresponding to at least two firing pixels, and  $N_{1pe}$  denotes the number of events containing exactly one pixel discharge.

Similar to the absolute PDE measurement, also the cross-talk probability needs to be corrected for the thermal-noise rate; the measured number of one photoelectron events,  $N'_{1\text{pe}}$ , is reduced, whereas the measured number of cross-talk events  $N'_c$  (red area in Figure 4.24(b)), is increased due to the thermal noise. If no correction is applied, hence the cross-talk probability would be overestimated. The same correction factor  $\epsilon$ , defined in Equation 4.18 can be used to correct the one photoelectron events<sup>10</sup>:

$$N_{1\text{pe}} = \epsilon \cdot N'_{1\text{pe}}. \quad (4.22)$$

Correspondingly, the corrected number of cross-talk events is given by:

$$\begin{aligned} N_c &= N'_c - (N_{1\text{pe}} - N'_{1\text{pe}}) \\ &= N'_c - (\epsilon \cdot N'_{1\text{pe}} - N'_{1\text{pe}}) \\ &= N'_c - N'_{1\text{pe}}(\epsilon - 1). \end{aligned} \quad (4.23)$$

The cross-talk probability (Equation 4.21) can hence be written as:

$$P_c = \frac{N'_c - N'_{1\text{pe}}(\epsilon - 1)}{N'_{1\text{pe}} + N'_c}. \quad (4.24)$$

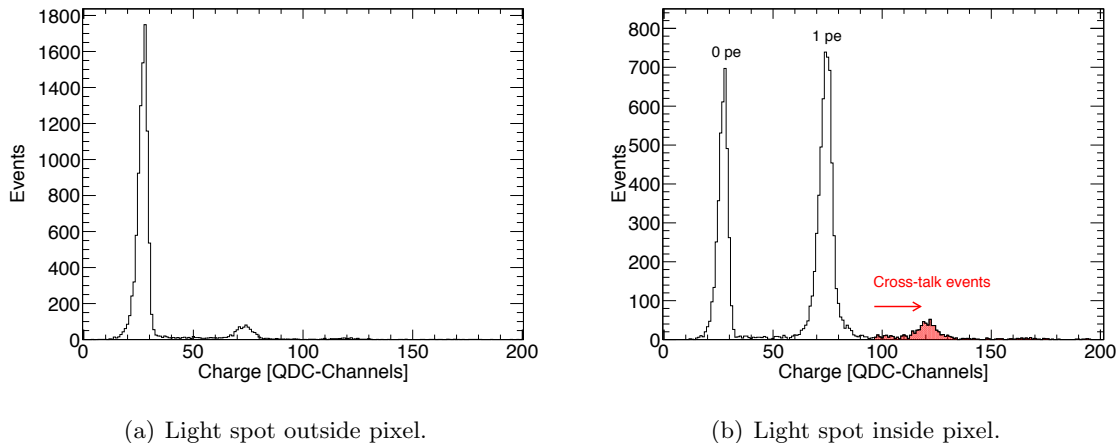


**Figure 4.24** – Typical charge spectra recorded during the uniformity scan measurement. Figure (a) shows the charge spectrum when the light spot illuminates an insensitive region on the SiPM. Most events are contained in the zero photoelectron peak, only due to the effect of the thermal noise, a few entries are generated with at least one firing pixel. Figure (b) shows the case when the light spot hits a photosensitive region. Only the corresponding pixel is expected to give a signal (1 pe). Events with more than one firing pixels must hence be caused by optical cross-talk.

<sup>10</sup>It should be noted, that the corrected number of 1pe events  $N_{1\text{pe}}$ , still includes some entries which are caused by the dark-rate effect. This causes a slight bias on the estimated cross-talk probability, since the actual position of the firing pixel is in this case unknown. However, the overall impact of the effect is expected to be small, as a short signal integration gate of only 30 ns is applied for the measurement.

## Discussion of the Uniformity Scan Results

The results of the uniformity scan measurement are presented in Figures 4.31 – 4.36. The sensitivity and gain of all tested sensor types shows a high degree of uniformity; measured variations are in the range of  $\sim 10\%$ . No completely insensitive cells are observed, which could for example be caused by broken electrical connection lines on top of the device. The results of the gain and cross-talk uniformity are only presented for regions where a sensitivity of larger than 50 % has been measured as in regions with a smaller sensitivity – for example in between two pixels – it cannot be unambiguously specified which pixel created the signal.

The cross-talk measurement results show a different characteristic as the probability for a second firing pixel is largely reduced at the borders of the active area of the SiPM. This effect is prominent in case of the SiPMs featuring large cells (S10362-11-050C and S10362-11-100C). The border pixels only have a reduced cross-talk probability as the number of neighbouring pixels is smaller; i.e. only the fraction of photons produced in the avalanche process which is emitted by accident into the direction of a pixel has the chance to trigger a second avalanche. In case of SiPMs with large pixels, even a variation of the cross-talk probability on the single pixel scale is observed. Again, regions facing outwards with respect to the active area have a smaller cross-talk probability. A possible explanation for this effect is that the avalanche, is more pronounced in the region where the initial photon was absorbed. Hence most secondary photons are emitted from this region. Depending on the position of initial photon absorption, hence different distances have to be traversed by the secondary photons which results in a variation of the cross-talk probabilities.

In case of the Hamamatsu S10362-11-100C and S10362-11-050C, an increased cross-talk probability is observed at the lateral borders of pixels, located in the approximate centre of the active area. It should be noted that this effect could be caused by an imperfect focussing of the light spot, such that more than a single pixel is illuminated. In order to exclude the possibility of a setup misalignment, an improved control over the light spot diameter is required. This will be enabled in the future, after the planned extension of the setup with a CCD camera.

The sensitivity maps (Figure 4.31 and Figure 4.34) facilitate a calculation of the geometrical efficiency. For this purpose a threshold needs to be defined; all measurement points with a sensitivity higher than the threshold value are labeled as ‘sensitive’, whereas the remaining measurement points are labeled ‘insensitive’. The geometrical efficiency is calculated according to the following equation:

$$\epsilon_{\text{geo}} = \frac{N_{\text{sensitive}}}{N_{\text{total}}}, \quad (4.25)$$

where  $N_{\text{total}}$  denotes the total number measurement points within the active area of the SiPM. The Hamamatsu MPPCs have an active area of precisely  $1 \times 1 \text{ mm}^2$ . The total number of measurements in this area is hence:  $N_{\text{total}} = 1 \times 1 \text{ mm}^2 / 3 \times 3 \mu\text{m}^2 = 111111$ , where  $3 \mu\text{m}$  corresponds to the step size of the measurement. Inspection of the SensL device sensitivity map shows that the active region is slightly larger ( $\sim 1.02 \times 1.0 \text{ mm}^2$ ). The total number of measurements hence corresponds to 113333.

In Figure A.11, the geometrical efficiency is shown as a function of the applied sensitivity threshold. For very small values of the sensitivity threshold, the geometrical efficiency reaches values greater than 100 %. This effect is described in section A.14. In case of the Hamamatsu S10362-11-100C and S10362-050C, a clear distinction between sensitive and insensitive regions is possible; i.e. a large fraction of the sensitivity values are either above  $\sim 80\%$ , or below  $\sim 20\%$ . Therefore,  $\epsilon_{\text{geo}}$  features only a relatively small sensitivity to a variation of the threshold

sensitivity in the region between 20 – 80 %. A qualitatively different observation is made for the SiPMs with a smaller pixel size (cf. Figures A.11(c) and A.11(d)). Here,  $\epsilon_{\text{geo}}$  is much stronger dependent on the value of the sensitivity threshold; i.e the slope of the curve is larger. A probable explanation for this effect could be a reduced electric field at the borders of pixels which results in a smaller photosensitivity. However, the effect may also be caused by the finite size of the light spot. Further measurements with a better control of the light spot diameter are required to settle this question.

The results of the geometrical efficiency measurement are listed in Table 4.4, together with the values quoted by the manufacturer. The measured values are based on a sensitivity threshold of 50 %. The threshold was varied in a range of  $\pm 15 \%$  in order to estimate the uncertainty. The measured values for  $\epsilon_{\text{geo}}$  are compatible with the reference values quoted by the producer.

**Table 4.4** – Measured values of the geometrical efficiency  $\epsilon_{\text{geo}}$  and the photon detection efficiency PDE. The PDE values are given for the highest possible over-voltage. For comparison, also the values provided by the manufacturers in Refs. [73, 84] are listed.

SiPM	$n_{\text{pixel}}$	$\epsilon_{\text{geo}}$ [%]	PDE <sup>a</sup> [%]	$\epsilon_{\text{geo}}$ [%]	PDE <sup>a</sup> [%]
		(Data sheet)	(Data sheet)	(Measured)	(Measured)
S10362-11-025C	1600	30.8	25 <sup>b</sup>	21 <sup>+6</sup> <sub>-7</sub>	$19.0 \pm 1.3$
S10362-11-050C	400	61.5	50 <sup>b</sup>	54 <sup>+6</sup> <sub>-5</sub>	$32.5 \pm 2.3$
S10362-11-100C	100	78.5	65 <sup>b</sup>	74 <sup>+3</sup> <sub>-3</sub>	$36.8 \pm 2.4$
SPMMICRO1020X13	1152	–	9 <sup>c</sup>	25 <sup>+8</sup> <sub>-7</sub>	$8.0 \pm 0.6$

<sup>a</sup>At peak wavelength.

<sup>b</sup>Results contain the effects of cross-talk and after-pulses. The underlying  $U_{\text{over}}$  value is not specified by the producer.

<sup>c</sup>At  $U_{\text{over}} = 2 \text{ V}$ .

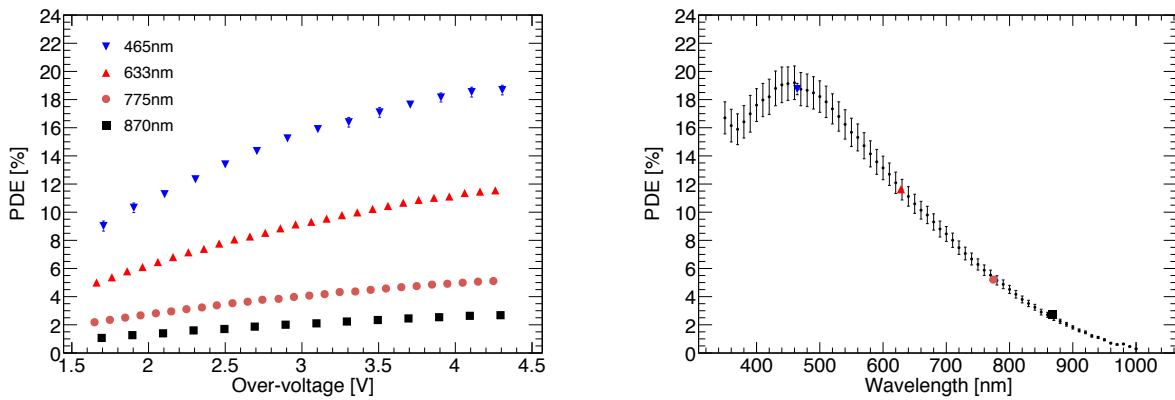


**Figure 4.25 – (left)** PDE of the Hamamatsu S10362-11-025C as a function of the applied over-voltage for different wavelengths of light. **(right)** PDE as a function of the wavelength at a fixed over-voltage of  $U_{\text{over}} = (4.3 \pm 0.05)\text{V}$ ; published in [4].

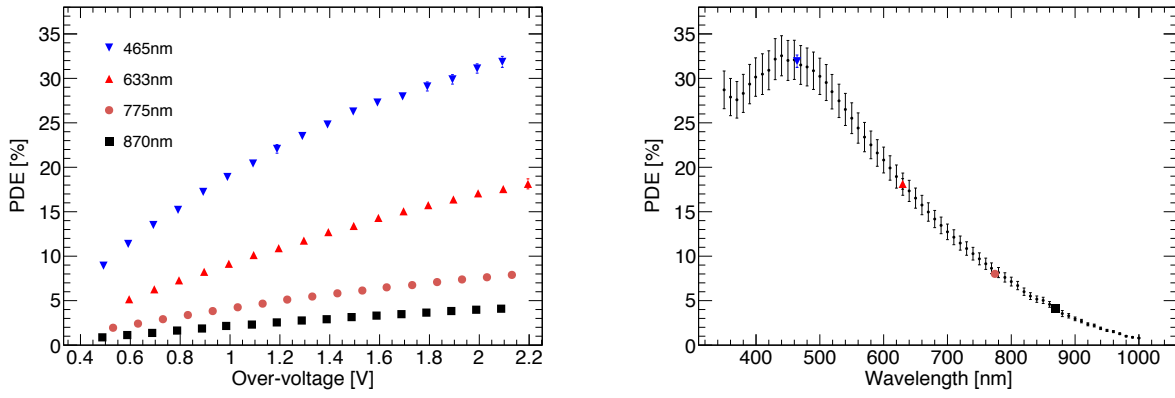


**Figure 4.26 – (left)** PDE of the Hamamatsu S10362-11-050C as a function of the applied over-voltage for different wavelengths of light. **(right)** PDE as a function of the wavelength at a fixed over-voltage of  $U_{\text{over}} = (2.15 \pm 0.05)\text{V}$ ; published in [4].

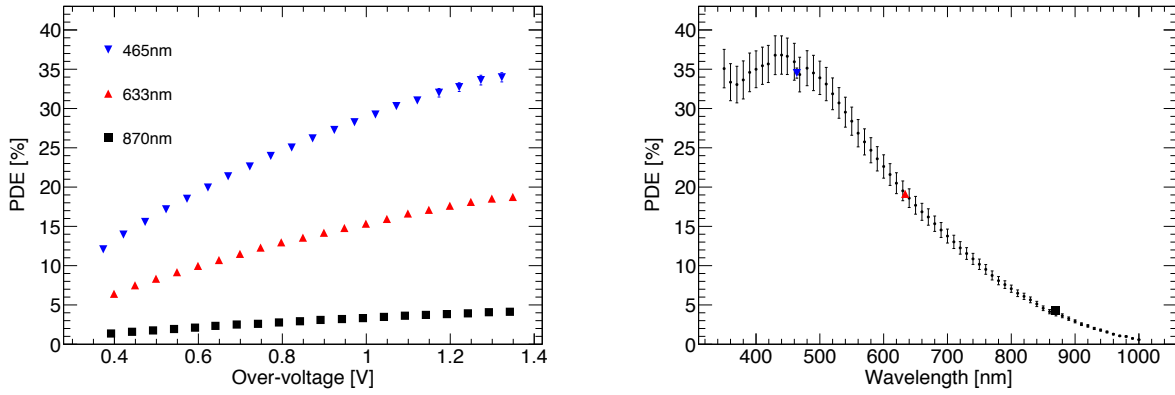


**Figure 4.27 – (left)** PDE of the Hamamatsu S10362-11-100C as a function of the applied over-voltage for different wavelengths of light. **(right)** PDE as a function of the wavelength at a fixed over-voltage of  $U_{\text{over}} = (1.3 \pm 0.05)\text{V}$ ; published in [4].

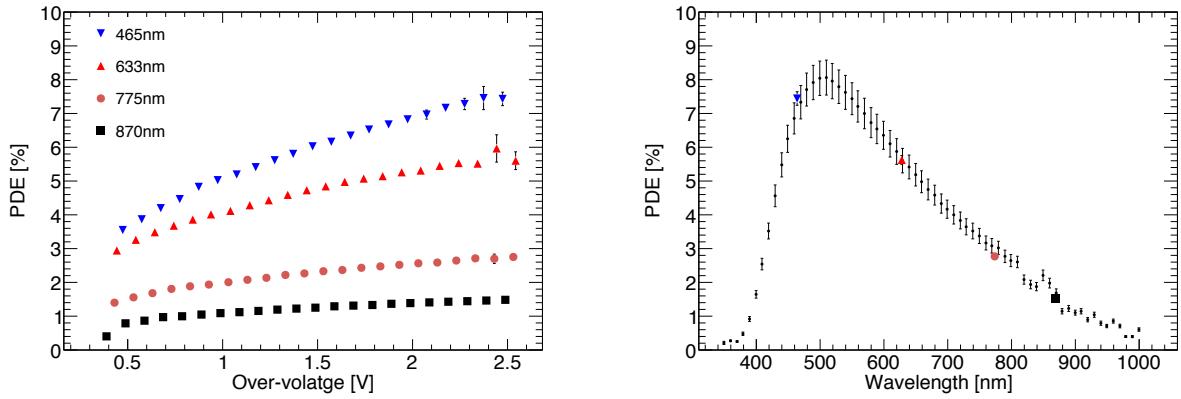


**Figure 4.28 – (left)** PDE of the SensL SPMMICRO1020X13 as a function of the applied over-voltage for different wavelengths of light. **(right)** PDE as a function of the wavelength at a fixed over-voltage of  $U_{\text{over}} = (2.5 \pm 0.05)$  V; published in [4].

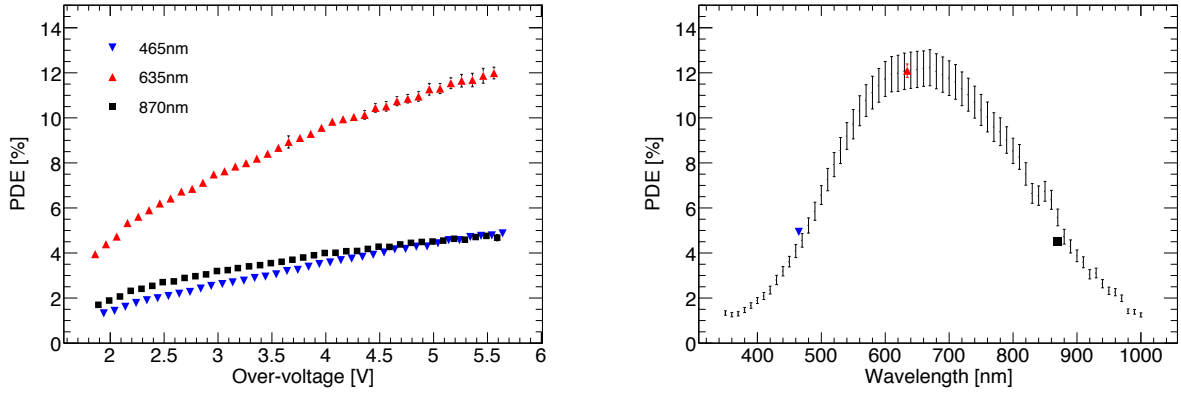


**Figure 4.29 – (left)** PDE of the MEPhI/Pulsar SiPM used in the AHCAL prototype as a function of the applied over-voltage for different wavelengths of light. **(right)** PDE as a function of the wavelength at a fixed over-voltage of  $U_{\text{over}} = (5.6 \pm 0.05)$  V.

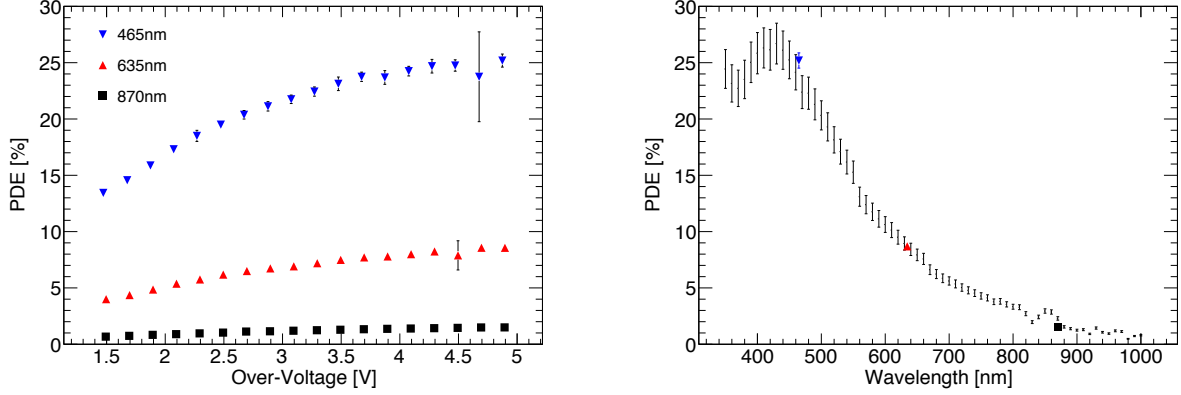


**Figure 4.30 – (left)** PDE of the Ketek SiPM as a function of the applied over-voltage for different wavelengths of light. **(right)** PDE as a function of the wavelength at a fixed over-voltage of  $U_{\text{over}} = (4.9 \pm 0.05)$  V.

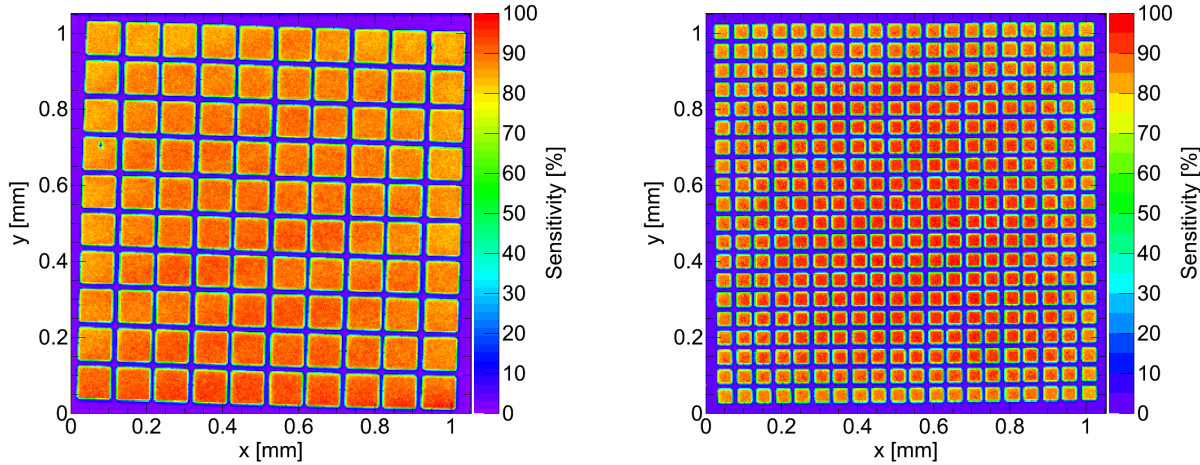


**Figure 4.31 – (left)** Sensitivity map of the S10363-11-100C ( $U_{\text{over}} = 1.1 \text{ V}$ ). **(right)** Sensitivity map of the S10362-11-050C ( $U_{\text{over}} = 1.3 \text{ V}$ ); published in [4].

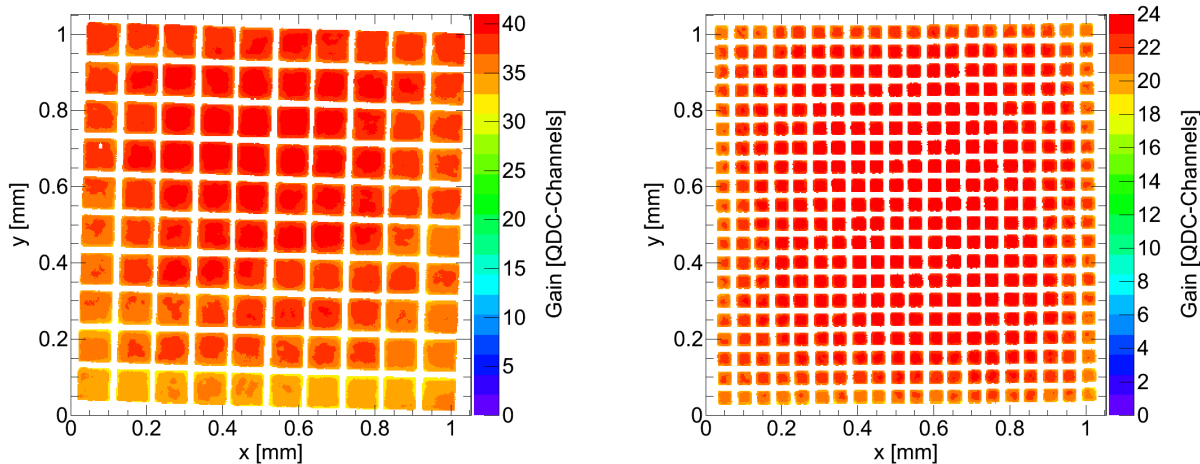


**Figure 4.32 – (left)** Gain map of the S10363-11-100C ( $U_{\text{over}} = 1.1 \text{ V}$ ). **(right)** Gain map of the S10362-11-050C ( $U_{\text{over}} = 1.3 \text{ V}$ ); published in [4].

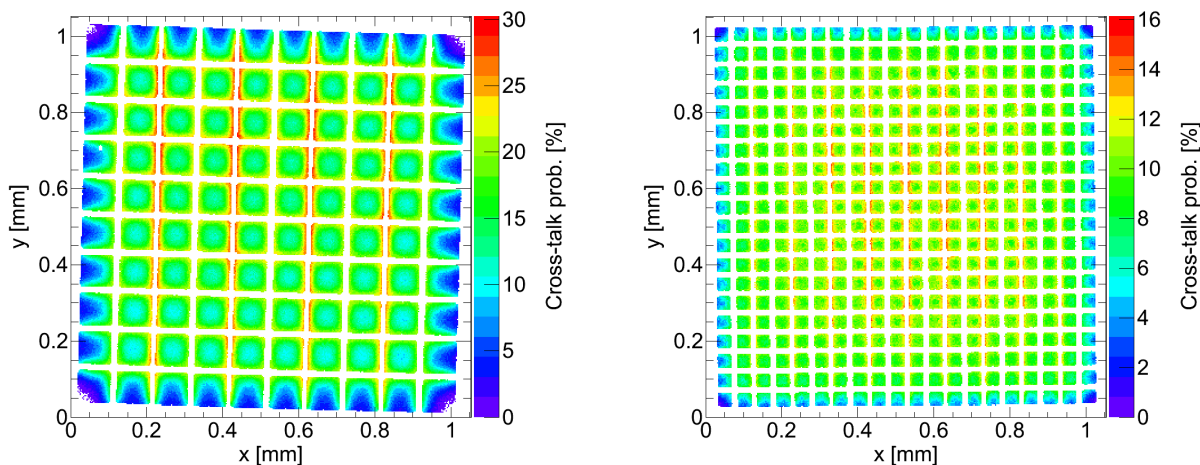


**Figure 4.33 – (left)** Cross-talk map of the S10363-11-100C ( $U_{\text{over}} = 1.1 \text{ V}$ ). **(right)** Cross-talk map of the S10362-11-050C ( $U_{\text{over}} = 1.3 \text{ V}$ ); published in [4].

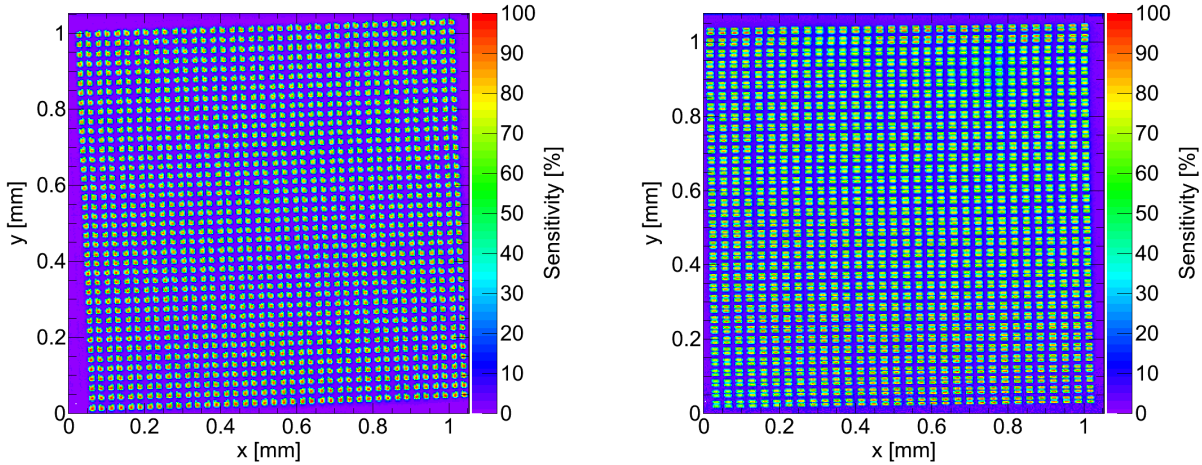


**Figure 4.34 – (left)** Sensitivity map of the S10363-11-025C ( $U_{\text{over}} = 2.3$  V). **(right)** Sensitivity map of the SPMMICRO1020X13 ( $U_{\text{over}} = 1.6$  V); published in [4].

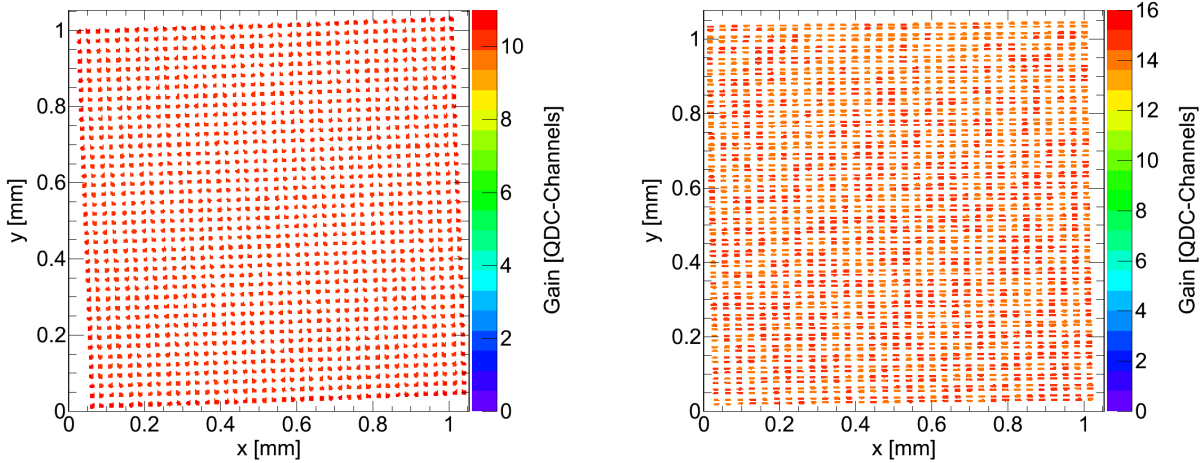


**Figure 4.35 – (left)** Gain map of the S10363-11-025C ( $U_{\text{over}} = 2.3$  V). **(right)** Gain map of the SPMMICRO1020X13 ( $U_{\text{over}} = 1.6$  V); published in [4].

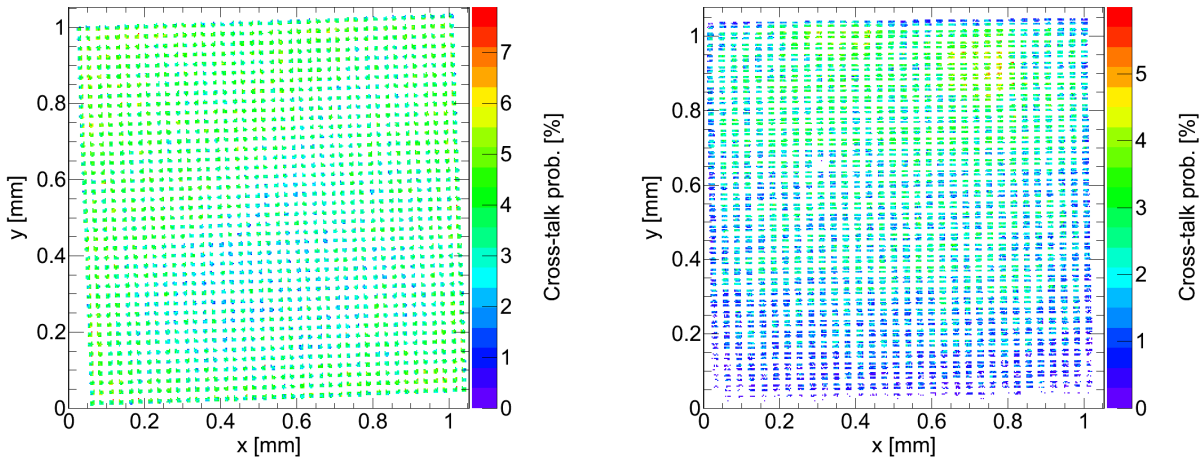


**Figure 4.36 – (left)** Cross-talk map of the S10363-11-025C ( $U_{\text{over}} = 2.3$  V). **(right)** Cross-talk map of the SPMMICRO1020X13 ( $U_{\text{over}} = 1.6$  V); published in [4].



# Chapter 5

## Construction and Commissioning of a Small-Scale PET Prototype

In the preceding sections, the general properties of silicon photomultipliers and the corresponding measurement principles were discussed. The properties found in the characterisation measurements are not only relevant for detectors in high energy physics experiments, but they are beneficial for a wide range of different fields of application. The high gain, the compactness, the insensitivity to magnetic fields, the excellent intrinsic time resolution, and the sensitivity to blue light makes the SiPM detector a promising candidate for the development of future detectors in *Positron Emission Tomography* (PET). First measurements concerning this application have been done within the scope of a diploma thesis [72]. The energy and timing resolution of small inorganic scintillator crystals made of LSO and LFS (cf. Table 1.3), coupled to blue sensitive SiPMs was measured. Excellent values, comparable to a classical photomultiplier tube readout have been measured. The positive results of this work motivated the following development of a small-scale PET prototype with silicon photomultiplier readout. The development and construction of this prototype was done at the *Kirchhoff Institute for Physics* in Heidelberg within the scope of this thesis. For the final commissioning of the readout electronics, the prototype was transported to the *Deutsches Elektronen Synchrotron* (DESY) in Hamburg, where also the first data were collected and the first images of radioactive source distributions were reconstructed.

This section gives a brief overview over the fundamental measurement principle in a PET detector, followed by a discussion of the important detector parameters such as the energy and timing resolution. In the following, the development, construction, and the commissioning of the small-scale PET prototype is described. The chapter concludes with a presentation of the first measurement and image reconstruction results obtained in a collaboration work.

### 5.1 Operation Principle of a PET Detector

Positron emission tomography denotes a non-invasive medical imaging technique which facilitates a visualisation of regions with an increased metabolic activity in a living organism. The reconstructed image of a PET scan provides information about the functional processes in a human body and is therefore complementary to the structural information obtained by other imaging techniques such as *computed tomography* (CT) or *magnetic resonance imaging* (MRI). The PET technique hence has become a powerful clinical tool for an early and precise diagnosis of cancer, and in the field of drug development.

Figure 5.1 shows a schematic description of a PET detector. The main components are detector elements arranged in a cylindrical shaped geometry around the body of the patient. In a classical PET device, these detector elements consist of scintillating crystals which are connected to photodetectors; usually photomultiplier tubes are used for that purpose. A positron

emitting radionuclide is incorporated into a biologically active substance – e.g. glucose – and injected into the body of the patient. After a short time, the concentration of the radionuclide will be increased in regions with an increased metabolism – e.g. cancer cells. The positrons are emitted with a certain energy distribution, depending on the used radionuclide. Table 5.1 lists the properties of some of the most commonly used radionuclide substances. The relatively short half life  $\tau_{1/2}$  of these substances – necessary in order to keep the radiation dose for the patient in a tolerable range – requires a cyclotron on-site for the production by means of proton-target collisions. The emitted positrons scatter in the surrounding tissue until they annihilate with an electron. The average traversed distance to the point of emission,  $R_{\text{mean}}$ , is one of the factors which fundamentally limits the spatial resolution of a PET detector. Typical values are listed in Table 5.1. The annihilation of the positrons goes along with the emission of two almost back-to-back photons, each carrying an energy of 511 keV. When these gamma rays are detected with the scintillating crystals within a short coincidence time interval of several nanoseconds, a so called *line of response* (LOR) is created by the reconstruction algorithm in between the corresponding detector elements. When a sufficient number of coincidence events is acquired, a three-dimensional image of the radionuclide distribution can be reconstructed; i.e. high concentrations of the substance are present in regions where a high density of lines of response is observed.

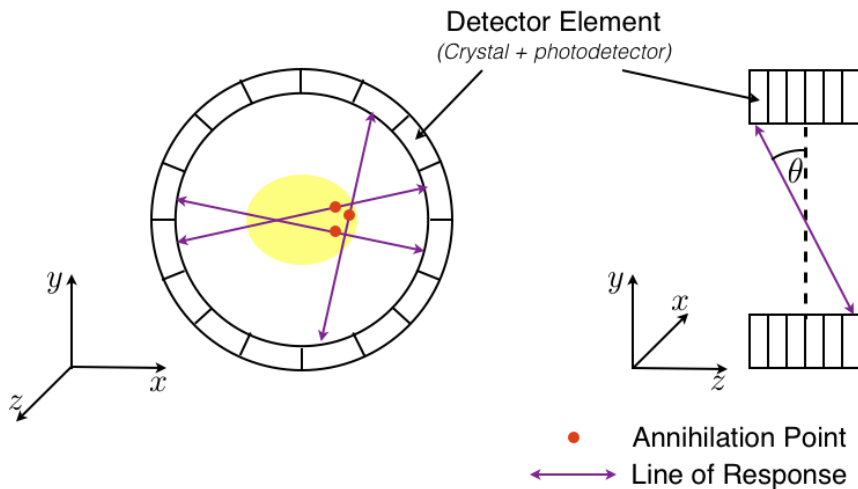


**Figure 5.1** – Schematic front and side-view of a PET detector. So called lines of response (LOR) are drawn in between two detector elements when two 511 keV photons are detected within a short coincidence time window.

**Table 5.1** – Properties of the most commonly used radionuclides in positron emission tomography.  $R_{\text{mean}}$  and  $R_{\text{max}}$  are the travelling distances of positrons before annihilation in water. The data have been taken from Ref. [85].

Radionuclide	$\tau_{1/2}$ [min]	$E_{\text{max}}$ [MeV]	$R_{\text{mean}}$ [mm]	$R_{\text{max}}$ [mm]
$^{15}\text{O}$	2.03	1.738	2.5	7.3
$^{13}\text{N}$	9.96	1.197	1.5	5.1
$^{11}\text{C}$	20.4	0.959	1.1	4.1
$^{18}\text{F}$	109.8	0.633	0.6	2.4

## 5.2 Time-of-Flight Method in PET

In a conventional PET detector, the actual position of the annihilation positron in a coincidence event is unknown. The only information available is that the annihilation point must lie somewhere on the reconstructed line of response. In case of the *time-of-flight PET* (TOFPET) method, a precise measurement of the arrival times of photons belonging to one coincidence event is used to reconstruct the approximate region of positron annihilation. It can be shown (for example in Refs. [72, 85, 86]) that the uncertainty of the reconstructed position  $\Delta x$  is related to the time resolution of the scintillator-photodetector system by the equation

$$\Delta x = \frac{c \cdot \Delta t}{2}, \quad (5.1)$$

where  $c$  denotes the speed of light. The equation shows, that in order to achieve a time-of-flight based position resolution  $\Delta x$ , which is comparable to the typical spatial resolution of a commercial PET system of roughly 5 mm, a coincidence time resolution of better than 50 ps would be required [87]. Such values are, however, out of scope of todays possibilities. Nevertheless, also slightly worse time resolutions allow for a significant improvement of the image signal-to-noise ratio as, sketched in Figure 5.2. Only the points on a LOR which lie within the position uncertainty  $\Delta x$  based on the time-of-flight measurement are considered for the image reconstruction. A timing resolution of  $O(500\text{ ps})$ , achievable with todays fast scintillators and photodetectors, hence provides a significant improvement of the image quality as shown for example in [88].

The TOFPET concept is not new, it has already been investigated in the 1980s. However, the only sufficiently fast scintillating crystal, BaF<sub>2</sub> (cf. Table 1.3), available by that time imposed some major constraints on the usefulness of the developed PET detectors. It is highly hygroscopic and the peak emission wavelength of the fast scintillation component lies in the ultraviolet part of the spectrum which makes an efficient detection with standard photodetectors difficult. Nevertheless, the fast signal decay times of newly developed inorganic scintillators such as LSO, LaBr<sub>3</sub> and LuAG in combination with the good timing properties of the SiPM have caused a reconsideration of this measurement technique during the last years.

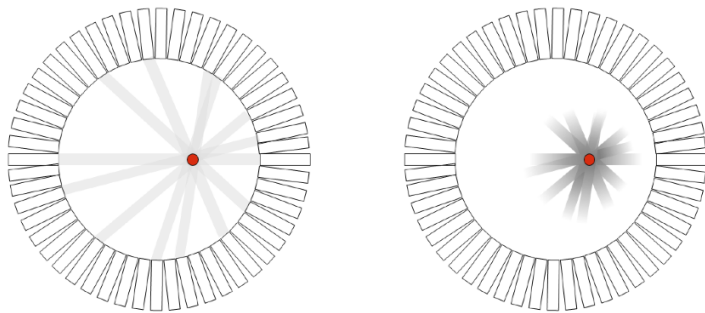


**Figure 5.2** – Schematic representation of the fundamental image generation process in a conventional and a time-of-flight based PET detector. Dark regions indicate the reconstructed positions with an increased probability for positron annihilation. In conventional PET, no information about the annihilation position is available. Hence, the noise variance of each point on the LOR propagates into the reconstructed image and causes a deterioration of the signal-to-noise-ratio. In case of TOFPET, only the points on the LOR which lie within the position uncertainty, determined by the timing resolution, are considered for the image reconstruction.

### 5.3 Background Reduction

Background effects – caused by the undesired physical interactions described below – are responsible for a significant deterioration of the achievable spatial resolution and signal-to-noise ratio of the reconstructed image. It is hence an important task of a PET detector to efficiently discriminate these background events without loosing valuable measurement data. In the following, the most important classes of background events will be introduced and methods capable to reduce these effects will be discussed.

In Figure 5.1, the ideal case of the gamma ray coincidence measurement is indicated. The reconstructed LORs exactly match the annihilation point which is considered as the ‘true’ position of the radionuclide. In reality, however, the annihilation position may be shifted due to the finite distance the positron can travel before it collides with an electron and creates two gamma rays. There is no possibility to determine this distance experimentally. Hence, in order to reduce this effect, and thus improve the spatial resolution, radionuclide substances with a characteristically small positron emission energy, and correspondingly with a small range parameter have to be used (see Table 5.1). A small emission energy provides a second advantage as it improves the co-linearity of the emitted gamma rays.

Besides these irreducible effects, there are several background effects which can be discriminated by means of a precise energy and time measurement. In Figure 5.3 two classes of such background events are presented.

#### Scattered coincidences – Energy Resolution

In case of the ‘scattered coincidence’ events, at least one of the 511 keV gamma rays from the positron annihilation is Compton scattered off an electron from the surrounding tissue before it is detected by one of the detector elements. Both detector signals are interpreted as a coincidence event and a LOR is drawn between the corresponding detector elements. This line of response, however, does not reflect the true position of the positron annihilation and hence causes a deterioration of the spatial resolution of the reconstructed image. However, as a fraction of the energy is transferred to the Compton electron in this process, the energy of

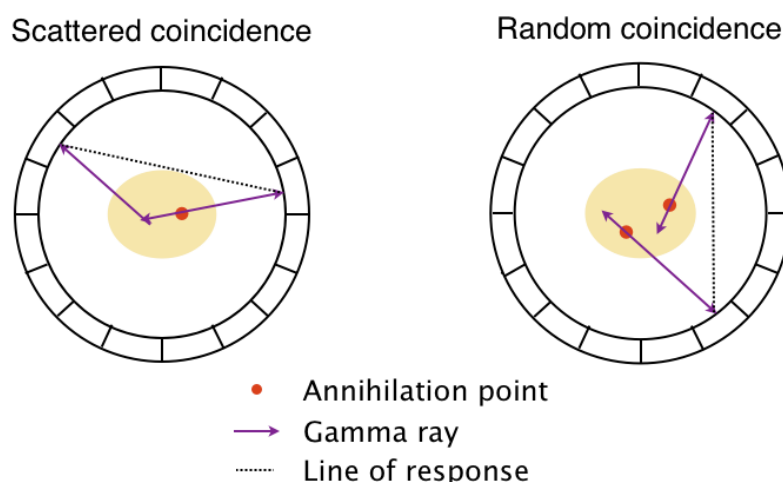


**Figure 5.3** – Two important classes of background events which can be reduced by means of precise energy-, and time-measurement of the gamma rays from the positron annihilation.

the gamma ray is reduced. If the gamma ray energy can be measured with high precision, this class of background events can be discriminated by applying a minimum threshold for the detected gamma ray energy. The effectiveness of this selection is mainly determined by the energy resolution of the combined crystal-photodetector system which is described by the following formula:

$$\frac{\sigma_{\text{scint}}}{E} \approx \frac{1}{\sqrt{N}} \oplus \sigma_{\text{intr}} \oplus \frac{\sigma_{\text{noise}}}{E} \quad (5.2)$$

The first term describes the statistical Poisson variation of the number of detected photons  $N$ . By choosing a photodetector which matches the emission spectrum of the scintillator, the contribution of this term can be reduced. SiPM detectors are well suited for the detection of the scintillation light of inorganic crystals, e.g. LSO, LaBr<sub>3</sub> or LuAG. In section 4.6 it was shown that the most recent devices have a high photon detection efficiency in the blue and green spectral range, matching the peak emission wavelength of these scintillators, which are indicated in Table 1.3.

The second term in Equation 5.2 describes the intrinsic energy resolution of the specific scintillator which is determined by several effects. The size of the crystal has an impact as photons produced at different positions in the scintillator have to travel different distances before they reach the photodetector, which results in a variation of the signal height. Secondly, the intrinsic non-linear response of most scintillators creates an additional signal variation as the total energy deposition of the incident gamma ray can be done in a single-, or a multi-step process; e.g. (multiple) Compton scattering followed by photoelectric absorption. In addition, the intrinsic energy resolution is deteriorated if inhomogeneities or impurities are present in the scintillator crystal, caused by an imperfect production process. The intrinsic energy resolution depends on the specific type of scintillator. A typical value for LSO crystals is  $\sigma_{\text{intr}} \approx 9\%$  [89].

The last term of Equation 5.2 comprises the influence of the noise, e.g. the thermal dark-rate of the photodetector, or the signal fluctuations caused by the readout electronics (amplifiers).

## Random Coincidences – Time Resolution

On the right of Figure 5.3, an example of a ‘random coincidence’ event is schematically illustrated. Two uncorrelated photons hit the scintillating detectors within a time window, smaller than the coincidence time window ( $2\tau$ ). The observed rate of random coincidence events is proportional to the coincidence time window  $R_{\text{random}} \propto 2\tau \cdot A$ , where  $A$  is the activity present in the scanner field of view. Hence, the most effective way of reducing  $R_{\text{random}}$  is the selection of a shorter coincidence time window. For this purpose, a good time resolution is required for the suppression of random coincidence events. However, it should be emphasised that the minimum value of  $2\tau$  is determined by the diameter of a whole body PET scanner of typically 1 m. Considering the speed of light, a photon requires about 3.3 ns in order to traverse the detector field of view. Hence, the coincidence time window of most PET scanner must be larger than this value. Even if a timing resolution of smaller than  $O(1\text{ ns})$  is achieved, the random coincidence rate cannot be further reduced. The motivation for timing resolutions in the sub nanosecond regime is therefore not a suppression of random coincidences, but the improvement of the image signal-to-noise ratio by means of the time-of-flight PET method.

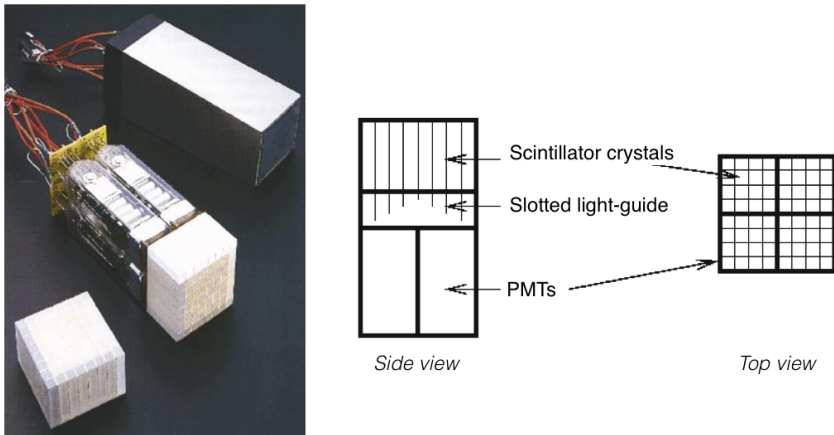


**Figure 5.4** – Example of a block-detector readout scheme based on the Anger positioning algorithm (e.g. Ref. [90]). The crystal array is connected to four PMTs via a slotted light guide. The gamma ray interaction position is determined by means of a weighting algorithm. The figure has been reprinted (modified) from Ref. [85].

## 5.4 Classical Detector Module Design

The detector modules of a PET scanner consist of scintillating crystals connected to a photodetector. The most commonly used photodetector is the photomultiplier tube as it has been available for a long time and it allows for a reliable measurement of the scintillation light signals without the demand for sophisticated signal amplification. Several light collection schemes have been developed in order to connect the PMTs to the scintillator crystals.

A connection scheme used in a variety of commercial PET detectors is the block-detector readout indicated in Figure 5.4. In the shown example, a densely packed array of individual scintillating crystals is coupled to four  $24 \times 24 \text{ mm}^2$  PMTs via a slotted light guide. The space in between the individual crystals is filled with a highly reflective material in order to concentrate the light signal to one single PMT channel. The position of the gamma ray interaction is determined by means of a weighting scheme, calculating the signal centre of gravity. This can in principle also be achieved with a single continuous crystal connected to several PMTs. However, the main advantage of the shown crystal array design is the reduced channel dead-time, as the light spread between the individual PMTs is largely reduced; i.e. a signal on one PMT of the array does only induce a negligible small signal in the neighbouring PMT which hence remains sensitive for the detection of an additional coincidence event. A small dead time increases the sensitivity of the PET detector and hence facilitates shorter scan times and correspondingly lower patient radiation doses.

In the so called ‘direct coupling’ scheme, the PMT is directly glued to an individual scintillating crystal. A complete PET detector is obtained by putting many of these modules, densely packed in a cylindrical layout. Very short dead times of each detector element can be achieved by the fact that each readout channel is operated completely independent. However, the spatial resolution achievable with this coupling scheme – using traditional PMTs – is limited as the size of these devices constrains the crystal size to values larger than  $\sim 2 \times 2 \text{ cm}^2$ . Hence, more compact photodetectors have to be used in order to improve the spatial resolution. Avalanche photodiodes fulfil the compactness requirement as they can be produced in densely packed arrays. However, the relatively low gain of these devices requires a sophisticated amplification of the electronic signals which complicates the detector design and increases its manufacturing cost.

Silicon photomultipliers have the same compact design as APDs and are therefore well suited for the direct coupling scheme. In addition, they provide a high internal signal amplification which reduces the complexity of the readout electronics. The development and construction of such a SiPM based coupling scheme using small scintillating crystals is described in the following.

## 5.5 Construction of a PET Detector with SiPMs

Figure 1.2 shows an example of one scintillating crystal, and one PET detector module developed within this work. In the following, the development and construction of the individual components of these detector modules will be discussed.

### Scintillating Crystals

For the development of the PET prototype *Lutetium Fine Silicate* (LFS) scintillating crystals are used [30]. The properties are listed in Table 1.3 together with some of the most common inorganic scintillators used in PET and electromagnetic calorimetry. The characteristics of LFS are very similar to the ones of LSO; the main difference – according to Ref. [30] – is the better uniformity of the scintillation parameters such as the light yield achieved in the production process.

In a previous study, the energy resolution of LFS crystals of the size  $3 \times 3 \times 15 \text{ mm}^3$  was measured and compared to the value achieved with LSO crystals of the same dimensions [72]. Almost identical values for the energy resolution of  $\Delta E/E \approx 10 - 11\% \text{ FWHM}$  have been found, which motivated the use of LFS crystals for the construction of the small-scale PET prototype described here.

Approximately 100 scintillating crystals of the dimensions specified above have been purchased. The first step was the measurement of the exact crystal sizes, which are important for the correct dimensioning of the PET detector module. For this purpose, a subset of 25 randomly selected scintillating crystals have been characterised. The result of this measurement is presented in Figure 5.5 which indicates the width and the length distribution of the crystal dimensions. In order to make sure that the majority of scintillating crystals fits into the detector modules, these variations had to be taken into account.

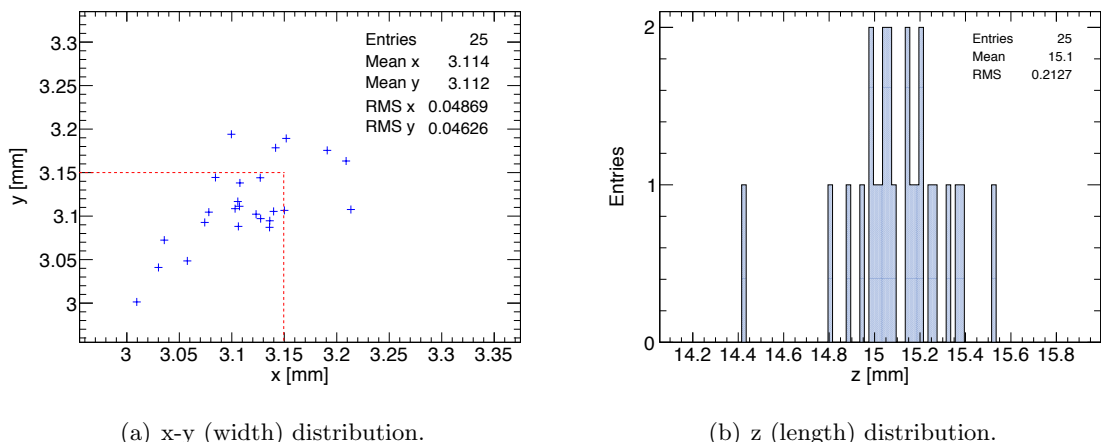
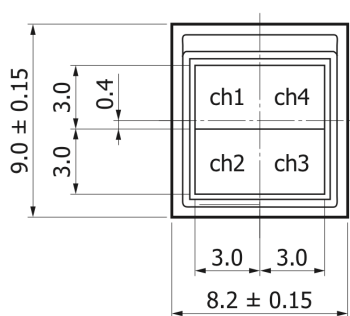


**Figure 5.5** – Measured distributions of the scintillating crystal dimensions. The dashed line in figure (a) indicates the chosen size of the crystal cavities in the detector module.

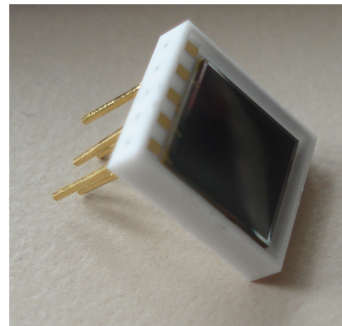
## MPPC Arrays

Blue sensitive SiPMs from Hamamatsu of the type S10985-050C are used to measure the light produced in the scintillating crystals. Each of the sensors consist of an array of  $2 \times 2$  individual MPPC detectors, each having 3600 pixels with  $50 \mu\text{m}$  pixel pitch on an active area of  $3 \times 3 \text{ mm}^2$ . The PDE of the device is expected to be similar to the S10362-11-050C presented in Figure 4.26, since the pixel pitch, and correspondingly the geometrical efficiencies  $\epsilon_{\text{geo}}$  are identical. The schematic layout and a photograph of the MPPC array is shown in Figure 5.6.

There is no spacing in between the individual channels of the array, hence, one of the main challenges was the development of a suitable crystal connection scheme which directs the scintillation light efficiently onto the active area of the corresponding MPPC channel such that most of the photosensitive area is used.



(a) Layout of the MPPC array.



(b) Picture of the MPPC array.

**Figure 5.6** – Figure (a) shows the geometrical layout of the MPPC array, taken from Ref. [84]. No insensitive space is left in between the individual channels of the array. Figure (b) shows a photograph of the MPPC array.

## Detector Modules

For an efficient direct light coupling, the individual scintillating crystals have to be separated optically from each other and must be carefully aligned on the active area of the SiPM array. The separating material must have a high reflectivity in the spectral region of the scintillator emission such that a large fraction of the scintillation light is guided to the active area of the MPPC. In addition, the structure should provide a sufficient mechanical stability such that several of the modules can be stacked together in order to create a larger detector. For these reasons, aluminium was chosen as the production material. A detail of the drawing of the developed module structure is presented in Figure 5.7(a). Taking into account the width distribution of the available scintillator crystals shown in Figure 5.5, it was decided to produce the opening for the crystals with a side length of 3.15 mm. In this way it is assured that most of scintillating crystals fit into the opening. Since the crystals can stick out at one side of the module, the depth of the crystal cavities was set to 15 mm. The thickness of the crystal separating walls was set to 0.2 mm; the process of electric discharge machining which was used for the production of the complex structure of the modules cannot create exact square corners as the metal wire used for the machining has a finite diameter of 0.35 mm. Hence, slightly more material had to be removed in the corners as indicated in Figure 5.7(a). In order to provide the required mechanical stability, a minimum of  $\sim 0.1 \text{ mm}$  material thickness is required, hence a wall thickness of 0.2 mm has been chosen as indicated in the figure.

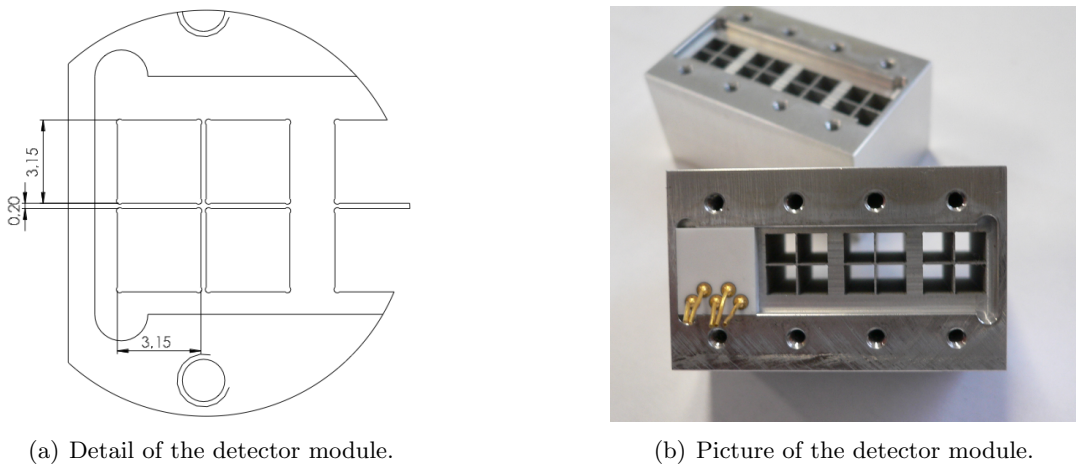


**Figure 5.7** – Figure (a) shows the drawing of a detector module detail (leftmost channel). Dimensions are in millimetres. Figure (b) shows a photograph of the final detector module made of aluminium, equipped with a single MPPC array. In total 4 MPPC arrays can be inserted, resulting in a total number of 16 readout channels.

Due to the average crystal width, slightly larger than 3 mm (cf. Figure 5.5), not the full crystal surface is connected to the corresponding MPPC. In addition, the finite thickness of the aluminium layers in between the crystals causes that a small fraction of the MPPC area remains unused. However, a geometrical calculation shows that more than 84 % of the crystal surface is directly connected to the active area of the photosensor.

In order to test the light collection capabilities of the specified aluminium detector module, the energy resolution for 511 keV gamma rays from a  $^{22}\text{Na}$  source was measured for a number of channels [91]. The average value found,  $\Delta E/E = 14\%$  FWHM, is only slightly worse compared to what is achieved with a teflon wrapped crystal,  $\Delta E/E = 10 - 11\%$  FWHM [72]. The difference is expected to be due to the reduced reflection properties of the aluminium as compared to the teflon tape. Also the slight misalignment described above is expected to have an influence on the result. However, the achieved energy resolution is still absolutely sufficient for an efficient discrimination of the Compton background.

### Construction of the Small Scale PET Prototype

In Figure 5.8(a), the conceptual idea of the PET prototype is shown. The design is based on two detector modules, rotating around a  $^{22}\text{Na}$  test-source, placed in the detector field of view. The concept of rotating detector modules is not new, instead it leads back to the first generation of PET detectors. The advantage of such a design is that only two detector modules are required in order to emulate a completely equipped detector ring. However, the drawback is the smaller sensitivity as the geometrical acceptance of the two detector heads is strongly reduced compared to a fully equipped detector ring. Hence, the information carried by the undetected photons is lost. As a consequence of the small sensitivity, long scanning times are required which results

in higher patient radiation doses. For this reason, rotating PET detectors are not used in clinical applications anymore. However, the concept allows for a flexible investigation of different detector configurations and remains therefore useful for scientific (non-clinical) purposes.

The following key parameters have been specified for the detector prototype:

- The detector radius  $r$  should be adjustable continuously from 3 cm up to 18 cm. The accuracy of the radial positioning should be  $\delta r \approx 0.1$  mm.
- The angle  $\phi$  between the opposing detector elements should be adjustable continuously from  $120^\circ$  to  $240^\circ$  with a precision of  $\delta\phi \approx 0.1^\circ$ . In this way it should be possible to mimic different detector configurations.
- The rotation (scanning) of the whole detector around the test-source in the middle should be automated and controllable by the lab-computer with a precision of  $\approx 0.01^\circ$ .
- The sources should be positioned in the centre and must not rotate with the detector elements.

A prototype detector which meets these requirements was developed in cooperation with the workshop of the *Kirchhoff Institute for Physics* (cf. Figure 5.8(b)). The construction is based on an aluminium plate which serves as a basis for the detector modules, movable in the radial and the  $\phi$ -direction. The plate is mounted on a precision rotation stage<sup>1</sup> which allows for completely automated scans with a precision of  $0.02^\circ$  over the full rotation range of  $360^\circ$ . Both, the aluminium plate, as well as the rotation stage feature a clear aperture of 120 mm which facilitates a flexible positioning of the source.

After the completion of the prototype construction, it was transported to DESY in Hamburg, where the final commissioning of the readout electronics was carried out. Photographs of the fully equipped system are presented in Figure A.12. In the present configuration, the MPPC signals are processed using a 16-channel 10-bit Flash ADC board with 100 MHz sampling frequency (ADCM-16). This type of readout represents only an intermediate solution as the timing capabilities of the described readout board are not sufficient for the envisaged investigation of the TOFPET method. With this readout, a time resolution of 870 ps FWHM has been measured which is below the capabilities of the fast scintillating crystals and SiPMs.

A possibility for a future readout of the MPPC signals is provided by the *SiPM timing chip* (STiC), dedicated for fast timing measurements in PET [92, 93]. With the first prototype of the chip already a coincidence timing resolution of 480 ps FWHM has been measured using teflon wrapped LFS crystals and  $3 \times 3 \text{ mm}^2$  MPPCs. In order to improve the timing resolution the chip design is currently further developed.

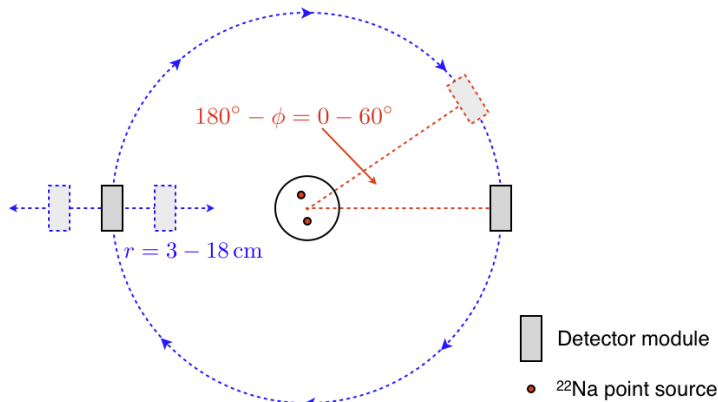
## 5.6 First Results

The following section provides a brief overview over the first measurement results obtained with the PET prototype. The emphasis is mainly put on the actual measurement results. A more detailed description of the measurement techniques and the used software tools is for example provided in [91].

For the results presented here, only the signals of eight of the 16 available scintillator channels of each detector module (lower crystal row) are read out. The angle between the opposing detector elements was fixed to  $180^\circ$ . The SiPM bias voltage is supplied by means of a USB

---

<sup>1</sup>MICOS, PRS-200.



(a) Sketch of the PET prototype.



(b) Photograph of the PET prototype.

**Figure 5.8** – Figure (a) shows the conceptual drawing of the PET prototype. It consists of two detector modules which can be rotated around a distribution of test sources positioned somewhere in the field of view. The distance, as well as the relative angle between the detector elements can be adjusted in the specified ranges in order to allow flexible investigations of different detector configurations. Figure (b) shows a photograph of the assembled PET prototype.

based multi-channel high voltage power supply which has a temperature sensor implemented, facilitating automatic bias voltage correction to compensate long term gain shifts of the SiPMs. Two  $^{22}\text{Na}$  point sources are placed in the centre of the device with a distance of  $\sim 1\text{ cm}$ . Each of the two sources has an activity of  $1\text{ MBq}$ . The signal charge as well as the timing information is determined using the ADCM-16 readout module. The readout is triggered if the signal of the corresponding channel exceeds a certain threshold. The Compton background is rejected by considering only detector hits with an integrated charge within two sigma of the photo-peak. Coincidence events are created if the time difference between two signals is smaller than  $2\text{ ns}$ . Finally, a two dimensional image is reconstructed applying a filtered back-projection algorithm using a ramp filter with a frequency cutoff [91].

Several measurement have been carried out using different settings of the scan parameters. A complete detector scan is defined by four parameters: the radial position of the detector modules  $r$ ; the number of measurement positions  $n$ ; the size of a single step in degree  $\Delta\Phi$ ; and the measurement time at each position. A summary of the different scan parameters is listed in Table 5.2. An example of a reconstructed image of the two point like test-sources is presented in

Figure 5.9(a). The two sources can be easily identified and are well separated from each other. Figure 5.9(b) shows the projection of the reconstructed image along the x-axis. A Gaussian function is fitted to the data in order to determine the spatial resolution which amounts to 2.5 mm FWHM in the displayed example. This good result achieved demonstrates the high potential of the developed highly granular PET detector with direct SiPM readout. Further studies are planned which involve the TOF method by using signal readout electronics – e.g. the STIC chip – with a much better timing performance.

**Table 5.2** – Summary of the different scan parameter settings and achieved spatial resolution as presented in Ref. [91].  $r$  denotes half the distance between the two detector modules (scan radius),  $n$  is the number of measurements carried out and  $\Delta\Phi$  indicates the angular steps in between the individual measurements.  $T$  denotes the measurement time at each position.

$r$ [mm]	$n$	$\Delta\Phi$ [ $^\circ$ ]	$T$ [min]	Resolution FWHM [mm]
90	20	9	10	2.5
90	10	18	10	2.5
180	21	8.5	20	2.3

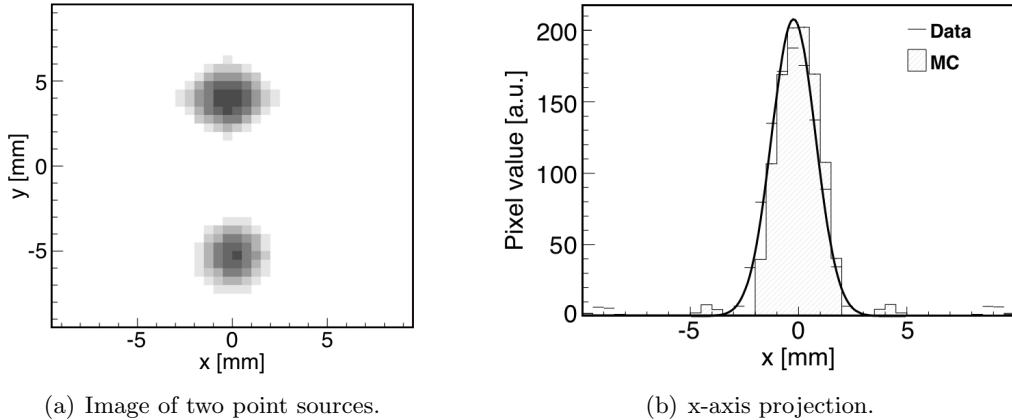


**Figure 5.9** – Figure (a) shows the reconstructed image of two point sources (1 mm in diameter) placed in the centre of the PET prototype. Figure (b) shows the projection of the reconstructed image along the x-axis. From a Gaussian fit to the distribution, a spatial resolution of 2.5 mm FWHM has been derived. The figure also includes the prediction of a Monte Carlo simulation of the PET prototype. The figures have been taken from Ref. [91].

# Chapter 6

## Conclusion

The presented work deals with the fluorescence light signals created in organic and inorganic scintillators, and their detection with *silicon photomultipliers* (SiPM). Two different fields of application are studied: imaging hadron calorimetry for future electron-positron colliders, and the medical imaging technique of positron emission tomography.

In the applications investigated, SiPMs are used to measure the weak light flashes produced in a scintillator, thus enabling an energy determination of the incident particle or radiation. If the specific energy loss  $dE/dx$  of a particle is large, the relation between the deposited energy and the created scintillation light output reveals a deviation from linearity, which is described by Birks' coefficient  $kB$ . In this work, a measurement of  $kB$  for the polystyrene based scintillator tiles of the *analogue hadronic calorimeter prototype* (AHCAL) was presented and a significantly larger value,  $kB = (0.151 \pm 0.07) \cdot 10^{-2}$  cm/MeV, has been found compared to the default value applied within the Geant4 calorimeter simulation of  $kB = (0.07943 \pm 0.0142) \cdot 10^{-2}$  cm/MeV. A comparison of the measured scintillator light output with the one predicted by the simulation shows that the present Geant4 implementation of Birks' law is – independent from the chosen  $kB$  – only valid for sufficiently high particle energies. An improved method is presented which takes into account the energy dependence of the specific energy loss  $dE/dx$ , thus describing the scintillator response more precisely. The measured  $kB$  and the improved implementation of Birks' law reduce the simulated scintillator response of the AHCAL for electromagnetic particle showers by  $\sim 2.3\%$ . In case of hadronic showers, the reduction amounts to  $4 - 5\%$ , depending on the incident particle energy. These corrections are significant, considering the overall quenching effect described by Birks' law and thus demonstrate the importance of the presented results.

In order to identify suitable sensors for the analogue hadronic calorimeter prototype, medical imaging, or other applications, and to gain a deeper understanding of the specific device properties, an experimental test environment was developed and constructed. It allows to measure a large variety of different SiPM characteristics, including the photon detection efficiency without the biasing contributions of cross-talk and after-pulses, and the spatial uniformity of the SiPM pixel response. Sensors, produced by several companies have been characterised and the results have been published [4]. As expected, SiPMs with a p-on-n structure have a larger photon detection efficiency for blue light compared to n-on-p devices. The measured photon detection efficiency of the Hamamatsu MPPCs is significantly smaller compared to the reference values quoted by the producer; the estimated deviation ranges between 24 % and 43 %. A difference is expected as the producers values include the contributions of cross-talk and after-pulses. This result underlines the necessity of the developed test environment. A high spatial uniformity of the SiPM pixel sensitivity and gain has been measured, whereas the optical cross-talk probability depends as expected on the number of neighbouring pixels. The determined geometrical efficiencies of the tested devices cover the range from 21 % for the highest pixel densities up to 74 % for lowest pixel densities. These values are compatible with the reference data quoted by

the manufacturers.

A small-scale PET prototype was developed and constructed. It uses SiPMs to readout the scintillation light created in miniaturised arrays of scintillating crystals. The prototype consists of two opposing detector modules which are rotated around the field of view, thus emulating a full detector ring. First characterisation measurements of the system are presented. The average energy resolution amounts to  $\Delta E/E = 14\%$  FWHM, which is sufficient for the required suppression of the background caused by scattered coincidence events. A spatial resolution of 2.5 mm FWHM has been determined by reconstructing two point sources with a distance of  $\sim 1$  cm placed in the centre of the device field of view. The results obtained demonstrate the high potential of such highly granular PET detectors, enabled by the compact SiPM dimensions.

# **Appendix**



# Appendix A

## Supplementary Material

### A.1 Measurement Setup for Birks' Coefficient

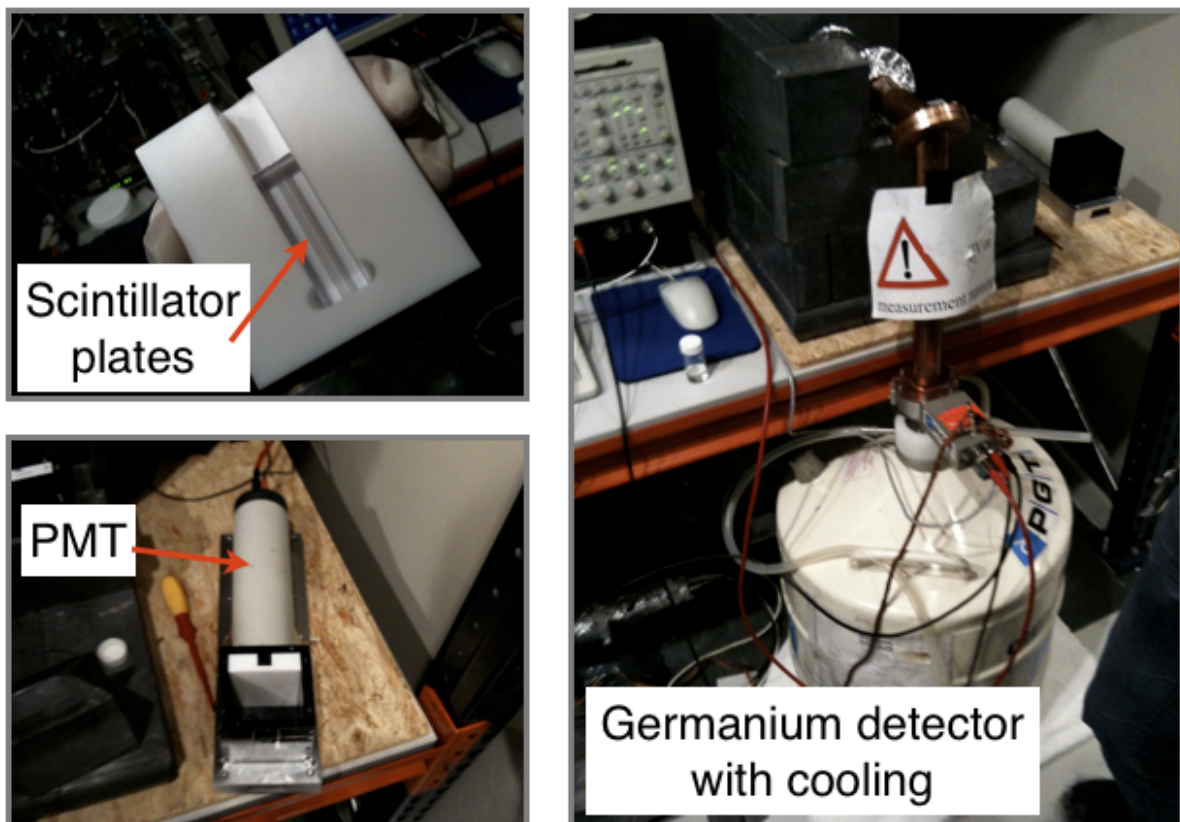


**Figure A.1** – Pictures of the experimental setup used for the measurement of Birks' coefficient. The upper left picture shows the polished scintillator plates inserted into a teflon block. The teflon block is then connected to a photomultiplier tube as shown on the lower left picture. The right picture shows the germanium detector and the corresponding liquid nitrogen cooling system. The radioactive source is positioned behind the lead bricks in the upper part of the picture.

## A.2 Germanium Detector Calibration

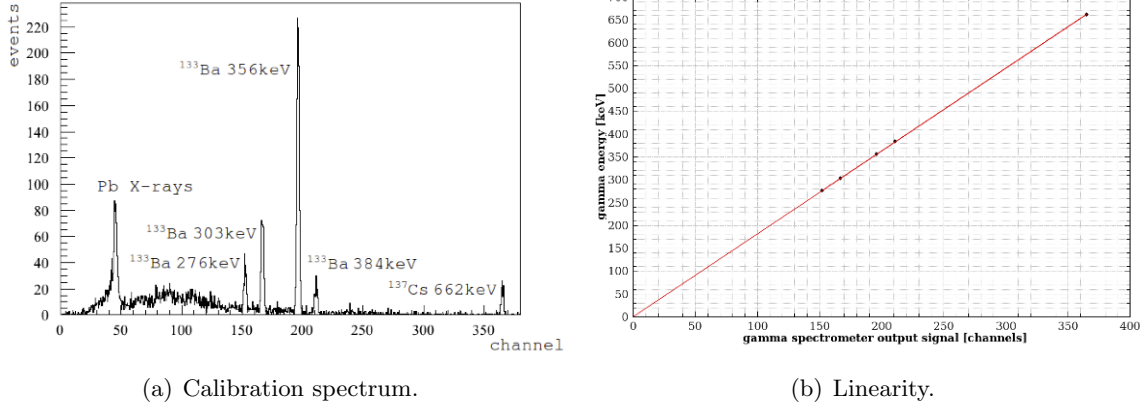


**Figure A.2** – Figure (a) shows a typical calibration spectrum recorded with the germanium detector before and after a measurement run. The individual energy lines of the different radioactive sources can be measured with high precision. Figure (b) shows the measured linearity of the germanium detector from which the calibration factor (slope) is determined. The figures have been taken from Ref. [44].

## A.3 Light Yield Measurement

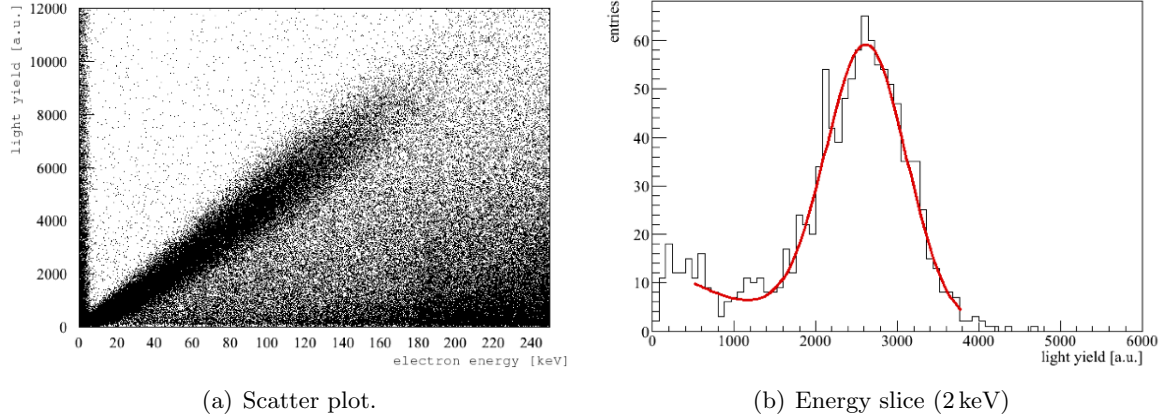


**Figure A.3** – Figure (a) shows the measured PMT amplitude as a function of the electron energy deduced from the measurement with the germanium detector. Figure (b) shows light yield distribution of a 2 keV wide energy bin. A gaussian is fitted to the peak in order to determine the position. The events on the left of the peak are background. The figures have been taken from [45].

## A.4 Simulation of the Test-beam Environment with MOKKA

The object oriented Geant4 simulation toolkit provides the basis for the simulations. Different physics processes can be activated by the use of different physics lists. In order to implement the large variety of materials, the detector geometry and the beam-line configuration into the Geant4 simulation program, the MOKKA<sup>1</sup> software is used [49]. Different detector models, such as the complete ILD detector or different test-beam configurations are available for simulation. The required information for each model is read from a central database. A schematic view of the CERN 2007 test-beam configuration, used for the present simulation study, is shown in Figure A.4. The particle beam enters from the left side, along the  $z$ -axis. Before the beam enters the calorimeter system, it traverses a variety of other detectors used to determine the important beam parameters. The detectors can be grouped into four systems:

### 1. Cerenkov counter

The particles provided by the beam-line are filtered to have equal momentum. However, the beam may still contain particles of different mass. In order to make sure, that only the selected particle type is used in the analysis of the calorimeter data, the Cerenkov detector is used. It consists of a vessel filled with a gas mixture. The refractive index is controlled by the gas pressure. By measuring with a photomultiplier tube whether Cerenkov light is produced, or not, it is possible to determine whether the mass of a particle is below, or above a certain threshold.

### 2. Trigger system

The system is used to determine the precise time of particle passage, which triggers the readout of the calorimeter signal. The detectors Sc1 and Sc3 are made of plastic scintillator plates and have a size of  $10 \times 10 \text{ cm}^2$ . Each scintillator plate is read out by a fast photomultiplier tube. A coincidence of both detectors generates the main trigger.

The Sc3 detector, sometimes referred to as ‘multiplicity counter’, has a larger size of  $20 \times 20 \text{ cm}^2$ . An event receives a multiplicity tag, if the measured signal is significantly larger than the signal of a single minimum ionising particle. This can for example be caused if the primary beam particle undergoes an interaction – creating secondary particles – before it reaches the trigger system. With the information provided by the Sc3 detector, these events can be excluded from the data in the offline analysis.

<sup>1</sup>Software version 7.02

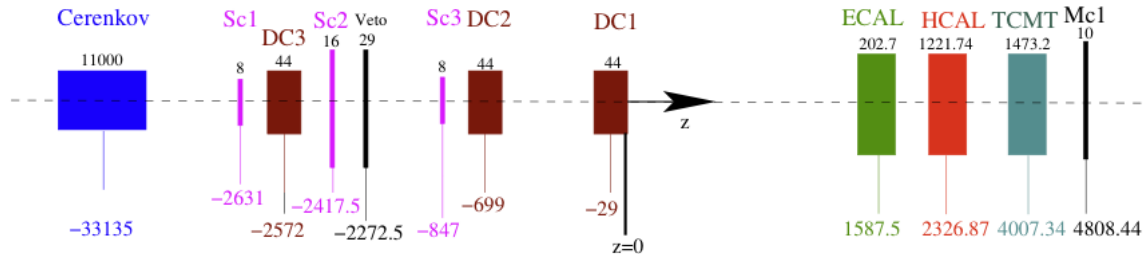


**Figure A.4** – Beam-line configuration for the CERN 2007 test-beam [52]. The numbers on the bottom indicate the positions along the  $z$ -axis, whereas the numbers on top denote the length of the corresponding detector. Dimensions are given in millimetre.

The detector labeled Veto has a size of  $100 \times 100 \text{ cm}^2$  with an opening in the middle of the size  $20 \times 20 \text{ cm}^2$ . It is mainly used to tag particles with a beam halo so that these events can be excluded in the offline analysis.

### 3. Tracking system

The tracking system consists of three drift chambers DC1 – DC3. By measuring the coordinates of particle passage, it is possible to reconstruct the corresponding tracks and the point of incidence in the calorimetric system. The endpoint of DC1 serves as the origin of the test-beam coordinate system.

### 4. Calorimeter system

This system contains the detector prototypes under development. In analogy to a real detector configuration in a high energy physics experiment, the detector prototypes are ordered beginning with an electromagnetic calorimeter (ECAL), the hadronic calorimeter prototype (HCAL), and a tail catcher and muon tagger (TCMT), used to determine shower leakage and to tag muons. This configuration allows for the development of particle flow energy reconstruction algorithms which require the information of all three detectors.

The QGSP-BERTINI physics list is used to implement the physics processes in the simulation. Two particle shower types are simulated: purely electromagnetic, and hadronic showers. The former ones are generated by positrons, whereas the latter ones are produced by shooting positive pions into the calorimeter. In each case, the particles hit the approximate centre of the first layer of the calorimeter in  $z$ -direction.

## A.5 Digitisation

It is a common practise in high energy physics, that not the complete process of signal generation – starting with an energy deposition in the detector, ending with the digital ADC values generated by the readout electronics – is implemented into the detector simulation. Only the fundamental particle interactions and energy depositions are simulated. In a second subsequent step denoted ‘digitisation’, the Monte Carlo is corrected for detector effects like non-uniformities in response, noise, and statistical fluctuations. The result of this correction is a Monte Carlo sample which can be treated and analysed in the same way as the measured test-beam data.

### Ganging

In the Geant4 simulation, the energy depositions in the active calorimeter layers are summed up within virtual cells of an equal size of  $1 \times 1 \times 0.5 \text{ cm}^3$ . In the ganging step of the digitisation process, the energy depositions are grouped according to the actual tile sizes used in the calorimeter (cf. Figure 2.5).

### Light Cross-talk Between Neighbouring Tiles

In the real detector prototype, the optical isolation of the scintillator tiles is not ideal, which allows small amounts of light to leak into neighbouring tiles. It is assumed that per 3 cm side length of the tile, 2.5 % of the produced scintillation light leaks into the neighbouring tile. The scintillation mechanism is not implemented into the simulation as it would be too time consuming. Hence, the effect of light cross-talk is implemented by distributing the visible energy deposition accordingly between adjacent tiles.

## Conversion to the MIP Scale

The AHCAL prototype is calibrated with a muons, so that energy depositions are measured on the scale of minimum ionising particles (MIP). Hence, the visible energy depositions of the Monte Carlo have to be converted to the MIP scale in order to make them comparable with data. This is achieved by simulating a muon beam in the calorimeter. The most probable energy deposition (*MPV*) of the muon is determined by fitting a Landau function to the hit energy spectrum. Its inverse serves as the conversion factor from the energy depositions of the simulation (GeV) to the MIP scale of the data.

It should be emphasised that the *MPV* of a muon reveals a slight dependence on the value of Birks' coefficient applied in the simulation. As a consequence, the *MPV* also depends on the secondary particle production cut  $T_{\text{cut}}$  introduced in section 2.3, as the relation between the energy deposition and the visible energy determined by Birks' law is non-linear. The dependence of the *MPV* on the value of  $kB$  and the calculation method of visible energy is determined in section A.6.

## SiPM Non-linearity and Statistical Fluctuations

As it is shown in Figure 3.12, the maximum number of photons detectable with a SiPM is fundamentally limited by its number of pixels. This effect results in a non-linear dependence which is implemented into the digitisation. Statistical fluctuations of the photo-detection process are implemented in digitisation by smearing the signal using Poisson statistics.

## Noise

To account for the detector noise, such as the SiPM dark-rate, the electronics noise, or single cells (hot spots) which always give a signal, a special noise run is acquired for each data-taking run. During a noise run, the calorimeter readout is triggered randomly, resulting in an almost pure noise data sample. The noise value of each cell in ADC counts is determined by subtracting the individual pedestal value. The noise events are then added cell by cell to the simulated events, which are transferred to the ADC scale for this purpose, using the SiPM gain and MIP calibration constants.

## A.6 GeV to MIP Conversion

In order to compare the Monte Carlo with the data acquired with the calorimeter prototype, the digitisation procedure must be applied to simulation results. Within this process, the conversion from the energy scale (GeV) to the MIP scale has to be adapted when the value of  $kB$  is changed; the conversion factor depends on the value of  $kB$  applied in the simulation. For this reason, it was studied how the measured  $kB$  value and the improved calculation method of visible energy influences the ‘MIP per GeV’ conversion factor. For this purpose, muons traversing the calorimeter with momenta of 30, 80 and 130 GeV/c are simulated and the energy spectra of the individual visible energy depositions in the active calorimeter layers are recorded. The spectra of the 80 GeV/c muons is shown in Figure A.5 for the different configurations of the simulation. A Landau fit is applied to each spectrum in order to determine the most probable value (*MPV*) of energy deposition. The summary of results in Table A.1 reveals a slight dependence of the *MPV* on the value of  $kB$  used; i.e. the *MPV* differs by  $\sim 1\%$ . The calculation method has as expected no significant impact on the *MPV* as the  $dE/dx$  of

muons remains due to the small energy loss approximately constant during the passage of the calorimeter. The improved calculation method on the other hand is expected to give a large contribution when the  $dE/dx$  changes rapidly during simulation steps (cf. Figure 2.12).

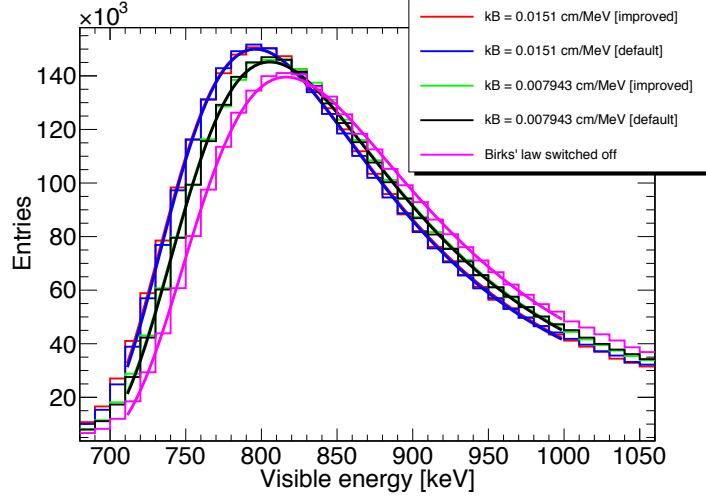


**Figure A.5** – Simulated visible hit energy spectrum of 80 GeV/c muons traversing the calorimeter. A difference between the spectra for different  $kB$  values is visible, whereas the improved calculation method has no impact, as the  $dE/dx$  of the muons is approximately constant.

**Table A.1** – Summary of the most probable energy values ( $MPV$ ) of muons with a momentum of 30, 80, and 130 GeV. The  $MPV$  depends on the  $kB$  value used, but it is independent on the calculation method of visible energy ([default] or [improved]).

$kB$ [ $10^{-2}$ cm/MeV] [method]	$MPV$ [keV] (30 GeV $\mu^-$ )	$MPV$ [keV] (80 GeV $\mu^-$ )	$MPV$ [keV] (130 GeV $\mu^-$ )
1.51 [improved]	805.5	806.2	806.8
1.51 [default]	805.7	806.3	807.1
0.7943 [improved]	815.3	816.2	816.8
0.7943 [default]	815.5	816.1	816.6
Birks' law switched off	826.4	827.3	827.7

## A.7 SiPM Active Area

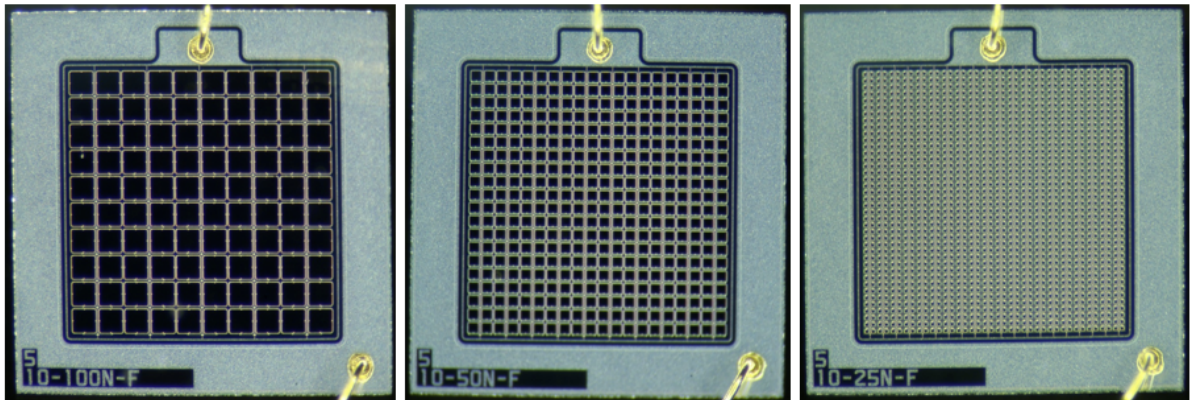


**Figure A.6** – Pictures of three different SiPM detectors (Hamamatsu MPPC): (left)  $100\text{ }\mu\text{m}$  pitch, (centre)  $50\text{ }\mu\text{m}$  pitch, (right)  $25\text{ }\mu\text{m}$  pitch.

## A.8 Gain Calibration Factor

Calibration from the QDC-channel unit to the gain scale is achieved by multiplication with the following conversion factor:

$$f = \frac{256\text{ pC}}{1024\text{ QDC-ch.} \cdot 50 \cdot q_e} = 31211 \left[ \frac{1}{\text{QDC-ch.}} \right], \quad (\text{A.1})$$

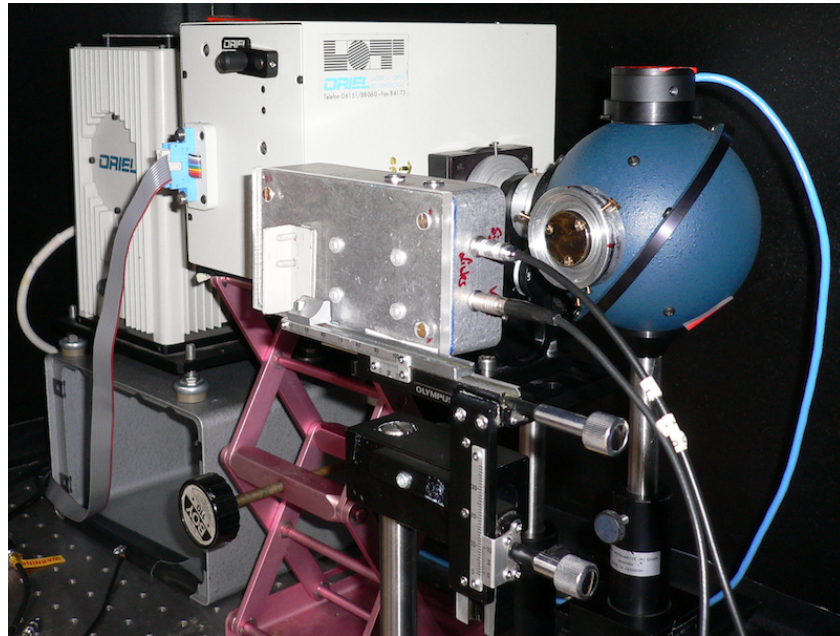
where 256 pC corresponds to the charge value of the 1024th QDC-channel and 50 denotes the signal amplification factor.  $q_e$  denotes the elementary charge.

## A.9 Pixel Recovery Time

**Table A.2** – MPPC pixel recovery times. The data has been taken from Ref. [94].

SiPM	Pixel pitch [ $\mu\text{m}$ ]	$\tau_r$ [ns]
S10362-11-025C	25	4
S10362-11-050C	50	9
S10362-11-100C	100	33

## A.10 PDE Measurement Setup



(a)



(b)

**Figure A.7** – Figure (a) shows a photograph of the PDE measurement setup. The displayed configuration is used to measure the relative spectral sensitivity of SiPMs. The main components are (from left to right) a xenon-lamp, a monochromator and an integrating sphere. An optical filter wheel in between the monochromator and the sphere blocks the higher order wavelengths ( $\lambda_i = \lambda/i$ ), which would otherwise bias the spectral measurement. The integrating sphere is equipped on the top connector port with a calibrated photosensor. The port in front of the sphere is covered with an aperture of 0.8 mm, or 0.6 mm diameter. For the measurement, the SiPM is aligned in front of the aperture such that the signal is maximal. Figure (b) shows a photograph of the unmounted integrating sphere and the calibrated photodiode. On the left port, the light source can be connected whereas the remaining two ports are used to couple the calibrated photodiode and the SiPM.

### A.11 Spectral Response of the PIN Photodiode and LED Emission Spectra

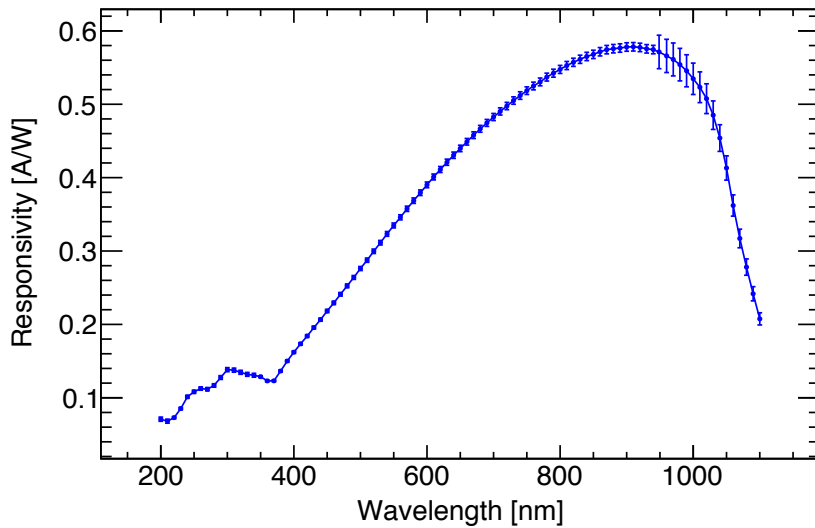


**Figure A.8** – Responsivity of the calibrated PIN photodiode used for the PDE measurement (Model Newport 818UV).

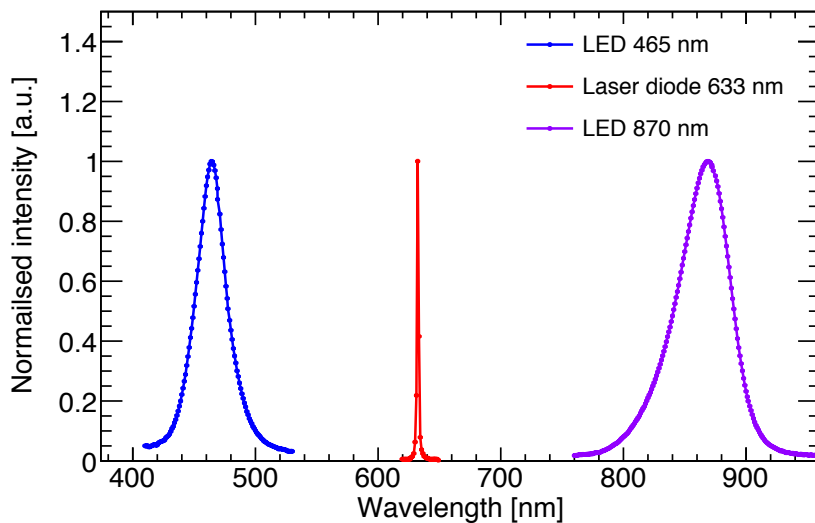


**Figure A.9** – Normalised emission spectra of two LEDs and one laser diode. The spectrum of the laser diode has a much smaller line width compared to the LEDs.

## A.12 Uniformity Scan Setup

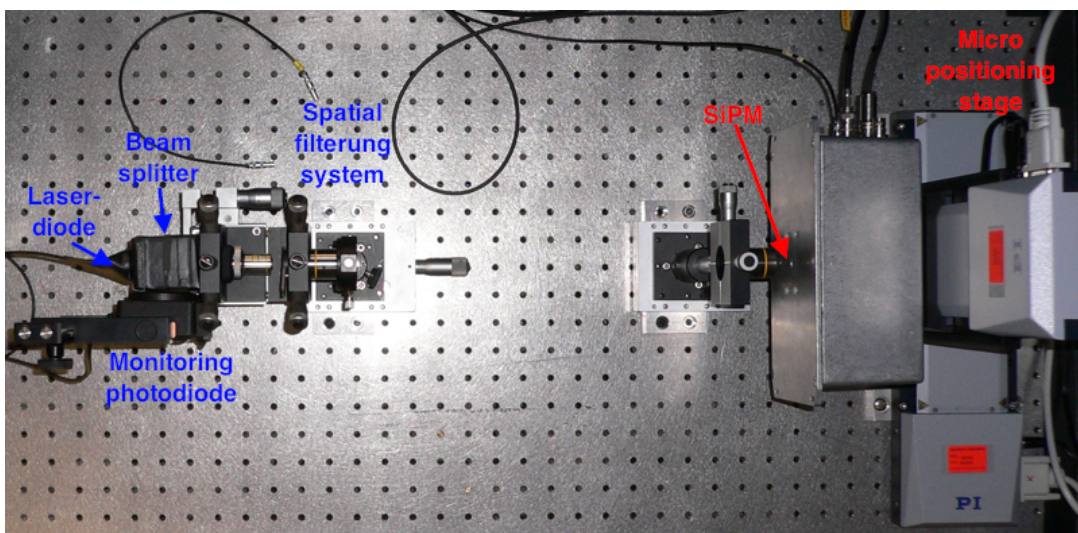


**Figure A.10** – Photograph of the experimental setup used to measure the uniformity of the SiPM pixels.

### A.13 Determination of the Geometrical Efficiency

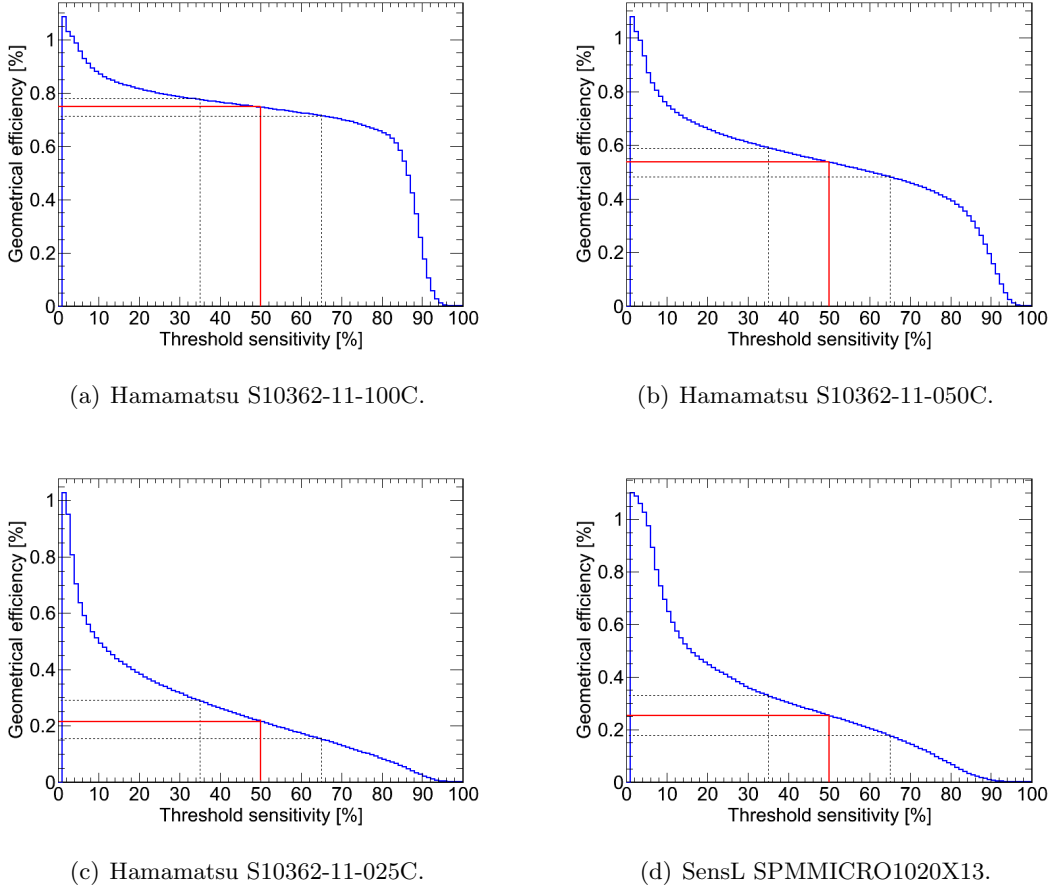
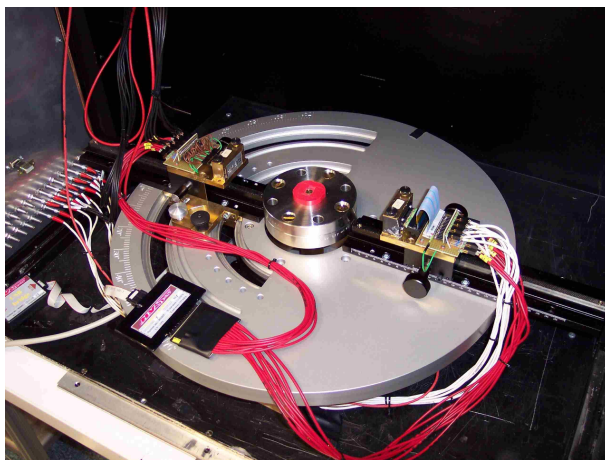


**Figure A.11** – Dependency of the geometrical efficiency  $\epsilon_{\text{geo}}$  on the value of the applied threshold sensitivity which represents the border between sensitive and insensitive areas of the SiPM surface. The dashed lines indicate the uncertainties of the estimated geometrical efficiencies, which is indicated by the red line. In case of the S10362-11-100C and the S10362-11-050C, a clear separation between active and inactive regions is possible as indicated in figures (a) and (b). In case of the smaller pixel devices S10362-11-025C and SPMMICRO1020X13, the transition between active and inactive regions is continuous, resulting in a larger measurement uncertainty.

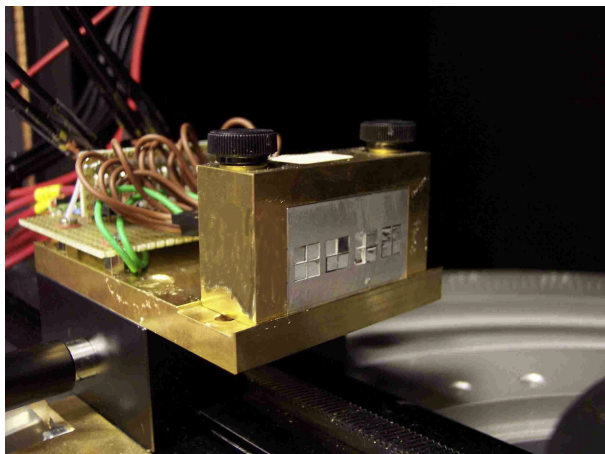
### A.14 Effect at Small Sensitivity Thresholds

The reason for the observation of a geometrical efficiency larger than 100 % at very small threshold values is that the total scanning area of the sensitivity measurement is larger than the total active SiPM area. For the normalisation described in Equation 4.25, however only the (smaller) active area of the SiPM is considered. For very low thresholds, the regions outside of the active SiPM area are also considered as ‘sensitive’ which results in the observed increase of  $\epsilon_{\text{geo}}$ . However, this effect doesn’t play a role at the 50 % threshold chosen for the determination of the geometrical efficiency.

## A.15 Development of a PET Prototype



(a) Photograph of the PET prototype.



(b) Photograph of one detector head.

**Figure A.12** – Figure (a) shows a Photograph of the fully commissioned PET prototype. The two opposing detector modules are mounted on an aluminium base plate. Figure (b) shows a photograph of one detector module. Only the lower row of the module is equipped with scintillating crystals. The visible side of each individual crystal is covered by a highly reflective foil.



# Nomenclature

AHCAL	analogue hadronic calorimeter
ALEPH	Apparatus for LEP Physics at CERN
APD	avalanche photodiode
CALICE	Calorimetry for the next linear collider experiment
CAMAC	Computer Automated Measurement and Control
CERN	European Organisation for Nuclear Research
DESY	Deutsches Elektronen Synchrotron
ENF	excess noise factor
G-APD	geiger mode APD
HERA	Hadron-Electron Ring Accelerator
ILC	International Linear Collider
LEP	Large Electron Positron Collider
LFS	Lutetium Fine Silicate
LHC	Large Hadron Collider
MAPD	multi pixel avalanche photodiode
MCP	micro channel plates
MEPhI	Moscow Engineering Physics Institute
MPPC	multi pixel photon counter
MRI	magnetic resonance imaging
MRS-APD	metal-resistor-semiconductor APD
NAF	National Analysis Facility
PDE	photon detection efficiency
PET	positron emission tomography
PFA	particle flow algorithm
PMT	photomultiplier tube

PPD	pixelated photon detector
QDC	charge to digital converter
QE	quantum efficiency
SiPM	silicon photomultiplier
SPAD	single pixel avalanche diode
SSPM	solid state photomultiplier
STiC	SiPM timing chip
TOF	time-of-flight

# Bibliography

- [1] H. Iams and B. Salzberg, “The secondary emission phototube,” *Proceedings of the Institute of Radio Engineers*, vol. 23, pp. 55–64, January 1935.
- [2] B. Lubsandorzhev, “On the history of photomultiplier tube invention,” *Nucl. Instr. and Meth. A*, vol. 567, pp. 236–238, June 2006.
- [3] C. Adloff *et al.*, “Construction and commissioning of the CALICE analog hadron calorimeter prototype,” *JINST*, vol. P05004, 2010.
- [4] P. Eckert *et al.*, “Characterisation studies of silicon photomultipliers,” *Nucl. Instr. and Meth. A*, vol. 620, pp. 217–226, August 2010.
- [5] S. Agostinelli *et al.*, “Geant4—a simulation toolkit,” *Nucl. Instr. and Meth. A*, vol. 506, pp. 250–303, 2003.
- [6] J. Allison *et al.*, “Geant4 developments and applications,” *IEEE Trans. Nucl. Sc.*, vol. 53, no. 1, pp. 270–278, 2006.
- [7] J. B. Birks, *The Theory and Practise of Scintillation Counting*. Pergamon Press, 1964.
- [8] D. Buskulic *et al.*, “Performance of the ALEPH detector at LEP,” *Nucl. Instr. and Meth. A*, vol. 360, pp. 481–506, June 1995.
- [9] M. A. Thomson, “Particle flow calorimetry and the PandoraPFA algorithm,” *Nucl. Instr. and Meth. A*, vol. 611, pp. 25–40, November 2009.
- [10] K. Deiters *et al.*, “Properties of the most recent avalanche photodiodes for the CMS electromagnetic calorimeter,” *Nucl. Instr. and Meth. A*, vol. 442, pp. 193–197, March 2000.
- [11] “ENDO TOFPET US: Endoscopic TOFPET & Ultrasound.” <https://endotofpet-us.web.cern.ch/endotofpet-us/cms/index.php?file=home>, (July 2011).
- [12] “Calorimetry.” <http://en.wikipedia.org/wiki/Calorimetry>, July 2011.
- [13] N. Akchurin *et al.*, “Hadron and jet detection with dual-readout calorimeter,” *Nucl. Instr. and Meth. A*, vol. 537, pp. 537–561, February 2005.
- [14] K. Nakamura *et al.*, “Passage of particles through matter,” *JPG*, vol. 37, no. 070521, 2010.
- [15] S. M. Seltzer and M. J. Berger, “Evaluation of the collision stopping power of elements and compounds for electrons and positrons,” *Int. J. Appl. Radiat. Isot.*, vol. 33, pp. 1189–1218, 1982.
- [16] S. M. Seltzer and M. J. Berger, “Improved procedure for calculating the collision stopping power of elements and compounds for electrons and positrons,” *Int. J. Appl. Radiat. Isot.*, vol. 35, no. 7, pp. 665–676, 1984.

- [17] C. Grupen, *Teilchendetektoren*. BI-Wiss.-Verl., 1993.
- [18] R. Wigmans, *Calorimetry*. Oxford University Press, 2000.
- [19] W. Lohmann *et al.*, “Energy loss of muons in the energy range 1–10,000 GeV,” *CERN*, vol. 85-03, March 1985.
- [20] C. Grupen and B. Schwartz, *Particle Detectors*. Cambridge Monographs on Particle Physics, Nuclear Physics and Cosmology 26, 2 ed., 2008.
- [21] K. Rajkhanan *et al.*, “Absorption coefficient of silicon for solar cell calculations,” *Solid-State Electronics*, vol. 22, pp. 793–795, 1979.
- [22] T. A. Gabriel *et al.*, “Energy dependence of hadronic activity,” *Nucl. Instr. and Meth. A*, vol. 338, pp. 336–347, 1994.
- [23] F. Pauli, ed., *Instrumentation in High Energy Physics*. Worls Scientific Publishing Co. Pte. Ltd., 1992.
- [24] K. Nakamura *et al.*, “Particle detectors at accelerators,” *JPG*, vol. 37, no. 075021, 2010.
- [25] “The benzene molecule.” <http://en.wikipedia.org/wiki/File:Benzene-2D-full.svg>, (September 2011).
- [26] “Trigonal planar structure.” <http://en.wikipedia.org/wiki/File:AX3E0-3D-balls.png>, (September 2011).
- [27] H. Spieler, “Introduction to radiation detectors and electronics.” Lecture Notes - Physics 198, UC Berkeley, 1998.
- [28] T. Kamon *et al.*, “A new scintillator and wavelength shifter,” *Nucl. Instr. and Meth.*, vol. 213, pp. 261–269, 1983.
- [29] P. Lecoq, “Scintillators – fundamentals.” Talk given at the EDIT2011 school on instrumentation in high energy physics, <http://indico.cern.ch/getFile.py/access?contribId=4&resId=0&materialId=slides&confId=124380>, February 2011.
- [30] V. A. Kozlov, “LFS-3 - new radiation hard scintillator for electromagnetic calorimeters,” *arXiv:0912.0366v1 [physics.ins-det]*, December 2009.
- [31] The CALICE collaboration, “A high granularity calorimeter system optimised for the particle flow measurement of multi-jet final states at the ILC running, with centre-of-mass energy between 90 GeV and 1 TeV.” <https://twiki.cern.ch/twiki/bin/view/CALICE/>, (August 2011).
- [32] A. Kaplan, *Hadronic Imaging Calorimetry*. PhD thesis, Kirchhoff-Institut für Physik – Universität Heidelberg, 2011.
- [33] The CALICE collaboration, “Tests of a particle flow algorithm with calice test beam data,” *JINST*, vol. 6, no. P07005, 2011.
- [34] “Picture of the AHCAL prototype at the CERN testbeam.” <http://www-flc.desy.de/hcal/cerntestbeam/img075.jpeg>, (July 2011).

- [35] J. I. Hopkins, "The response of the anthracene scintillation counter to monoenergetic electrons," *Phys. Rev.*, vol. 77, no. 3, pp. 407–407, 1950.
- [36] J. I. Hopkins, "Electron energy studies with the anthracene scintillation counter," *The Review of Scientific Instruments*, vol. 22, no. 1, pp. 29–33, 1951.
- [37] F. X. Roser and T. Bowen, "The problem of using scintillation crystals as proportional counters for high energy particles," *Phys. Rev.*, vol. 82, pp. 284–285, 1951.
- [38] J. B. Birks, "Scintillations from organic crystals: Specific fluorescence and relative response to different radiations," *Proceedings of the Physical Society*, vol. 64, pp. 874–877, 1951.
- [39] G. T. Wright, "Scintillation response of organic phosphors," *Phys. Rev.*, vol. 91, no. 5, pp. 1282–1283, 1953.
- [40] R. V. et al., "Influence of the nature of ionizing particles on the specific luminescence of organic scintillators," *The Journal of Chemical Physics*, vol. 45, no. 9, pp. 3306–3311, 1966.
- [41] C. N. Chou, "The nature of the saturation effect of fluorescent scintillators," *Phys. Rev.*, vol. 87, no. 5, pp. 904–905, 1952.
- [42] R. L. Craun and D. L. Smith, "Analysis of response data for several organic scintillators," *Nuclear Instruments and Methods*, vol. 80, no. 2, pp. 239–244, 1970.
- [43] M. J. Berger et al., "ESTAR, PSTAR, and ASTAR: Computer programs for calculating stopping-power and range tables for electrons, protons, and helium ions (version 1.2.3, 2005)." <http://physics.nist.gov/Star>, (May 2011).
- [44] S. Wagner, "Ionization quenching by low energy electrons in the double chooz scintillators," diploma thesis, Max-Planck-Institut für Kernphysik – Heidelberg, 2010.
- [45] C. Aberle et al., "Light output of Double Chooz scintillators for low energy electrons," *to be published in JINST*, 2011.
- [46] "ROOT – a data analysis framework." <http://root.cern.ch/drupal/>, (September 2011).
- [47] M. Hirschberg et al., "Precise measurement of birks kB parameter in plastic scintillators," *IEEE Trans. Nucl. Sc.*, vol. 39, no. 4, pp. 411–514, 1992.
- [48] *Geant4 Physics Reference Manual Version 4.9.3*, December 2009.
- [49] P. de Freitas et al., "MOKKA, a detailed Geant4 simulation for the International Linear Collider detectors." <http://polzope.in2p3.fr:8081/MOKKA/>, (April 2011).
- [50] V. Ivanchenko, "G4EmSaturation, v. February 2008." <http://www-geant4.kek.jp/lxr/source/processes/electromagnetic/utils/src/G4EmSaturation.cc?v=9.3>, (September 2011).
- [51] M. Galassi et al., *GNU Scientific Library Reference Manual*. Network Theory Ltd., 3rd ed., January 2009.
- [52] A. Lucaci-Timoce, "Description of the Analog HCAL prototype in Mokka," November 2009.

- [53] “Photomultiplier tube image.” <http://upload.wikimedia.org/wikipedia/commons/thumb/5/52/Photomultipliertube.svg/2000px-Photomultipliertube.svg.png>, (August 2011).
- [54] K. Arisaka, “New trends in vacuum-based photon detectors,” *Nucl. Instr. and Meth. A*, vol. 442, pp. 80–90, 2000.
- [55] Kwok K. Ng, *Complete Guide to Semiconductor devices*. New York: John Wiley & Sons, second ed., 2002.
- [56] R. J. McIntyre, “The distribution of gains in uniformly multiplying avalanche photodiodes: Theory,” *IEEE Trans. Nucl. Sc.*, vol. 19, pp. 703–713, 1972.
- [57] R. J. McIntyre, “Multiplication noise in uniform avalanche diodes,” *IEEE Trans. Electron Dev.*, vol. 13, pp. 164–168, 1966.
- [58] D. Renker and E. Lorenz, “Advances in solid state photon detectors,” *JINST*, vol. P04004, 2009.
- [59] T. Frach *et al.*, “The digital silicon photomultiplier — principle of operation and intrinsic detector performance,” *IEEE Nucl. Sci. Conf. R. (NSS/MIC)*, pp. 1959 – 1965, 2009.
- [60] R. H. Haitz, “Model for the electrical behavior of a microplasma,” *J. Appl. Phys.*, vol. 35, p. 1370, 1964.
- [61] R. J. McIntyre, “Theory of microplasma instability in silicon,” *J. Appl. Phys.*, vol. 32, p. 983, 1961.
- [62] P. Buzhan *et al.*, “An advanced study of silicon photomultiplier,” *ICFA Instrum. Bull.*, vol. 23, pp. 28–41, 2001.
- [63] P. Eckert, “Tile tester status and sipm simulation.” Talk given at the CALICE week in Heidelberg, <http://ilcagenda.linearcollider.org/contributionDisplay.py?sessionId=20&contribId=38&confId=5213>, (September 2011).
- [64] V. Andreev *et al.*, “A high-granularity scintillator calorimeter readout with silicon photomultipliers,” *Nucl. Instr. and Meth. A*, vol. 540, pp. 368–380, 2005.
- [65] P. Eckert, “Advanced silicon-photomultiplier characterization for calorimetric applications,” diploma thesis, Kirchhoff-Institut für Physik – Universität Heidelberg, 2010.
- [66] R. Newman, “Visible light from a silicon p-n junction,” *Phys. Rev.*, vol. 100, pp. 700–703, June 1955.
- [67] A. G. Chynowth and K. G. McKay, “Photon emission from avalanche breakdown in silicon,” *Phys. Rev.*, vol. 102, pp. 369–376, January 1956.
- [68] A. L. Lacaita *et al.*, “On the bremsstrahlung origin of hot-carrier-induced photons in silicon devices,” *IEEE Trans. Electron Dev.*, vol. 40, pp. 577–582, March 1993.
- [69] C. Joram, “Photo-detection – principles, performance and limitations.” Talk given at the EDIT2011 school on instrumentation in high energy physics, <http://indico.cern.ch/getFile.py/access?contribId=0&resId=1&materialId=slides&confId=124395>, February 2011.

- [70] P. Buzhan *et al.*, “Silicon photomultipliers and its possible applications,” *Nucl. Instr. and Meth. A*, vol. 504, p. 48ff., 2003.
- [71] A. G. Stewart, “Performance of 1mm<sup>2</sup> silicon photomultipliers.” [http://www.ptbmagazine.com/features/2008/feat1\\_0508.html](http://www.ptbmagazine.com/features/2008/feat1_0508.html), (August 2011).
- [72] A. Tadday, “Characterisation of silicon photomultipliers,” Diploma thesis, Kirchhoff-Institut für Physik – Universität Heidelberg, March 2008.
- [73] “SPMMICRO datasheet, Rev. Jan-10.” [http://www.azimp.ru/pdf/sensl/spmmicro\\_datasheet.pdf](http://www.azimp.ru/pdf/sensl/spmmicro_datasheet.pdf), (September 2011).
- [74] “LeCroy CAMAC model 2249A 12 channel A-to-D converter.” <http://www.fnal.gov/projects/ckm/jlab/2249a-spec.htm>, (August 2011).
- [75] “An introduction to CAMAC.” <http://www-esd.fnal.gov/esd/catalog/intro/introcams.htm>, (August 2011).
- [76] V. Balagura *et al.*, “Study of scintillator strip with wavelength shifting fiber and silicon photomultiplier,” *Nucl. Instr. and Meth. A*, vol. 564, pp. 590–596, May 2006.
- [77] “Spectralon diffuse reflectance standards.” <http://www.labsphere.com/products/reflectance-standards-and-targets/spectralon-reflectance-standards/default.aspx>, (September 2011).
- [78] F. Simon and C. Soldner, “Uniformity studies of scintillator tiles directly coupled to SiPMs for imaging calorimetry,” *Nucl. Instr. and Meth. A*, vol. 620, pp. 196–201, August 2010.
- [79] G. Blazey *et al.*, “Directly coupled tiles as elements of a scintillator calorimeter with MPPC readout,” *Nucl. Instr. and Meth. A*, vol. 605, pp. 277–281, April 2009.
- [80] F. Abu-Ajamieh *et al.*, “Beam tests of directly coupled scintillator tiles with MPPC readout,” *Nucl. Instr. and Meth. A*, (article in press), 2011.
- [81] G. Bonanno *et al.*, “Precision measurements of photon detection efficiency for sipm detectors,” *Nucl. Instr. and Meth. A*, vol. 610, no. 1, pp. 93–97, 2009.
- [82] H. Miyamoto *et al.*, “Talk given at 11th pisa meeting on advanced detectors,” May 2009.
- [83] N. Dinu *et al.*, “Electro-optical characterization of sipm: A comparative study,” *Nucl. Instr. and Meth. A*, vol. 610, no. 1, pp. 423–426, 2009.
- [84] “Multi pixel photon counter (MPPC) product information.” <http://sales.hamamatsu.com/en/products/solid-state-division/si-photodiode-series/mppc.php>, (September 2011).
- [85] D. L. Bailey *et al.*, eds., *Positron Emission Tomography: Basic Sciences*. Springer London, 2005.
- [86] V. C. Spanoudaki and C. S. Levin, “Photo-detectors for time of flight positron emission tomography (ToF-PET),” *Sensors*, vol. 10, pp. 10484–10505, September 2010.
- [87] W. Moses, “Recent advances and future advances in time-of-flight PET,” *Nucl. Instr. and Meth. A*, vol. 580, pp. 919–924, 2007.

## Bibliography

---

- [88] W. Moses, “Advantages of improved timing accuracy in PET cameras using LSO scintillator,” *IEEE Nucl. Sci. Conf. R.*, vol. 3, pp. 1670–1675, November 2002.
- [89] M. Balcerzyk *et al.*, “YSO, LSO, GSO and LGSO. A study of energy resolution and nonproportionality,” *IEEE Trans. Nucl. Sc.*, vol. 47, pp. 1319 – 1323, August 2000.
- [90] H. O. Anger, “Scintillation camera with multichannel collimators,” *J. Nucl. Med.*, vol. 5, pp. 515–531, 1964.
- [91] E. Auffray *et al.*, “Towards a time-of-flight positron emission tomography system based on multi-pixel photon counter read-out,” *IEEE Nucl. Sci. Conf. R. (NSS/MIC)*, 2010.
- [92] W. Shen and H.-C. Schultz-Coulon, “STIC – a current mode constant fraction discriminator for positron emission tomography using SiPMs (MPPC),” *IEEE Nucl. Sci. Conf. R. (NSS/MIC)*, pp. 364–367, 2009.
- [93] W. Shen and H.-C. Schultz-Coulon, “STIC – an ASIC CHIP for silicon-photomultiplier fast timing discrimination,” *IEEE Nucl. Sci. Conf. R. (NSS/MIC)*, pp. 406–408, 2010.
- [94] H. Oide *et al.*, “Study of afterpulsing of MPPC with waveform analysis,” *Proceedings of Science*, vol. PoS(PD07)008, June 2007.

# Danksagung

Mit der Fertigstellung dieser Doktorarbeit neigt sich ein bedeutender Lebensabschnitt langsam dem Ende zu. Aus diesem Grund ist es für mich an der Zeit den Menschen zu danken, welche mir in den letzten Jahren mit Ihrer Unterstützung geholfen haben und somit einen großen Anteil an dem erfolgreichen Abschluss dieser Arbeit haben.

Ich möchte meinem Doktorvater Herrn Prof. Dr. Hans-Christian Schultz-Coulon für das ermöglichen dieser Arbeit danken. Sein großes Interesse und die Freude an der Physik, welche er mir in vielen motivierenden Gesprächen vermittelt hat, hatten einen großen Einfluss auf die hier vorgestellte Arbeit. Außerdem möchte ich mich für die freundschaftliche und verständnisvolle Atmosphäre bei der Betreuung bedanken.

Herrn Prof. Dr. Norbert Herrmann gilt mein besonderer Dank für die Bereitschaft diese Arbeit als Zweitgutachter zu bewerten. Zusätzlich möchte ich mich für die vielen interessanten Diskussionen im Rahmen des Graduiertenkollegs *Entwicklung und Anwendung der intelligenten Detektoren* bedanken. Dem Graduiertenkolleg verdanke ich zudem einen großen Teil der Finanzierung dieser Arbeit.

Bei Herrn Dr. Rainer Stamen bedanke ich mich für die gute Betreuung, die vielen interessanten Gespräche über aktuelle Themen der Physik und die Beratung bei komplizierten Aufgabenstellungen. Außerdem möchte ich mich für das geduldige Korrekturlesen dieser Arbeit bedanken.

Frau Dr. Erika Garutti danke ich für die schöne und lehrreiche Zeit am DESY in Hamburg, sowie für die vielen guten Ideen und Vorschläge zu den behandelten Arbeitsthemen.

Ich danke den Mitgliedern der gesamten ILC, ATLAS und H1 Gruppen am *Kirchhoff-Institut für Physik* für die tolle Arbeitsatmosphäre und für die vielen gemeinsam verbrachten Stunden beim Institutsgrillen, beim Feiern in der Altstadt, Kickern, Kubb spielen, Wasserskifahren ...

Nicht zuletzt möchte ich mich bei meiner gesamten Familie für die langjährige Unterstützung bedanken. Mein ganz besonders herzlicher Dank gilt meiner Frau Stephanie und unserem Sohn Carl-Richard welcher uns jeden Tag aufs neue mit großer Freude erfüllt.